



PHD

## Atomistic Simulation of Oxide Interfaces in Materials for Energy Technologies

Statham, Joel

*Award date:*  
2023

*Awarding institution:*  
University of Bath

[Link to publication](#)

### Alternative formats

If you require this document in an alternative format, please contact:  
[openaccess@bath.ac.uk](mailto:openaccess@bath.ac.uk)

Copyright of this thesis rests with the author. Access is subject to the above licence, if given. If no licence is specified above, original content in this thesis is licensed under the terms of the Creative Commons Attribution-NonCommercial 4.0 International (CC BY-NC-ND 4.0) Licence (<https://creativecommons.org/licenses/by-nc-nd/4.0/>). Any third-party copyright material present remains the property of its respective owner(s) and is licensed under its existing terms.

#### Take down policy

If you consider content within Bath's Research Portal to be in breach of UK law, please contact: [openaccess@bath.ac.uk](mailto:openaccess@bath.ac.uk) with the details. Your claim will be investigated and, where appropriate, the item will be removed from public view as soon as possible.

# **Atomistic Simulation of Oxide Interfaces in Energy Technologies**

**A Thesis Submitted for the degree of Doctor of Philosophy**

**Joel Mark Statham**

**Supervisor: Professor Steve Parker**

**University of Bath**

**September 2019**

## **COPYRIGHT**

Attention is drawn to the fact that copyright of this thesis rests with the author. A copy of this thesis has been supplied on condition that anyone who consults it is understood to recognise that its copyright rests with the author and that they must not copy it or use material from it except as permitted by law or with the consent of the author

## Abstract

Materials used for energy conversion applications normally have a complex microstructure and the resulting interfaces within materials profoundly affect their properties. In this project the aim was to develop a tool for investigating such interfaces at the atomic level. The research carried out focuses primarily on four materials; strontium titanate, cerium dioxide, lithium lanthanum titanate and lithium lanthanum zirconate. Current research into energy applications has focussed on the improvement of solid oxide fuel cells (SOFCs) and lithium ion batteries (LIBs) in a variety of different ways, an example of such is the lowering of the operating temperature. Research into the structural and transport properties of bulk materials have been extensive; however, the study of interfaces in these materials has been less prevalent. A model has developed which allows the investigation of grain boundary structures and their effect on the transport properties at the interface.

The focus of this research was initially to develop a method with which we could accurately obtain the structure of grain boundary models for homogenous crystal lattices where a number of different interface models were obtained, some of which have been observed experimentally. The approach to achieving this was through energy minimisation techniques combined with a number of different interatomic potential models where the stability of a boundary could be quantified along with an accurate structural representation. This was further expanded on through molecular dynamics simulations, to investigate the role of the interface and how the local structure influences anionic and cationic diffusion.

Chapter 1 is an overarching review of the relevant literature related to each material, covering predominantly SOFCs and LIBs, with other supporting information. Chapter 2 summarises the computational methodologies used and how energy minimisation and molecular dynamics can be applied to generate structural models. Chapter 3 describes the investigation into the chosen rigid ion interatomic potential models and justifies the case for using each particular model with comparisons to a number of experimentally observed structural, elastic and dynamic properties. Chapters 4 and 5 focus on the interfaces of ceria and strontium titanate, respectively. A work flow was developed and further used to accurately model grain boundaries which are consistent with those observed experimentally. In each case the oxygen transport is suppressed by the presence of grain boundaries. Chapter 6 will expand on the previous two by considering heterointerfaces of STO || CeO<sub>2</sub> including the incorporation of defects to determine the effect this has on both diffusion and stability. Chapters 7 and 8 will describe work on modelling lithium diffusion in bulk and selected grain boundary dynamics of LLTO and LLZO. Each chapter investigates the bulk and how intrinsic and extrinsic dopants can be incorporated in order to enhance lithium ion diffusion and further grain boundaries

of the LIB electrolyte materials. Chapter 9 will conclude this research and will discuss the major findings, the consequences of these findings and how they may be used to drive future research in the field.



***“Seek strength, the rest will follow...”***

- King Vendrick

## Contents

<b>1 Literature Review</b>	8
1.1 Strontium Titanate	8
1.2 Cerium Dioxide	16
1.3 Heterointerfaces of STO   CeO <sub>2</sub>	21
1.4 Lithium Lanthanum Titanate	24
1.4 Lithium Lanthanum Zirconate	34
1.5 Aims and Objectives	37
<b>2 Computational Methodology</b>	38
2.1 Potential Models	38
2.2 Energy Minimisation	43
2.3 Molecular Dynamics	47
2.4 Computational Techniques	53
2.5 Dynamical Studies of Bulk and Interfaces	64
<b>3 Potential Model Justification</b>	66
3.1 Background and Justification of Resources	66
3.2 Structural Comparisons	67
3.3 Point Defect Simulations	74
3.4 Bulk Diffusion of Oxygen	80
3.5 Chapter Summary	85
<b>4 Surfaces and Interfaces of Cerium Dioxide</b>	86
4.1 Scan Overview and Interface Structure and Stability	86
4.2 Mixed Interface Stability	100
4.3 Stability of Ceria Boundaries	102
4.4 Intrinsic and Extrinsic Defect Segregation	103
4.5 Molecular Dynamics of Ceria Interfaces	108
4.6 Chapter Summary	110
<b>5 Surfaces and Interfaces of Strontium Titanate</b>	111

5.1 Scan Overview and Interface Structure and Stability	111
5.2 Stability of Strontium Titanate Interfaces	125
5.3 Intrinsic and Extrinsic Defect Segregation	126
5.4 Molecular Dynamics of Strontium Titanate Interfaces	127
5.5 Chapter Summary	130
<b>6 Heterointerfaces of Strontium Titanate and Ceria</b>	131
6.1 Interface Models	131
6.2 (111) SrTiO <sub>3</sub>    (111) CeO <sub>2</sub> Interface Structure	139
6.3 Chapter Summary	142
<b>7 Lithium Lanthanum Titanate</b>	143
7.1 Overview & Simulations of Bulk Phases of LLTO	145
7.2 Sodium Lanthanum Titanate Bulk Investigation	160
7.3 Grain Boundaries of LLTO	161
7.4 Chapter Summary	170
<b>8 Lithium Lanthanum Zirconate</b>	171
8.1 Bulk Simulations of LLZO	172
8.2 Grain Boundaries of LLZO	177
8.3 Chapter Summary	187
<b>9 Conclusions and Future Work</b>	188
9.1 Potential Models	188
9.2 Grain Boundaries of Ceria and Strontium Titanate	189
9.3 Heterogeneous Grain Boundaries of STO    CeO <sub>2</sub>	190
9.3 Bulk and Grain Boundaries of LLTO and LLZO	191
<b>References</b>	194

## **Acknowledgements**

I would like to thank all members of the Parker group, in particular Dr Marco Molinari and Professor Steve Parker for their continuous help, support and guidance throughout this project, without whom it would not have been possible. Further I would like to thank both my internal and external collaborators on all of my publications for their contributions to furthering the research carried out in this project.

I would also like to thank the University of Bath for access to the high-performance computing (HPC) facilities, namely the Balena supercomputer resource. Further I would like to thank the EPSRC for support of the Energy Materials: Computational Solutions Programme Grant lead by Professor M S Islam and the University of Bath contribution to the grant which has funded my studentship.

Finally, I would like to thank my family, friends and Sarah for their continued support over the last four years and in particular during the writing of this thesis.

## **Declaration of Authorship**

I am the author of this thesis, and the work described therein was carried out by myself personally, with the exception of Chapter 7 where the initial bulk structures for the LLTO phases (L10 to L40) were generated using Monte Carlo, by Dr John Purton (Staff Member of the Computational Chemistry Group, Science and Technology Facilities Council).

# 1 Introduction & Literature Review

Perovskite and fluorite oxides are both significantly important in the field of energy technologies<sup>(1, 2)</sup>. There are many studies on the bulk structures of perovskite and fluorite models<sup>(3, 4)</sup>. However, despite their importance to the material properties, the study of interfaces in such materials has been less extensively studied. Therefore, obtaining good structural models of interfaces as well as their effect on the transport properties at the interface are essential when attempting to understand the importance of interfaces in application. When considering a potential application of perovskite and fluorite materials, solid-oxide fuel cells are one of the more extensively researched applications<sup>(5-7)</sup>. The improvement of these fuel cells can be achieved in a variety of ways such as lowering the activation energy or operating temperature which improves the efficiency, running cost and overall safety of the fuel cell.

In this chapter an in depth literature review will be presented covering the materials which will be simulated throughout this research.

## 1.1 Strontium Titanate

Strontium titanate (STO) is a material which is cubic and adopts the known perovskite structure ( $\text{ABO}_3$ ,  $\text{Pm}3\text{m}$  space group), with strontium ions occupying the A-site and titanium ions occupying the B-site. It was initially considered that STO was only a synthetic material until a natural form of the compound, namely Tausonite, was recognised by the International Mineralogical Association (IMA) in 1982.

There have been many previous studies of STO on transport, thermal and electronic properties which are a result of the overall atomistic structure. One such property is the electrical conductivity of STO. Under standard conditions non-defective STO is an electrical insulator<sup>(3)</sup>. However, the introduction of defects or changes in stoichiometry of the structure can result in STO becoming electronically conductive. The electronic properties of both stoichiometric and acceptor doped STO (e.g Fe or Mn at Ti site<sup>(8)</sup>) have been investigated at high temperatures (600 °C-1400 °C) over a range of partial oxygen pressure where upon increasing the electrical conductivity initially decreases yet once a minimum has been passed through an increase in electrical conductivity is observed with an increase in oxygen partial pressure<sup>(2)</sup>. This occurs as a result of the change of semi conducting regions from n-type to p-type with an increase in oxygen partial pressure<sup>(9, 10)</sup>.

One energy application of STO is its performance as a thermoelectric material<sup>(11)</sup>. Thermoelectric energy conversion is the conversion of heat energy into electrical energy which is achieved across a

temperature gradient. Thermoelectric materials are ranked on their figure of merit (ZT) which is described by equation 1.1 where  $ZT > 1$  is considered to be a good candidate for a thermoelectric material<sup>(12)</sup>.

$$ZT = \frac{\sigma S^2 T}{\kappa} \quad (1.1)$$

$\sigma$  represents electrical conductivity,  $S$  represents Seebeck coefficient,  $\kappa$  represents thermal conductivity and  $T$  represents temperature.

As shown in equation 1.1, three factors are considered and therefore three desirable properties are proposed for a candidate thermoelectric material by Ohta<sup>(11)</sup>, which are;

- High Seebeck coefficient – required to obtain a high voltage
- High electrical conductivity – low internal resistance
- Low thermal conductivity – significant temperature gradient across the material

From these three factors STO has been tuned in different ways in order to improve its thermoelectric performance. Ohta *et al.*<sup>(13)</sup> doped STO by  $\text{Nb}^{5+}$  substitutions at the  $\text{Ti}^{4+}$  site. They found that when heating the crystal to 1000 K and incorporating 20% Nb-dopant to form  $\text{SrTi}_{0.8}\text{Nb}_{0.2}\text{O}_3$  (Nb-doped STO), a significant increase in electronical conductivity was observed which resulted in an increase in figure of merit from 0.1 to 0.37 compared to stoichiometric STO. Other dopant incorporation has also been investigated in STO to improve the thermoelectric properties, where a significant decrease in the magnitude of  $S^2\sigma$  was observed by Yamamoto *et al.*<sup>(14)</sup> when  $\text{Sr}^{2+}$  was substituted by  $\text{Ba}^{2+}$  or  $\text{Ca}^{2+}$  dopants. It was concluded that for Nb-doped STO,  $\text{Sr}^{2+}$  substitution could not be used to improve the value of ZT in a bulk crystal.

Doping of STO with lanthanum has been found to increase the electrical conductivity<sup>(15)</sup> and Seebeck coefficient<sup>(16)</sup> with little effect on the thermal conductivity, therefore an improvement in the value of ZT is observed. However, doping with lanthanum can promote the formation of the Ruddlesden-Popper phase of STO,  $(\text{SrO})(\text{SrTiO}_3)_n$  where stoichiometric layers are separated by strontium oxide layers<sup>(17)</sup>. This structure is represented in figure 1.1.

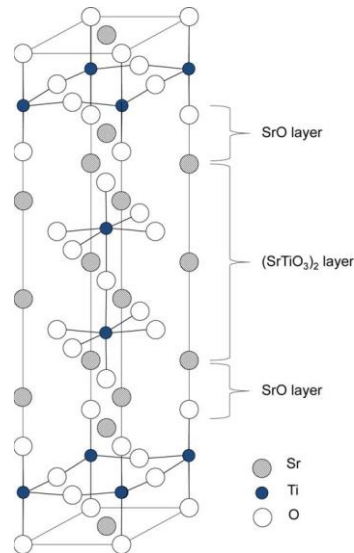


**Figure 1.1** – Ruddlesden-Popper phase of  $(\text{SrO})(\text{SrTiO}_3)_2$ <sup>(17)</sup>

Although a decrease is seen in thermal conductivity of the Ruddlesden-Popper phase of STO, a decrease in electrical conductivity has also been observed which does not result in the improvement of  $ZT$ <sup>(18)</sup>. Other doping schemes have proven successful such as doping with both lanthanum and dysprosium at the Sr site, which has found to increase both Seebeck coefficient and electrical conductivity as well as decrease thermal conductivity<sup>(19)</sup>. Doping with niobium has proven to be more ambiguous. An increase in electrical conductivity has been reported with a similar Seebeck coefficient<sup>(20)</sup>. Differing results on the effect of niobium doping on thermal conductivity have been reported, for example it has been seen to increase<sup>(21)</sup>, decrease<sup>(22)</sup> and have little to no change at all<sup>(20)</sup>.

In real world devices, STO exists in the polycrystalline phase, hence interfaces are a critical component which will affect both doping and conductivity and thus this will affect the  $ZT$  value.

Akhtar *et al.*<sup>(3)</sup> used computer simulations in order to observe the dopant mechanisms for monovalent divalent, trivalent and tetravalent defects in STO in order to potentially improve the electronic conductance. In the case of aliovalent doping mechanisms, charge neutrality was achieved through the incorporation of oxygen vacancies in order to compensate for the excess negative charge. It was found that monovalent, divalent and large trivalent ( $\text{La}^{3+}$ ) as well as tetravalent ( $\text{Th}^{4+}$ ) ions (low charge density) were more likely to substitute at the Sr-sites whereas smaller trivalent ( $\text{Al}^{3+}$ ) and tetravalent ( $\text{Mn}^{4+}$ ) cations (high charge density) were observed to substitute more favourably at the Ti-sites. Cations of intermediate size ( $\text{Yb}^{3+}$ ) were found to exhibit self-compensation mechanisms of substitution thereby occupying both Sr and Ti-sites. Differences between the defect schemes of incorporation for STO and  $\text{BaTiO}_3$  (BTO) were also compared from

previous simulations by Lewis *et al.*<sup>(23)</sup> where all tetravalent ions were found to be energetically favoured to substitute at the Ti sites in BTO. Whereas in STO, tetravalent ions with a larger ionic radius and therefore a smaller charge density were found to be energetically favoured to substitute at the Sr site where electron compensation occurred.

Expanding from the bulk properties, surfaces and interfaces of strontium titanate have proven to be significant in the field of energy materials. For example, in the case of thermoelectrics the presence of interfaces will lower the thermal conductivity and increase the  $ZT$ <sup>(24)</sup>. Surfaces and interfaces exist as an extended defect system from the bulk. Structural characterisation of these features is important; therefore, understanding an interface structure at the atomistic scale can be crucial when investigating mechanical or transport properties at the interface. A large range of experimental and computational techniques have been used in the structural analysis of interface structures in STO. These will be discussed in order to identify the most suitable route for obtaining a reliable grain boundary structure, quickly and efficiently.

Kienzle *et al.*<sup>(25)</sup> investigated the  $\Sigma 3$  (111)/[110] symmetric tilt boundary of polycrystalline STO through both computational and experimental analysis. A  $\Sigma 3$  (111) bicrystal of STO was doped with 0.06% Fe which was used for structural analysis by high-resolution transition electron microscopy (HRTEM) where the images obtained by this procedure were quantitatively analysed in order to develop a refined image of the interface structure. The structure of the interface was also modelled for comparison with the experimental structure using the MIDAS and GULP<sup>(26)</sup> codes with an interatomic potential model. Agreement to within an average precision of 0.015 nm was observed at the interface structure between the computational and experimental structures. It was concluded from the experimental and theoretical study of this  $\Sigma 3$  (111) interface that there was a structural similarity observed between this boundary in STO and NiAl.

Iron doped boundaries of STO were further explored by De Souza<sup>(27)</sup> in order to investigate the atomistic structure as well as the electrical properties of a  $5.4^\circ$  [100] tilt boundary by transmission electron microscopy (TEM) and impedance spectroscopy. Significant impedance was observed at this boundary suggesting high resistivity, which implied that a continuous space charge zone was present at the interface as a result of the segregation of oxygen ions towards dislocation cores.

Benedek *et al.*<sup>(28)</sup> investigated the structure of the  $\text{SrO}_3$   $\Sigma 3$  (111)/[110] boundary as well as two terminations of the  $\Sigma 3$  (112)/[110] boundary, namely the SrTiO-terminated and the O-terminated tilt boundaries, through the use of density functional theory (DFT) with the local density approximation (LDA) using the CASTEP<sup>(29)</sup> code. The structure of each grain boundary was relaxed containing either



60 or 120 atoms where the energy and expansions were obtained. The  $\Sigma 3$  (111) boundary was found to be more energetically stable than the two  $\Sigma 3$  (112) boundaries and in all cases the boundary comprised of 60 atoms was found to be energetically favoured over the boundaries comprised of 120 atoms. The two  $\Sigma 3$  (112) boundaries were found to be comparable in energy however the O-terminated interface exhibited a significantly larger expansion. Interplanar spacing was also investigated where the O-terminated  $\Sigma 3$  (112) interface was found to have the shortest interplanar spacing, as unlike with the SrTiO-terminated (112) interface and the  $\Sigma 3$  (111) interface, this structure did not bring together two species of like charge at the boundary. The three boundary systems were also investigated using four interatomic potential models, both rigid ion and shell models. When using potential models to investigate the energetics of each boundary, the expansion observed was similar to that seen in the first-principles method, however, generally a larger grain boundary energy was observed. Furthermore, a good structural agreement was observed between the quantum and classic methods when considering the boundary structure obtained. The models obtained in this research were quantified by Dudeck *et al.*<sup>(30)</sup> where high-resolution electron microscopy was used along with best-fit simulation parameters to measure the agreement with both the bulk region and boundary structure. From analysis of the two proposed boundaries, the mirror symmetric (SrTiO-terminated) was found to have the best fit when compared to the experimentally obtained boundary structure.

Pickard *et al.*<sup>(31)</sup> used an alternative approach for calculating the structure of grain boundaries in both STO and graphene. This approach was based on first-principles calculations and is known as the *ab initio* random structure searching method (AIRSS) where the interface and stoichiometry are randomly changed within a randomisation region (9.5 Å x 9.2 Å x 5.5 Å in [112], [111] and [110] directions). This method inserted a known number of atoms into this interface region at random atomic positions where structural optimisation was then performed in order to observe the interface structure. Different interface terminations (SrO<sub>3</sub> terminated and Ti terminated) with different degrees of stoichiometry (SrO rich and TiO<sub>2</sub> rich) were observed. The structures obtained were found to be consistent with previous studies for the energetics and structural comparison of the SrO<sub>3</sub> terminated stoichiometric interface, whereas a much lower energy variant of the Ti-terminated interface was found, compared to what had previously been observed<sup>(32)</sup>. This suggests that the new method developed had obtained a new low energy structure of a particular interface as well as developed a method which could use DFT approaches for a field which had been primarily studied using an interatomic potential model approach.

Zheng *et al.*<sup>(33)</sup> investigated phonon scattering in the  $\Sigma 5$  (210)/[001] and  $\Sigma 5$  (310)/[001] tilt boundaries of STO through molecular dynamics simulations through the phonon wave packet dynamics (WPD) method<sup>(34)</sup>. Phonons are the dominant method of thermal transport at the interface region and the degree of phonon scattering in this region has been related to both the amount of disorder at the boundary and the energy of the boundary<sup>(35)</sup>. The Kapitza conductance (inverse of interfacial thermal resistance) was measured where from the results it was hypothesised that on the contrary to previous investigations, the optical modes in STO account for around half of the Kapitza conductance, which is therefore a significant contribution.

Lee *et al.*<sup>(36)</sup> used a first-principles projector-augmented wave method combined with high annular dark field (HAADF) scanning transmission electron microscopy (STEM) to investigate the atomistic structures and defect energies of the  $\Sigma 3$  (111)/[110],  $\Sigma 5$  (210)/[001] and  $\Sigma 13$  (510)/[001] boundaries. Upon investigation, an increased grain boundary energy was observed with increasing number of atoms with low coordination at the grain boundary core. These low coordination atoms generally give lower defect energies, as they are bonded to two atoms as opposed to four, therefore requiring a lower energy to remove.

Ravikumar *et al.*<sup>(37)</sup> investigated the energetics and structure of the  $\Sigma 5$  (310)/[001] tilt boundary using interatomic potentials where the (310) plane at the interface was considered to either be a positively charged SrTiO plane or a negatively charged oxygen plane. From the energetic data obtained it was found that when the boundary was constructed from the SrTiO “cation rich” plane, upon energy minimisation a lower boundary energy was observed compared to an O “anion rich” plane along with a smaller overall volume change. This project was extended where comparisons with experimental studies were also made<sup>(38)</sup>. A direct comparison was made between the calculated structure and Z-contrast scanning transmission electron microscope images of the  $\Sigma 5$  (310)/[001] tilt boundary where a reasonable degree of agreement was observed. It was concluded that a similar structural unit pattern was observed between the two models yet a quantitative analysis would be required in order to obtain a more “refined” computational and experimental boundary structure.

The atomistic structure of the  $\Sigma 9$  (221)/[110] boundary was observed directly through transmission electron microscopy (TEM) and scanning transmission electron microscopy by Mitsuma *et al.*<sup>(39)</sup>. Their results showed that the grain boundary structure was constructed of repeat units of Sr-O and Ti-O columns which occupied the centre of the interface. The energetics of this boundary were investigated using first-principle calculations where it was found that the theoretically derived structure for this boundary was both stable and in structural agreement with experimental evidence.

Waldow *et al.*<sup>(40)</sup> used molecular dynamics simulations with an interatomic potential model in order to observe the atomistic structure and oxygen diffusion at the symmetric [100] 6 ° tilt boundary in STO, which forms as a result of a periodic array of edge dislocations. Ionic migration at dislocations or boundaries in oxides such as STO has been found to play a role in a phenomenon known as resistive switching<sup>(41)</sup>. This procedure involves the reversible switching of a structure's resistance dependent on the applied voltage; therefore, such models could be useful in rapid switching memory devices. The results presented show that no transport of oxygen was observed along the  $a[100]$  dislocations, in either stoichiometric or oxygen deficient STO, which was determined by tracer diffusion coefficient measurements between 1000 K-2300 K as the activation enthalpy at the grain boundary was found to be 0.9 eV higher than the bulk values as well as a lower tracer diffusion coefficient. Although not actually investigated in this research, a resistive switching model of STO was proposed where ionic and electronic conduction occur along separate pathways. This theory is based upon the space charge zone that surrounds a dislocation where electrons will accumulate.

The inclusions of microscale and nanoscale grain boundaries into bulk STO have also been proposed to decrease the thermal conductivity by 30% in the bulk region of Nb-doped STO by Wang *et al.*<sup>(42)</sup>. An overall improvement to the ZT value by a factor of 2.6 was observed. Two different samples were synthesised from different reagent ratios where the heating times also differed when using a molten salt synthesis method (MSS). The SEM images of the two samples are shown in figure 1.2.

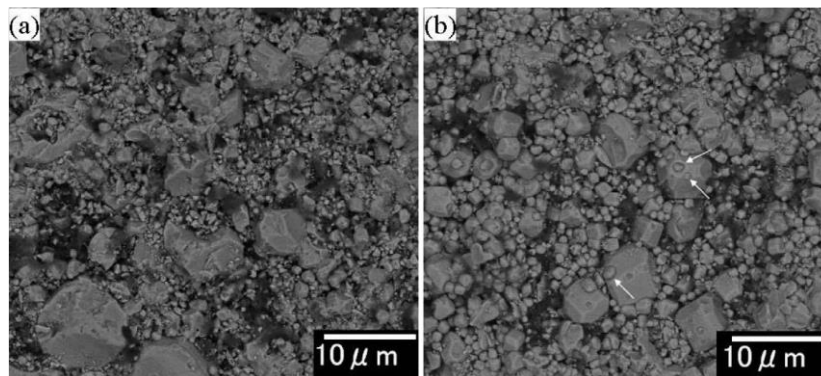


**Figure 1.2** – SEM images of Nb-doped STO containing micro and nanoscale grain boundaries<sup>(42)</sup>. Sample (a) was heated to 1250 °C for 5 hours; sample (b) was heated to 1250°C for 12 hours.

Sample (b) was found to have around twice the electrical conductivity of sample (a). This was attributed to the regular sized crystal structures where a denser packing of the crystals was observed (noted by the white arrows) compared to sample (a). A lower thermal conductivity was also observed for sample (b) compared to sample (a). This was considered to be an effect of phonon scattering at the nanoscale boundaries across the phonon spectrum. It was further considered that

the microscale boundaries would attribute to the remainder of the phonon scattering which attributes to the lower thermal conductivity observed. The ZT value of both samples was measured as a function of temperature, as is shown in figure 1.3.

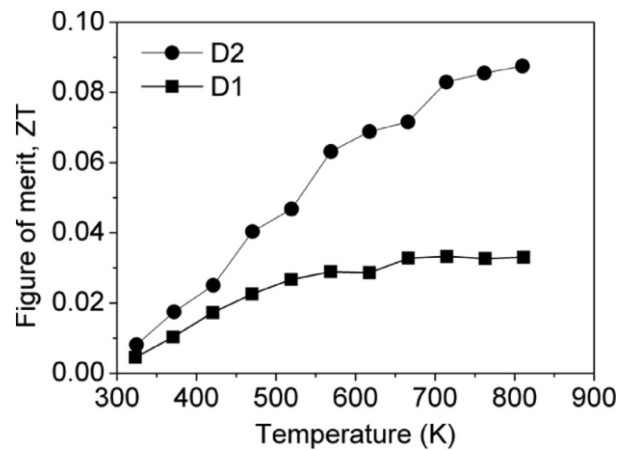


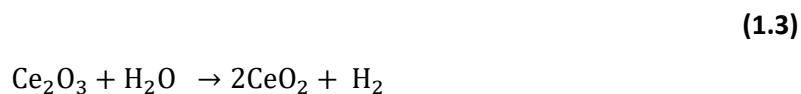
**Figure 1.3** – ZT as a function of temperature for sample (a, D1) and (b, D2) of Nb-doped STO.

The data obtained in figure 1.3 was compared to other experimental studies where the ZT of D1 was found to be comparable to the ZT value reported for Nb-doped STO<sup>(20)</sup>. Whereas the ZT of D2 was found to be as high as 2.6x the magnitude which was attributed to the micro and nanosized boundaries shown in figure 1.2. This further demonstrates the importance of grain boundaries and being able to develop reliable models of them due to their relationship with the ZT value. With reference to the thermal properties, this highlights the importance of grain boundaries with regards to real world polycrystalline systems.

As highlighted there have been a number of studies of grain boundary structure. Most are individually constructed and therefore are unsuitable for high-throughput computing. Whilst the approach demonstrated by Pickard<sup>(31)</sup> is promising, this appears to depend on DFT approaches, and requires a lot of CPU. Thus, new techniques are required through the use of high-throughput computation to generate grain boundary structures and further investigate their transport properties.

## 1.2 Cerium Dioxide

Cerium dioxide ( $\text{CeO}_2$ ), also referred to as ceria, exists as a cubic fluorite type crystal ( $\text{CaF}_2$ ) which adopts the space group  $Fm3m$ . Each cerium is eight-fold coordinated to each oxygen whereas each oxygen is four-fold coordinated. Ceria has been investigated for a number of technological applications. Hydrogen production through the water splitting process<sup>(43)</sup> is one example of such which is described in equations 1.2 and 1.3.

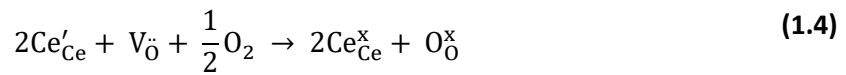


Equation 1.2 represents the thermal dissociation of cerium IV oxide into cerium III oxide with half the stoichiometric amount of oxygen, where at sufficiently high temperature and low partial pressure, reduction occurs. The cerium III oxide produced by this reaction will then react with water in the system to complete the redox reaction forming cerium IV oxide and hydrogen gas.

Due to the mixed ionic-electronic conductivity of ceria it has been studied in intermediate and low temperature SOFCs as a solid electrolyte material<sup>(44)</sup>. One of the most common practices to improve the performance of ceria as a solid electrolyte is by doping with gadolinium ions ( $\text{Gd}^{3+}$ ) therefore forming gadolinium doped ceria (GDC). Due to the reduced charge of Gd compared to Ce ions, charge compensation occurs by means of oxygen vacancy formation where an oxygen vacancy is able to form for every two Gd substitutions at Ce sites, thereby promoting ionic flow through the material. GDC has been shown to operate at lower operating temperatures of 500 °C-800 °C<sup>(45)</sup>. This is an improvement on other materials used as solid electrolyte materials such as YSZ which has a higher operating temperature of  $\geq 800$  °C<sup>(45)</sup>. The study of cubic fluorite structures as solid electrolytes SOFCs has not proven to be without issues. For example Chen *et al.*<sup>(5)</sup> reported problems with deposition temperatures. Electrode performance was enhanced by the addition of a porous NiO-YSZ layer to the anode material of a fuel cell. The increase in deposition temperature promoted thermal expansion mismatch of the lattice, oxidation of Ni and the formation of an interdiffusion layer which efficiently blocks the transport of oxygen through the cell, therefore resulting in a negative impact on performance.

When considering the functionality of the transport in applications such as SOFCs, this promotes the understanding not only of transport in the bulk material of ceria, but the transport through the

interface is also of critical importance. The study of ceria grain boundaries has provided a better insight into the atomistic structure as well as the oxygen transport at the interface. Feng *et al.*<sup>(46)</sup> used both experimental (HAADF-STEM) combined with computational (DFT) methods to investigate the atomistic structure of five ceria grain boundaries ( $\Sigma 3$ - $\Sigma 13$ ) where an excellent agreement was observed between the experimental and theoretical structures. Structural distortion relative to the bulk was further quantified where an increased degree of structural distortion resulted in an increased density of oxygen vacancies at the boundary. The  $\Sigma 5$ ,  $\Sigma 11$  and  $\Sigma 13$  boundaries showed the largest degree of structural distortion at the boundary as well as non-stoichiometry due to the reduced coordination of oxygen at the interface compared to the bulk (four-fold to three-fold). From the study of structural distortion, it was concluded that the greater the degree of distortion in the grain boundary structure, the greater the number of oxygen vacancies formed. Local oxygen reduction reactivity was used in order to quantify the reactivity at the boundary by means of electrochemical strain microscopy (ESM). The oxygen reaction occurring at this boundary is shown in equation 1.4 and the ESM profiles for each of the five interfaces is shown in figure 1.4.



$\text{Ce}'$  corresponds to  $\text{Ce}^{3+}$  from the equivalent  $\text{Ce}_2\text{O}_3$  shown in equations 1.2 and 1.3. A redox reaction also occurs here as the reduction of oxygen correlates with the oxidation of cerium.

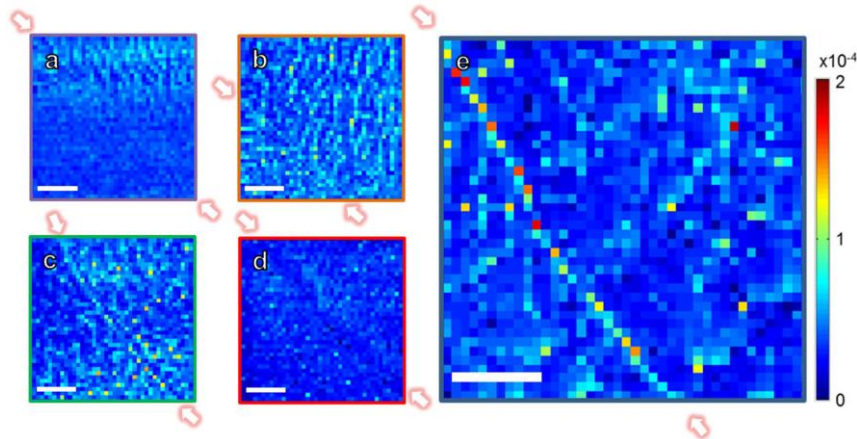


**Figure 1.4** – ESM maps of bulk and grain boundary (denoted by arrows) for (a)  $\Sigma 9$  (b)  $\Sigma 11$  (c)  $\Sigma 13$  (d)  $\Sigma 3$  and (e)  $\Sigma 5$  grain boundaries<sup>(46)</sup>.

From the maps shown in figure 1.4 little difference was observed between the bulk and grain boundary regions for (a)-(d). Yet boundary (e) which corresponds to the  $\Sigma 5$  (210)/[001] boundary is

where the highest structural distortion and largest density of oxygen vacancies was observed, thus implying an increased reactivity of oxygen reduction compared to the bulk. This observation supported the proposal that oxygen vacancies have a significant influence on the reactivity at the boundary. This conclusion was supported by a theoretical approach conducted by An *et al.*<sup>(47)</sup>.

The segregation of oxygen vacancies has been investigated by first-principle calculations by Yuan *et al.*<sup>(48)</sup> in the  $\Sigma 3$  (111)/[110] symmetric tilt boundaries. It was observed that under oxygen poor conditions (low Fermi levels), oxygen vacancies would tend to migrate towards the core of the grain boundary. However, the oxygen ions were found to get trapped in the oxygen layers close to the boundary, which as a result helps to stabilise the boundary. The enhancement in oxygen sites close to the grain boundary were proposed to both facilitate oxygen diffusion due to a decreased migration barrier<sup>(49)</sup> as well as a potential adsorption site for products of fission namely helium or neon.

Other intrinsic defects have been found to have a role in oxygen lattice diffusion, such as the Frenkel pair formation, which was investigated by Walsh *et al.*<sup>(50)</sup>. Through the use of an interatomic potential model, an excellent agreement was observed for bulk properties such as lattice parameters, bulk modulus and elastic constants. Defect energies were calculated using the GULP code<sup>(26)</sup> where the anion Frenkel pair was found to be significantly more stable than the cation Frenkel pair (3.21 eV/defect vs 15.94 eV/defect). The large difference in defect energies was attributed to the larger cationic charge present. A potential energy map was used to represent the global minimum and the nearest two interstitial sites with corresponding saddle points. This was shown in order to represent the local minimum of the interstitial anion sites investigated relative to the location of the global minimum. The reaction pathway for the formation of an isolated (unbound) Frenkel pair is shown in figure 1.5.

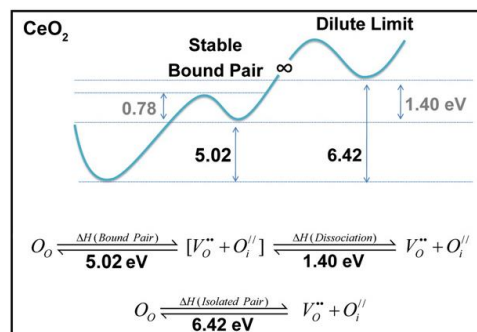


**Figure 1.5** – Energetic schematic for the formation of a stable anionic Frenkel pair in ceria where thermodynamic barriers are shown<sup>(50)</sup>.

As shown in figure 1.5, 5.02 eV was the energy required to form the Frenkel pair where a saddle point of 0.78 eV was present. Finally, a binding energy of 1.40 eV was overcome in order to form the isolated defect pair. A further calculation was considered in order to observe the threshold displacement energy for radiation damage. An energy of 35.4 eV was observed when using the Bubble code<sup>(51)</sup> where a trajectory of displacement is set for an oxygen ion and the energy is computed at each point in order to measure the overall energy of displacement. The threshold for radiation damage was reported to be within the agreement of experimental values, 25 eV-33 eV<sup>(52)</sup>.

Grain boundary capacitance in samarium doped ceria has been investigated by Souza *et al.*<sup>(53)</sup>.  $\text{Ce}_{0.8}\text{Sm}_{0.2}\text{O}_{1.9-\delta}$  was investigated using a.c impedance spectroscopy at a low partial pressure of oxygen between the ranges of 250 to 400 °C. The observed capacitance was concluded to be a result of the space charge region. A schematic of this region is shown in figure 1.6.

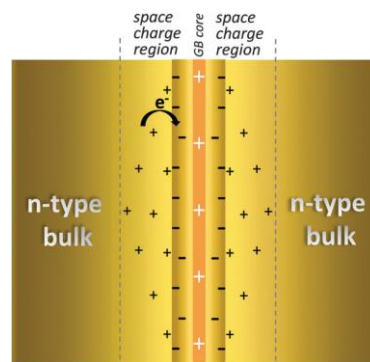


**Figure 1.6** – Space charge region at the interface for Sm doped ceria where the bulk and boundary regions are shown.

An internal electric field was set up at this interface, as this phase consisted of a  $\text{Ce}^{3+}$  grain where the other consisted of a  $\text{Ce}^{4+}$  grain. Mobile  $4f^1$  electrons were able to move across the interface region where an effective positive charge resulted at the core with a surrounding negative charge. As a result, a grain boundary capacitance is observed.

Blocking effects with respect to electronic conductivity has been investigated for 2% Nb-doped ceria by Gobel *et al.*<sup>(54)</sup>. The electronic conductivity in thin films of the material was found to decrease with an increasing grain boundary density. A direct comparison was made between epitaxially grown Nb doped ceria compared to a nanocrystalline sample. The nanocrystalline sample was found to have a significantly higher activation energy and lower ionic conductivity by two orders of magnitude which was attributed to the presence of grain boundaries in the nanocrystalline samples.

As with STO, there have been a number of studies of grain boundary structure. Again, most are individually constructed and therefore are unsuitable for high-throughput computing. Thus, new



techniques are required through the use of high-throughput computation to generate grain boundary structures and further investigate their transport properties.

### 1.3 Heterointerfaces of $\text{SrTiO}_3$ | $\text{CeO}_2$

Heterointerfaces are also of significant importance in technological applications and hence a working target of simulations is to evaluate their impact. Nanocomposites of perovskite-fluorite materials have been found to exhibit mixed ionic-electronic conductivity which results in such models being a good cathode material in intermediate temperature solid oxide fuel cells (SOFCs)<sup>(55)</sup> as well as being used for oxygen separation membranes in SOFCs due to the fast ion conduction observed<sup>(56)</sup>.

However, current research on interfaces in  $\text{CeO}_2$  |  $\text{STO}$  models is currently minimal. Dholabhai *et al.*<sup>(57)</sup> investigated the (100)  $\text{CeO}_2$  || (100)  $\text{STO}$  stepped interface where the investigation of radiation induced point defects was carried out. The structure of the interface was optimized using DFT+U where mixed terminations of the  $\text{STO}$  surface ( $\text{SrO}$  and  $\text{TiO}_2$ ) were used. Cationic and anionic vacancies and interstitials were investigated at four different stepped regions of the interface. It was shown that in these regions through measuring the atomic volume of each species at the interface compared to the bulk region that an expansion was seen at all four steps. This was considered to be a result of differing coordination of atoms as well as lattice mismatch. The importance of the volume calculations however was to stress the importance of the differing of environments at each stepped region in which the point defect calculations would be measured. The four regions defined at the interface are shown in figure 1.7.

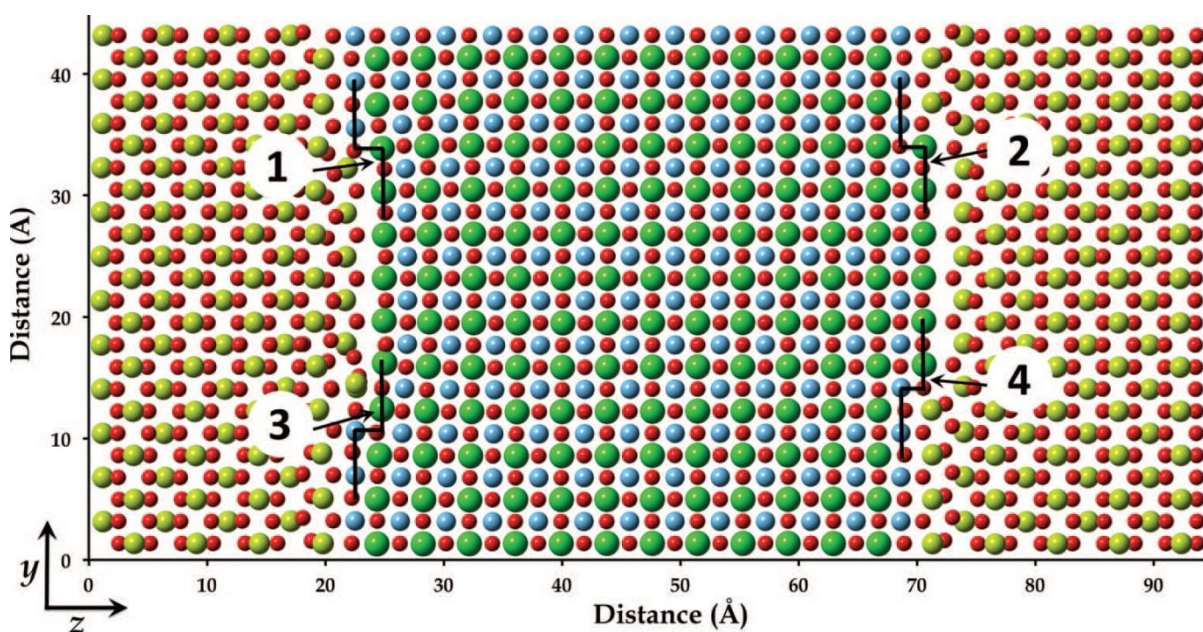


**Figure 1.7** – Stepped interface of structurally optimised (100)  $\text{CeO}_2$  || 100  $\text{SrTiO}_3$  where four regions were specified in order to observe the difference in behaviour of point defects<sup>(57)</sup>.

Cationic vacancies were introduced into each region where  $V_{\text{Ce}}$  was found to have a strong affinity for region 4.  $V_{\text{Ti}}$  was found to have an even stronger affinity for region 3. A much smaller affinity for region 3 was observed for  $V_{\text{Sr}}$ . It was concluded that the steps at the interface would be a stronger sink for Ce and Ti vacancies compared to Sr vacancies. This conclusion was quantified between the differences in most and least energetically favoured sites for each defect. Anionic vacancies were also introduced to each region where an affinity for region 1 and 2 was observed. This was considered to be due to a larger free volume in these two regions and therefore more accessible for  $V_{\text{O}}$  formation. It was also observed that  $V_{\text{O}}$  had an energetic preference of 1.6 eV for existing in the STO phase compared to the  $\text{CeO}_2$  phase. The cationic interstitial sites were found to have a strong affinity for regions 3 and 4 and were repelled by sites 1 and 2 where the opposite was found to be true for the anionic interstitial sites. The behaviour of anionic interstitial sites was found to be similar to the behaviour at vacant sites where a larger free volume was present. As an overall summary of the findings it was deduced that atomic position and local atomic volume was a significant contributing factor in the energetics and likelihood of the formation of point defects. The implications of radiation damage were also discussed by Dholabhai *et al.*<sup>(57)</sup> where it was hypothesised that due to the preference of specific point defects at specific regions, upon irradiation of the interface the material could effectively heal itself as the four regions shown can act as recombination centres which defects are able to migrate towards dependent on their energetic preference.

Nanocomposites of STO/ $\text{CeO}_2$  as well as other perovskite-fluorite systems have been investigated for a number of applications. The system however is substrate dependent where the use of a different crystal as the substrate results in a different application. For example, when  $\text{CeO}_2$  is grown on STO, this system has been investigated for high temperature superconductor application by Wakana *et al.*<sup>(58)</sup> where  $\text{CeO}_2$ /STO bilayers act as a barrier material in a superconductor-insulator-superconductor (SIS) tunnel junction. The superconductive properties of  $\text{EuBa}_2\text{Cu}_3\text{O}_{7-\delta}$  (EBCO) were investigated above 90 K where the  $\text{CeO}_2$ /STO barrier was found to prevent the deterioration of EBCO as well as the suppression of pinhole formation, which is necessary when improving the performance of a superconductive material. However, when STO is grown on a  $\text{CeO}_2$  substrate, this system has been used to study the ferroelectric properties of STO for potential use in microwave devices due to the high dielectric constant present in STO<sup>(59, 60)</sup>.

Again, models of the interface are generated in a bespoke way, and hence there is a need for an automatic method of interface generation.

In addition to fuel cells, another area of importance in the field of energy technologies is that of lithium ion batteries (LIBs). Commercially LIBs are one of the most common types of battery found in a wide variety of electronic devices. Many efforts have recently been pursued in order to improve their safety, reliability and longevity. One key proposal in this field of research is the use of solid electrolytes as opposed to the more commonly used liquid electrolytes, thereby improving their safety through the prevention of dendrite formation<sup>(61)</sup>. The key drawback of solid electrolytes however is the relatively smaller lithium ion mobility compared to their liquid counterparts<sup>(62)</sup>. Current research on candidate solid electrolyte material has focused on the improvement of lithium diffusion in such materials through the incorporation of intrinsic and extrinsic defects<sup>(63)</sup>.

## 1.4 Lithium Lanthanum Titanate

Lithium lanthanum titanate (LLTO) is another material which adopts the perovskite structure ( $ABO_3$  where  $A = \text{La, Li}$  and  $B = \text{Ti}$ ) in the form of  $\text{Li}_{3x}\text{La}_{(2/3-x)}\text{V}_{\text{La} (1/3-2x)}\text{TiO}_3$  where the concentration of lithium, lanthanum and vacancies varies dependent on the study. Two variants of the structure of LLTO showing a “high concentration” and “low concentration” of lithium is shown in figure 1.8.

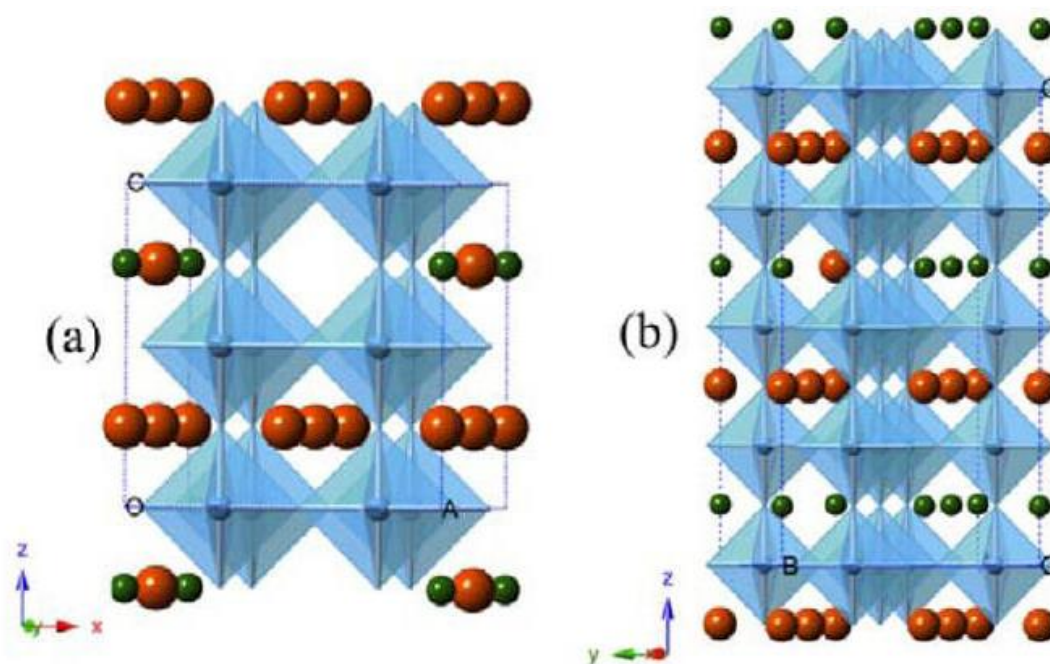


**Figure 1.8** – Two variants of a relaxed structural model of LLTO where (a)  $\text{Li}_{0.125}\text{La}_{0.625}\text{TiO}_3$  and (b)  $\text{Li}_{0.35}\text{La}_{0.55}\text{TiO}_3$  presented by Qian *et al.*<sup>(63)</sup>.

LLTO is considered to be one of the fastest lithium ion conductors available where bulk ionic conductivity of  $1.0 \times 10^{-3} \text{ S cm}^{-1}$  has been achieved at room temperature by Inaguma *et al.*<sup>(64)</sup>. Unlike traditional electrolyte materials such as lithium hexafluorophosphate,  $\text{LiPF}_6$ , LLTO exists in the solid phase, which improves the safety of the material. However, unlike in liquid-based electrolyte materials, due to the layering of the structure as shown in figure 1.8 in order to achieve the desired ionic conduction, the orientation of the material is of significant importance.

Qian *et al.*<sup>(63)</sup> used computational and experimental techniques where LLTO was used as a fast ionic conductive coating for lithium ion battery cathodes. Computationally, first-principles nudged elastic band (NEB) calculations were carried out to obtain the activation energy of lithium diffusion within

the plane. The highest reported energy obtained was found to be 0.23 eV which was reported to be significantly lower than other layered materials used in similar applications such as  $\text{LiNi}_{0.8}\text{Co}_{0.15}\text{Al}_{0.05}\text{O}_2$  (NCA). Two different Li diffusion pathways were proposed in the La-deficient layer dependent on whether high or low concentrations of lithium ions were present. These mechanisms are represented in figure 1.9.

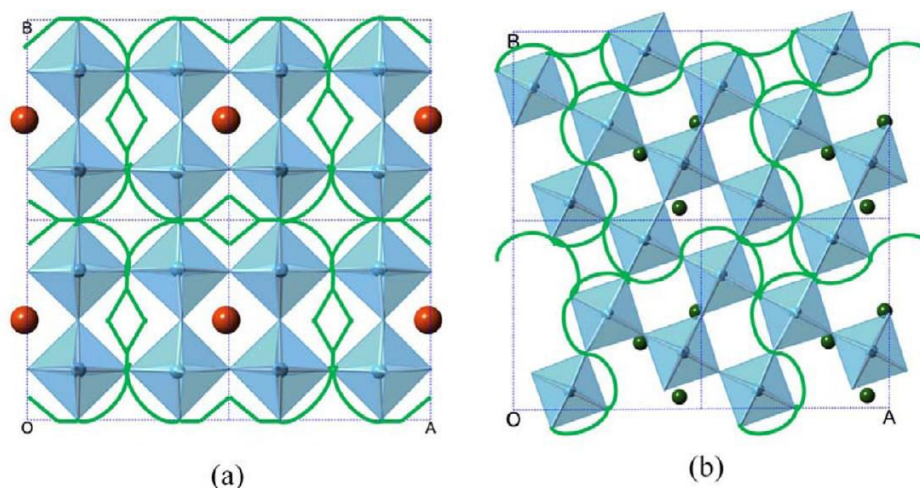


**Figure 1.9** – Predicted diffusion pathways in the La-deficient layer for (a) low concentration of Li and (b) high concentration of Li<sup>(63)</sup>.

Experimentally LLTO was used to coat a NCA cathode where a variety of different experimental techniques. These include energy-dispersive spectroscopy (EDS) and X-ray diffraction (XRD), which were used in order to observe the mechanism of LLTO as a solid electrolyte as well the electrochemical performance of the sample. The electrodes tested were a pristine and a coated sample. When electrochemical cycling was carried out for ten cycles, the coated electrode maintained 99% of its initial discharge capacity, which was a 14% improvement over a stoichiometric sample as well as improved rate capabilities. The coated LLTO layer was also found to reduce the impedance of Li diffusion in the electrode as well as the interface between the cathode and electrode coating.

Lithium storage in LLTO has been investigated by Hua *et al.*<sup>(65)</sup> where the electrochemical performance was investigated. Compared to the work carried out by Qian *et al.*<sup>(63)</sup> an intermediate concentration was used where the stoichiometry was  $\text{Li}_{0.27}\text{La}_{0.54}\text{TiO}_{2.945}$ . In this research, LLTO was used as an anode material where a reverse capacity of  $145 \text{ mA h g}^{-1}$  was observed. Prior to electrochemical cycling a carbon coating was added by chemical vapour deposition (CVD) where this coating was found to improve the durability and therefore cycling performance of the anode. The improved performance when carbon coating was applied was attributed to the large increase in

electrical conductivity ( $3.9 \times 10^{-3} \text{ S cm}^{-1}$ ). It was also observed that the solid electrolyte interphase layer was formed during the initial charge cycle and was found to be stable up to a voltage of 3.0 V.

Abhilash *et al.*<sup>(66)</sup> studied the temperature dependence of the transport properties in LLTO. Through impedance measurements an increase in conductivity (lower grain resistance) was seen upon increasing temperature where a range between 298 K-448 K was considered. Two diffusion mechanisms were observed where at low temperatures, below 378 K, an activation energy of 0.37 eV was observed. Whereas at high temperatures, above 398 K, an activation energy of 0.47 eV was observed, thereby suggesting that a higher energy diffusion mechanism occurs with increasing temperature. Dielectric constants were also measured over the temperature range where a linear increase was reported up to 348 K, suggesting a consistent conduction mechanism. However, a non-linear behaviour is observed at higher temperatures, therefore implying that a different diffusion mechanism occurs. This is supported by the activation energy calculations and is not fully temperature dependent due to the non-linear relationship. The low temperature diffusion mechanism was considered to be a result of the simple diffusion of Li ions with the required degree of thermal energy. However, ionic redistribution was proposed to occur at temperatures exceeding 340 K where tilting of the  $\text{TiO}_6$  octahedra was reported to contribute towards the diffusion mechanism which may account for the higher activation energy observed.

The local structure of LLTO has been probed by Gao *et al.*<sup>(67)</sup> in order to clarify the exact lattice positions of Li ions as well as the vacancy distribution as this was considered to be previously poorly understood. STEM was combined with electron energy loss spectroscopy (EELS) methods in order to develop a precise structural representation. The key findings showed that clusters of A-site vacancies were present in La poor areas where these clusters are also associated with the formation of oxygen vacancies, clustering of Li ions,  $\text{TiO}_6$  octahedral tilting and distortion, decreased coordination of La and reduction of Ti. All these factors considered represent the complexity of the local structure in LLTO and why characterisation had previously proven to be difficult. It was further considered that due to the octahedral tilting the space group when a high concentration of Li was present would be better described as  $P4/nbm$  as opposed to the  $P4/mmm$  space group seen for cubic perovskites where tilting of the octahedra is not considered. Furthermore, as a low concentration ( $\text{La}_{0.62}\text{Li}_{0.16}\text{TiO}_3$ ) and a high concentration ( $\text{La}_{0.56}\text{Li}_{0.33}\text{TiO}_3$ ) sample were used, a differing diffusion mechanism, therefore a difference in the dimension of conductivity was observed. In the low concentration Li sample, conductivity was found to be two dimensional as it was only observed in the layers where A-site vacancies were present. However, in the high concentration Li sample, three



dimensional conductivity was observed in certain regions, suggesting that Li ions were able to diffuse through the fully occupied lanthanum layers.

One of the critical areas in need of further investigation in LLTO is the mechanism of diffusion which results in the enhanced ionic conductivity compared to other solid electrolytes. An insight into the diffusion dimension and pathways has been presented through a genetic algorithm method using molecular dynamics by Jay *et al.*<sup>(68)</sup>. A schematic of the possible diffusion pathways for A-site vacancies and Li ions is shown in figure 1.10.

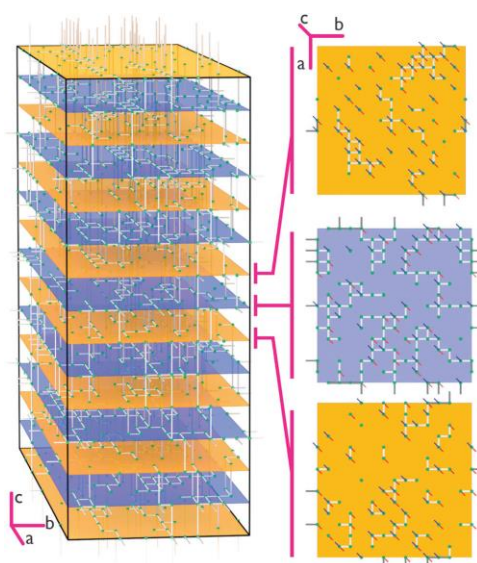


**Figure 1.10** – Schematic of Li and  $V_O$  diffusion pathways in La rich (yellow) and La poor (blue) layers<sup>(68)</sup>.

As shown in figure 1.10, diffusion occurs in both the lanthanum rich and poor layers as well as interlayer diffusion which is represented by the blue lines. The complexity of the diffusion pathways shown are a key feature of the complex local structure presented by Gao *et al.*<sup>(67)</sup>. The genetic algorithm method used also observed that when Li ions have complete coordination by La, this can result in trapping thereby limiting ionic migration which has been supported experimentally by Salkus *et al.*<sup>(69)</sup>. The genetic algorithm method further observed that Li ions are able to either move individually into vacant sites or as coordinated chains, as proposed by Catti<sup>(70)</sup>.

The diffusion mechanism in LLTO has been further established by Chen *et al.*<sup>(71)</sup>. Molecular dynamics with an interatomic potential model were used to study nine different concentrations of Li ions ( $x=0.037-0.157$ ) with random distribution throughout each composition. The highest reported diffusion coefficient from this method was observed when  $x=0.067$  at 600 K where the magnitude of the diffusion coefficient was found to be  $1.59 \times 10^{-5} \text{ cm}^2 \text{ S}^{-1}$ . The activation energy was obtained via an



Arrhenius plot from MD simulations between 400 K and 800 K. Equation 1.6 represents the variant of the Arrhenius equation used.

$$D = D_0 e^{(-E_a/RT)} \quad (1.6)$$

D represents the diffusion coefficient at temperature T with activation energy  $E_a$ .

From the Arrhenius plot, the activation energy of Li diffusion was found to be 0.216 eV which agreed with previous first-principles calculations carried out using a nudged elastic band (NEB) method where an activation energy of 0.23 eV was observed<sup>(63)</sup>. The increase in La vacancies along with Li incorporation was found to decrease the  $a$ ,  $b$  and  $c$  lattice parameters by approximately 0.01 Å in the bulk region up to where  $x=0.12$  after which the lattice parameters remained fixed. This migration procedure and the corresponding energetics are shown in figure 1.11.

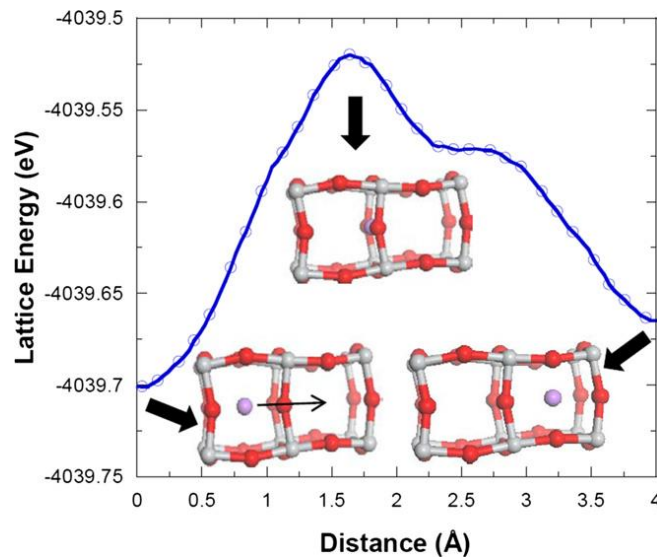


**Figure 1.11** – Energy barrier and mechanism of diffusion through bottleneck structure reported by Chen *et al.*<sup>(71)</sup>.

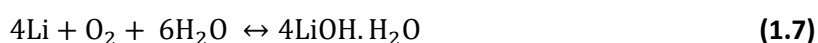
The observed bottleneck structure represents the mechanism of Li diffusion to a vacant A site. When passing through the bottleneck region as shown by the upper arrow, an energy barrier must be overcome. An 8-10% lattice expansion was also observed at this transition state. Due to the expansion, it was proposed that doping the A site with a large cation would dilate the bottleneck structure and hence increase the size of the pathway through which lithium ions diffuse and therefore increase ionic conductivity.

Doped LLTO has been extensively studied by Stramere *et al.*<sup>(72)</sup>. An example of a different lattice system from the cubic structure previously discussed is the “tetragonal, perovskite-like structure”

proposed by Swamy *et al.*<sup>(73)</sup>. The lattice parameters of this structure were found to be  $a = 3.8714 \text{ \AA}$  and  $c = 7.7370 \text{ \AA}$ , characterised by XRD analysis, and a distortion in the perovskite structure was observed by a Fourier transform infrared spectrum (FTIR). Again, high bulk conductivity was reported with an activation energy of 0.19 eV which was in agreement with other presented research. Direct current measurements were also taken at ambient temperature where a conductivity of  $1.9 \times 10^{-8} \text{ S cm}^{-1}$  was reported, thereby showing the presence of electronic and ionic conductivity.

As well as crystalline samples of LLTO being studied for their transport properties, Furusawa *et al.*<sup>(74)</sup> have investigated the ionic conductivity of amorphous LLTO thin film. The films were prepared using a pulsed laser deposition method (PLD) and the amorphization was confirmed from XRD data. The temperature dependence of ionic conductivity was measured within the temperature range of 300 K to 475 K where an activation energy of 0.35 eV was reported. Fast ion conduction was observed for the thin films at 298 K and above. This study concluded that due to the amorphous nature of the thin film, the lack of grain boundaries present was responsible for the increased conductivity compared to the polycrystalline phase of LLTO.

Another practical application of LLTO which has been investigated is the performance of LLTO in a “lithium-air battery” by Uhlmann *et al.*<sup>(75)</sup>. Such batteries have a theoretical energy output of 3456 Wh kg<sup>-1</sup> as proposed by Imanishi *et al.*<sup>(76)</sup>. The reaction in an aqueous lithium air battery is described in equation 1.7.



It is proposed by Uhlmann *et al.* that batteries of this format have three key advantages over other types as quoted;

- Robustness (lack of reactivity) to naturally occurring gases such as carbon dioxide or water vapour.
- Lithium hydroxide (reaction product) is soluble in the electrolyte solution.
- Reaction reversibility prevents the degradation of the electrolyte upon charging the battery.

A visual schematic of a lithium air battery is shown in figure 1.12.

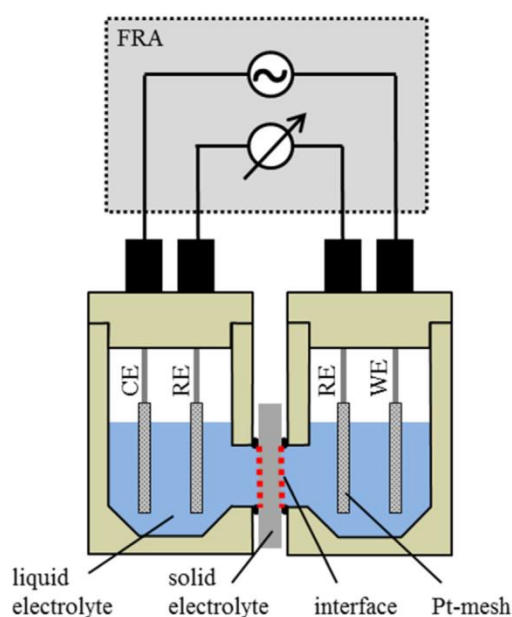


**Figure 1.12** – Setup of a lithium air battery where excitation occurs through the outer electrodes (CE and WE) and is measured by the inner electrodes (RE).

Resistance with respect to temperature, pH and  $[\text{Li}^+]$  was observed for the LLTO solid electrolyte by means of impedance measurements. An  $\text{H}^+/\text{Li}^+$  reaction was observed at the solid electrolyte-aqueous  $[\text{Li}^+]$  interface, where the activation energy of this process was found to be 0.46 eV. One consideration that was made when concluding this investigation was the need for a separation layer between the lithium metal anode and the aqueous layer in order to prevent corrosion at the anode.

Several different practical applications in various energetic systems have been reviewed for LLTO. However, these procedures are not without their drawbacks. Stramare *et al.*<sup>(72)</sup> proposed a number of potential issues when using LLTO as a solid electrolyte. One such example is; when in contact with lithium metal, Li insertion will readily occur. As a result of this, reduction of  $\text{Ti}^{4+}$  to  $\text{Ti}^{3+}$  occurs which diminishes the ionic conductivity in favour of electrical conductivity.

Ramezanipour *et al.*<sup>(77)</sup> used neutron diffraction, impedance spectroscopy and DFT analysis to identify the diffusion pathway and lithium ion mobility for  $\text{Li}_2\text{La}(\text{TaTi})\text{O}_7$ . This phase was fabricated with octahedral stacks of  $(\text{Ta}/\text{Ti})\text{O}_6$  separated by lithium layers, thereby forming a Ruddlesden-Popper structure. Through such techniques, shortening the  $\text{Li}^+$  hopping distance and increasing defects into the lithium layers were found to significantly increase ionic conductivity. When comparing this phase with  $\text{Li}_2\text{SrTa}_2\text{O}_7$  the ionic conductivity observed was two orders of magnitude higher in the Ti phase. This is attributed to the increased size of the  $\text{Sr}^{2+}$  compared to the  $\text{Ti}^{4+}$  ion as

the Li<sup>+</sup> hopping distances were shortened from 2.8 Å to 2.75 Å. The Ti:Ta ratio was further found to have a significant effect on ionic conductivity. When the ratio was converted from 1:1 to 1.2:0.8 with 10% lithium vacancies incorporated, a decrease in activation energy from 0.61 eV to 0.58 eV was observed.

Ge<sup>4+</sup> doping of Li<sub>0.33</sub>La<sub>0.56</sub>TiO<sub>3</sub> was investigated by Wong *et al.*<sup>(78)</sup>. A number of phases were investigated existing of the form Li<sub>0.33+2x</sub>La<sub>0.56</sub>Ti<sub>1-x</sub>Ge<sub>x</sub>O<sub>3</sub> where  $x = 0, 0.05, 0.08$  and  $0.1$ . When  $x = 0.05$ , this phase was found to exhibit the highest sinterability and Li<sup>+</sup> ion conductivity ( $1.2 \times 10^{-5} \text{ S cm}^{-1}$ ); one order of magnitude higher than the parent LLTO phase. The improved conductivity was attributed to the increased densification and structural integrity. Y<sup>3+</sup> doping of Li<sub>0.33</sub>La<sub>0.56</sub>TiO<sub>3</sub> was further found to reduce lattice strain and increase bulk conductivity ( $9.51 \times 10^{-4} \text{ S cm}^{-1}$  at 25 °C)<sup>(79)</sup>.

The ionic conduction of Li<sub>3x</sub>La<sub>2/3-x</sub>TiO<sub>3</sub> in polycrystalline phases is crucial when comparing bulk lithium transport to transport observed at grain boundaries. Wei *et al.*<sup>(80)</sup> investigated the ionic conductivity in LLTO by synthesising three pellets, sintered at increasing temperatures. An increase in sintering temperature resulted in a general increase in ionic conductivity for both the bulk and grain boundary regions in all samples with the bulk region approximately an order of magnitude higher. This characteristic feature was considered to be a result of the TiO<sub>6</sub> octahedra with a 2-3 unit cell thickness located close to the boundary as this has been attributed to prevention of Li<sup>+</sup> ion transport<sup>(81)</sup>. This phenomenon highlights the importance of microstructure in such polycrystalline phases as the total conductivity is clearly governed by the influence of grain boundaries<sup>(82)</sup>.

LLTO has further been used in strategies in order to improve the stability of Li ion anodes by Yan *et al.*<sup>(83)</sup>. Li ion anodes whilst possessing a high energy density are susceptible to both the formation of dendrites and electrolytic corrosion<sup>(84)</sup> where thin films of LLTO were used in anode stabilisation. LLTO is a mixed ionic and electronic ceramic conductor (MIEC) where it was observed when an interface forms between LLTO and Li metal via chemical reaction. This results in stabilisation<sup>(85)</sup> which results in the prevention of formation of dendrites.

Cathode performance has also been found to be improved through the use of an LLTO coating by Zhu *et al.*<sup>(86)</sup>. In this circumstance stoichiometric LiNi<sub>0.5</sub>Mn<sub>1.5</sub>O<sub>4</sub> (LNMO) cathodes were coated with 3% weight LLTO<sup>(87)</sup>. When incorporating LLTO into LNMO an increase in lattice constant and a decrease in interfacial charge transfer impedences were observed. This was considered to be a result of the high ionic conductivity of LLTO. Therefore, LLTO doping resulted in a significantly increased ionic conductivity, improved reversible capacity and rate capability. The significantly

improved rates were attributed to the size of the  $\text{La}^{3+}$  ions, which resulted in the expansion of the size of the  $\text{Li}^+$  diffusion channels.

The mechanical stability of LLTO has been explored by Wolfenstine *et al.*<sup>(88)</sup> in order to ensure the possible safety of such materials when used as a solid electrolyte in LIBs. Mechanical properties are not only important when considering the overall safety of the battery but also the processing and assembly. The experimental Young's modulus of LLTO was found to be  $200 \pm 3$  GPa through a nano technique, a hardness of  $9.4 \pm 0.84$  GPa through a micro technique and a fracture toughness of  $1.15 \pm 0.11$  MPa  $\text{m}^{-2}$  through an indentation technique<sup>(89)</sup>. These values are attributed to the stability of LLTO when used in an LIB application as it is hypothesised that said values are sufficient to prevent the formation of dendrites within the bulk.

The mechanical and further electrochemical stability of LLTO in LIB electrolyte applications has been investigated by Hu *et al.*<sup>(90)</sup>. Samples of LLTO were charged to four different voltages between 0.2 V - 4.5 V, where 3.2 V was found to be the optimum voltage with a Li-ion conductivity of  $9.55 \times 10^{-5}$  S  $\text{cm}^{-1}$ . In all samples the grain boundary conductivity was found to be the limiting factor where conductivity was between 1-2 orders of magnitude lower in each circumstance when compared with bulk. This feature resulted in an approximate decrease of  $\sim 4$  kJ  $\text{mol}^{-1}$  in activation energy for each cycled voltage. The bulk conductivity obtained at 3.2 V was found to be  $1.65 \times 10^{-3}$  S  $\text{cm}^{-1}$ . This is amongst the highest observed and comparable to the conductivity observed by Trong *et al.*<sup>(91)</sup>,  $1.8 \times 10^{-3}$  S  $\text{cm}^{-1}$ . The high conductivity was attributed to the cubic phase structure and low porosity. In contrast the conductivities and thereby activation energies differ vastly for grain boundary regions, distributed between  $6.0 \times 10^{-6}$  S  $\text{cm}^{-1}$  to  $9.2 \times 10^{-4}$  S  $\text{cm}^{-1}$  for grain sizes between 1-3  $\mu\text{m}$ <sup>(62, 64, 91-93)</sup> however for the upper limit of this range, the grain size used was 10  $\mu\text{m}$ <sup>(94)</sup>, implying the grain size is a further important factor when considering boundary conductivity.

Correlations between the formation enthalpy and ionic conductivity of LLTO were investigated by Guo *et al.*<sup>(95)</sup> for differing compositions of  $x$  ranging between 0.04 to 0.15. The experimental formation enthalpies were negative for all values of  $x$ , thereby implying thermodynamic stability. With an increasing  $x$  value and therefore lithium concentration, two trends were observed with respect to formation enthalpy. In the first case where  $x \leq 0.08$ , a small variation in formation enthalpy was observed with the lowest stability composition at  $x = 0.06$ , where at this composition both the maximum concentration of charge carriers and lowest activation energy were observed. A significant change in formation enthalpy was seen when  $x \geq 0.1$ , where at this exact value ( $x = 0.1$ ) the maximum lithium ion conductivity was observed along with a sharp decrease in formation enthalpy with increasing  $x$ .

Whilst the literature relating to bulk LLTO is extensive, only recently have more studies arisen focusing on the structure of LLTO grain boundaries<sup>(81, 96)</sup>. However, questions do still remain resulting from gaps within the literature. How does a change in structural dimensionality affect the ionic diffusion mechanism? How does the octahedral tilting affect ionic transport? And to what effect do the presence of grain boundaries influence ionic transport?

## 1.5 Lithium Lanthanum Zirconate

Lithium lanthanum zirconate (LLZO) is a stuffed garnet existing in the stoichiometric form of  $\text{Li}_7\text{La}_3\text{Zr}_2\text{O}_{12}$  from the garnet formula of  $\text{Li}_x\text{M}_2\text{M}'_3\text{O}_{12}$  and has been proposed as a candidate material for solid electrolytes in batteries. When regarding LLZO as a solid electrolyte, there is a growing demand for an increase in high energy density LIBs, particularly due to the increasing supply of electrically powered vehicles<sup>(97)</sup>. The success of LLZO as a solid electrolyte has been attributed to a number of different properties such as high ionic conductivity<sup>(98, 99)</sup>, reduced electronic conductivity<sup>(100)</sup> and a resistance to the formation of dendrites during cycling<sup>(84)</sup> attributed to the large shear modulus of LLZO<sup>(89)</sup>.

Improving the performance of LLZO as a solid electrolyte is one of the key challenges in current LIB research. With regards to this, a number of defect incorporation schemes have been proposed in order to improve lithium diffusion. Extensive research has been carried out on cationic doping at each of the cation occupying sites however anionic doping mechanisms have also been investigated. Yeandel *et al.*<sup>(101)</sup> used classic potential based simulations to incorporate  $\text{F}^-$  ions to substitute at  $\text{O}^{2-}$  sites where low energies ( $\sim 1.9$  eV) of incorporation were observed suggesting stability of such substitutions. The fluoride defects were considered to both stabilise the cubic phase<sup>(102)</sup> at low temperatures ( $>650$  K) and further facilitate lithium diffusion where at temperatures lower than 500 K, compared to stoichiometric LLZO, diffusion coefficients were observed to be two orders of magnitude higher. Stoichiometric LLZO diffusion was found to exceed that of the F-doped phase which was predicted to occur at around 900 K experimentally<sup>(103)</sup>. This suppression of diffusion was attributed to the clustering of lithium vacancies with lithium ions due to the charge on the fluoride site, effectively +1 causing repulsion. This was supported by the calculated RDFs between the relevant ions. The obtained activation energies were found to be in excellent agreement with experimental values with 0.59 eV for the stoichiometric tetragonal phase (500 K-700 K<sup>(104)</sup>), 0.19 eV for the stoichiometric cubic phase (700 K – 1000 K<sup>(105)</sup>) and 0.26 eV for the F-doped cubic phase (500 K-1000 K<sup>(102)</sup>). The F-doped activation energies were comparable to a number of experimentally doped cationic compositions such as  $\text{Al}^{3+}$  (0.26 eV<sup>(106)</sup>),  $\text{Ta}^{5+}$  (0.22 eV<sup>(107)</sup>) and Nb (0.47 eV<sup>(108)</sup>) suggesting that for low temperature applications, anionic dopant mechanisms could be considered to improve to functionality of LLZO as a solid electrolyte.

One technique which has been investigated in order to improve lithium diffusion in LLZO is aliovalent cationic doping<sup>(109)</sup>. Both stabilisation of the low temperature cubic phase combined with significantly increased lithium diffusion was observed through  $\text{Al}^{3+}$  occupying  $\text{Li}^+$  sites where the charge compensating lithium vacancies were attributed to the stabilisation of the cubic phase at

room temperature due to the tuning of the lithium composition<sup>(110, 111)</sup>. Poorer conduction of lithium is observed in the low temperature tetragonal phase<sup>(112)</sup> as represented by the previously discussed activation energies compared to the high temperature cubic phase<sup>(101)</sup>, therefore the stabilisation is important when considering the functionality at lower temperatures.

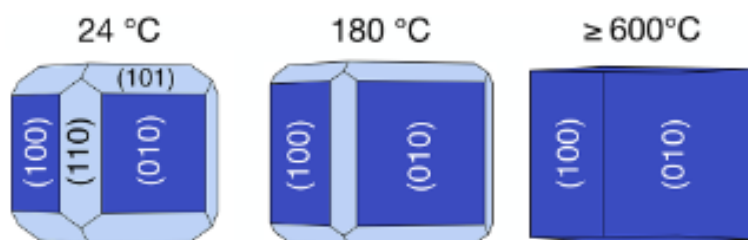


**Figure 1.13** – Particle morphologies of LLZO with increasing temperature<sup>(113)</sup>.

Canepa *et al.*<sup>(113)</sup> investigated the equilibrium morphology which is in agreement with the phase transitions previously discussed. Through the use of first-principles methods this research showed that the expected surfaces presented in figure 1.13 are predicted to be lithium terminated due to their low surface energy relative to other terminations. Furthermore, the presence of lithium segregation towards the surfaces has been implied to contribute towards the formation of dendrites. Synthesis of LLZO in low temperature, oxygen rich environments was proposed in order to minimise lithium diffusion towards the surface and thereby dendrite formation.

This study is highlighted as the shape of crystal will define which surfaces are involved in boundary formation. A thorough investigation of the most stable phases is important as it allows the identification of which surfaces are most likely to form the boundary structures.

$\text{Ge}^{4+}$  has been further proposed to stabilise the cubic phase of LLZO by Brugge *et al.*<sup>(114)</sup> where a lower critical concentration for stabilisation of the cubic phase was observed (0.1 mol of  $\text{Ge}^{4+}$  occupying Li sites) with bulk conductivities of up to  $2.8 \times 10^{-4} \text{ S cm}^{-1}$  at 298 K.  $\text{Ga}^{3+}$  has also been proposed in both the stabilisation and increase of lithium diffusion in LLZO where an ionic conductivity of  $1.09 \times 10^{-3} \text{ S cm}^{-1}$  with a corresponding activation energy of 0.22 eV was confirmed using  $^7\text{Li}$  MAS NMR at  $\text{Li}^+$  concentration of 6.55 moles<sup>(115)</sup>. Decreases in diffusion were seen with further decreasing lithium content, therefore suggesting a possible optimum lithium concentration with regards to doping.  $\text{Sm}^{3+}$  has also been a successful candidate dopant. When doping at the  $\text{Zr}^{4+}$  site, a bulk ionic conductivity of  $6.4 \times 10^{-4} \text{ S cm}^{-1}$  was observed at 293 K for  $\text{Li}_{7.06}\text{La}_3\text{Zr}_{1.94}\text{Sm}_{0.06}\text{O}_{12}$ <sup>(116)</sup>.

LLZO as a solid electrolyte achieves stability when coupled with a Li-metal anode as seen in a number of proposed anode|electrolyte models<sup>(117, 118)</sup>. Sakamoto *et al.*<sup>(119)</sup> investigated both Nb and



Ta doped LLZO surfaces against metallic Li through the use of direct current and electronic impedance spectroscopy (EIS). A discolouration was observed in the Nb doped sample along with an increase in interfacial resistance. This was attributed to the reduction of  $\text{Nb}^{5+}$  to  $\text{Nb}^{4+}$ . On the contrary, no observable change in either colour or interfacial resistance was seen for the  $\text{Ta}^{5+}$  doped phase implying that consideration should be taken when doping for stabilisation as reduction can occur at the interface during battery cycling impeding overall performance.

Another consideration in the synthesis of LLZO and in the application of LIBs is polycrystalline phases<sup>(120)</sup>. As a result of this, grain boundaries of LLZO must be carefully considered when evaluating the functionality of a fuel cell with regards to the lithium ion transport<sup>(121)</sup> and the potential of short circuiting<sup>(61)</sup>. Varying the synthesis conditions has been considered experimentally, where grain boundary resistance can be reduced<sup>(122, 123)</sup>. The alternation of synthesis conditions has been considered experimentally in order to reduce such resistance and thereby both increase density and grain size<sup>(124-126)</sup>. Siegel *et al.*<sup>(127)</sup> investigated the structure of low Miller index grain boundaries using kinetic Monte Carlo simulations. It was found that understanding interfacial resistance was of crucial importance when characterising such boundaries.

Again, with the extensive literature focusing predominantly on bulk LLZO recent studies have investigated the structure of grain boundaries<sup>(127)</sup>. However, the role of ionic transport at the interface has been largely under-researched and will therefore be investigated as part of this research.

## 1.6 Aims and Objectives

Whilst there has been significant and extensive research in the area of SOFC and LIB bulk materials, gaps remain within the literature, which will be addressed in this study.

- To investigate the extent to which a rigid ion, partial charge interatomic potential model based high-throughput method can be used to generate grain boundaries of the four materials discussed in this chapter for structural and energetic characterisation.
- To further extend the generation of grain boundary structures to those currently not seen experimentally, generally with Miller indices greater than four. Secondly, to investigate grain boundary stability of such boundaries
- Investigation into the bulk anionic and cationic diffusion, using MD techniques, in order to observe both diffusion coefficients and activation energies of oxygen and lithium, respectively. A number of the boundary structures, predominantly those which have been experimentally characterised, will further be simulated using MD techniques. This will be carried out order to observe what influence the presence of interfaces have on anionic or cationic transport for each material. Therefore, investigating whether diffusion is facilitated or suppressed.

## 2 Computational Methodology

An important requirement for atomistic level computer simulation is the ability to model the forces between atoms. Two methods are commonly used when calculating forces, namely quantum mechanics and interatomic potential models. Interatomic potential models describe the interactions using parameterised analytical expressions and thus are far quicker than quantum methods, particularly when looking at larger systems, comprised of multiple thousands of atoms. As a result of this, interatomic potential models will be used for the simulations within this study.

### 2.1 Potential Models

When using an interatomic potential model approach to simulate systems, the Born model of solids<sup>(128)</sup> is used where this model summates the two body interactions within a system to calculate the total lattice energy (U), as shown in equation 2.1.

$$U_{(r_{i,j})} = \sum_{i,j} \frac{q_i q_j}{r_{i,j}} + \sum_{i,j} \phi_{i,j}(r_{i,j}) \quad (2.1)$$

Equation 2.1 accounts for the long range electrostatic forces described, where  $r_{i,j}$  represents the ionic separation between ions i and j with charges  $q_i$  and  $q_j$  and  $\phi_{i,j}(r_{i,j})$  is the two-body short range interaction, described below.

The simulations carried out in this study assumed periodic boundary conditions, which assume that each ion (i) is interacting with ion (j) within the simulation cell and in all periodic images. Periodicity is assumed as a way of efficiently accounting for extended solids.

#### 2.1.1 Long Range Forces

The long range interactions in solid lattices are accounted for by the electrostatic contribution. This coulombic interaction is represented by the following.

$$U_{(r_{i,j})} = \frac{q_i q_j}{4\pi\epsilon_0 r_{i,j}} \quad (2.2)$$

U corresponds to the long range forces between all atoms,  $\epsilon_0$  represents the permittivity of free space and  $r_{i,j}$  represents the distance between ions i and j. The main disadvantage in the calculation of  $1/r$  is that it converges slowly. This issue is addressed by two summations, namely, the Ewald

summation<sup>(129)</sup> for 3D systems such as bulk or interfaces and the Parry summation<sup>(130)</sup> for 2D systems such as surfaces.

### 2.1.1.1 Ewald Summation

The Ewald summation<sup>(129)</sup> is used to ensure convergence of the electrostatic energy in 3D systems. The approach is to replace point charges by a Gaussian distribution charge (equation 2.3) which is then transformed into reciprocal space. The resulting Fourier series then becomes rapidly convergent in terms of reciprocal lattice vectors. The overlap between Gaussian distributions is subtracted in real space, expressed as a series involving complementary error functions, and converges rapidly. The width of Gaussian charge distribution is given by  $\sqrt{2/\alpha}$ .

$$\rho_{Gaussian}(r) = -q_i \left(\frac{\alpha}{\pi}\right)^{\frac{3}{2}} e^{-\alpha r^2} \quad (2.3)$$

$\alpha$  is a value chosen to ensure maximum computational efficiency.

### 2.1.1.2 Parry Summation

The Parry summation is used for investigating systems of 2D periodicity. This summation divides the lattice into charged planes of infinite size. The vectors which describe the long range electrostatic interactions are divided into two directions, those in the divided planes and perpendicular to the plane. As a result, the sum of charges in a given plane is no longer zero. However, as the reciprocal lattice vector term (1/r) must still be evaluated this results in a longer convergence time than the Ewald method, and therefore a greater use of computational resources.

## 2.1.2 Short Range Forces

Short range forces are described by interatomic potential models where attractive and repulsive terms are expressed at short distances in each of the potential models discussed in this section.

### 2.1.2.1 Lennard Jones (12-6) Potential

The most widely expression used to describe the short range two-body interaction between two atoms not covalently bonded in molecular simulations is the Lennard Jones potential. This is due mainly to it being computed quickly while retaining the important interaction components.

The Lennard Jones 12-6 potential is represented in equation 2.4.

$$U_{LJ}(r_{i,j}) = \frac{A_{i,j}}{r_{i,j}^{12}} + \frac{B_{i,j}}{r_{i,j}^6} \quad (2.4)$$

$A_{i,j}$  and  $B_{i,j}$  represent independent parameters. The  $r^{-12}$  term represents the repulsive forces which correspond to the repulsion between electron charge clouds. Due to this, repulsive forces are found to be very strong at short distances. The  $r^{-6}$  term represents the attractive forces which is a result of Van der Waals forces or dispersion and occurs over longer distances. However, in this thesis the potentials selected all use an exponential form of the short range repulsion, as they arguably better reflect the curvature of the repulsive interaction, these potentials are discussed below.

### 2.1.2.2 Buckingham Potential

The Buckingham potential model is represented in equation 2.5.

$$U_{Buck}(r_{i,j}) = A_{i,j}e^{\left(\frac{-r_{i,j}}{\rho_{i,j}}\right)} - \frac{C_{i,j}}{r_{i,j}^6} \quad (2.5)$$

$A_{i,j}$  represents ionic size and  $\rho_{i,j}$  represents the short range repulsion. These terms represent the attractive and repulsive forces respectively.  $C_{i,j}$  is similar to the  $B_{i,j}$  parameter described in equation 2.4 and is representative of the attractive Van der Waals forces. Due to the addition of the extra parameter for this potential compared to the Lennard-Jones model, the Buckingham potential is more commonly used in modelling due to the improved flexibility. A typical sketch is shown in figure 2.1. One of the issues with the Buckingham potential is the failure at small distances as the forces should be far more repulsive. This can result in failures of simulations when carried out at high temperatures. The potential models were chosen for this study due to their success of modelling properties in the studied systems.

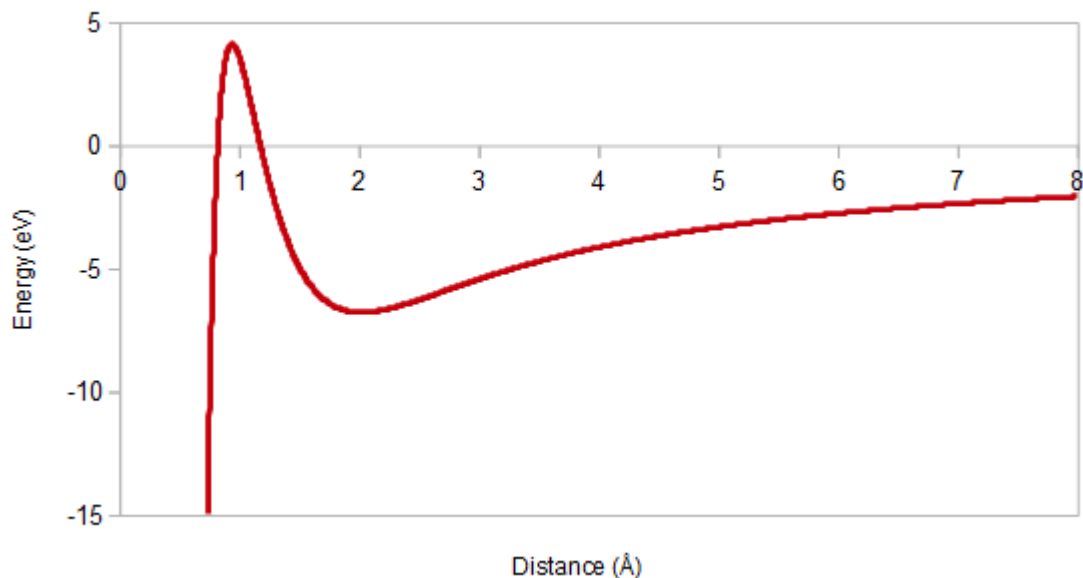


**Figure 2.1** – Example of energy versus distance graph of Buckingham potential model<sup>(131)</sup>.

There are two Buckingham potential models described in this section, the first of which was developed by Teter *et al.*<sup>(132)</sup> and will be described as the “Teter” potential throughout. The second potential used was derived by Chen *et al.*<sup>(71)</sup> and will be described as the “Chen” potential throughout. The difference between this and the Teter potential model is the larger value for  $A_{i,j}$  observed for the oxygen-oxygen interaction as shown in table 2.1a.

Ionic Interaction <sup>(132)</sup>	$A_{i,j}$ / eV	$\rho_{i,j}$ / Å	$C_{i,j}$ / eV Å <sup>6</sup>
Ce <sup>2.4</sup> - O <sup>-1.2</sup>	31697.724	0.21836	90.689
Gd <sup>1.8</sup> - O <sup>-1.2</sup>	8158.1479	0.236719	1.4594
Sr <sup>1.2</sup> - O <sup>-1.2</sup>	14566.637	0.245015	81.773
Ti <sup>2.4</sup> - O <sup>-1.2</sup>	23707.909	0.18558	14.513
La <sup>1.8</sup> - O <sup>-1.2</sup>	4369.393	0.278603	60.278
Zr <sup>2.4</sup> - O <sup>-1.2</sup>	17943.394	0.226627	127.65
Li <sup>0.6</sup> - O <sup>-1.2</sup>	41051.938	0.156116	0.0
O <sup>-1.2</sup> - O <sup>-1.2(132)</sup>	1844.7458	0.343645	192.58
O <sup>-1.2</sup> - O <sup>-1.2(71)</sup>	2029.2204	0.343645	192.58

**Table 2.1a** – Teter<sup>(132)</sup> and Chen<sup>(71)</sup> potential parameters for all ionic species used in this work.

### 2.1.2.3 Morse Potential

The Morse potential model is represented in equation 2.6

$$U_{Morse}(r_{i,j}) = (D_{i,j} (1 - e^{[-B_{i,j}(r_{i,j}-r_0)]})^2 - D_{i,j}) \quad (2.6)$$

From equation 2.6,  $D_{i,j}$  represents the depth of the potential energy well where  $r_0$  is the ionic separation where  $U_{Morse}$  is at a minimum. An extra parameter is included in this model,  $B_{i,j}$ , which defines the width of the potential energy well. This parameter is defined by equation 2.7.

$$B_{i,j} = \sqrt{\frac{k_{i,j}}{D_{i,j}}} \quad (2.7)$$

$k_{i,j}$  expresses the force constant between atoms  $i$  and  $j$ . The key advantage of the Morse potential is that at low values of  $r_{ij}$  the energy does not tend towards zero.

### 2.1.2.4 Morl Potential

The Morl potential model is represented by equation 2.8.

$$U_{Morl}(r_{i,j}) = (D_{i,j} (1 - e^{[-B_{i,j}(r_{i,j}-r_0)]})^2 - D_{i,j}) + \frac{A}{r^{12}} \quad (2.8)$$

The difference shown between this model and the Morse potential model is the addition of the  $r^{-12}$  term, which is used to ensure that significant repulsion occurs at short distances and ensures that ions do not get too close.

The two Morl potential models described were developed firstly by Pedone<sup>(133)</sup> where all cationic interactions apart from Ce are described by the potential interactions. In each case the potentials derived have been tested on a vast number of different oxides and will be known as the “Pedone” potential when investigating LLTO and LLZO throughout. The second potential model derived by Sayle *et al.*<sup>(134)</sup> was derived specifically for ceria. This potential model will be referred to as the “Sayle” potential when discussing ceria interactions. The second lanthanum-oxygen interaction was specifically derived for simulations using LLTO, in order to ensure that the energetics of the crystal structures were similar to those observed experimentally. This potential is an adapted form of the Pedone potential model.

<b>Ionic Interaction<sup>(133)</sup></b>	<b>D<sub>i,j</sub> / eV</b>	<b>a<sub>i,j</sub> / Å<sup>-2</sup></b>	<b>r<sub>0</sub> / Å</b>	<b>C<sub>i,j</sub> / eV Å<sup>12</sup></b>
Ce <sup>2.4</sup> - O <sup>-1.2(134)</sup>	0.098352	1.848592	2.930147	1.00
Gd <sup>1.8</sup> - O <sup>-1.2</sup>	0.00007	2.306374	4.218163	3.00
Sr <sup>1.2</sup> - O <sup>-1.2</sup>	0.019623	1.886	3.32833	3.00
Ti <sup>2.4</sup> - O <sup>-1.2</sup>	0.024235	2.254703	2.708943	1.00
La <sup>1.8</sup> - O <sup>-1.2</sup>	0.070053	1.3984	3.382429	3.00
La <sup>1.8</sup> - O <sup>-1.2(135)</sup>	0.00016129	2.02310	4.40068	3.00
Li <sup>0.6</sup> - O <sup>-1.2</sup>	0.001114	3.429506	2.68136	1.00
Zr <sup>2.4</sup> - O <sup>-1.2</sup>	0.206237	2.479675	2.436997	1.00
O <sup>-1.2</sup> - O <sup>-1.2</sup> (CeO <sub>2</sub> ) <sup>(134)</sup>	0.04173	1.886824	3.189367	22.00
O <sup>-1.2</sup> - O <sup>-1.2</sup> (STO/LLTO) <sup>(133)</sup>	0.042395	1.379316	3.618701	22.00

**Table 2.1b** – *Mori potential parameters for all ionic species used in this work.*

Once the parameters describing the energies and forces between atoms have been defined, different simulation techniques can be used to obtain the optimum structure such as energy minimisation and molecular dynamics.



## 2.2 Energy Minimisation

Energy minimisation (EM) is used in order to obtain the optimum or lowest energy configuration of the bulk, surface or interface in an oxide material. Energy minimisation is coupled with a potential model and is used in different simulation codes in order to obtain optimum structures. Such simulation codes include METADISE<sup>(136)</sup>, GULP<sup>(26)</sup> and CHAOS<sup>(137)</sup>. In order to carry out an EM calculation, trial lattice parameters of a chosen material must be known in order to generate an initial structure. Minimisation can be carried out either by using a constant pressure algorithm, where both the lattice parameters and ions are allowed to move; or by using constant volume, where the lattice parameters are kept fixed, therefore only the ions are able to move. When considering a system, the ionic configuration can be described by a known vector which defines the ionic position; the energy of the system can therefore be described as a function of these positions and upon carrying out a minimisation calculation, structural optimization occurs when the ionic positions locate to a local energy minimum. Thus, the first derivative of energy with respect to ionic position is equal to zero, as described in equation 2.9.

$$Force = - \frac{\delta U}{\delta r} = 0 \quad (2.9)$$

$\delta U$  represents the change in system energy and  $\delta r$  represents the displacement in ionic position when an EM calculation is carried out.

When using energy minimisation there are two drawbacks which must be considered. Firstly, temperature is not included in this approach. Therefore, when considering that the kinetic and potential energy of a system will be zero and at a minimum respectively, this means that structures may differ from those seen experimentally. Secondly, as energy minimisation cannot distinguish between a local and a global minimum, there is a risk that a local minimum could be presented as the global minimum and therefore complete minimisation has not been achieved. In order to ensure a global minimum has been achieved, other methods which involve searching configurational space would need to be included such as Monte Carlo or molecular dynamics.

Energy minimisation can be carried out using a first order or second order derivative approach. First order methods use the forces only to locate the minimum. Two examples of first order derivative methods used, both of which employ an iterative formula, are the steepest descent and conjugate gradient methods.

### 2.2.1 Steepest Descent

The steepest descent method is carried out by considering the steepest gradient. Atoms are displaced iteratively from an initial point and continue until the net force on each atom is zero. Equation 2.10 describes this process.

$$r_{n+1} = r_n - \alpha_n S_n \quad (2.10)$$

$r_{n+1}$  and  $r_n$  represent the final and initial ionic positions respectively,  $\alpha$  represents the numerical step length and  $S$  represents the displacement vector which acts in the opposing direction to the force.

$$S_n = -g_n \quad (2.11)$$

The steepest descent method does not use the second derivatives and controls the minimisation with a step length. Therefore, the step length throughout the procedure is changed in order to direct the system closer to an energy minimum. For example, if the step length is increased and this brings the system further from the energy minimum, the next iteration will decrease the step length in order to bring the system towards the energy minimum. The steepest descent method is quick per step as it does not calculate the second derivative. However, the lack of information for the second derivative means that the step length is ill defined, and hence more iterations are required to be performed to achieve the global minimum.

### 2.2.2 Conjugate Gradient

The conjugate gradient method<sup>(138)</sup> begins in a similar manner to the steepest descent method, beginning at the steepest gradient. However, this method differs in that each iteration is not considered to be independent unlike in the steepest descent method. Thus, when carrying out iterations after the first, the further displacement vectors are calculated using information from the previous iteration.

$$S_n = -g_n + \gamma_n S_{n-1} \quad (2.12)$$

$S$  represents the displacement vector,  $g_n$  represents the magnitude and direction of the force and  $S_{n-1}$  represents the displacement vector from the previous calculation.

$$\gamma_n = \frac{g_n^T g_n}{g_{n-1}^T g_{n-1}} \quad (2.13)$$

$\gamma_n$  is a scalar constant which is obtained from the gradient obtained in the previous iteration.

Using information from the previous iteration means that the number of iterations required is much less than that required for the steepest descent method. However, this method still suffers by not having a calculated step length.

### 2.2.3 Newton Raphson

Newton Raphson<sup>(139)</sup> minimisation differs from the previous two methods in that the second derivative of energy with respect to ionic position is calculated. This is represented by equations 2.14 and 2.15.

$$\text{Gradient } (g) = \frac{\delta U}{\delta x} = kx > \frac{d^2 U}{dx^2} = k \quad (2.14)$$

$k$  represents the bond stiffness and hence is the second derivative matrix. Therefore, this is represented by a 3Nx3N matrix.

The gradient of the energy with respect to displacement can be used to represent the ionic displacement between two points.

$$g = k(x_1 - x_0) \quad (2.15)$$

$$x_1 = x_0 + \frac{g}{k} \quad (2.16)$$

$$x_1 = x_0 - \frac{\text{Force}}{k} \quad (2.17)$$

In the first order derivative methods, the  $k^{-1}$  term is approximated, which is a limitation of the methods. Whereas the Newton Raphson method requires that  $k^{-1}$  is calculated but is more accurately described as a 3Nx3N matrix (the force constant between each atom in the x, y and z directions), and as shown in the following equation.

$$x_1 = x_0 - \text{force} \times k^{-1} \quad (2.18)$$

Equation 2.18 corresponds to Hooke's Law; and as the energy is not exactly harmonic with respect to displacement, further iterations are required. The Newton Raphson method is also computationally expensive, requiring the calculation of  $k^{-1}$  (the inverse of a  $3N \times 3N$  matrix), thus more approximate methods such as the quasi-Newton BFGS method have been developed.

#### **2.2.4 Broyden-Fletcher-Goldfarb-Shanno (BFGS)**

The BFGS method<sup>(140)</sup> is a quasi-Newton method, where for each iteration the value of  $k^{-1}$  is approximated as opposed to calculated. Throughout, the values of  $k^{-1}$  are calculated at set intervals or when there is a large shift in energy in order to maintain an accurate value of  $k^{-1}$ . This is achieved by the storing of information from the previous iteration similar to that of the conjugate gradient method. The BFGS method will converge more slowly than the Newton-Raphson method, and due to the approximation of  $k^{-1}$ , an increased number of iterations will be required to achieve the global minimum.

While energy minimisation is quick to locate an optimum structure, it cannot evaluate the effect of temperature and time. When making such considerations it is therefore important to further use molecular dynamics.

## 2.3 Molecular Dynamics

Molecular Dynamics (MD) is used to calculate the dynamic properties of a system by numerically calculating Newton's Laws over a given timescale. Standard MD has the advantage over EM by being able to include the effect of temperature. However, for simulation times corresponding to less than 10 ns, as used in this work, the atoms may largely remain confined in local minima if the energy barriers are more than  $1-2 k_B T^{(257)}$ .

$$F = ma \quad (2.20)$$

In equation 2.20,  $F$  is the force acting upon an atom within a system,  $m$  and  $a$  represent the mass and acceleration of an atom where this equation is solved over an entire system.

System parameters such as temperature and pressure can be controlled by the input. Through the evolution of a system, particles will obey Newton's Laws, where MD solves these laws over the system in order to calculate properties. By assigning initial coordinates and momenta of particles within a system, the energy of the system is calculated by updating the positions and velocities of particles.

$$v_i(t + \delta t) = v_i(t) + a_i(t)\delta t \quad (2.21)$$

$$x_i(t + \delta t) = x_i(t) + a_i \frac{\delta t^2}{2} \quad (2.22)$$

$v_i$  and  $x_i$  represent the velocities and position of each particle of a system at the next time step with respect to the previous time step. These two equations are only relevant over a small time step, which introduces errors in the calculation. Thus, to minimise errors occurring at each time step, integration algorithms are applied in the code used; DL\_POLY\_Classic<sup>(141)</sup>. Integration algorithms are expressed in terms of a third order Taylor series expansion.

$$x_i(t + \delta t) = x(t) + v(t)\delta t + \frac{1}{2}a(t)\delta t^2 + \frac{1}{6}b(t)\delta t^3 \quad (2.23)$$

$$v(t + \delta t) = v(t) + a(t)\delta t + \frac{1}{2}b(t)\delta t^2 \quad (2.24)$$

$$a(t + \delta t) = a(t) + b(t)\delta t \quad (2.25)$$

$$b(t + \delta t) = b(t) \dots \quad (2.26)$$

### 2.3.1 Integration Algorithms

The Verlet algorithm is a third order expansion used in the DL\_POLY codes which updates the positions within a system by accounting for the integration steps carried out in the previous iteration as shown in equations 2.27 and 2.28.

$$x(t + \delta t) = x(t) + v(t)\delta t + \frac{1}{2}a(t)\delta t^2 \quad (2.27)$$

$$x(t - \delta t) = 2x(t) + v(t)\delta t + \frac{1}{2}a(t) \quad (2.28)$$

$x(t + \delta t)$  and  $x(t - \delta t)$  represent the integration of ionic positions at the corresponding and previous iterations respectively. When combining these two equations the following overall equation is used to determine the updated ionic position.

$$x(t + \delta t) = 2x(t) + x(t)\delta t + a(t)\delta t^2 + \theta(\delta t^2) \quad (2.29)$$

From this equation it can be noted that the Verlet algorithm does not calculate velocities, as the velocities are not required to calculate the particle trajectories. However, an estimate of particle velocity can be calculated by equation 2.30.

$$v(t) = \frac{x(t + \delta t) - x(t - \delta t)}{2\delta t} + \theta(\delta t^4) \quad (2.30)$$

However, the main disadvantage to using the Verlet algorithm is that the velocities cannot be calculated until the ionic positions have been determined, thus introducing a small error. This can be overcome using the Verlet Leapfrog algorithm. This algorithm allows the calculation of velocities at half integer steps as well as the updated ionic position, this algorithm is implemented in the DL\_POLY codes.

$$v\left(t + \frac{1}{2}\delta t\right) = \frac{x(t + \delta t) - x(t)}{\delta t} \quad (2.31)$$

$$v\left(t - \frac{1}{2}\delta t\right) = \frac{x(t) - x(t + \delta t)}{\delta t} \quad (2.32)$$

When combining these two equations, this represents how the velocities of each half integer time step can be calculated by using the information calculated in the previous half integer time step.

$$x(t + \delta t) = x(t) + v(t + \delta t)\delta t + \frac{1}{2}a(t)\delta t^2 \quad (2.33)$$

However, the main disadvantage to using the Verlet Leapfrog algorithm is that the ionic positions and velocities are not calculated simultaneously. As a result of this, the potential and kinetic energies of the system are also not updated simultaneously. This describes why the velocities calculated in the Verlet Leapfrog algorithm are of the order of  $\delta t^3$  compared to  $\delta t^4$  for the Verlet algorithm, thereby increasing the margin of error for each time step calculated when using this algorithm.

As the velocities are known, the temperature can therefore be calculated by equation 2.34 and the momentum of the simulation cell is set to zero as shown in equation 2.35.

$$\sum_{i=1}^N m v^2 = 3Nk_B T \quad (2.34)$$

$$\sum_{i=1}^N m v = 0 \quad (2.35)$$

N represents the number of particles in the system and  $k_B$  is the Boltzmann constant.

### 2.3.2 Dynamic Ensembles

In order to control the parameters of a system such as temperature and pressure when simulating with MD codes, ensembles are used in order to implement the desired conditions within the input of a system simulation. The two ensembles used in MD simulations will be described in this section.

Firstly, the NPT ensemble (constant number of particles, constant stress and constant temperature) ensemble was used. This ensemble is a form of the NPT ensemble (isothermal-isobaric) where the unit cell vectors of a system are able to contract or dilate yet both the temperature and pressure of the system remain constant. This ensemble is usually simulated over a number of large time scales, multiple nanoseconds, in order to obtain the average volume of the system through the change in unit cell vectors.

In order to maintain constant pressure and temperature of the system, the Nose-Hoover algorithm<sup>(142)</sup> is applied which couples a thermostat and a barostat to the system in order to achieve a constant temperature and pressure, respectively. The effective mass of the thermostat and barostat are described by equations 2.36 and 2.37.

$$Q = N_f k_B T_{ext} \tau_T^2 \quad (2.36)$$

$$W = N_f k_B T_{ext} \tau_P^2 \quad (2.37)$$

Q and W describe the effective mass of the thermostat and barostat respectively,  $N_f$  describes the number of degrees of freedom,  $k_B$  represents the Boltzmann constant,  $T_{ext}$  represents the temperature of the heat bath and  $\tau_T$  and  $\tau_P$  represent the instantaneous temperatures and pressures respectively. Within the DL\_POLY codes<sup>(141)</sup>,  $\tau_T$  and  $\tau_P$  represent the thermostat and barostat relaxation times respectively. These two values are always set at different values to ensure that there is no exchange in energy between the thermostat and barostat which could result in an energy shift on the system. The Nose-Hoover<sup>(142)</sup> algorithm includes a friction coefficient,  $\chi$ , which is controlled by a first order differential represented by equation 2.38.

$$\frac{d\chi(t)}{dt} = \frac{N_f K_B}{Q} (T(t) - T_{ext}) \quad (2.38)$$

As the NST ensemble allows the system volume to fluctuate, this is achieved by the Melchionna modification of the Hoover algorithm, where the lattice parameters of a system may change under either isotropic or anisotropic conditions.

When using this approach, a constant average configurational energy as well as a minimal change in average lattice parameters is desired for a defined timeframe. Upon achieving this, the system is further simulated using the canonical ensemble (NVT). This ensemble keeps the number of atoms, volume and temperature fixed where the Nose-Hoover algorithm is used once again to maintain a fixed temperature.

As there are conserved quantities in this system the Hamiltonian describing this system is described in equation 2.39.

$$H_{NVT} = U + K.E + \frac{1}{2} Q \dot{x}_{(t)}^2 + \frac{Q}{\tau_T^2} \int_0^\tau \chi_{(s)} \delta s \quad (2.39)$$



In this system, as  $v_{(t)}$  is required in order to calculate  $T_{(t)}$ , an initial prediction is obtained by the Verlet algorithm in the DL\_POLY code<sup>(141)</sup>.

### 2.3.3 System Properties

MD is used to calculate a number of different properties of a system. As previously discussed, it is important to observe the potential energy of a system. Equation 2.40 represents how the overall potential energy is calculated by the summation of all particles.

$$U = \left[ \sum_{i=1}^N \sum_j^N U_{(r)_{i,j}} \right] \quad (2.40)$$

When calculating dynamic data for a system, this data is used in the calculation of diffusion coefficients. Two important properties required to be calculated are the radial distribution function (RDF), which gives useful structural information; secondly, the mean square displacement (MSD) which is used to describe the average displacement over a given time from an atom's initial position. Equations 2.41 and 2.42 describe how each of these two properties are calculated respectively.

$$g_{(r)} = \frac{1}{N^2} \left[ \sum_{i,j}^N \delta(r - r_{i,j}) \right] \quad (2.41)$$

$$2Dt = \frac{1}{3} \left[ (|r_{i(t)} - r_{i(0)}|)^2 \right] \quad (2.42)$$

The MSD can be expressed as a diffusion coefficient in a defined direction which can be more meaningful than a value which describes the overall system. The diffusion coefficient can be measured in the x, y and z directions as shown by equations 2.43-2.45.

$$D_{(x)} = \frac{\lim_{t \rightarrow \infty} [(x_{(t)} - x_{(0)})^2]}{2t} \quad (2.43)$$

$$D_{(y)} = \frac{\lim_{t \rightarrow \infty} [(y_{(t)} - y_{(0)})^2]}{2t} \quad (2.44)$$

$$D_{(z)} = \frac{\lim_{t \rightarrow \infty} [(z_{(t)} - z_{(0)})^2]}{2t} \quad (2.45)$$

In each of these equations,  $t$  represents time and  $x, y$  and  $z_{(0)}$  and  $x, y$  and  $z_{(t)}$  represent the particle trajectory as shown by equation 2.46.

$$x_{(0)} \rightarrow x_{(t)} \quad (2.46)$$

When measuring a diffusion coefficient, the trajectory size must be large enough to ensure that the diffusion coefficient is independent of trajectory size.

## 2.4 Computational Techniques

Surfaces and grain boundaries can be considered as an array of extended intrinsic defects of a crystal lattice; however, point defects such as a single cationic vacancy can be modelled using the Mott-Littleton method. The Mott-Littleton method allows the variation of segregation energy as a function of depth and therefore can identify as to whether a particular dopant has a preference for surface, subsurface or bulk. This is required towards developing structural models of the interfaces.

### 2.4.1 Mott-Littleton Method

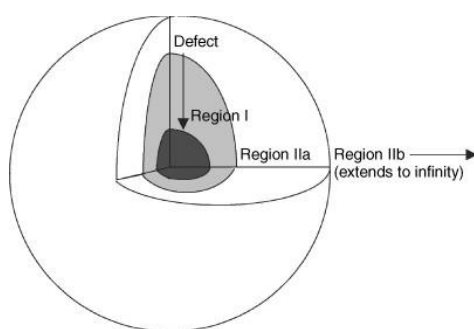


**Figure 2.4a** – Visual representation of Mott-Littleton defect regions<sup>(143)</sup>

The Mott-Littleton<sup>(144)</sup> approach divides the crystal into two regions based around the defect centre where infinite dilution is assumed. The two regions are known as region I and region II where region II is split into two sub regions, namely IIa and IIb. The defect centre is located at the centre of region I where all ions in this region are allowed to fully relax explicitly. Whereas in region two the forces acting upon each ion are much weaker and the overall relaxation is approximated. Region IIa acts as an interface between region I and IIb. Further, region IIb uses a continuum approximate for electrostatic response to a charged defect.

All calculations carried out using the GULP code<sup>(26)</sup> made use of the Mott-Littleton method. Two region sizes were required to be defined in order for convergence to be achieved over the smallest region size to ensure that all energies had converged without the need for further computational expense. As a result of this several different region sizes were tested where it was found that convergence had been achieved ( $0.2 \text{ eV} \leq$ ) when defining the region sizes as  $10 \text{ \AA}$  for region one and  $20 \text{ \AA}$  for region two, therefore these two region sizes were used throughout.

In order to incorporate defects into the bulk and interface regions where a clear difference in behaviour could be observed between the bulk and interface region, the region I depth of each block was fixed to approximately 60 Å where such region sizes have been thoroughly tested to ensure convergence of energy. Upon reconstruction of the interface, cationic defects such as Gd<sup>3+</sup> substitution at Ce<sup>4+</sup> sites and anionic defects such as oxygen vacancies were incorporated along the x-direction for the region I of both blocks. Through the use of the CHAOS<sup>(137)</sup> code, energy minimisation steps were performed at each defective site. The dipole and energy were measured, and the bulk defect energies were compared to those at the interface.

## 2.4.2 Bulk Crystal and Surface Generation

In order to generate a bulk crystal structure using the METADISE code, several parameters are required for each species, namely the unit cell parameters, space group and fractional coordinates. The information for a desired crystal structure can be obtained from the Inorganic Crystal Database<sup>(145)</sup>. The information is combined with a set of interatomic potentials where the structure is minimised either at constant volume or pressure. When generating bulk crystals, constant pressure is used for the simulations carried out as this allows the lattice to relax and this allows either expansion or contraction of the lattice depending on the potential used. As a result, lattice strains are reduced which may be present if the volume was held fixed. Once a reliable model of the bulk crystal has been generated this can then be used to generate a surface. In order to produce a given surface, a block of crystal is cut from the bulk along defined Miller Indices. The block is constructed of planes, commonly described as *hkl*. By analysis of these surfaces, different terminations can be ranked in order of stability through the relaxed surface energies in order to deduce which surfaces will be used to generate interface structures. Furthermore, it can be assessed whether a low energy surface termination results in a low energy interface. Surfaces can be split into three separate types which were described by Tasker<sup>(146)</sup>.

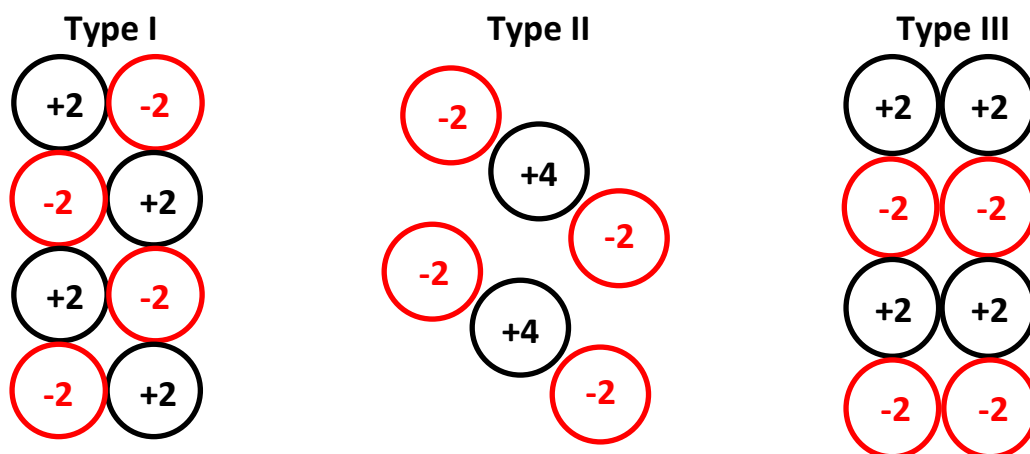


**Figure 2.4b** – Surface types I, II and III as described by Tasker<sup>(147)</sup>.

Figure 2.4b shows the three surface types. Type I consists of neutrally charged planes where stoichiometry is maintained in each of these planes. Due to the balance in charge, there is no net dipole at the surface. Type II consists of charged planes and due to the symmetric stacking of these planes results in charge and dipole cancellation. Therefore, there is no net dipole. Type III consists of asymmetrically stacked charged planes which should result in an overall dipole moment at the surface. However, the cancellation of this net dipole is achieved by translating atoms from the top of the surface to the bottom of the surface, to ensure there is no net dipole present upon surface reconstruction.

When considering the three types of surfaces discussed, the bulk crystal in the cases of type II and III would therefore be constructed by a large number of charged planes. Therefore, when simulating minimisation calculations on such crystals, the charge density across each plane will increase the computational time for each simulation and therefore increase the time taken for energy to converge and therefore the computational expense. In order to decrease the computational time and expense the two region approach is considered<sup>(148)</sup>. The two region approach divides a block into two defined regions. Region I is located close to the surface where atoms in this region are allowed to relax, and region II is located further from the surface and the atoms are held at their fixed equilibrium positions. It is important that several different region sizes are considered when performing energy minimisation simulations as region I must be large enough that complete relaxation and thereby energy convergence is achieved, yet not too large that unnecessary computational time and expense occurs. This two region approach is depicted in figure 2.4c which gives a representation for how region I and region II are represented as part of a block.

Surface energy minimisations are carried out by utilising one block however when considering bulk simulations and the construction of interfaces, in this case two blocks are considered where the two blocks are aligned so that the region I of each is adjacent to the other as shown in figure 2.4c.

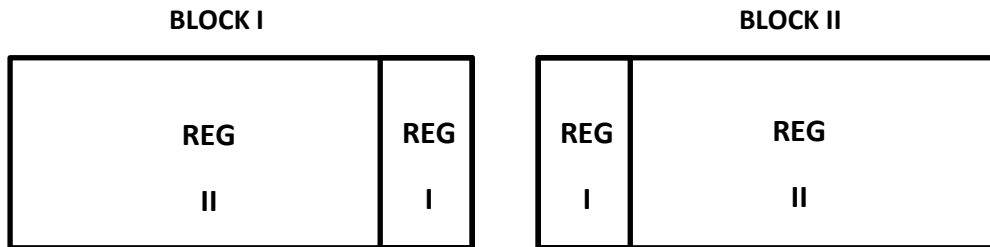


**Figure 2.4c** – Visual representation of two block approach to energy minimisation where the region I and region II of each block are shown.

The bulk energy ( $U_B$ ) accounts for interactions in both block I and block II, and surface energy ( $U_S$ ) only accounts for interactions in block I. The system is able to be calculated by considering the interaction of adjacent regions in each block.

$$U_B = (E_{I-I}^B + E_{I-II}^B) + (E_{II-I}^B + E_{II-II}^B) \quad (2.47)$$

$$U_S = (E_{I-I}^S + E_{I-II}^S) + (E_{II-I}^S + E_{II-II}^S) \quad (2.48)$$

Equations 2.47 and 2.48 show the interactions between each region in order to calculate the bulk and surface energies of each block where the notations <sup>B</sup> and <sup>S</sup> define bulk or surface interactions. The notation of  $E_{I-I}$ ,  $E_{I-II}$ ,  $E_{II-II}$  describes the energy of the ionic interactions between region I and region I atoms, region I and region II atoms, and region II and region II atoms respectively. Furthermore, in order to reduce computational time and expense, as region II atoms are held at fixed equilibrium positions in this approach, the energy of the ionic interactions between region II and region II atoms are considered to be equal for surface and bulk. Therefore, these calculations are not required, and are represented by equation 2.49.

$$E_{II-II}^B = E_{II-II}^S \quad (2.49)$$

The surface energy ( $\gamma$ ) for the block can be defined by the difference in energy between the bulk energy ( $U_B$ ) and surface energy ( $U_S$ ) for the same number of atoms per unit area as described by equation 2.50.

$$\gamma = \frac{U_B - U_S}{A} \quad (2.50)$$

A represents the surface area of the surface.

### 2.4.2 Grain Boundaries

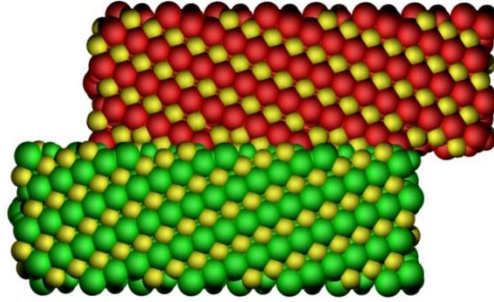


**Figure 2.4d** – Visual representation of two surfaces of a crystal adjoining to form a grain boundary.

Grain boundaries can be described as a two-dimensional defect between two grains of either the same phase (homogenous) or different phases (heterogeneous), where the separation between the two grains is defined as the interface region as shown in figure 2.4e.

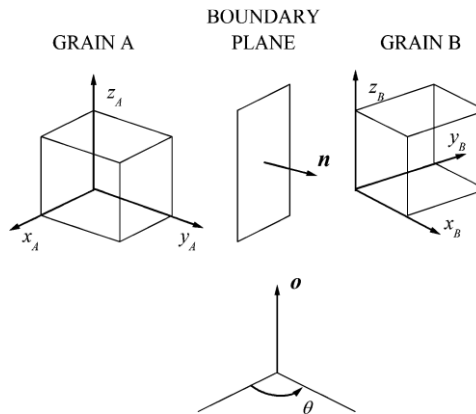


**Figure 2.4e** - Crystallographic depiction of grain boundary construction and the variables which define this where  $x_{A,B}$ ,  $y_{A,B}$  and  $z_{A,B}$  describe the crystallographic direction of the lattice parameters for grain A and grain B,  $o$  defines the rotation axis and  $\vartheta$  is the rotation angle used to define the grain boundary and  $n$  defines the position of the grain boundary plane<sup>(149)</sup>. This figure shows nine degrees of freedom which is reduced to five as the boundary describes the misorientation of one grain with respect to another.

Figure 2.4e represents the parameters which are necessary when defining and naming a specific interface. In order to fully characterise and define the orientation of a grain boundary, five degrees

of freedom (DOFs) are considered which provide information on bicrystal preparation from the two initial grains<sup>(150)</sup>. Of these five DOFs, three define the misorientation of grains A and B as shown in figure 2.4e where the further DOFs are described by the rotation axis and rotation angle. The DOFs considered are important when categorising boundaries, where relationships between the grain boundary normal (**n**) and the rotation axis (**o**) are used to define either tilt or twist interfaces where boundaries which do not fit into either of these categories are described as random or mixed interfaces. Table 2.4a describes the four categories of interfaces which were described by Wolf and Lutsko<sup>(151)</sup>.

<b>Symmetrical Tilt Grain Boundary</b>	$[h_1k_1l_1] = [h_2k_2l_2]$	$\vartheta = 0$
<b>Asymmetrical Tilt Grain Boundary</b>	$[h_1k_1l_1] \neq [h_2k_2l_2]$	$\vartheta = 0$
<b>Twist Grain Boundary</b>	$[h_1k_1l_1] = [h_2k_2l_2]$	$\vartheta \neq 0$
<b>Mixed Grain Boundary</b>	$[h_1k_1l_1] \neq [h_2k_2l_2]$	$\vartheta \neq 0$

**Table 2.4a** – Nomenclature and definition of the four interface types defined by Wolf and Lutsko<sup>(151)</sup> where *h*, *k* and *l* define the Miller Indices of each grain and  $\theta$  represents the misorientation of one grain with respect to the other.

As shown in table 2.4a the first two types of interfaces are the symmetric and the asymmetric tilt boundaries, where the Miller indices are equal and unequal respectively. In the cases of both, such interfaces have a misorientation angle ( $\vartheta$ ) of zero and therefore are theoretically reflected in a mirror plane for the case of the symmetric tilt boundary. The twist and mixed boundaries however have a degree of misorientation relative to the rotation axis where again the Miller indices are equivalent and inequivalent respectively.

### 2.4.2.1 Grain Boundary Atomic Structure

Modern research on grain boundaries categorises them into two groups with respect to grain boundary structure, namely low-angle and high-angle grain boundaries. Low-angle grain boundaries occur when the misorientation angle is low enough that the interfacial equilibrium structure is a result of an array of dislocations<sup>(152)</sup>. In the case of tilt boundaries, an array of edge dislocations (dislocation model) are responsible for the boundary structure, whereas for twist boundaries the boundary structure is a result of an array of screw dislocations<sup>(150)</sup>. The misorientation angle is related to the magnitude of the Burgers vector and is represented by equation 2.51.



$$\sin \frac{\theta}{2} = \frac{|b|}{2D} \quad (2.51)$$

**b** represents the Burgers vector and D represents the dislocation spacing between the two grains.

The transition between low angle and high angle grain boundaries occurs when the dislocation model between the arrays fails; this has been experimentally deduced to occur when the misorientation angle in equation 2.51 is between 13 ° and 15 °<sup>(153)</sup>. At the threshold where the dislocation model fails, which is due to the overlap of individual dislocations<sup>(150)</sup>, the structural unit model was further developed to describe the structural arrangement of high angle grain boundaries<sup>(154)</sup>. The structural unit model for a high angle grain boundary is repeating structural units which when combined form the interface structure. Although a limited number of structural units have been seen in interfacial structures, Ashby *et al.*<sup>(155)</sup> investigated a number of different structural formula units where a number of different polyhedra such as pentagonal bipyramid and tetragonal dodecahedron were investigated. Low energy grain boundaries are often found to be similar in structure to the bulk crystal and are therefore described as “bulk like”. Boundaries which are constructed of a single structural unit are called singular<sup>(152)</sup>. Higher energy interfaces comprised of two or more structural units are described as general grain boundaries. A third category of grain boundaries are described as vicinal where such boundaries are found to be a transition from singular to general where the composition is close to that of a singular boundary however secondary dislocations are observed which correlate with structures similar to low angle grain boundaries<sup>(152)</sup>. A final classification of boundary types is the special type. In this case special boundaries are found to have sharp extremes where property-orientation dependence occurs in properties such as fracture toughness<sup>(156)</sup>. Four different categories of boundary types have been discussed, yet as these names are generalised and not associated with any specific boundary, in order to name specific boundaries based on their structure, the coincidence-site lattice model is used.

#### **2.4.2.2 Coincidence Site Lattice (CSL) Model**

The CSL model is used when naming special grain boundaries and was initially proposed by Kronberg and Wilson<sup>(157)</sup>. The CSL model assumes that the higher the number of coincidence sites, the lower the boundary energy as a smaller number of dislocations are required when the boundary is formed. The sites which are located in the same atomic position in both crystals are described as coincidence sites. The reciprocal value of the density of coincidence sites ( $\Sigma$ ) is used in the definition of CSL.

$$\Sigma = \frac{\text{Number of atomic coincidence sites}}{\text{Total number of atomic lattice sites}} \quad (2.52)$$

As it may not be practical to calculate the value of  $\Sigma$  directly from equation 2.52, in order to obtain an accurate value of  $\Sigma$  for a cubic lattice the following is considered.

$$\Sigma = \delta(h^2 + k^2 + l^2) \quad (2.53)$$

In equation 2.53  $h$ ,  $k$  and  $l$  represent the Miller indices of the surface used to generate the boundary and  $\delta$  is a numerical constant which is 0 if  $(h^2 + k^2 + l^2)$  is odd and is 0.5 if  $(h^2 + k^2 + l^2)$  is even as the value of  $\Sigma$  is always odd for a cubic system<sup>(150)</sup>. Through the use of the value of  $\Sigma$ , it can be considered that a perfect bicrystal would be equivalent to a system where  $\Sigma=1$  as all lattice sites would also be coincidence sites along with a misorientation angle of 0°, therefore this would be classified as a singular boundary with an interface formation energy of zero. Experimental studies which have investigated body centred cubic (bcc) and face centred cubic (fcc) boundaries where  $\Sigma=3$  are considered to be singular grain boundaries where the previously discussed special behaviour was found to be exhibited in such boundaries<sup>(158)</sup>. Due to this it is often considered that boundaries which have a low value of  $\Sigma$  are commonly found to exhibit special properties which are dependent on their orientation<sup>(150)</sup>.

#### 2.4.2.3 Generation of Tilt and Twist Boundaries

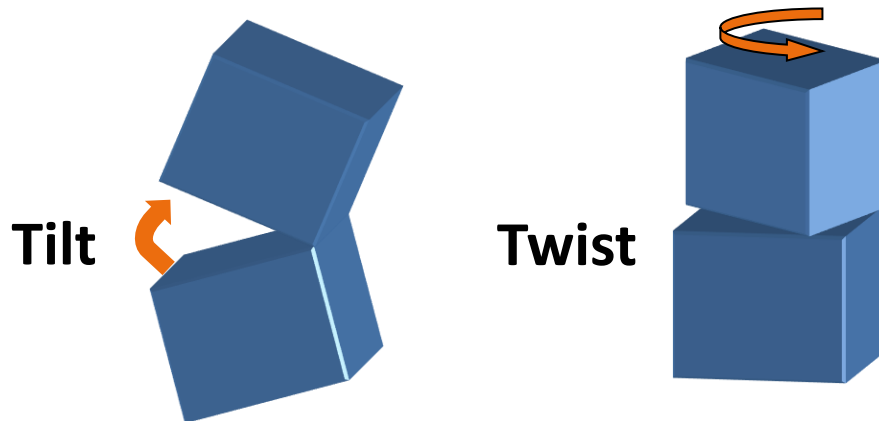


**Figure 2.4f** – Visual representation of the formation of tilt and twist grain boundaries.

The METADISE code<sup>(136)</sup> was used for grain boundary generation in this study. Once the minimum energy surface termination had been identified upon the full relaxation of each surface, this surface

is then used to generate an interface as shown in figure 2.4f where a mirror plane is placed on top of the region I of block I and to generate a tilt boundary the block is reflected in this plane, and to generate a twist boundary the block is also reflected in this plane and further rotated perpendicular to the plane at a rotation angle of  $180^\circ$ . One of the aims of this work has been to examine whether we could use a high-throughput approach for generating grain boundaries. A fixed vector displacement of  $2 \text{ \AA}$  is used throughout in order to ensure there was no overlap between the two blocks resulting in any undesirable repulsion. As shown in figure 2.4c the interface region is defined by the two region I locations of each block where the size of this region is large enough to allow full relaxation and thereby convergence of surface energy is achieved, yet not too large that unnecessary computational resources are used. Again, the region II atoms are held at their fixed equilibrium position. Due to orientation dependence of the interface previously discussed it is necessary to use a method which obtains the optimum orientation of one surface relative to the other in order to obtain the minimum energy structure of the interface. In order to achieve this desired structure, a virtual grid is placed on top of one of the surfaces, directly above region I. The second block is scanned over the first block in two dimensions along this grid at set step lengths where the smaller the step length, the larger the grid, therefore a more accurate and reliable scanning procedure at the expense of further computational resources. The step length chosen for each scan was  $0.2 \text{ \AA}$ , as this step length was found to produce results consistent with those seen experimentally within a reasonable timeframe. At each grid point an energy minimisation calculation was carried out which overall produced a potential energy surface which displayed the minima and maxima for all possible orientations. An example of a potential energy surface produced is shown in figure 2.4g.

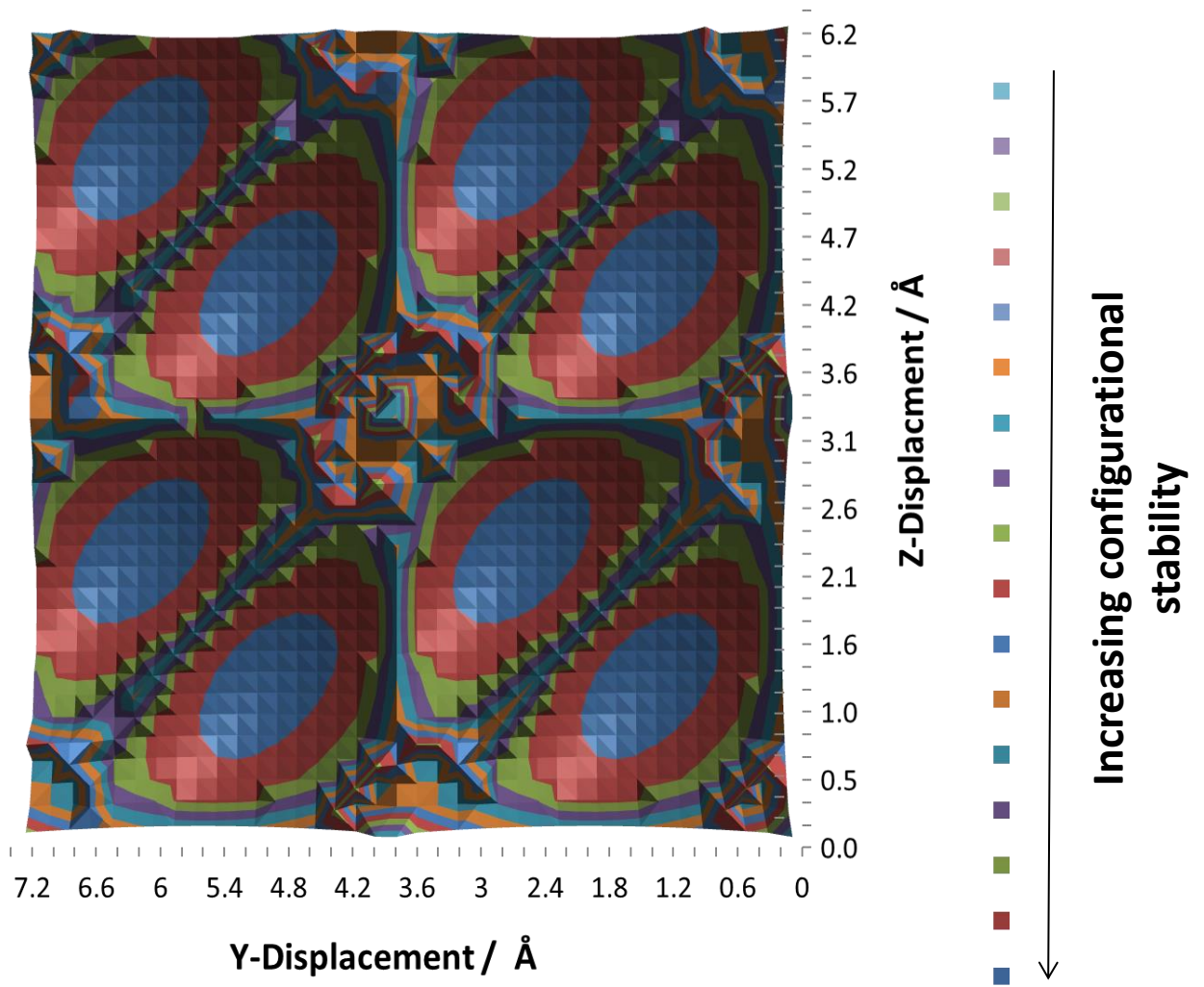


**Figure 2.4g** – Potential energy surface for  $\Sigma 3$  (111)  $\text{CeO}_2$  symmetric tilt interface where the global minima is located at 6.4 Å by 5.5 Å (y vs z displacement).

Figure 2.4g is an example of one of the potential energy surfaces obtained for  $\text{CeO}_2$  where the potential energy surface shows the energy minima shown by the blue oval wells and energy maxima shown by peaks of varying colours located at the centre and corners of the potential energy surface. From locating the global minimum of the potential energy surface, the stability of the interface can be expressed by the formation ( $E_f$ ) and cleavage ( $E_c$ ) energies obtained which are calculated by equations 2.54 and 2.55.

$$E_f = \frac{E_{GB} - E_B}{A} \quad (2.54)$$

$$E_c = \frac{2E_S - E_{GB}}{A} \quad (2.55)$$

$E_{GB}$  is the energy of the interface obtained from the global minima of the scan,  $E_B$  is the bulk energy of a crystal with the same number of atoms,  $E_s$  is the energy of the surface for half the number of atoms per unit area of the bulk and  $A$  is the surface area of the interface. As well as obtaining these two energies, the scanning procedure also provides the most energetically favoured interface structure which could further be compared to experimental and other computational research to determine the reliability of the procedure where possible.

#### 2.4.2.4 Generation of Mixed Homogenous/Heterogeneous Interfaces

The mixed interfaces were generated using a similar approach with the scanning procedure. However, in the case of this approach, although the Miller indices were identical for the two surfaces, different terminations of the surface were used. For example, SrO terminated  $\Sigma 5$  (210) STO || TiO<sub>2</sub> terminated  $\Sigma 5$  (210) STO interface. Although the procedure of generation had minimal changes, equations 2.56 and 2.57 are updated to account for the differences in surface ( $E_s$ ) and bulk ( $E_B$ ) energies as well as surface area ( $A$ ) changes

$$E_f = \frac{E_{GB} - \left( \frac{E_{B1} + E_{B2}}{2} \right)}{\left( \frac{A_1 + A_2}{2} \right)} \quad (2.56)$$

$$E_c = \frac{(E_{S1} + E_{S2}) - E_{GB}}{\left( \frac{A_1 + A_2}{2} \right)} \quad (2.57)$$

As shown in equations 2.56 and 2.57, both have been updated to include the surface energies, bulk energies and surface areas of the respective surfaces used where each has been averaged in order to obtain an accurate value of formation and cleavage energy for the mixed interfaces and ensure both blocks are evenly accounted for in energy calculations.

When generating heterointerfaces, this required the combination of two surfaces in order to achieve an energetically favoured lattice match. The assumption made in this procedure was that two surfaces with a similar surface area for different phases would achieve an energetically favoured match due to the lack of strain on either surface. In the case of generation, once two candidate surfaces had been selected, the lattice vectors of each were scaled in order to achieve a match with the lowest strain energy, therefore energetic stability.

## 2.5 Dynamical Studies of Bulk and Interfaces

In this section the study of the cubic perovskite LLTO and garnet LLZO will be simulated through the use of molecular dynamics; namely the DL\_POLY code<sup>(141)</sup>. As previously discussed LLTO exists in the form of  $\text{Li}_{3x}\text{La}_{(2/3)-x}\text{V}_{\text{La} (1/3)-2x}\text{TiO}_3$  where in this study four different compositions of varying lithium content will be simulated, in order to determine which composition exhibits the highest lithium diffusion rates. Different phases of the crystal structure of LLTO have been investigated experimentally where a range of different Li:La ratios have been identified<sup>(64), (72)</sup>. By identification of the phase which exhibits the lowest energy barrier to lithium diffusion in LLTO, this phase will be used further in grain boundary generation by using the previously discussed techniques (2.4.2.3) to construct low Miller index ( $\geq 3$ ) grain boundaries to investigate the effect of grain boundaries on lithium ion diffusion.

A similar procedure was carried out when investigating bulk LLZO.

In terms of both electrolyte materials, both the magnitude and direction of diffusion were investigated due to the importance of crystal orientation when considering polycrystalline or battery system phases.

The same types of simulations were carried out on bulk and grain boundaries ceria and STO where in this case the diffusion of oxygen was taken into consideration.

### 2.5.1 Annealing and Thermal Stability of Grain Boundaries

Prior to measuring diffusion in each phase, the lattice parameters were first equilibrated using the NST ensemble in the DL\_POLY code at the desired temperature for 1.1 ns.

In the case of the grain boundaries, each boundary was heated in intervals of 300 K per ns in order to anneal the two surfaces but to ensure that amorphization did not occur at temperatures in excess of 3000 K. The system was then cooled at the same rate to 300 K where the simulation procedure carried out on the bulk was then repeated on the grain boundary. This demonstrates whether the scanning procedure was sufficient or whether additional annealing was required.

### 2.5.2 Diffusion of Lithium and Oxygen

The diffusion of lithium and oxygen were measured by simulating each relevant phase using the NVT ensemble within the DL\_POLY code. The bulk structures were simulated for 10 ns as due to their

smaller size relative to the grain boundaries, significantly faster simulations could be carried out without the need for exhaustive computational expense and time. The diffusion for each grain boundary was measured over 1.0 ns due to the large increase in size resulting in a large computational expense and timeframe per simulation.

### 2.5.3 Activation Energies and Diffusion Coefficients

In order to obtain the activation energy for each range of temperatures, Arrhenius plots were constructed and represented by equations 2.61-2.62.

$$D = D_0 e^{\left(\frac{-E_a}{RT}\right)} \quad (2.61)$$

$$\ln D = \ln D_0 - \frac{E_a}{RT} \quad (2.62)$$

Equations 2.61 and 2.62 represent how the diffusion coefficient is used in order to obtain the activation energy from each plot where D and  $D_0$  are the diffusion coefficient at a given temperature and at an infinitely high temperature, respectively.  $E_a$  is the activation energy; R represents the molar gas constant and T represents the temperature.

One of the analyses that would be useful to further develop in the future would be the separate in-plane and out-of-plane diffusion coefficients. Calculations including these differences were initially tested, in particular the diffusion perpendicular to the boundary. However, the obtained statistics were generally poor and hence not reported in this body of work. Thus, to be confident in the extent of diffusion at and through particular boundaries. Simulations would therefore be required to be ran for many tens of nanoseconds, which was not feasible with respect to both time and resources. Thus, the results quoted are for the simulation cells themselves. However, the in-plane and out-of-plane analysis of diffusion coefficients is important next step and is included as an important recommendation for future work.

## 3 Potential Model Justification

### 3.1 Background and Justification of Resources

This chapter will describe the different potential models used in this study and how the interatomic potentials are used to calculate the bulk properties of a system. In each case the structural information obtained is compared with experimental and computational examples. Throughout this study a rigid ion partial charge (60%) model has been used, consistent with the potential models developed by Teter<sup>(132)</sup> and Pedone<sup>(133)</sup>. A rigid ion partial charge model was chosen for the following reasons. Firstly, the partial charge mimics one of the effects of polarization by effectively immersing the ions in a dielectric continuum of 2.8. This reduces the need for the computational expense of a shell model. Secondly, by keeping a fixed partial charge this allows non-stoichiometric compositions to be investigated without the need for adjustment of charges. And finally, the use of a rigid ion model increases the speed of each calculation resulting in an overall more efficient process when carrying out high-throughput calculations.

The parameters chosen for justification are consistent with other computational studies<sup>(159-161)</sup> where a general acceptance of within 3% of the experimentally observed structural parameters was considered to be acceptable for the purposes of this work. Further properties such as elastic constants, bulk moduli, vibrational frequencies, defect energy schemes and activation energies will also be investigated to further confirm consistency with experimental evidence of bulk studies. Where such properties give values consistent with those seen experimentally, this gives confidence in the interatomic potential model. However, it should be recognised that polarization may be important in broken symmetry environments such as near to grain boundaries and hence such models are tested against those which include polarization explicitly.



## 3.2 Structural Comparison

### 3.2.1 Strontium Titanate

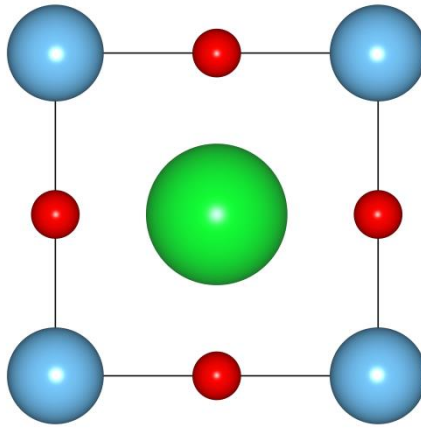


**Figure 3.2a** – Single unit cell of  $\text{SrTiO}_3$  which adopts the cubic perovskite structure ( $\text{ABO}_3$ ). Displayed using “Visualization for Electronic and Structural Analysis” (VESTA<sup>(162)</sup>).

$\text{SrTiO}_3$	Teter <sup>(132)</sup>	Chen <sup>(71)</sup>	Pedone <sup>(133)</sup>	Sayle <sup>(134)</sup>	Experimental <sup>(163)</sup>
$a / \text{\AA}$	3.88	3.92	3.92	3.85	3.89
$b / \text{\AA}$	3.88	3.92	3.92	3.85	3.89
$c / \text{\AA}$	3.88	3.92	3.92	3.85	3.89
$\alpha / ^\circ$	90.0	90.0	90.0	90.0	90.0
$\beta / ^\circ$	90.0	90.0	90.0	90.0	90.0
$\gamma / ^\circ$	90.0	90.0	90.0	90.0	90.0
$C_{11} / 10^{11} \text{ dyne cm}^{-2}$	31.87	30.98	27.99	31.80	31.72
$C_{12} / 10^{11} \text{ dyne cm}^{-2}$	12.71	13.34	13.69	14.03	10.25
$C_{44} / 10^{11} \text{ dyne cm}^{-2}$	13.12	13.34	13.03	14.29	12.35
Bulk Modulus / GPa	201.49	192.24181	168.87	199.54	179.00

**Table 3.2a** – Optimised lattice parameters ( $a$ ,  $b$ ,  $c$ ,  $\alpha$ ,  $\beta$  and  $\gamma$ ), elastic constants ( $C_{ij}$ ) and bulk modulus ( $B$ ) of  $\text{SrTiO}_3$ .

Wavenumber <sub>Teter</sub> / cm <sup>-1</sup>	Wavenumber <sub>Pedone</sub> / cm <sup>-1</sup>	Mode	Correlation <sup>(163)</sup>
191.75	169.34	Sr-O	Sr-TiO <sub>3</sub> transverse vibration
371.31	358.83	O-O	O-O rattling
470.13	386.44	Ti-O	Sr-TiO <sub>3</sub> longitudinal vibration
740.81	688.85	O-O	O-O rattling

**Table 3.2b** – Calculated and experimental infrared vibrational frequencies of SrTiO<sub>3</sub>. Vibrational frequencies were calculated using the lattice dynamics routines in GULP<sup>(26)</sup>.

Table 3.2a and 3.2b show the structural comparisons between the lattice parameters, elastic constants, bulk moduli and infrared frequencies for the two potential models used along with experimental comparisons for strontium titanate. The data included from both tables was obtained using the METADISE<sup>(136)</sup> and GULP<sup>(26)</sup> codes where both produced similar values. When comparing the two potential model values to each other, the lattice parameters have a high degree of agreement, with the Pedone potential lattice having a slightly larger volume (~1.8 Å<sup>3</sup> expansion) than the one obtained with the Teter potential, yet all parameters agree with the experimental lattice parameters. The discussed Teter potential has also been successful in reproducing lattice parameters consistent with experimental data within other computational studies<sup>(24, 164)</sup>. The elastic constants are also in agreement with experimental values. The significance of the elastic constants is that they are related to the second derivative of energy with respect to strain. Therefore, the agreement of elastic constants with experimental values is also valuable as any difference may significantly affect the overall structure upon relaxation and potentially surface energies. The bulk modulus values are also within good agreement with the experimental value quoted. A range of bulk moduli are quoted in experimental and computational research<sup>(165)</sup> which are consistent with the values obtained for each potential model. When considering the vibrational frequencies, the observed frequencies likely correspond with those seen in experimental publications, where the transverse and longitudinal vibrational modes between Sr-TiO<sub>3</sub> are seen based on the frequencies and intensities output by the GULP code, along with the oxygen vibrations which are not quoted in experimental examples. The clear difference observed in the infrared frequencies is that the wavenumbers obtained for the Teter potential are significantly larger than those observed for the Pedone potential. This shows that the Teter potential results in a stronger Sr-O and O-O bond along with a much stronger Ti-O bond, represented by the large increase (~100 cm<sup>-1</sup>) in wavenumber. When considering all the factors discussed, the bulk properties obtained are in good agreement with experimental values therefore implying strength in both potential models used for strontium titanate, thereby giving us confidence when expanding to interface construction.

### 3.2.2 Cerium Dioxide

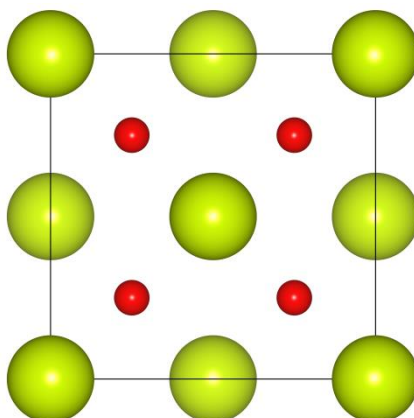


**Figure 3.2b** – Single unit cell of  $\text{CeO}_2$  which adopts the cubic fluorite structure ( $\text{CaF}_2$ ).

$\text{CeO}_2$	Teter <sup>(132)</sup>	Chen <sup>(71)</sup>	Pedone <sup>(133)</sup>	Sayle <sup>(134)</sup>	Experimental <sup>(4)</sup>
$a / \text{\AA}$	5.40	5.44	5.49	5.41	5.41
$b / \text{\AA}$	5.40	5.44	5.49	5.41	5.41
$c / \text{\AA}$	5.40	5.44	5.49	5.41	5.41
$\alpha / ^\circ$	90.0	90.0	90.0	90.0	90.0
$\beta / ^\circ$	90.0	90.0	90.0	90.0	90.0
$\gamma / ^\circ$	90.0	90.0	90.0	90.0	90.0
$C_{11} / 10^{11} \text{ dyne cm}^{-2}$	43.88	45.53	38.56	40.46	40.30
$C_{12} / 10^{11} \text{ dyne cm}^{-2}$	10.41	9.58	7.24	9.43	10.50
$C_{44} / 10^{11} \text{ dyne cm}^{-2}$	9.44	8.69	6.80	8.35	7.30
Bulk Modulus / GPa	224.61	215.63	176.80	197.34	220.00

**Table 3.2c** – Optimised lattice parameters ( $a$ ,  $b$ ,  $c$ ,  $\alpha$ ,  $\beta$  and  $\gamma$ ), elastic constants ( $C_{ij}$ ) and bulk modulus ( $B$ ) of  $\text{CeO}_2$ .

Wavenumber <sub>Teter</sub> / $\text{cm}^{-1}$	Wavenumber <sub>Pedone</sub> / $\text{cm}^{-1}$	Mode	Correlation <sup>(166)</sup>
399.23	358.33	Ce-O	Ce-O vibration
609.16	590.40	O-O	O-O rattling

**Table 3.2d** – Calculated and experimental infrared vibrational frequencies of  $\text{CeO}_2$ . Vibrational frequencies were calculated using the lattice dynamics routines in GULP<sup>(26)</sup>.

Table 3.2c and 3.2d show the structural comparisons between the lattice parameters, elastic constants, bulk moduli and infrared frequencies for all potential models used along with experimental comparisons for ceria. Again, the structural information has been obtained using the METADISE and GULP codes and the discussed Teter potential has been successful in reproducing lattice parameters consistent with experimental data within other computational studies<sup>(134)</sup>. When comparing the lattice parameters obtained, both the parameters obtained for all potential models agree with the experimental values. Like strontium titanate, the Sayle potential model gives a small lattice expansion ( $\sim 1.8 \text{ \AA}^3$  expansion), compared to the Teter potential. The elastic constants are also in good agreement with the experimental values where the constants obtained for the Pedone potential are almost identical to the experimental values, therefore giving confidence in the potential model upon relaxation of the structure. The bulk modulus values are also consistent with the experimentally observed values<sup>(4)</sup> where the Teter potential outperforms the Pedone with respect to the bulk modulus. The infrared frequencies obtained for ceria using the GULP code show vibrational modes that would be expected, Ce-O vibration and O-O rattling. Again, the vibrational frequencies obtained are seen to be larger, yet not significantly in this case, for the Teter potential, thereby showing that the Ce-O and O-O interactions would be stronger when using the Teter potential model.

### 3.2.3 Lithium Lanthanum Titanate (LLTO)

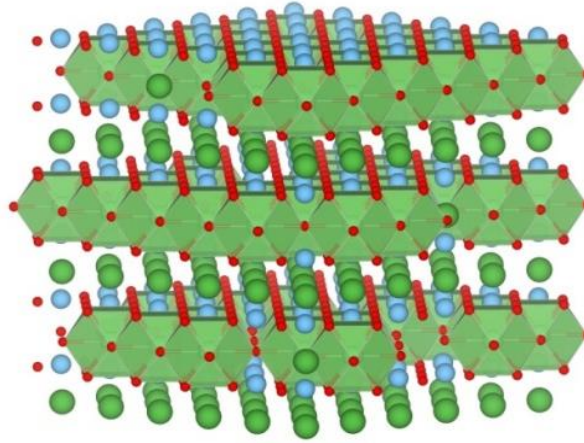


**Figure 3.2c** – Structure of layered perovskite LLTO ( $\text{Li}_{3x}\text{La}_{(2/3)-x}\text{VLa}_{(1/3)-2x}\text{TiO}_3$ ) where  $x=0.1$

LLTO	Teter <sup>(132)</sup>	Chen <sup>(71)</sup>	Pedone <sup>(133)</sup>	Sayle <sup>(134)</sup>	Purton <sup>(167)</sup>	Experimental <sup>(63)</sup>
a / Å	7.71	7.77	7.73	7.61	7.718	7.83
b / Å	7.70	7.76	7.73	7.61	7.709	7.75
c / Å	15.66	15.87	16.01	15.56	7.821	15.74
$\alpha$ / °	90.02	90.03	90.00	90.00	90.00	90.00
$\beta$ / °	90.00	90.00	90.00	89.97	90.00	90.00
$\gamma$ / °	90.00	90.00	89.99	90.00	90.00	90.00
$C_{11}$ / $10^{11}$ dyne $\text{cm}^{-2}$	29.25	26.64	22.03	29.49	29.12	No exp data
$C_{12}$ / $10^{11}$ dyne $\text{cm}^{-2}$	11.42	11.66	11.32	13.20	11.59	No exp data
$C_{44}$ / $10^{11}$ dyne $\text{cm}^{-2}$	9.86	10.15	10.18	10.73	10.05	No exp data
Bulk Modulus / GPa	174.87	164.91	153.21	188.10	179.51	No exp data

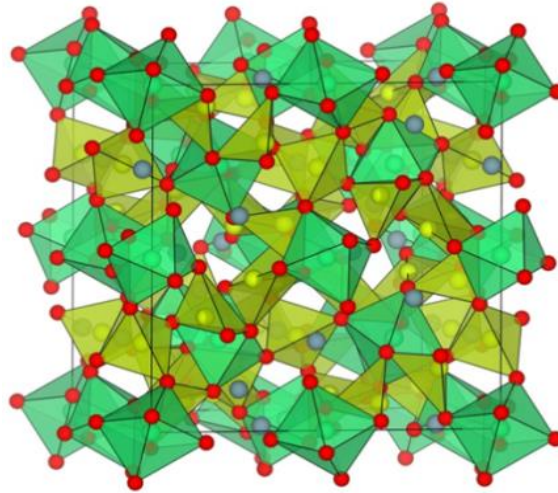
**Table 3.2e** – Optimised lattice parameters ( $a$ ,  $b$ ,  $c$ ,  $\alpha$ ,  $\beta$  and  $\gamma$ ), elastic constants ( $C_{ij}$ ) and bulk modulus ( $B$ ) of LLTO.

Table 3.2e shows the optimised lattice parameters, elastic constants and bulk moduli using four different potential models for LLTO. As shown the three potential models used in calculation all have an excellent agreement with the experimental parameters, despite the loss of symmetry in all three structures due to the small deviations in the  $\beta$  and  $\gamma$  angles. Furthermore, in the case of the Teter potential model there is a further breaking of symmetry due to the small contraction in the  $b$  lattice parameter (0.01 Å). Experimentally it is observed that there is a difference of 0.12 Å between the  $a$  and  $b$  lattice parameters which is not observed in any of the three potential model calculations. There is also no distortion of any of the angles seen experimentally. When comparing the Pedone

and Sayle potential models, a difference of 0.12 Å is observed between the a and b lattice parameters with the Pedone oxygen potential calculating lattice parameters closer to the experimentally seen values. Whereas the Sayle oxygen potential was specifically derived for use in CeO<sub>2</sub> thereby concluding that the Pedone oxygen potential appears to be more suitable when investigating non-fluorite structures. Therefore, the Pedone oxygen potential is used in this research. Unfortunately, there is no experimental data available for the elastic constants and bulk modulus. However, firstly when comparing the three elastic constants all are within good agreement with each other giving us an overall confidence in the results obtained despite the lack of experimental comparisons. The bulk moduli obtained also are also in agreement with each other where similarly to STO and ceria there is a range of different bulk moduli seen for LLTO.

Like the bulk modulus and elastic constants no data was available experimentally for the vibrational frequencies of LLTO. Furthermore, the calculated output showed around two hundred different vibrational frequencies which display the complexity of the structure due to the possible shift of lithium sites upon relaxation due to the concentration of vacancies present within the structure.

### 3.2.3 Lithium Lanthanum Zirconate (LLZO)



**Figure 3.2d** – Structure of garnet LLZO ( $\text{Li}_7\text{La}_3\text{Zr}_2\text{O}_{12}$ ).

LLZO	Teter <sup>(132)</sup>	Pedone <sup>(133)</sup>	Experimental <sup>(168)</sup>
$a / \text{\AA}$	13.046	13.250	13.103
$b / \text{\AA}$	13.177	13.385	13.103
$c / \text{\AA}$	12.697	12.687	12.654
$\alpha / ^\circ$	90.0	90.0	90.0
$\beta / ^\circ$	90.0	90.0	90.0
$\gamma / ^\circ$	90.0	90.0	90.0

**Table 3.2f** – Optimised lattice parameters ( $a$ ,  $b$ ,  $c$ ,  $\alpha$ ,  $\beta$  and  $\gamma$ ) of LLZO.

Experimental structural characterisation of LLZO was conducted at 298 K, thereby the comparisons made are relative to the low temperature (500 K<) tetragonal phase as opposed to the cubic phase observed at high temperatures. The two potential models show agreement with the experimental lattice parameters where in the case of the  $a$  and  $b$  parameters, a deviation of roughly 0.1 Å is observed with respect to the experimental parameters. This resulted in the final structures being orthorhombic in character as opposed to the tetragonal phases seen experimentally.

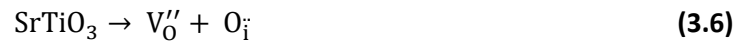
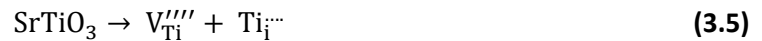
### 3.3 Point Defect Simulations

One of the issues with the analysis of the bulk structures is that only high symmetry structures were considered for validation. Comparison of defect properties allows for the testing of potential models in broken symmetry structures. Whilst this section investigates point defects, surfaces and grain boundaries can be considered as an array of defects in two dimensions and three dimensions, respectively, which will be discussed in detail in each of the results chapters.

Simulations of point defects on each structure were carried out using the GULP code where the Mott-Littleton approximation is applied. In each case, Schottky and Frenkel defects were considered using all potential models. All calculations in this section carried out using the GULP code made use of the Mott-Littleton method in which two region sizes were required to be defined in order for convergence to be achieved over the smallest region size to ensure that all energies had converged without the need for further computational expense. As a result of this a number of different region sizes were tested where energetic convergence was achieved when defining the region sizes as “10 Å<sup>3</sup>” for region one and “20 Å<sup>3</sup>” for region two, therefore these two region sizes were used throughout.

#### 3.3.1 Strontium Titanate

The following defect schemes<sup>(3)</sup> represent the Schottky and Frenkel defects for STO, where the energetics of each scheme will be further investigated.





It should be noted that of these five schemes, schemes 3.1 and 3.2 remove the stoichiometry of the structure and therefore are not true Schottky defects. Therefore, they will be referred to as “Schottky-like” when discussed. The following table represents the defect energies for each defect and further incorporation of the defects into schemes.

Species	Teter <sup>(132)</sup> / eV	Chen <sup>(71)</sup> / eV	Pedone <sup>(133)</sup> / eV	Sayle <sup>(134)</sup> / eV	Catlow <sup>(3)</sup> / eV	Begg <sup>(169)</sup> / eV
SrTiO <sub>3</sub>	-62.86	-62.12	-61.21	-62.47	-149.18	-
SrO	-13.85	-13.82	-13.39	-13.25	-35.61	-
TiO <sub>2</sub>	-47.76	-47.13	-46.95	-47.84	-110.10	-
Sr <sub>VAC</sub>	10.94	10.83	9.85	10.01	20.51	18.30
Ti <sub>VAC</sub>	46.18	45.33	43.37	45.11	82.23	41.70
O <sub>VAC</sub>	9.83	9.17	8.83	10.12	18.16	11.40
Sr <sub>INTERSTITIAL</sub>	-0.01	-0.65	-0.66	0.65	-12.62	-1.80
Ti <sub>INTERSTITIAL</sub>	-22.29	-22.95	-21.16	-22.63	-68.03	-23.50
O <sub>INTERSTITIAL</sub>	2.26	2.60	1.70	2.00	-13.02	-1.30
Sr <sub>Ti</sub>	34.83	34.01	34.49	32.78	-	-
Ti <sub>Sr</sub>	-19.38	-18.98	-20.70	-20.02	-	-

**Table 3.3a** – Raw Intrinsic defect energies for all potential models in STO where Begg et al. used DFT methods. The first four columns represent values calculated in this study which includes the lattice energies calculated in the first three rows.

Scheme	Teter <sup>(132)</sup> / eV	Chen <sup>(71)</sup> / eV	Pedone <sup>(133)</sup> / eV	Sayle <sup>(134)</sup> / eV	Catlow <sup>(3)</sup> / eV	Begg <sup>(169)</sup> / eV
Sr <sub>VAC</sub> + O <sub>VAC</sub> + SrO	3.46	3.09	2.64	3.44	1.53	-
Ti <sub>VAC</sub> + 2O <sub>VAC</sub> + TiO <sub>2</sub>	6.02	5.51	4.69	5.84	2.48	-
Sr <sub>VAC</sub> + Ti <sub>VAC</sub> + 3O <sub>VAC</sub> + SrTiO <sub>3</sub>	4.75	4.31	3.70	4.60	1.61	-
Sr <sub>VAC</sub> + Sr <sub>INTERSTITIAL</sub>	5.47	5.09	4.59	5.33	3.94	14.60
Ti <sub>VAC</sub> + Ti <sub>INTERSTITIAL</sub>	11.94	11.19	11.10	11.24	7.10	-
O <sub>VAC</sub> + O <sub>INTERSTITIAL</sub>	6.04	5.88	5.26	6.06	2.57	9.80
Sr <sub>Ti</sub> + Ti <sub>Sr</sub>	7.72	7.52	6.90	6.38	-	9.80

**Table 3.3b** –Energy per number of defects for “Schottky-like”, Schottky, Frenkel and antisite defects in STO. Again, the first four columns show the values calculated in this study.

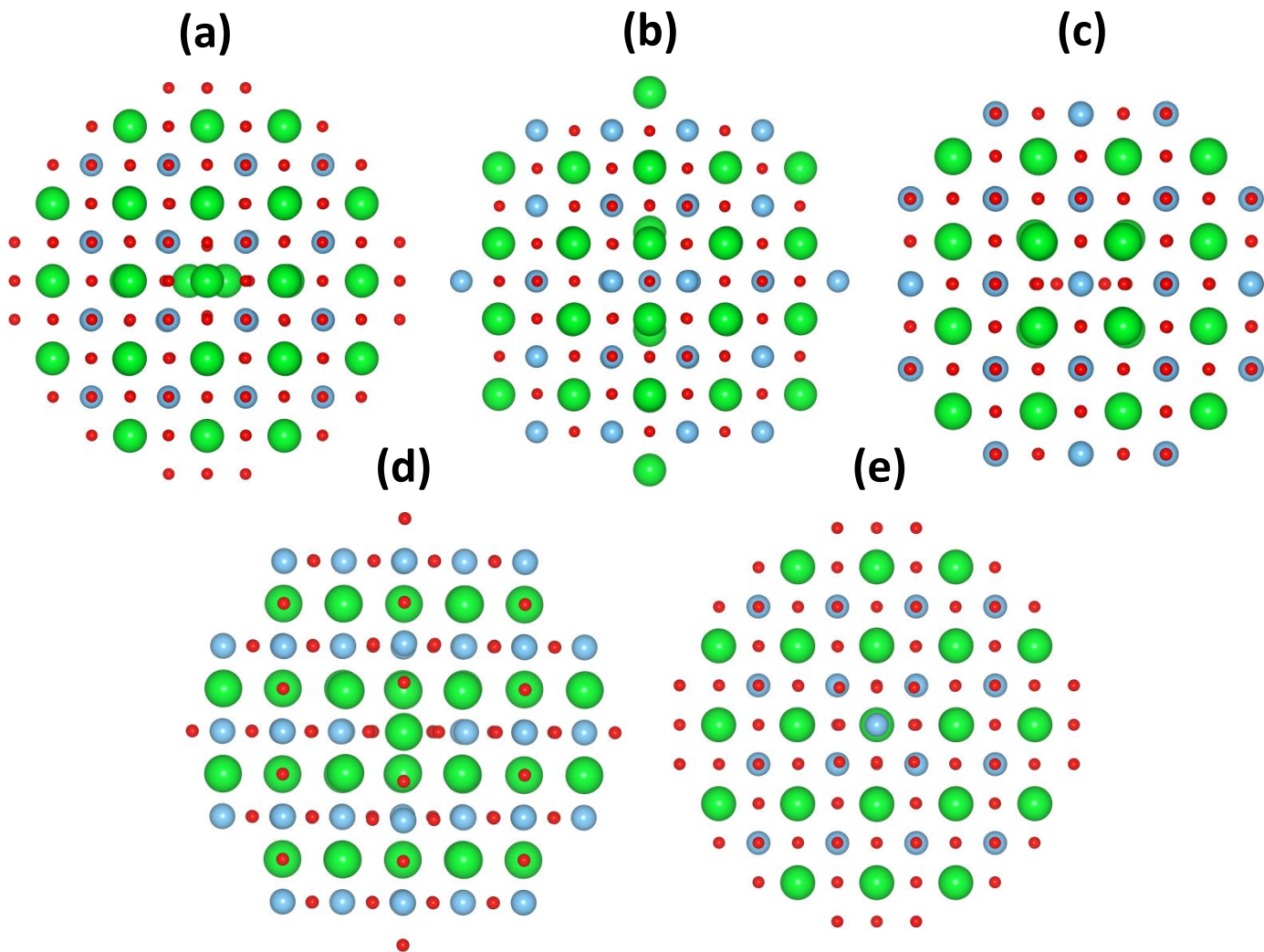


**Figure 3.3a (a)-(e)** – Structural representations of (a) Sr-twin split interstitial in (100) plane (b) Ti-interstitial with Sr distortion in (010) plane (c) O-twin split interstitial in (100) plane (d) Sr-antisite ion occupying Ti-site (e) Ti-antisite ion occupying Sr-site.

Table 3.3a and 3.3b show the defect energies and defect scheme energies for all potential models calculated using the Mott Littleton approximation in the GULP code. It should be noted that although “raw” defect formation energies cannot be used to compare different potentials or computational schemes, because these ignore possible differences in reference elemental energies, they are useful in assessing the relative contributions of each component to the intrinsic defect energies given in Table 3.3b. Further, comparisons to other studies where structural representations of the interstitial and antisite defects are represented in figure 3.3 a-e. The lattice energies of each respective compound represented in table 3.3a all agree with respect to each other for each of the potential models investigated. However, the calculated values are approximately 40% of the value of the lattice energy, as described in equation 2.1, of those obtained by Catlow *et al.*<sup>(3)</sup>. As a rigid ion, partial charge model was used in this research compared to the fully charged, shell model used by Catlow, the polarization effect would not be as significant as when using the shell model and

therefore this may account for the large discrepancy in lattice energy. The order of stability of the vacancies of each ion agrees with both the Catlow and Begg<sup>(169)</sup> order of stability despite each defect energy being half the approximate magnitude of those calculated by Catlow. The titanium and oxygen vacancy energies show good agreement with the research carried out by Begg despite the strontium vacancy once again being half the magnitude of the two literature values. Each interstitial value is within good agreement with those reported by Begg where the best agreement is seen by the Ti-interstitial energy. With reference to table 3.3b each of the “Schottky-like” defects obtained are larger than those obtained by Catlow. However, the order of magnitude of these defects does agree with the strontium oxide “Schottky-like” defect being the most energetically favoured defect and the titanium oxide “Schottky-like” defect being the least energetically favoured thereby giving some confidence in the results obtained despite the difference in magnitude. Furthermore, when considering the structural properties discussed, for each defect scheme the energies obtained using the Teter potential are most commonly the largest in energy. This correlates with the larger bulk modulus obtained using this potential model and therefore if the lattice is more resistant to stress, then defects will be less likely to form. The Frenkel defect energies result in a different observation than that seen for the Schottky and “Schottky-like” defects. In the case of all potential models investigated, the strontium Frenkel was found to be energetically more stable than the oxygen Frenkel where both Begg and Catlow found this not to be the case, thereby limiting the reliability of the ordering of these defects. Yet for all potential models and both literature studies the titanium Frenkel was found to be the least energetically favoured defect scheme. The antisite defect scheme was also found to be energetically unfavourable although the magnitude is somewhat smaller than the values obtained by Begg. The defect energies are in broad agreement with each other. Perhaps due to the use of a rigid ion model some are slightly larger. The effect on activation energies and thermal properties will be discussed in section 3.4.

### 3.3.2 Cerium Dioxide

The following defect schemes represent the Schottky and Frenkel defects for ceria.



Species	Teter <sup>(132)</sup> / eV	Chen <sup>(71)</sup> / eV	Pedone <sup>(133)</sup> / eV	Sayle <sup>(134)</sup> / eV	Sokol <sup>(50)</sup> / eV
CeO <sub>2</sub>	-43.37	-42.92	-42.09	-42.65	-102.87
Ce <sub>VAC</sub>	42.61	42.10	39.91	40.73	94.41
O <sub>VAC</sub>	8.12	7.29	7.11	8.40	12.91
Ce <sub>INTERSTITIAL</sub>	-21.04	-21.64	-21.88	-20.84	-62.53
O <sub>INTERSTITIAL</sub>	-0.37	0.32	-0.82	-1.89	-6.49

**Table 3.3c** – Intrinsic defect energies for all potential models in CeO<sub>2</sub>.

Scheme	Teter <sup>(132)</sup> / eV	Chen <sup>(71)</sup> / eV	Pedone <sup>(133)</sup> / eV	Sayle <sup>(134)</sup> / eV	Sokol <sup>(50)</sup> / eV
O <sub>VAC</sub> + O <sub>INTERSTITIAL</sub>	3.88	3.81	3.15	3.26	3.21
Ce <sub>VAC</sub> + Ce <sub>INTERSTITIAL</sub>	10.78	10.23	9.01	9.95	15.94
Ce <sub>VAC</sub> + 2O <sub>VAC</sub> + CeO <sub>2</sub>	5.16	4.59	4.01	4.96	5.79

**Table 3.3d** –Energy per number of defects for Schottky and Frenkel defects in CeO<sub>2</sub>.

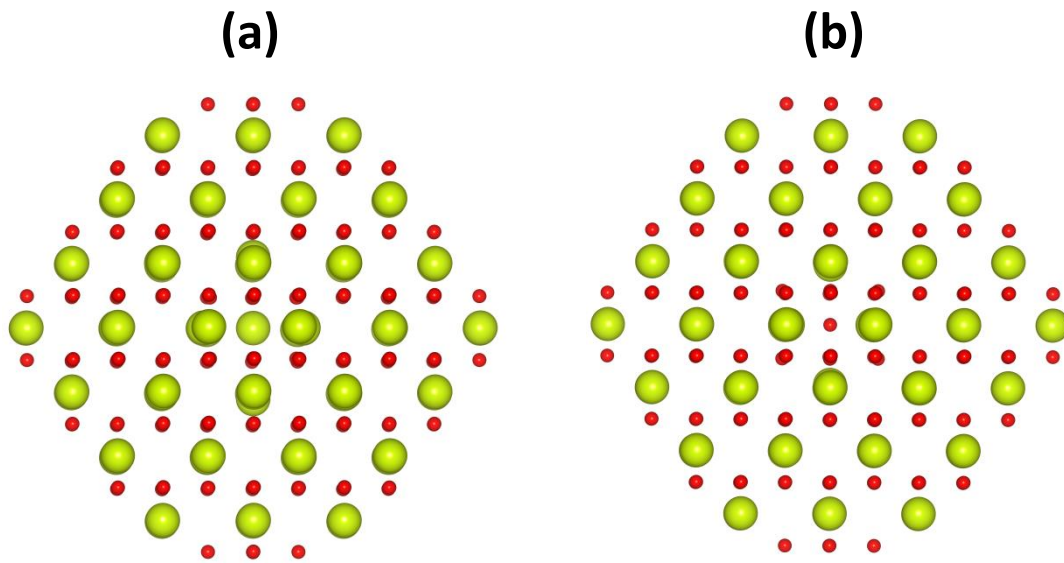


**Figure 3.3b (a)-(b)** – Structural representations of (f) Ce interstitial site in (100) plane (g) Ce interstitial site in (100) plane.

Table 3.3c and 3.3d show the defect energies and defect scheme energies for all potential models investigated along with comparisons to other studies, where structural representations of the interstitial defects are represented in figure 3.3f and 3.3g. The raw energies obtained for the lattice

energy of ceria show a similar trend as all four potential model values agree with each other, however they are again approximately 40% of the value obtained by Sokol. This is also found to be true for the cerium ion vacancy energy, yet better agreement was achieved for the oxygen ion vacancy. Sokol further used a full charge model and therefore energies were higher. There is also a large discrepancy between the four interstitial values for each species despite all potential models having a strong agreement with each other, where the value reported by Sokol was three times larger. However, when the oxygen Frenkel and Schottky are considered, the calculated potential energy is in good agreement with the value reported by Sokol. Despite the smaller magnitude achieved by all four potential models compared to the Sokol energy, all four have a good agreement with each other as well as predicting that the cerium interstitial defect would be the least energetically favoured of the three schemes investigated which are consistent upon comparison. The defect energies are in broad agreement with each other. Similar to strontium titanate, perhaps due to the use of a rigid ion model some energies are slightly larger. The effect on activation energies and thermal properties will be discussed in section 3.4.

### 3.4 Bulk Oxygen Diffusion

Simulations were carried out in order to obtain diffusion coefficients and activation energies of bulk oxygen diffusion to assess the potential model further, prior to expanding this towards the investigation of interfaces.

A bulk system of the size of approximately  $20 \times 20 \times 20 \text{ \AA}^3$  for both ceria and STO was constructed using the METADISE<sup>(136)</sup> code. Two systems were investigated, a stoichiometric structure where no defects had been incorporated previous to simulations and secondly a system containing 0.5% oxygen vacancies. Simulations were carried out using molecular dynamics (DL\_POLY\_Classic code<sup>(141)</sup>) where each system was heated to a temperature between 1500 K-3900 K (at intervals of 300 K) for 1 ns (100 ps equilibration time) using the NVT ensemble, therefore allowing relaxation of lattice parameters. The average volume of the system was fixed using the NVT ensemble where the system was simulated for a further 5 ns over which the diffusion of oxygen was measured. All four potential models were investigated in this procedure to observe the overall diffusion in each.

### 3.4.1 Strontium Titanate

Figure 3.4a shows the diffusion coefficients obtained for the 0.5%  $O_{vac}$  model of STO. When simulating the stoichiometric phase, no long range diffusion was observed throughout the selected temperature range and therefore a diffusion profile was unable to be constructed. Hence, an initial defective system was selected.

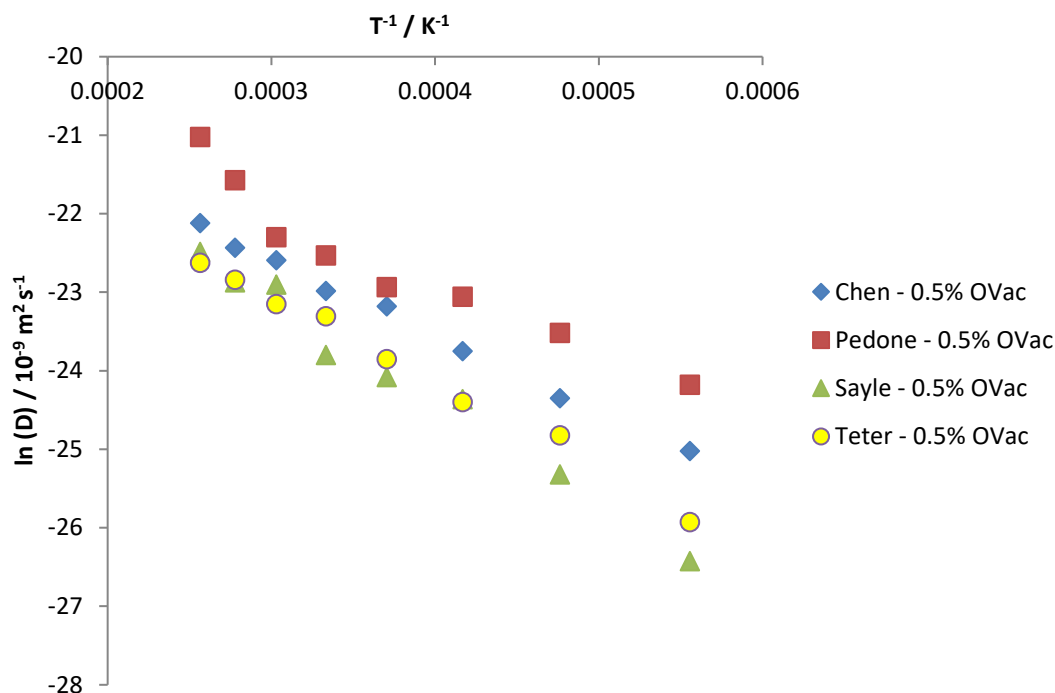


**Figure 3.4a** – Diffusion coefficients obtained for 0.5%  $O_{vac}$  STO between 1500 K-3900 K. Uncertainties are quoted in Table 3.4a

	Chen	Pedone	Sayle	Teter
$E_a$ / eV	$0.86 \pm 0.01$	$0.75 \pm 0.07$	$1.10 \pm 0.03$	$0.95 \pm 0.02$
$D_0$ / $10^{-9} \text{ m}^2 \text{ s}^{-1}$	$3.09 \pm 0.25$	$3.91 \pm 1.34$	$4.31 \pm 0.80$	$2.61 \pm 0.26$

**Table 3.4a** – Activation energies ( $E_a$ ) and  $D_0$  values observed in bulk STO.

The activation energies were calculated by the measurements of the regression of the linear data in figure 3.4a which is shown in equation 3.9.

$$E_a = \frac{-mR}{F} \quad (3.9)$$

m is the gradient; R is the molar gas constant and F is the Faraday constant.

Figure 3.4a and table 3.4a show the diffusion coefficients and activation energies with their respective uncertainties for each of the four potential models. The range of activation energies of STO are similar to those reported experimentally by Wang *et al.*<sup>(170)</sup>. In this study, values between 0.71 eV and 0.89 eV were obtained. The Chen and Pedone values are both within this range and the Sayle and Teter values are slightly higher. As the energy to form an oxygen Frenkel defect is higher, a larger energy barrier must be overcome to facilitate long range diffusion when using these potential models. As previously discussed, the introduction of oxygen vacancies was required to observe long range diffusion in bulk STO. In stoichiometric STO, a significant amount of initial energy is required to form the oxygen vacancy. Yet in models such as the those simulated in figure 3.4a, the oxygen vacancy has already formed, therefore the energetic behaviour is long range diffusion, which is consistent with other simulation studies<sup>(171-173)</sup>.

### 3.4.2 Cerium Dioxide

Unlike in STO, bulk diffusion was observed in both stoichiometric and defective ceria, therefore both models will be investigated in this section. As shown previously in section 3.3, the formation of O Frenkel defects is around half of that of STO. The diffusion profiles for stoichiometric and defective ceria are presented in figure 3.4b and c.

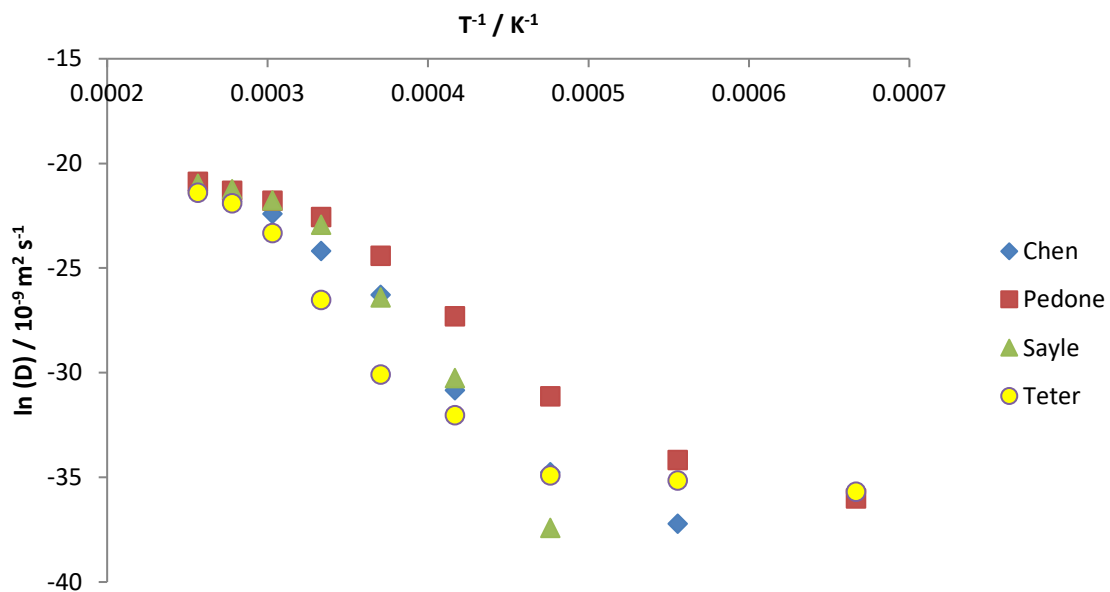


**Figure 3.4b** – Diffusion profiles obtained for stoichiometric ceria between 1500 K-3900 K



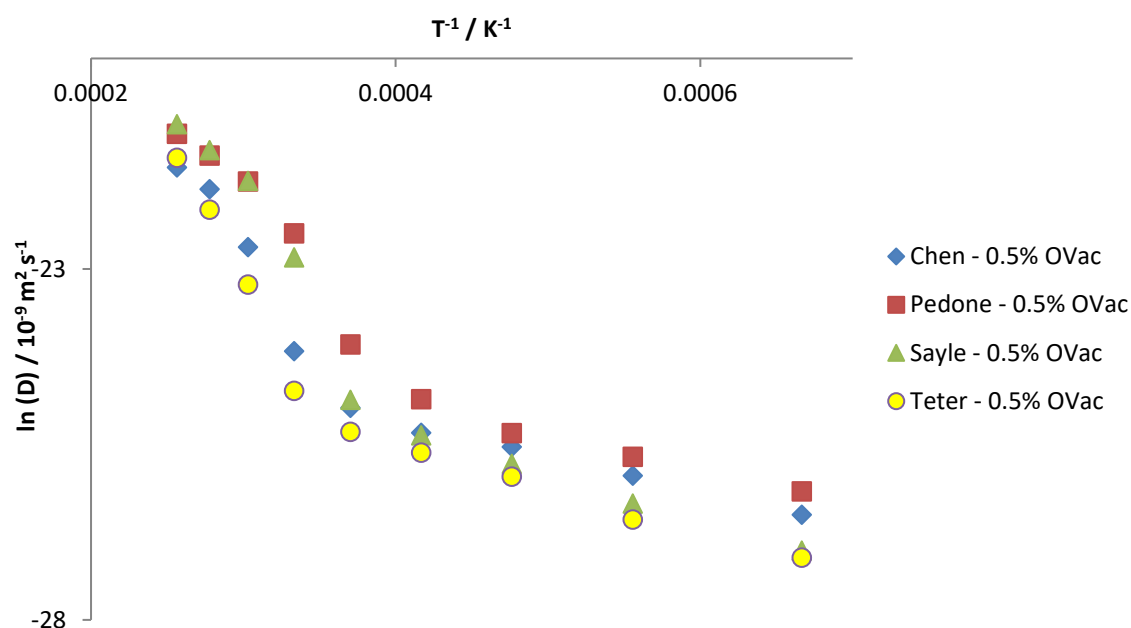


**Figure 3.4c** – Diffusion coefficients obtained for 0.5%  $O_{vac}$  ceria between 1500 K-3900 K.

Scheme	Stoichiometry	Chen	Pedone	Sayle	Teter
$E_a$ / eV	Stoichiometric	$5.01 \pm 0.32$	$3.60 \pm 0.25$	$6.47 \pm 0.74$	$3.35 \pm 0.56$
$E_a$ / eV	0.5% $O_{vac}$	$1.02 \pm 0.19$	$1.15 \pm 0.18$	$1.35 \pm 0.21$	$1.11 \pm 0.21$
$D_0$ / $10^{-9} \text{ m}^2 \text{ s}^{-1}$	0.5% $O_{vac}$	$3.47 \pm 3.37$	$12.53 \pm 10.85$	$21.07 \pm 22.20$	$3.61 \pm 3.78$

**Table 3.4b** – Activation energies ( $E_a$ ),  $D_0$  values and their uncertainties observed in stoichiometric and defective ceria. The  $D_0$  values were not reported for stoichiometric ceria as no long range diffusion was reported for two of the potential models below 2400 K.

Figure 3.4b and figure 3.4c show the observed diffusion coefficients for stoichiometric and defective bulk ceria. As can be clearly seen, the gradient does show a strong temperature dependence and hence a detailed discussion of mechanism would benefit by an analysis of the diffusion mechanisms as a function of temperature. However, here the aim is to provide a straightforward comparison between the different models and as an assessment of the effect of adding a low concentration of oxygen vacancies, across the complete temperature range. Hence, in both figures the gradients have been treated as linear. The comparison shows, firstly, that no long range diffusion was observed for the Teter or Sayle potential models at low temperatures (below 2400 K), which is shown by the consistent diffusion coefficient with increasing temperature within this region. For the stoichiometric phase, the results obtained show that when using the Teter and Pedone potential models this resulted in activation energies which were comparable to the activation energy reported by Ackermann *et al.*<sup>(174)</sup> of 3.57 eV. The results obtained when using the Chen and Sayle potential

models were significantly higher. This suggests an additional energy barrier, which could be the formation of additional oxygen vacancies<sup>(171)</sup>. Similar to the STO simulations, increasing temperature and therefore increasing kinetic energy results in the formation of oxygen vacancies, hence the increased diffusion at high temperatures. This was found to be consistent with other simulation studies<sup>(171-173)</sup>. As shown in table 3.4b, the introduction of 0.5% oxygen vacancies results in a significant reduction in the activation energy for all four potential models.

In summary, by incorporating intrinsic defects into the bulk, this has shown to result in a significant reduction in the activation energy and therefore enhance oxygen diffusion. One of the aims of this research is to investigate how the presence of grain boundaries affects oxygen diffusion compared to the bulk material. As a grain boundary is an extended array of intrinsic defects, the discussed results imply that the presence of grain boundaries could have a profound effect on oxygen transport.

### 3.5 Chapter Summary

In this chapter, the interatomic potential models used throughout this research have been justified with regards to structural, elastic, spectroscopic and energetic properties for bulk phases of the investigated materials. Good structural agreement was observed within the desired percentage range (3% for structural parameters and 10% for elastic properties), for structural parameters giving confidence in further investigation of surfaces and interfaces of such materials. Defect energy schemes showed that the calculated energies were generally higher than those observed in other computational studies. However, the Frenkel anionic defect energy of ceria was similar with that seen in  $\text{UO}_2^{(171)}$ , another fluorite structure. The activation energies and diffusion coefficients observed for the stoichiometric bulk suggested that vacancies were formed at high temperature, which led to enhanced oxygen diffusion. The obtained activation energies were consistent with those observed experimentally. Further simulations would be required to deduce whether a change in diffusion mechanism is observed with increasing temperature using more sophisticated techniques such as a NEB method. As highlighted, the incorporation of a small number of intrinsic defects had a significant effect on the activation energy and therefore oxygen diffusion in STO and ceria. This implied that the presence of grain boundaries could have a profound effect on oxygen transport which will be further investigated for both materials.

Based on results described in this chapter and availability of potential model parameters for each interaction, throughout this body of research, the Teter potential model will be used when modelling the SOFC materials, ceria and STO. The Pedone and Teter potential model will be used for modelling LLZO; this will be discussed in detail in chapter 8. Finally, the Purton potential model will be used for modelling LLTO. This is an adapted form of the Pedone potential model where the La-O interaction has been specifically fitted for LLTO.

## 4 Surfaces and Interfaces of Ceria

Solid oxide fuel cells are an example of a modern energy technology due to their energy conversion efficiency and low emissions relative to other forms of energy conversion<sup>(175)</sup>. One of the key challenges in fuel cell development is decreasing the operating temperature without having a profound detrimental effect on the fuel cell performance<sup>(176, 177)</sup>.

Ceria is a promising and versatile electrode material. The current evidence shows the success of ceria phases as an anode<sup>(7, 178, 179)</sup>, cathode<sup>(180)</sup> and most commonly as a solid electrolyte<sup>(176, 181)</sup>. In such fuel cell applications, electrolytes such as ceria are likely in polycrystalline form, meaning the presence of plentiful grain boundaries is of crucial importance in the functionality of fuel cells<sup>(182)</sup>. Characterisation of the structure and dynamics of ceria grain boundaries has been extensively studied using both experimental<sup>(46)</sup> and computational<sup>(183)</sup> methods where the presence of grain boundaries has been reported to suppress ionic transport<sup>(184)</sup>.

With regards to improving the functionality of ceria electrolytes, gadolinium doped ceria (GDC) has been widely considered to be effective at reducing the operating temperature, improving stability and increasing ionic diffusion<sup>(185-187)</sup>.  $Gd^{3+}$  doping has been found to exhibit high ion diffusion with respect to stoichiometric ceria<sup>(188, 189)</sup>.

This research focuses on using a high-throughput computational method to determine the structure and energetics of ceria grain boundaries, focussing initially on those which have been structurally characterised and further those which have not, generally of a higher Miller index ( $>4$ ). Further simulations using a combination of single point defects and MD simulations were carried out on stoichiometric ceria grain boundaries to further quantify whether the presence of grain boundaries in a polycrystalline phase would either facilitate or suppress oxygen ion diffusion.

### 4.1 Scan Overview

In this chapter, the surface and interface structure and stability of tilt  $CeO_2$  boundaries will be investigated using high-throughput computational techniques. Chapter 2 provided an insight into how the interfaces were constructed and how the stability and structure of each were obtained. The initial surface terminations were identified where the minimum energy surface with no dipole was chosen to ensure electrostatic convergence, where the chosen surfaces were consistent with those observed experimentally. Each scan was carried out either by reflecting the surface or by a  $180^\circ$  rotation and superimposing the initial surface on top of itself and carrying out a full minimisation at each grid point. For each interface, the scanning procedure discussed was carried out using both

approaches. It will be investigated which method resulted in the more energetically favoured interface as well as a comparison to other experimental and computational studies. Within this chapter each interface will be described by its  $\Sigma$  value where this was obtained using equation 2.54 as previously described. Furthermore, defect energy profiles will also be presented for each interface where intrinsic and extrinsic defect segregation energies were obtained. In addition to the structural characterisation of several ceria grain boundaries which have been experimentally characterised, the scanning methodology will be used to investigate boundaries that have not been structurally characterised. This chapter will further discuss the calculated dynamics for six structurally characterised ceria boundaries.

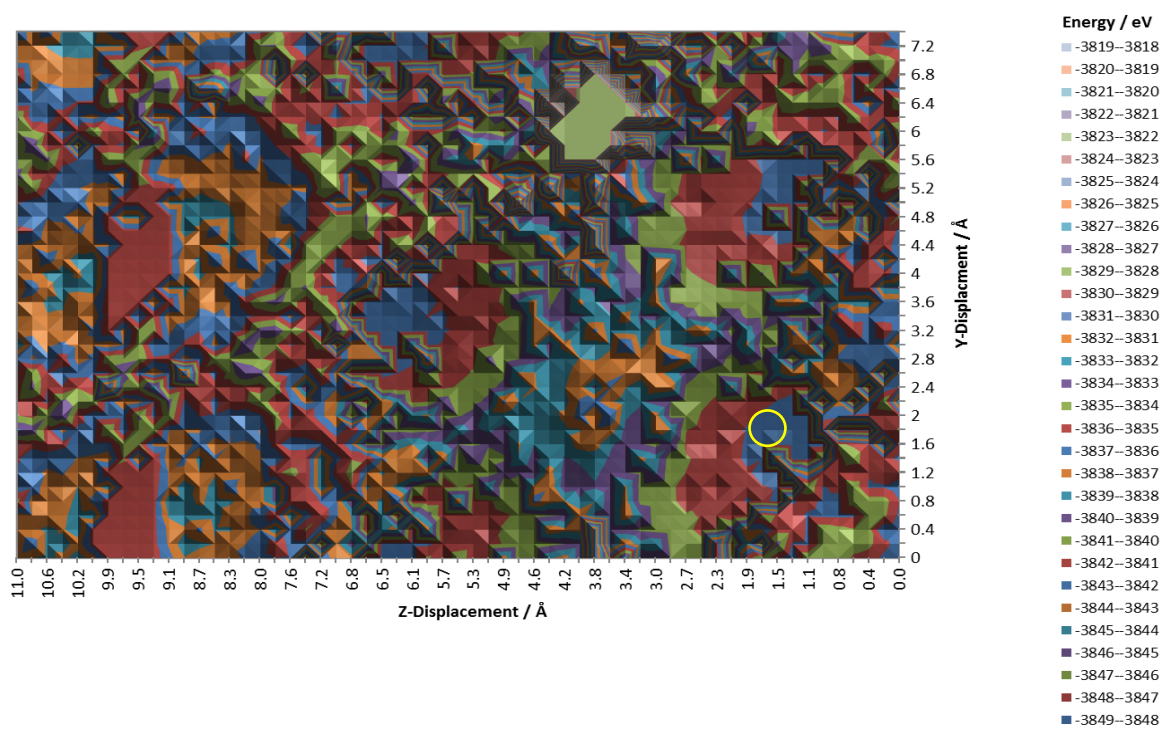


**Figure 4.1a** – Raw configurational potential energy surface of the  $\Sigma 9$   $(221)_{\text{Rot}}$   $\text{Ce}_2$  terminated interface of ceria by scanning one surface over the other. Yellow circle denotes region where global minimum is located. The complexity of this potential energy surface figure is representative of how a small step length is required to locate a global minimum.

A scan was carried out for a range of ceria interfaces ( $\Sigma 3$ -19), where all possible terminations of surfaces obtained through using the METADISE<sup>(136)</sup> code were used when constructing the interface, combining both identical surfaces and surfaces of different terminations, therefore constructing mixed interfaces. An example of a scan is presented in figure 2.4d where the global minimum was clearly defined and could therefore be easily interpreted. However, when carrying out each scan, more complex potential energy surfaces were obtained where a defined minimum potential well

was not present. As shown in figure 4.1a, the potential energy surface is much more complex than the potential energy surface shown in figure 2.4g. In this representation, the potential energy surface lacks well defined local minima and maxima regions and is comprised of sharp peaks which are very close in proximity therefore a small shift in the interface orientation could result in a drastic change in the structure. This shows the requirement for a small step length when performing each scan.

However, this approach required a lot of computer CPU time. Therefore, three approaches were considered to determine the most effective procedure.

- 'min' - The scan was carried out as previously discussed where a minimisation calculation was carried out at each grid point.
- 'conf' - The probe which carries out the minimisation acts at constant force where all forces perpendicular to the grain boundary were minimised. The surfaces were able to move away from each other but not parallel to each other.
- 'xonly' – When minimisation is carried out the overall structure (region I of each block) may only relax in the x-direction (depth of the block), therefore no relaxation occurs in the y and z direction.

In order to deduce which approach would be most suitable, the  $\text{CeO}_2$   $\Sigma 5$  (310) symmetric tilt interface was explored. A scan was carried out using each of the three approaches.

Approach	$E_f / \text{J m}^{-2}$	$E_c / \text{J m}^{-2}$	$t / \text{s}$
'conf'	1.85	5.61	65
'min'	1.98	5.48	83
'xonly'	3.43	4.04	18

**Table 4.1a** – Formation and cleavage energies obtained by using three scanning approaches for the  $\text{CeO}_2$   $\Sigma 5$  (310) symmetric tilt interface.

From the data obtained in table 4.1a, the 'conf' approach provided the lowest formation energy and the highest cleavage energy therefore deeming this as the favoured approach compared to the other methods. The 'min' approach obtained a formation and cleavage energy slightly less favoured than the 'conf' approach. However, due to the lack of constraints on this procedure, the overall scan required more computational time and therefore more computational resources which are further limitations of this method, however a similar structure was observed as shown in figure 4.1b. As shown the 'xonly' approach provided a much larger formation and much smaller cleavage energy compared to the two other methods thereby showing that, despite being much quicker due to the

limited relaxation, this method results in an energetically unfavourable structure which, when carrying out a further full minimisation, was structurally different to the those observed experimentally and was therefore deemed to be an unsuitable technique despite the significantly reduced computational time.

To further understand which of the three methods was most appropriate when carrying out further scans, the three structures obtained from the global minimum of each scan with their corresponding dipoles are shown in figure 4.1b.

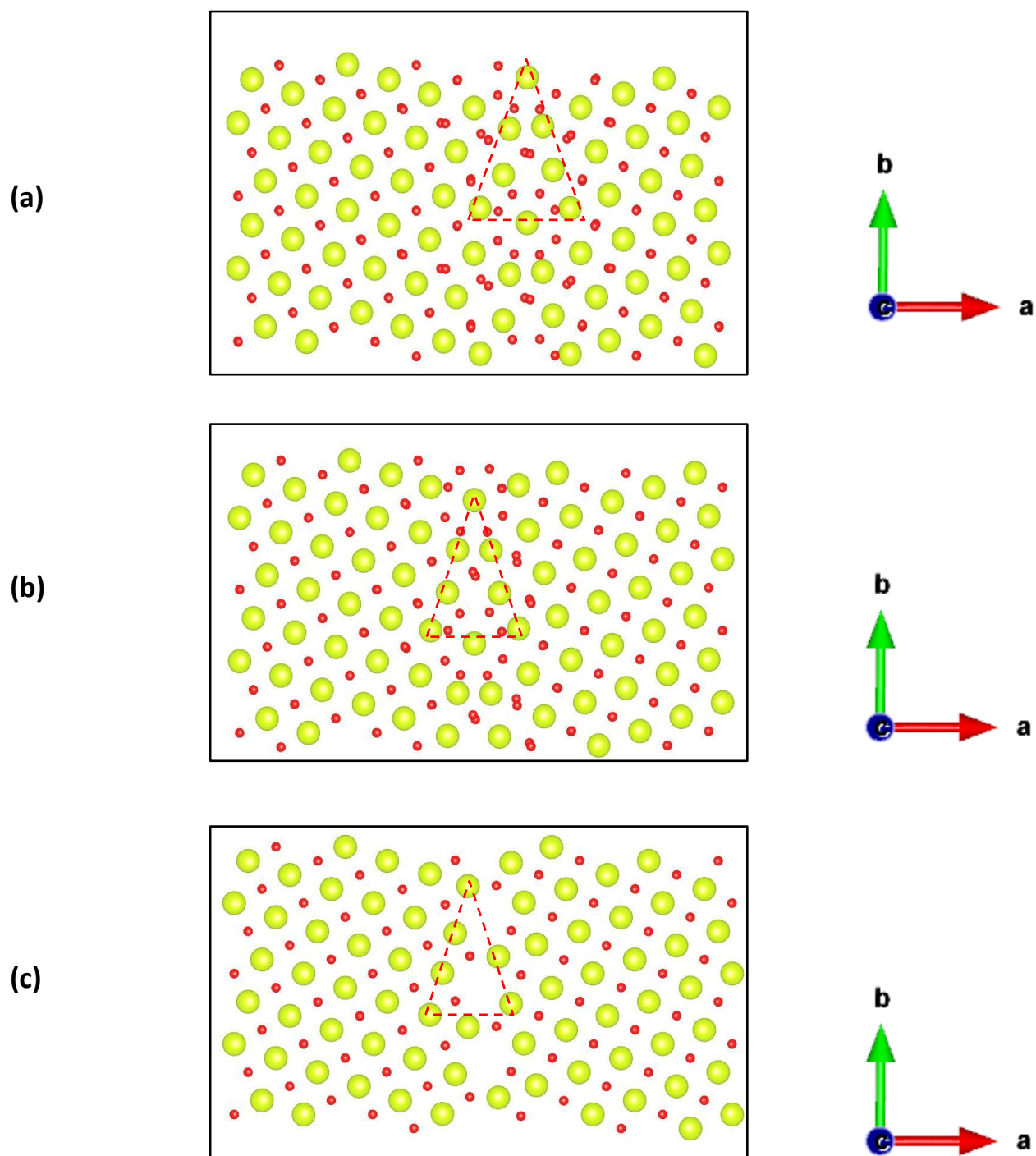


**Figure 4.1b** – Structural representations of the optimum  $\text{CeO}_2$   $\Sigma 5$  (310) symmetric tilt interface using (a) ‘conf’ (b) ‘min’ (c) ‘xonly’ approaches.

Approach	Dipole
‘conf’	-0.0053
‘min’	0.10472
‘xonly’	-0.0001

**Table 4.1b** – Dipoles at each of the three interfaces shown in figure 2.4e. Dipoles are relative to the stoichiometric bulk material and are calculated by the METADISE code.



Figure 4.1b (a)-(c) shows the three structures obtained from the scans displayed in decreasing order of stability. The structures obtained by the 'conf' and 'min' approaches show a similar  $\text{Ce}^{4+}$  sublattice symmetric triangular pattern at the interface which is observed in both structures with some minor distortion observed. Furthermore, both structures show increased distortion in the oxygen sublattice relative to the stoichiometric structure. This distortion is accounted for in the dipoles observed in table 4.1b however a significantly larger dipole is seen for the structure obtained using the 'min' approach because of the oxygen sublattice distortion which accounts for a larger formation and lower cleavage energy relative to the unrelaxed structure. When using the 'xonly' approach, the structure observed clearly shows that as relaxation is only allowed in the x-direction (represented by the a-direction in figure 4.1b); there is a shift in the cerium sublattice where the triangular pattern observed in the two previous methods is shifted. However, in this case there is no observable distortion in either the cerium or oxygen sublattice which, despite the decreased stability of this interface, accounts for the significantly smaller dipole.

As the 'conf' approach resulted in the most energetically favoured interface within a reasonable timeframe, each scan used to investigate all interface structures will be using this approach.

In order to determine whether the structures obtained by using the scanning procedure were reliable, each obtained structure was compared to other computational or experimental studies where available. However the limitation to this was that not all interfaces investigated have previously been structurally characterised, therefore in order to confirm the reliability and accuracy of the structures obtained, each minimum energy structure was annealed using molecular dynamics (DL\_POLY code<sup>(141)</sup>) to confirm if a similar structure was observed .

No further scan diagrams will be presented as the information provided by each scan will be interpreted to obtain both the interface stability and structure. The previous two examples discussed represent the two extremes in complexity when using this procedure and highlight the need for a small step length.

### 4.1.1 Surface and Interface Stability

Boundary	Surface Termination	$\gamma / \text{J m}^{-2}$	$E_f / \text{J m}^{-2}$	$E_c / \text{J m}^{-2}$
$\Sigma 3$ (111)	O <sub>4</sub>	1.61	1.17	2.04
$\Sigma 3$ (111)	Ce <sub>2</sub>	3.79	1.17	6.42
$\Sigma 3$ (112)	Ce <sub>2</sub> O <sub>4</sub>	2.91	2.43	3.39
$\Sigma 3$ (112)	CeO <sub>2</sub>	2.59	2.25	2.94
$\Sigma 5$ (210)	O <sub>2</sub>	3.87	1.84	5.91
$\Sigma 5$ (210)	Ce	3.78	1.84	5.73
$\Sigma 3$ (221)	O <sub>2</sub>	1.95	2.13	1.76
$\Sigma 9$ (221)	Ce	2.87	2.15	3.59
$\Sigma 5$ (310)	Ce <sub>2</sub> O <sub>4</sub>	4.13	2.21	6.05
$\Sigma 5$ (310)	CeO <sub>2</sub>	3.79	2.10	5.47
$\Sigma 11$ (311)	O <sub>4</sub>	3.30	1.48	5.13
$\Sigma 11$ (311)	Ce <sub>2</sub>	3.01	1.48	4.54
$\Sigma 19$ (331)	O <sub>4</sub>	2.07	2.02	2.12
$\Sigma 19$ (331)	Ce <sub>2</sub>	3.19	2.01	4.37
$\Sigma 17$ (410)	O <sub>2</sub>	3.69	2.24	5.14

**Table 4.1c** – Surface stability ( $\gamma$ ), formation ( $E_f$ ) and cleavage ( $E_c$ ) of the structurally investigated boundaries of ceria (Miller indices  $\geq 4$ ). The correlation between free surface energy and the grain boundary formation and cleavage energies validates the earlier assumption that lower free surface energies result in relatively energetically favoured boundary formation.

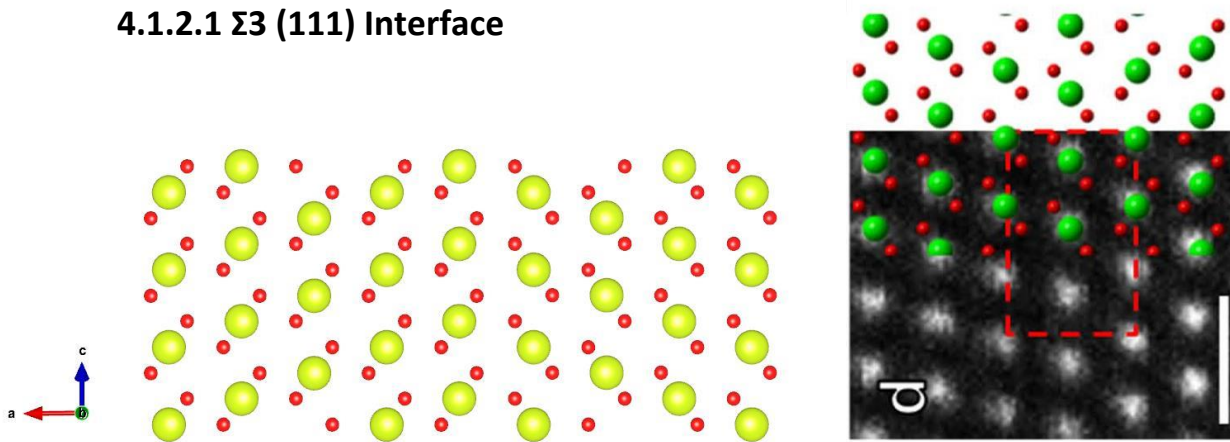
Two important energies can be considered when modelling grain boundaries. Firstly, is the formation energy. This is the energy required to form a grain boundary from a perfect crystal. As a grain boundary is always energetically less stable than a perfect bulk crystal, this will always be a positive energy. The second is the cleavage energy. This is the energy of a grain boundary relative to the two respective free surfaces. If a grain boundary is likely to exist, it should always be energetically favoured when compared with the two free surfaces otherwise the boundary will spontaneously separate. Thus, the cleavage energy represents a useful way of commenting on the stability of grain boundaries. Although, it should be emphasised that the formation energy is also useful as it provides an insight of energetic unfavorability relative to a perfect bulk crystal.

Table 4.1c shows the surface and interfacial energies of all surfaces and interfaces investigated. With respect to surface energies, the O<sub>4</sub> terminated (111) surface was found to be the most energetically

stable whereas the  $\text{Ce}_2\text{O}_4$  surface was found to be the least energetically stable. A relationship between surface energy and coordination of  $\text{Ce}^{4+}$  is observed which agrees with the results obtained by Williams *et al.*<sup>(190)</sup> for  $\text{UO}_2$ , another fluorite structure. This relationship between surface energy and coordination number shows that the higher the coordination number of  $\text{Ce}^{4+}$ , the lower the surface energy. In the bulk crystal,  $\text{Ce}^{4+}$  ions are eight-fold coordinated with respect to oxygen, however the deviation from bulk structure results in a change in the coordination number. Low surface energies are observed for the oxygen terminated (111), (221) and (331) surfaces as a higher coordination of oxygen is present at the surface. However, for surfaces such as the oxygen terminated (210) and (410) surfaces as well as the  $\text{Ce}_2\text{O}_4$  terminated (310) surface, a higher surface energy is observed. Although the absolute values of surface energy differ from those obtained by Williams *et al.*<sup>(190)</sup>, as different compositions are being investigated despite adopting the same crystal structure, some discrepancy in surface energy would be expected. Perhaps not surprisingly, as the same crystal structure is used in both studies, an identical pattern in the ranking of surface stability is observed. When observing formation and cleavage energies for each interface, apart from the Ce terminated  $\Sigma 33$  (441)<sub>Rot</sub> interface, whether using the reflect or rotate method of construction, all values agreed to within  $0.02 \text{ J m}^{-2}$  suggesting that an identical structure was obtained by both methods, which was confirmed upon structural analysis. Both terminations of the  $\Sigma 3$  (111) interface show an identical formation energy, however a significantly larger cleavage energy was calculated for the Ce-terminated interface suggesting that this would be the more energetically favoured structure. The  $\Sigma 3$  (111) interface has the lowest formation energy compared to all other interfaces investigated which is supported by the results obtained by Williams *et al.*<sup>(190)</sup> as a similar relationship is observed. The O-terminated  $\Sigma 9$  (221) is the only surface where the cleavage energy is greater than the formation energy, therefore suggesting that the (221) boundary is energetically more likely to exist as two free surfaces. Interfaces such as the O-terminated  $\Sigma 5$  (210),  $\Sigma 11$  (311) and the  $\text{Ce}_2\text{O}_4$  terminated  $\Sigma 5$  (310) also show a similar relationship where despite the surface energies being high and therefore less stable, each interface produced by these surfaces has a relatively low formation energy with a significantly larger cleavage energy. No clear trend was observed between formation and cleavage energies with the value of  $\Sigma$ . From the energetic results obtained it can be concluded that the value of  $\Sigma$  cannot be used to measure relative stability.

## 4.1.2 Interface Structures

### 4.1.2.1 $\Sigma 3$ (111) Interface



**Figure 4.1c** – Relaxed structure of the  $\Sigma 3$  (111) interface of ceria with corresponding experimental comparison<sup>(46)</sup>.

The structure of the  $\Sigma 3$  (111) interface as shown in figure 4.1c exhibits a “bulk like” structure as this structure is similar in atomic structure to the bulk material with vertical channels of Ce<sup>4+</sup> ions in the z (c) direction. The structure also shows no observable distortion in the sublattice of Ce<sup>4+</sup> or O<sup>2-</sup> therefore a symmetric structure was obtained. However, due to the rows of oxygen diagonal to the boundary terminating at different points, the boundary is not considered to be completely symmetric. Furthermore when comparing the structure obtained to the experimentally produced HAADF-STEM image of CeO<sub>2</sub> obtained by Ikuhara *et al.*<sup>(46)</sup>, a strong structural agreement is observed. The structure also agrees with the results produced by Williams *et al.*<sup>(190)</sup> for UO<sub>2</sub>.

#### 4.1.2.2 $\Sigma 3$ (112) Interface

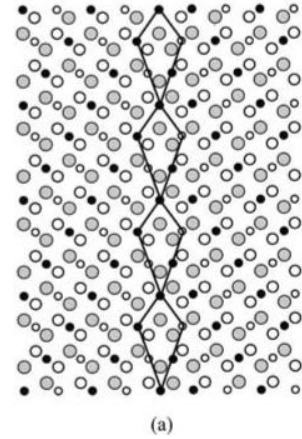
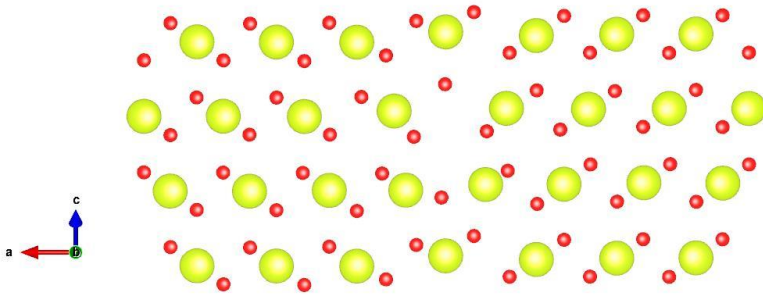


**Figure 4.1d** – Relaxed structure of the  $\Sigma 3$  (112) interface of ceria with corresponding computational comparison of yttria stabilised zirconia (YSZ)<sup>(191)</sup>.

The structure of the  $\Sigma 3$  (112) interface shown in figure 4.1c exists as a highly symmetric kite shaped pattern as displayed in the c-direction where no observable distortion is exhibited in either sublattice. The structure obtained for the  $\Sigma 3$  (112) interface is similar to that of the computationally derived  $\Sigma 3$  (112) interface of YSZ by Shibata *et al.*<sup>(191)</sup> which also exists in the fluorite crystal phase therefore supporting the observed structure of this interface.

#### 4.1.2.3 $\Sigma 5$ (210) Interface

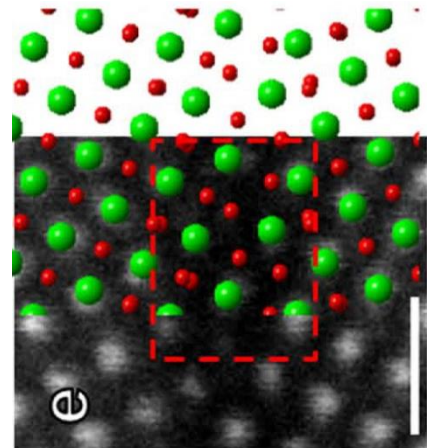
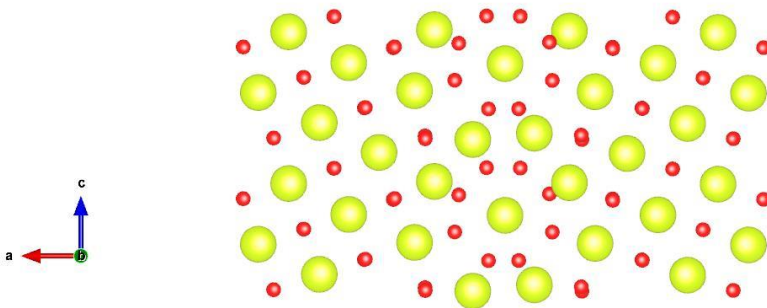


**Figure 4.1e** – Relaxed structure of the  $\Sigma 3$  (210) interface of ceria with corresponding experimental comparison<sup>(46)</sup>.

The structure of the  $\Sigma 5$  (210) interface as shown in figure 4.1e exists as a diamond shaped formation of  $\text{Ce}^{4+}$  ions in the c-direction with a small amount of distortion of the  $\text{Ce}^{4+}$  sublattice seen in the a-direction. There is also minor distortion seen in the oxygen sublattice however the notable feature is the highly symmetric circle of oxygen ions surrounding the upper and lower  $\text{Ce}^{4+}$  ions in the diamond

pattern. The pattern observed by the ceria sublattice is similar to the structure obtained by Shibata *et al.*<sup>(46)</sup>, however the circular oxygen alignment is not seen in the experimental structure, yet some distortion of the oxygen sublattice is observed.

#### 4.1.2.4 $\Sigma 9$ (221) Interface

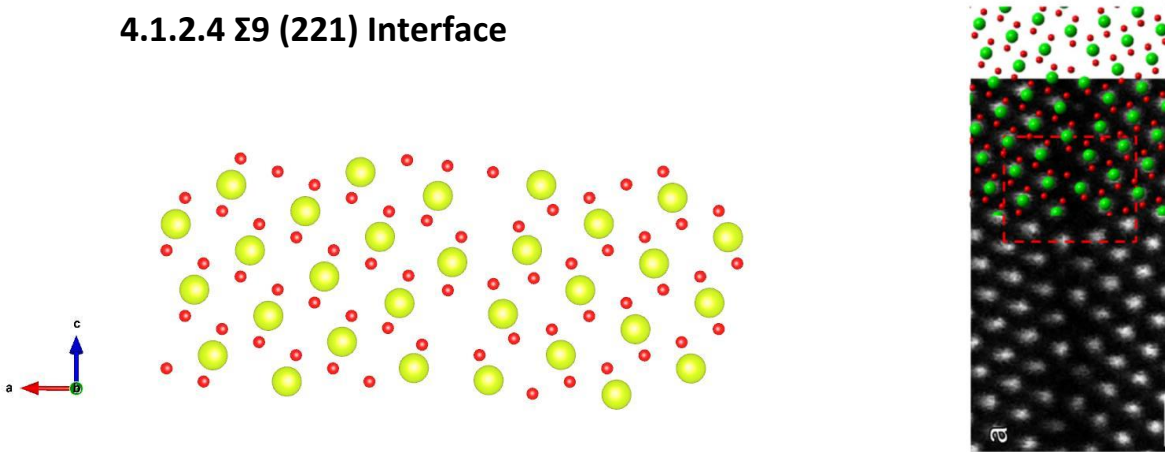


**Figure 4.1f** - Relaxed structure of the  $\Sigma 9$  (221) interface of ceria with corresponding experimental comparison<sup>(46)</sup>.

The structure of the  $\Sigma 9$  (221) interface as shown in figure 4.1f exists as a pentagonal pattern in the c-direction where the upper face of one pentagon is shared with the bottom face of the next corresponding pentagon. Symmetry is conserved at this interface as no observable distortion is seen in either the cerium or oxygen sublattice. The structure obtained is in agreement with the experimentally derived structure by Shibata *et al.*<sup>(46)</sup> and the computationally derived structure by Williams *et al.*<sup>(190)</sup>.

#### 4.1.2.5 $\Sigma 5$ (310) Interface

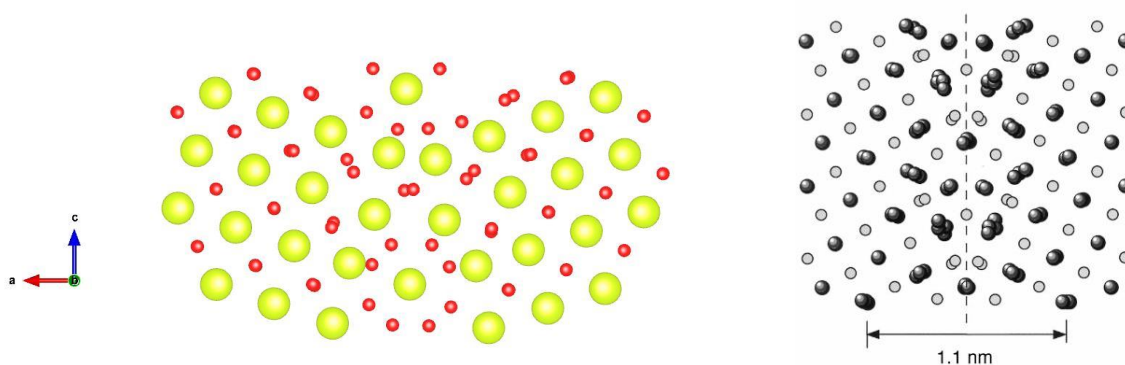


**Figure 4.1g** – Relaxed structure of the  $\Sigma 5$  (310) interface of ceria with corresponding computational comparison of yttria stabilised zirconia (YSZ)<sup>(192)</sup>

The structure of the  $\Sigma 5$  (310) interface as shown in figure 4.1g is constructed of a distorted triangular pattern in the c-direction where there is clear distortion in both the cerium and oxygen sublattices. Like the  $\Sigma 5$  (210), symmetric circles of oxygen ions are located at the upper and lower most points of each triangle structure that constructs the interface. The structure obtained is in good agreement with the computationally obtained structure of YSZ by Fisher *et al.*<sup>(192)</sup> and  $\text{UO}_2$ <sup>(190)</sup>.

#### 4.1.2.6 $\Sigma 11$ (311) Interface

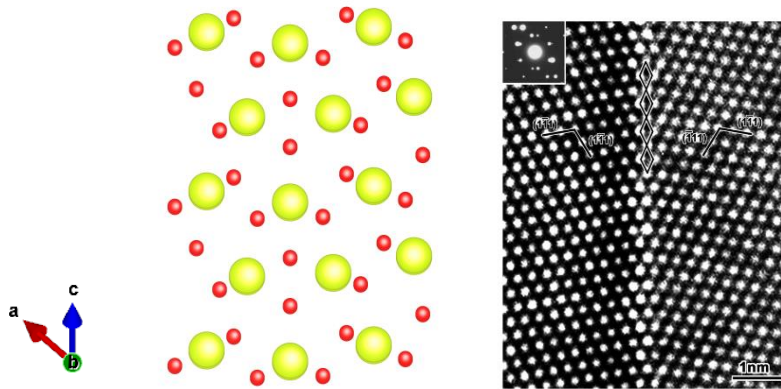


**Figure 4.1h** – Relaxed structure of the  $\Sigma 11$  (311) interface of ceria with corresponding experimental comparison of yttria stabilised zirconia (YSZ)<sup>(193)</sup>.

The structure of the  $\Sigma 11$  (311) interface as shown in figure 4.1h is constructed of a similar diamond pattern to the structure observed for the  $\Sigma 5$  (210) interface. The structure obtained is symmetric in nature with no observable distortion in either sublattice. Unlike the  $\Sigma 5$  (210) interface, a channel of oxygen ions is aligned at the interface in the c-direction which differs from the circular oxygen pattern observed. The structure obtained agrees with the computationally derived structure of  $\text{UO}_2$ <sup>(190)</sup>.



#### 4.1.2.7 $\Sigma 19$ (331) Interface

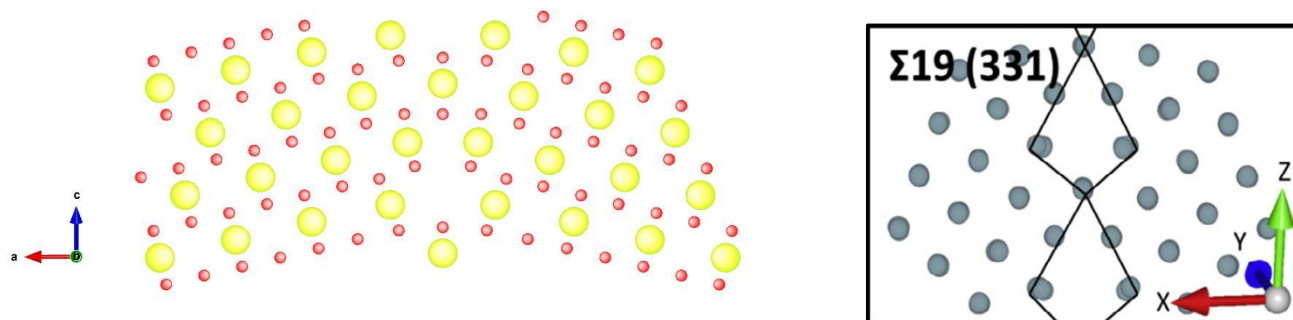


**Figure 4.1i** – Relaxed structure of the  $\Sigma 19$  (331) interface of ceria with corresponding computational comparison of  $\text{UO}_2^{(190)}$ .

The structure of the  $\Sigma 19$  (331) interface is shown in figure 4.1i. The structure consists of a kite-like arrangement of  $\text{Ce}^{4+}$  ions, similar to the one observed in the  $\Sigma 3$  (112) interface, however arranged in the opposite direction. No observable distortion is seen in either the ceria or oxygen sublattice and a strong agreement is observed with the computationally derived structure of  $\text{UO}_2$  constructed by Williams *et al.*<sup>(190)</sup>.

Each of the structures discussed have a strong resemblance with the structures seen within the literature in terms of both experimental and computational research therefore suggesting a high level of accuracy in the methodology used.

#### 4.1.2.8 $\Sigma 17$ (410) Interface

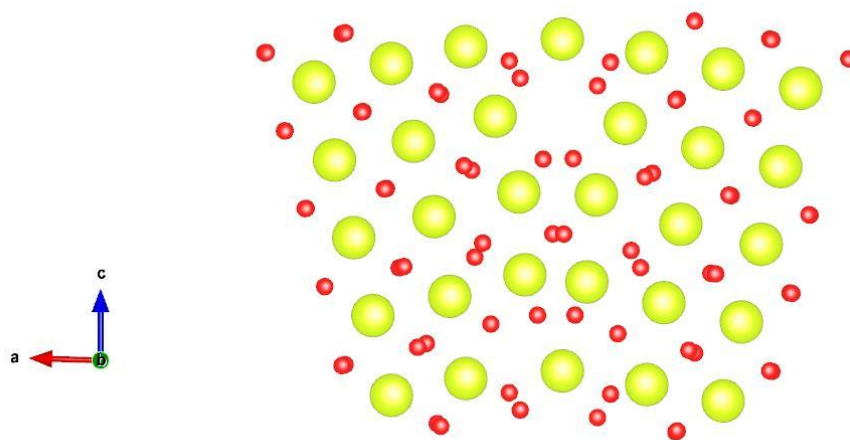


**Figure 4.1j** – Relaxed structure of the  $\Sigma 17$  (410) interface of ceria.



Figure 4.1j shows the relaxed structure of the  $\Sigma 17$  (410) interface. Structurally distortion is observed in both the cerium and oxygen sublattice where a triangular structure similar to the  $\Sigma 5$  (310) interface is observed in the opposing c-direction.

As a reliable structural model of each interface had been developed, defect segregation profiles could be investigated by comparing the bulk region to the interface region. However, before investigating defect insertion into the structures, for surfaces where multiple terminations were observed, for example the (210) surface, the two terminations will be combined to form a mixed interface where the formation and cleavage energies can be compared to the homogenous interfaces to consider relative stability. The resulting asymmetric grain boundaries are constructed and discussed in section 4.2.

## 4.2 Mixed Interface Stability

The following table presents the surface termination of both surfaces at the interface along with the formation and cleavage energy of each.

Boundary	Termination	$E_f / \text{Jm}^{-2}$	$E_c / \text{Jm}^{-2}$
$\Sigma 3 (111)_{\text{Ref}}$	$\text{O}_4    \text{Ce}_2$	4.76	0.62
$\Sigma 3 (111)_{\text{Rot}}$	$\text{O}_4    \text{Ce}_2$	3.57	1.82
$\Sigma 3 (112)_{\text{Ref}}$	$\text{Ce}_2\text{O}_4    \text{CeO}_2$	2.49	3.02
$\Sigma 3 (112)_{\text{Rot}}$	$\text{Ce}_2\text{O}_4    \text{CeO}_2$	2.70	2.81
$\Sigma 5 (210)_{\text{Ref}}$	$\text{O}_2    \text{Ce}$	2.85	4.81
$\Sigma 5 (210)_{\text{Rot}}$	$\text{O}_2    \text{Ce}$	2.63	5.03
$\Sigma 9 (221)_{\text{Ref}}$	$\text{O}_2    \text{Ce}$	2.63	2.19
$\Sigma 9 (221)_{\text{Rot}}$	$\text{O}_2    \text{Ce}$	2.70	2.12
$\Sigma 5 (310)_{\text{Ref}}$	$\text{Ce}_2\text{O}_4    \text{CeO}_2$	3.07	4.85
$\Sigma 5 (310)_{\text{Rot}}$	$\text{Ce}_2\text{O}_4    \text{CeO}_2$	2.53	5.40
$\Sigma 11 (311)_{\text{Ref}}$	$\text{O}_4    \text{Ce}_2$	2.39	3.93
$\Sigma 11 (311)_{\text{Rot}}$	$\text{O}_4    \text{Ce}_2$	2.40	3.91
$\Sigma 19 (331)_{\text{Ref}}$	$\text{O}_4    \text{Ce}_2$	2.46	2.80
$\Sigma 19 (331)_{\text{Rot}}$	$\text{O}_4    \text{Ce}_2$	2.46	2.80

**Table 4.2a** – Surface termination, cleavage and formation energy of mixed interfaces of ceria.

As shown in table 4.2a each of the mixed interfaces were constructed by the combination of different surface terminations of the same Miller Indices in contrast to those of like terminations seen in table 4.1c. In the case of each of the mixed interfaces generated, a higher formation energy and a lower cleavage energy were observed for each. Therefore, this suggests that mixed interfaces are less energetically stable than their homogenous counterparts.

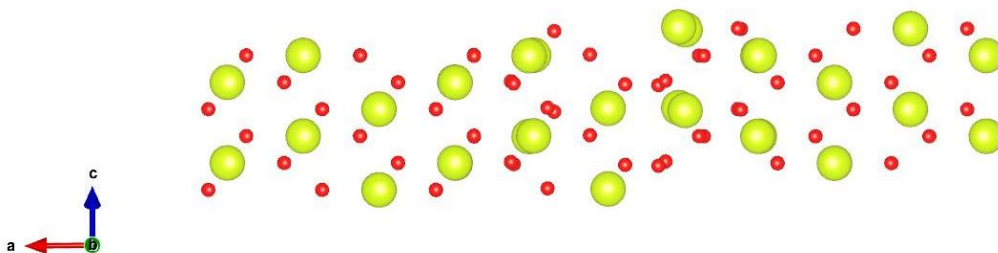


**Figure 4.2a**–  $\Sigma 3 (111)$  mixed interface ( $\text{O}_4 || \text{Ce}_2$ ) of ceria.

As shown in figure 4.2a, distortion of the cerium and oxygen sublattice is present which is not the case for the model shown in figure 4.1b. This distortion results in the significantly greater formation energy and lower cleavage energy, therefore much lower energetic stability of this interface.

The energetics and structures of several grain boundaries of ceria have been investigated within this section. As shown, there is a clear energetic favourability for homogenous ceria interfaces compared to those with a mixed surface termination. As shown, the methodology used has developed a reliable model for the characterisation of interfaces of ceria. Experimentally, the lower Miller index boundaries ( $3 \leq$ ) are those which have been structurally observed. The following section will aim to investigate boundaries with a higher Miller index ( $\geq 4$ ) to compare and contrast the energetics with those previously investigated.

### 4.3 Stability of Ceria Boundaries

$$\Delta E = E_C - E_f \quad (4.1)$$

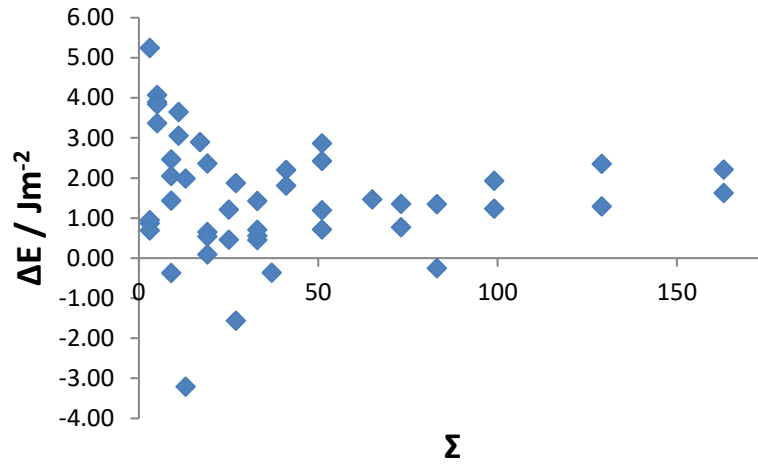


**Figure 4.3a** –  $\Delta E$  vs  $\Sigma$  of the grain boundaries of ceria ranging from  $\Sigma=3$ -163. This figure supports the assumption that boundary stability cannot be predicted by  $\Sigma$  value.

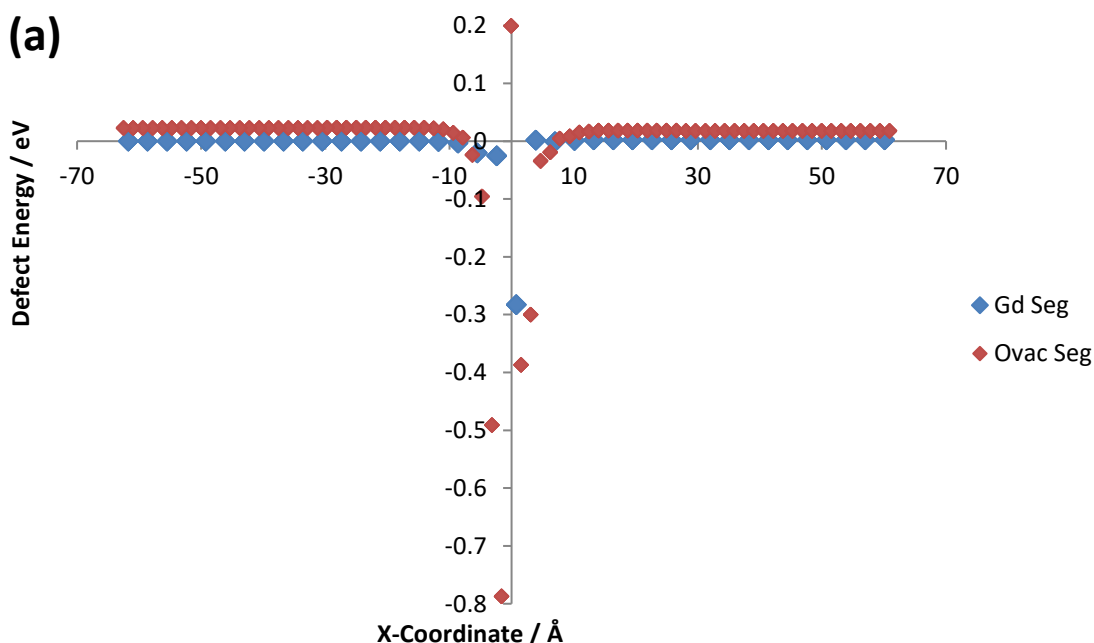
Equation 4.1 was used to calculate  $\Delta E$  values in figure 4.3a. The difference between the cleavage and formation can be used as a prediction of the boundary's stability, therefore a positive value of  $\Delta E$  predicts a stable grain boundary relative to two free surfaces. A low formation energy alone cannot be used to predict boundary stability as the formation energy is relative to the bulk whereas cleavage energy is relative to the surface. As shown in figure 4.3a, around 90% of the simulated boundaries were found to be energetically stable relative to the two free surfaces. Those with low  $\Sigma$  values represent the majority of the most energetically stable boundaries ( $\Delta E \geq 4.00 \text{ J m}^{-2}$ ) with corresponding  $\Sigma$  values lower than 10. Of the boundaries simulated, five were found to be energetically unfavourable although this appeared not to be influenced by the  $\Sigma$  value. The general trend shows that it can be predicted that most boundaries of ceria are energetically favoured with respect to the two free surfaces, yet the overall stability does show a small decrease with the increasing  $\Sigma$  value which predicts that such boundaries could be experimentally feasible.

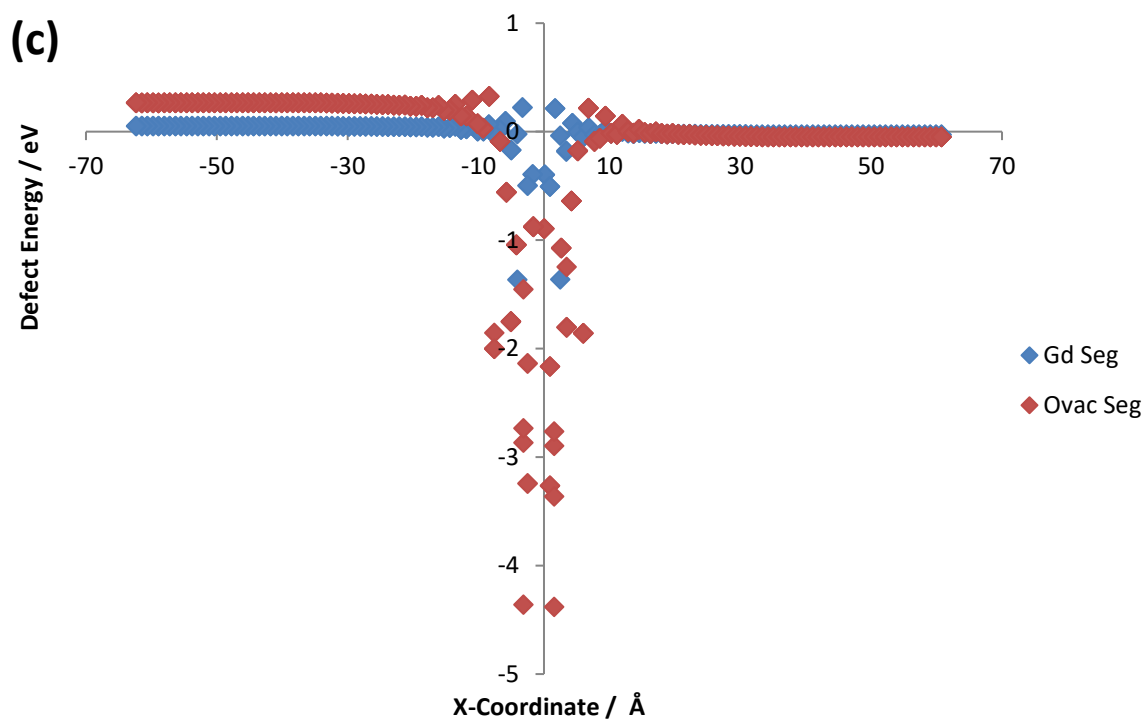
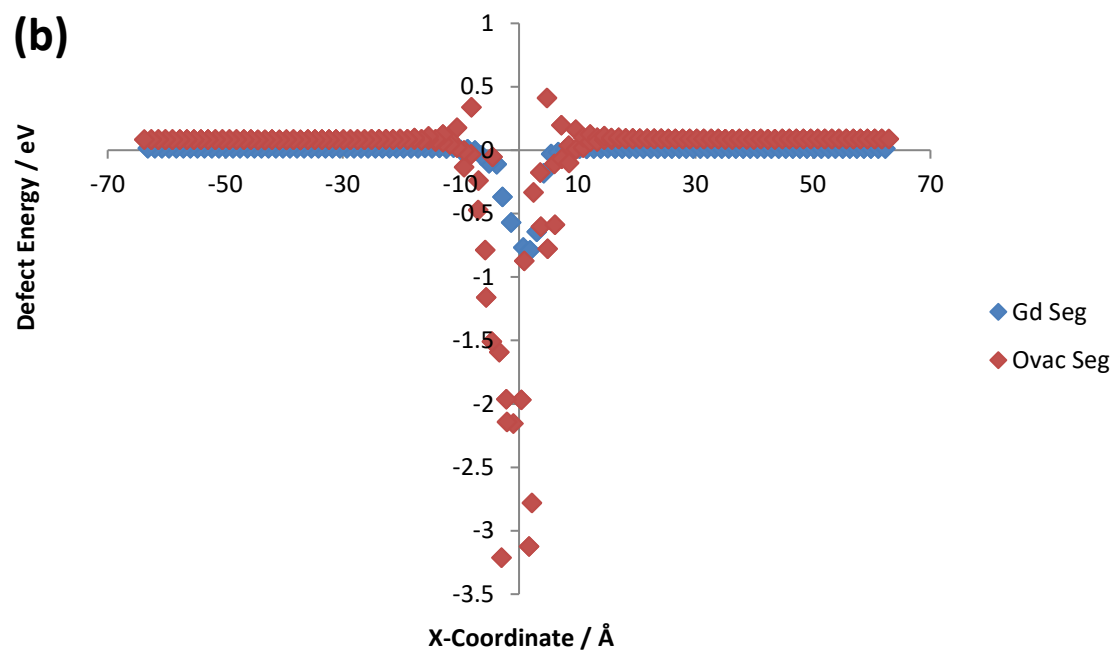
## 4.4 Intrinsic and Extrinsic Defect Segregation

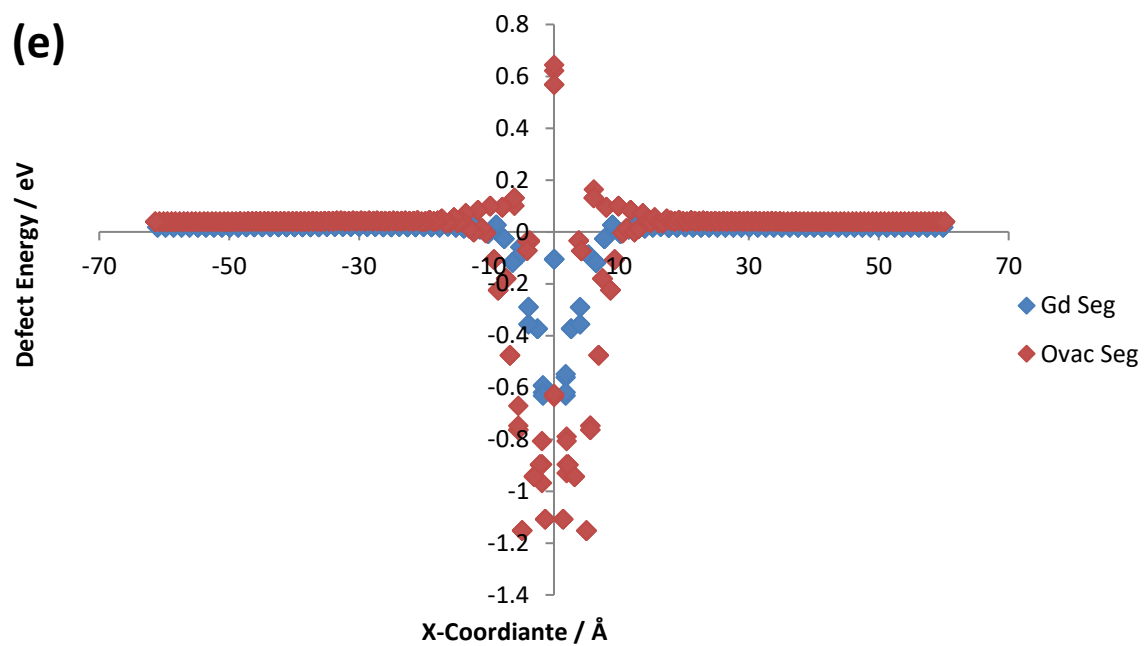
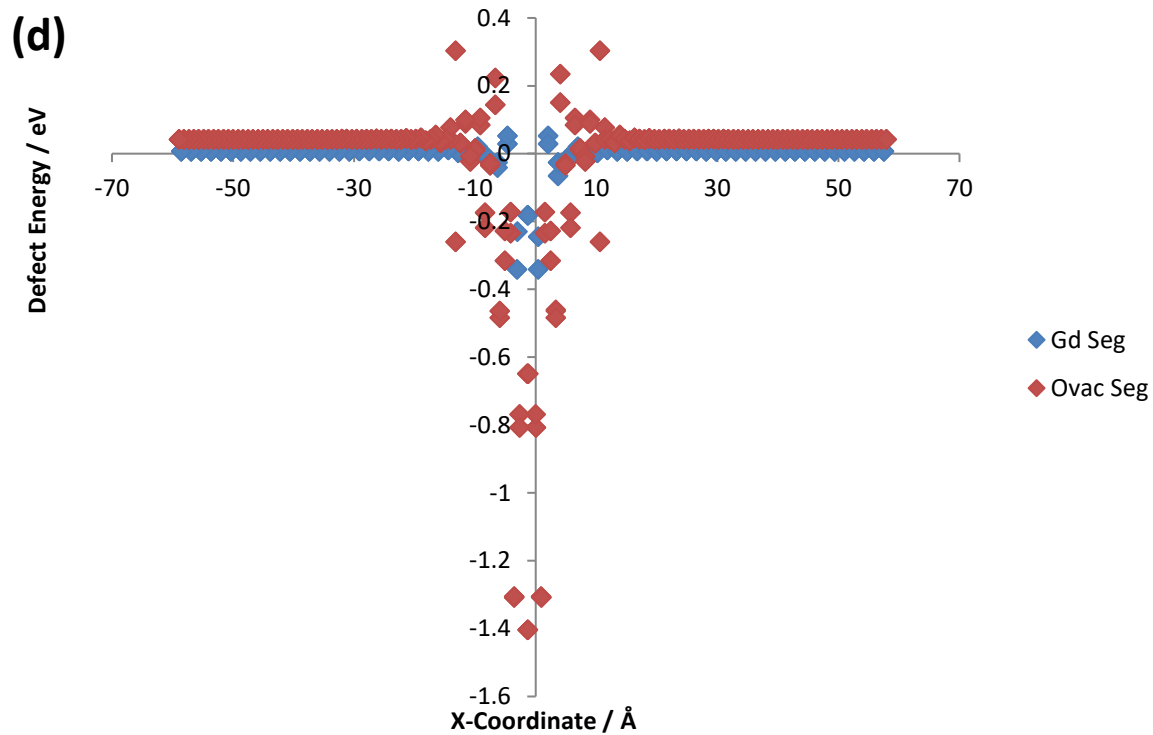
When considering the practical applications of ceria, defect chemistry is one of the most crucial aspects in materials such as solid oxide fuel cells (SOFCs) where ceria can be used as an electrolyte material<sup>(6, 194-196)</sup>. As ionic conductivity is essential in these materials, doping of ceria is carried out to satisfy these conditions. The incorporation of  $\text{Gd}^{3+}$  ions to form gadolinium doped ceria (GDC) is one of the most common and researched electrolytes. This is due to GDC being a successful functional electrolyte in intermediate temperature fuel cells<sup>(197)</sup>. The substitution of  $\text{Ce}^{4+}$  by  $\text{Gd}^{3+}$  results in the need of charge compensation by way of oxygen vacancies where for every two  $\text{Gd}^{3+}$  substitutions at  $\text{Ce}^{4+}$  sites, one oxygen vacancy will form which promotes ionic conductivity.

In this section, both  $\text{Gd}^{3+}$  occupying  $\text{Ce}^{4+}$  sites as well as oxygen vacancy ( $\text{O}_{\text{vac}}$ ) defect segregation profiles for several of the interfaces were generated. In each profile the bulk energy has been set to zero by averaging all bulk values, therefore the defect energy quoted is calculated by equation 4.2. The raw defect energy represents the defect energy relative to gaseous ions.

$$E_{\text{Defect}} = E_{\text{Def-Raw}} - E_{\text{Bulk}} \quad (4.2)$$







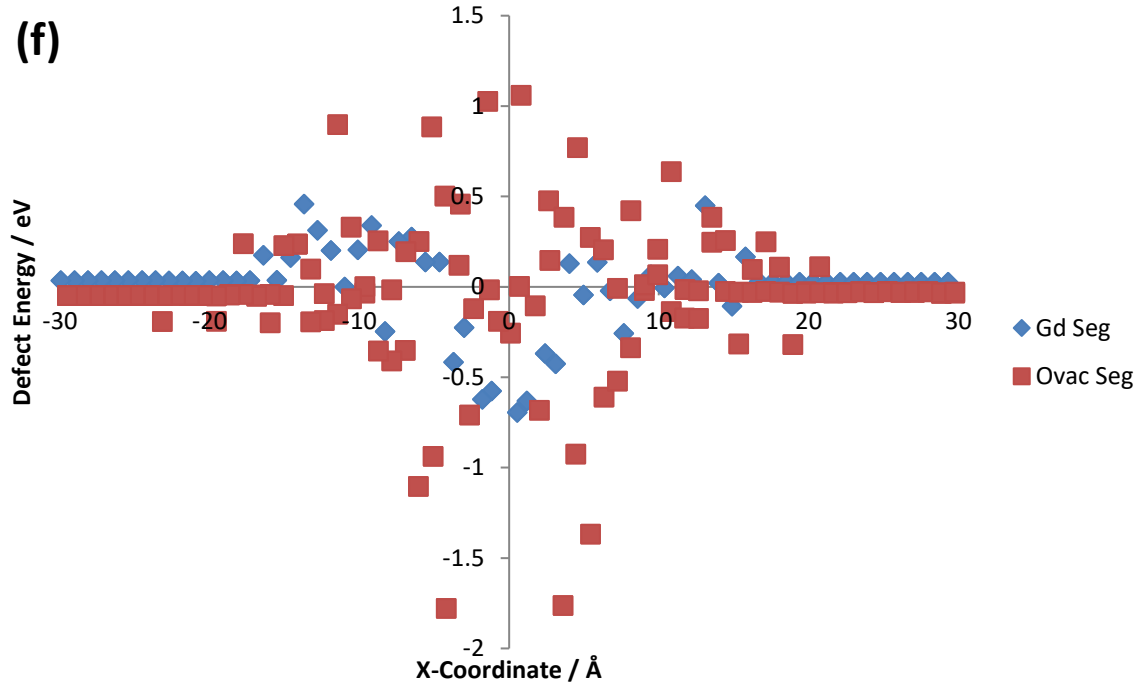


**Figure 4.4** – Defect segregation profiles of (a)  $\Sigma 3$  (111) (b)  $\Sigma 5$  (210) (c)  $\Sigma 5$  (310) (d)  $\Sigma 11$  (311) (e)  $\Sigma 19$  (331) (f)  $\Sigma 9$  (221) interfaces of ceria.

The defect segregation profiles for each interface are shown in figure 4.4 for both intrinsic and extrinsic defects. Each calculation was carried out using the CHAOS code where the Mott-Littleton region sizes were set to 13 and 35 respectively, as convergence testing was carried out on smaller and larger region sizes where the region size chosen was the smallest possible where energetic convergence was achieved.

Segregation energies were calculated using the point defect Mott-Littleton approach for calculating defect energies. As shown in figure 4.4, some of the segregation energies do not appear to converge to zero. In these calculations, the defect energy from the bulk calculations was used as the zero energy. Thus, if the grain boundary generates additional electrostatic interactions, e.g., a dipole as is evident for the (111) boundary, the energy does not converge to zero. If a dipole is present, then the energy of the charged defect furthest from the grain boundary is positive on one side and negative on the other. Clearly, this can be corrected by formerly assuming that the defect energies furthest from the boundary are zero, but there the effect is presented as observed.

Profile (a) represents the segregation profile for the  $\Sigma 3$  (111) interface, where the interface region of defects is observed to be approximately 20 Å in width (between 10 Å and -10 Å) where at distances outside of this region, defect energies are identical and hence make up the bulk region.  $\text{Gd}^{3+}$  and  $\text{O}_{\text{vac}}$



defects were generally found to be more energetically favoured at the interface relative to the bulk where one oxygen position was found to be less energetically favoured (0.2 eV greater than bulk defects). When comparing  $\text{Gd}^{3+}$  to  $\text{O}_{\text{vac}}$  energies, the majority of  $\text{O}_{\text{vac}}$  defects located in the interface region were found to be more energetically favoured compared to the  $\text{Gd}^{3+}$  defects in this region. The asymmetric nature of both defect profiles could be a result of a small dipole which was observed at the interface, where the presence of a dipole results in a shift in energy for both positive and negative defects. The  $\Sigma 5$  (210) interface (b) shows a similar behaviour with regards to both bulk and interface defect energies where primarily the defects at the interface are energetically favoured when compared to the bulk region. Again, a small dipole is observed at the interface which accounts for the asymmetric nature of the defect energies which with reference to figure 4.2 could be the result of a small amount of distortion in the cerium and oxygen sublattice. The profile obtained for the  $\Sigma 5$  (310) interface (c) shows a dramatic change in the behaviour of bulk defects. The profile shows a shift in bulk defect energy is observed ( $\approx 0.1$  eV) between either side of the interface, however no dipole was observed. The distortion of both sublattices shown in figure 4.2 could account for the shift in bulk defect energies as this distorts the lattice symmetry. Like the previously discussed profiles, both defects were generally found to be more energetically favoured at the interface compared to in the bulk region. The  $\Sigma 11$  (311) profile (d),  $\Sigma 19$  (331) profile (e) and  $\Sigma 9$  (221) profile (f) are symmetric in nature in the bulk region like the  $\Sigma 3$  (111) and  $\Sigma 5$  (210) profiles, however symmetry is also observed in the bulk defect energies in this region. This can be accounted for due to the symmetric natures of the structures obtained in figure 4.2 and where no sublattice distortion was observed and therefore no dipole was found to exist at the interface. As shown in previous segregation profiles, most defects in the interface region are energetically favoured compared to the bulk region, however both profiles show an increased number of  $\text{O}_{\text{vac}}$  defects in the interface region which were less energetically favoured when compared to the bulk region. The proportion of energetically favoured defects in the grain boundary region is important when considering defect concentrations.

When considering all six profiles obtained, the general conclusion is that defects are energetically more likely to form at the interface compared to the bulk region. This conclusion is important when referring to the practical applications as when considering a potential cathode-electrolyte model, the flow of charge through the interface region is critical in the performance of a fuel cell. Whilst no observable trend was seen between the boundary energetics and defect formation energies, further incorporation of higher defect concentrations could prove insightful in boundary energetics. The likelihood of defect formation is therefore important as the presence of more defects results in a larger concentration of charge carriers which further results in increased ionic conductivity.

## 4.5 Molecular Dynamics of Ceria Interfaces

Of the structurally characterised boundaries discussed in section 4.1, six of these boundaries, which were all found to be relatively energetically stable with respect to the values in table 4.1c, were simulated using the DL\_POLY<sup>(141)</sup> code using the techniques discussed in chapter 2. Initial simulations were carried out using the NVT ensemble for 1.1 ns and further simulations of 1.0 ns using the NVT ensemble over which oxygen diffusion was measured. In section 4.4 incorporation of defects into both the boundary and bulk regions were investigated. However, due to the simulations being carried out at fixed temperature, one of the drawbacks of energy minimisation, the transport properties could not be investigated. This issue is resolved by using MD simulations. With regards to all the simulated boundaries, no long range diffusion was observed at temperatures below 2000 K and amorphization of the boundary occurred when exceeding 3500 K therefore all simulations were carried out within this range of temperatures.

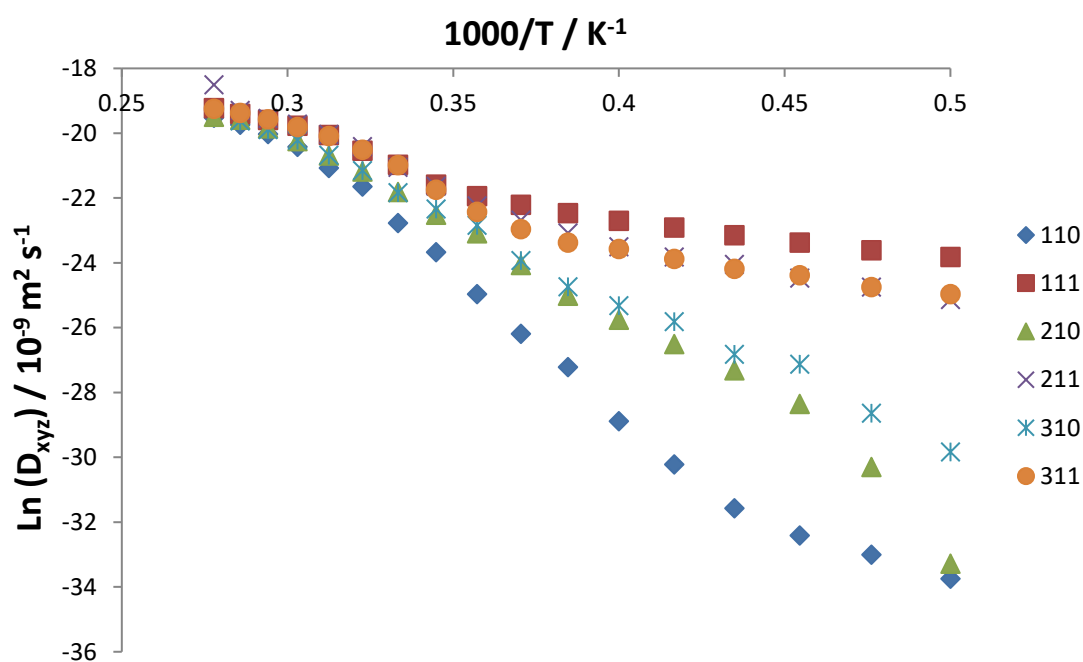


**Figure 4.5** – Arrhenius plot of natural log of total diffusion of oxygen vs reciprocal temperature for six simulation cells containing grain boundaries of ceria. All MD simulations were carried out using the Teter potential model.

Boundary	$E_a$ / eV	$D_0$ / $\text{m}^2 \text{s}^{-1}$
(110)	$4.92 \pm 0.46$	$3.35 \times 10^{-2} \pm 5.49 \times 10^{-2}$
(111)	$2.68 \pm 0.21$	$2.81 \times 10^{-5} \pm 2.07 \times 10^{-5}$
(210)	$3.69 \pm 0.26$	$6.32 \times 10^{-4} \pm 5.83 \times 10^{-4}$
(211)	$3.64 \pm 0.13$	$9.45 \times 10^{-4} \pm 4.63 \times 10^{-4}$
(310)	$4.32 \pm 0.17$	$5.68 \times 10^{-3} \pm 3.58 \times 10^{-3}$
(311)	$3.61 \pm 0.17$	$6.90 \times 10^{-4} \pm 4.46 \times 10^{-4}$

**Table 4.5** – Activation Energies ( $E_a$ ) and  $D_0$  values of oxygen diffusion in the six simulated grain boundaries of ceria.

The activation energies calculated in table 4.5 only consider one mechanism of diffusion. Each gradient was treated as linear, thereby calculating one associated activation energy. When compared to the activation energy obtained for the stoichiometric bulk ( $3.35 \pm 0.56$  eV), five of the six simulated boundaries were found to have a higher activation energy where only the value reported for the (111) boundary was lower. This by itself would suggest that the presence of grain boundaries suppress oxygen transport in ceria and is consistent with experimental evidence<sup>(184)</sup>. However, the reported  $D_0$  values are significantly higher when compared to those observed in the bulk. This substantial increase in diffusion could be the result of structural changes at the boundary that occur with increasing temperature, which are not observed in the bulk, such as a clustering of oxygen ions in the boundary region. This could correlate with a change in mechanism of diffusion with increasing temperature. Further simulations could be carried using a NEB method to determine whether this is the case. Furthermore, the obtained activation energies and  $D_0$  values account for the combined x, y and z components of diffusion. Future work would include isolating each of these individual components to investigate the differences in oxygen transport parallel to the boundary and perpendicular to the boundary. Thus, gaining a deeper insight as to whether the presences of grain boundaries suppress or enhance oxygen diffusion in ceria.

## 4.6 Chapter Summary

A high-throughput computational method has been used to investigate the structure and energetics of grain boundaries of ceria. The importance of both step length and minimisation probe was initially highlighted to achieve a reliable structure without the requirement of significant strain on computational resources. The computationally obtained energetics and structures of grain boundaries of ceria were consistent with those seen experimentally. Surface termination was found to have a profound impact on the boundary stability where energetically favoured surfaces generally resulted in a relatively stable grain boundary energy with respect to that of two free surfaces. Furthermore, surfaces of like terminations resulted in grain boundaries of improved stability relative to their mixed counterparts. The success of being able to generate structures consistent with those observed experimentally gives confidence when modelling grain boundaries which have not been structurally characterised. Through use of the scanning process, by using a wide range of  $\Sigma$  values, most grain boundaries of ceria were energetically favoured with respect to existing as two free surfaces, and therefore there is potential for experimental characterisation. High-throughput techniques were further used to investigate single point defects in ceria. Both  $\text{Gd}^{3+}$  and  $\text{O}_{\text{Vac}}$  defects were found to be energetically favoured to form at the boundary relative to the bulk region therefore suggesting that defect segregation towards the interface is likely. Oxygen migration in boundaries was further quantified using MD techniques for six experimentally characterised boundaries, where no obvious relationship between the defect energies and diffusion was observed. The presence of grain boundaries was found to suppress oxygen diffusion in ceria when compared to the bulk. Further simulations would be required to quantify the extent of which defects could improve oxygen diffusion in ceria grain boundaries. These include using intrinsic and extrinsic doping schemes with longer time scale simulations. As previously discussed, future work would also include isolating the individual x, y and z diffusion trajectories. By isolating the individual components, quantitative analysis could be used to compare diffusion parallel to the boundary and perpendicular to the boundary to further understand how the presence of grain boundaries influences oxygen transport.

## 5 Surfaces and Interfaces of Strontium Titanate

Strontium titanate is a versatile electrode material in SOFC application and has been considered to be both an effective anode<sup>(198)</sup> and cathode<sup>(199, 200)</sup> through differing dopant schemes. Such dopants include lanthanum doped STO, which has been found to exhibit high stability and conductivity<sup>(198, 201-203)</sup>, and cobalt doping, which saw a further increase in ionic conductivity<sup>(204)</sup>. STO has further been used in electronic memory applications<sup>(205)</sup> and as a candidate thermoelectric material<sup>(11)</sup>.

Similar to ceria, both experimental<sup>(25, 206, 207)</sup> and computational<sup>(31, 208, 209)</sup> methods have been used to characterise the grain boundaries of STO, however fewer considerations have been made towards the ionic diffusion through grain boundaries where one report suggests that the presence of grain boundaries suppresses oxygen transport in STO<sup>(210)</sup>.

This research focuses on using a high-throughput computational method to determine the structure and energetics of STO grain boundaries focussing initially on those which have been structurally characterised and further those which have not, generally of a higher Miller index ( $>4$ ). Further simulations using a combination of single point defects and MD simulations were carried out on stoichiometric STO grain boundaries to further quantify whether the presence of grain boundaries in a polycrystalline phase would either facilitate or suppress oxygen ion diffusion.

### 5.1 Scan Overview

In this chapter, the surface and interface structure and stability of STO boundaries will be investigated using high-throughput computational techniques. Chapter 2 provided an insight into how the interfaces were constructed and how the stability and structure of each were obtained. The initial surface terminations were identified where the minimum energy surface with no dipole was chosen to ensure electrostatic convergence. As per the results presented in chapter 4, this resulted in structures consistent with those observed experimentally. Each scan was carried out either by reflecting the surface or by a 180 ° rotation and superimposing the initial surface on top of itself and carrying out a full minimisation at each grid point. For each interface, the scanning procedure discussed was carried out using both approaches. This chapter will investigate which method resulted in the more energetically favoured interface as well as a comparison to other experimental and computational studies. Within this chapter each interface will be described by its  $\Sigma$  value where this was obtained using equation 2.54 as previously described. Furthermore, defect energy profiles will also be presented for each interface where intrinsic and extrinsic defect segregation energies were obtained. In addition to the structural characterisation of several STO grain boundaries which

have been experimentally characterised, the scanning methodology will be used to investigate boundaries that have not been structurally characterised. This chapter will further discuss the calculated dynamics for six structurally characterised STO boundaries.

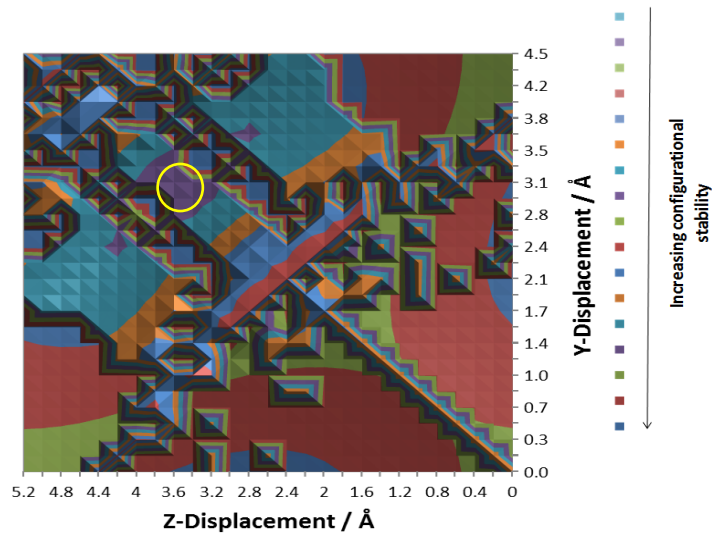


**Figure 5.1a** - Configurational potential energy surface for  $\Sigma 3$  (111)<sub>Rot</sub> interface of STO

From the potential energy surface shown in figure 5.1a, the global minimum obtained was in the yellow circle shown at 3.8 Å vs 3.0 Å (y vs z direction). Compared to the previous potential energy surface (figure 2.4g) shown, many more, shallower, smaller sized local minima are shown resulting in this potential energy surface possessing a less visually recognisable minimum. In figure 2.4d the global minima were in a well-defined potential energy well. Because of this, a small shift in the interface orientation in either direction is unlikely to cause any significant change in structure or energy. On the contrary, the global minimum obtained in figure 5.1a is in a small, yet deep potential energy well where a small change in orientation could have a significant impact on the interface energy and structure. This follows on from chapter 4 where a small step length is required when using the scanning procedure to obtain the most stable interface structure.

### 5.1.2 Surface and Interface Stability

Surface and interface construction of STO was carried out. The data shown in table 5.1a represents the surfaces and corresponding interfaces obtained by the METADISE code<sup>(136)</sup>. The interfaces chosen were of similar Miller indices to those chosen for chapter 4. This is again due to the experimental characterisation of many of the simulated grain boundaries being previously studied.

Boundary	Surface Termination	$\gamma / \text{J m}^{-2}$	$E_f / \text{J m}^{-2}$	$E_c / \text{J m}^{-2}$
$\Sigma 3 (111)_{\text{Ref}}$	$\text{SrO}_2$	2.70	3.39	2.01
$\Sigma 3 (111)_{\text{Rot}}$	$\text{SrO}_2    \text{O}$	2.70	0.90	4.50
$\Sigma 3 (112)_{\text{Ref}}$	$\text{Sr}$	3.00	2.66	3.35
$\Sigma 3 (112)_{\text{Rot}}$	$\text{Sr}    \text{TiO}$	3.00	1.53	4.48
$\Sigma 3 (112)_{\text{Ref}}$	$\text{O}$	2.23	1.53	2.92
$\Sigma 3 (112)_{\text{Rot}}$	$\text{O}    \text{O}$	2.23	1.53	2.92
$\Sigma 5 (210)_{\text{Ref}}$	$\text{TiO}_2$	2.39	1.16	3.62
$\Sigma 5 (210)_{\text{Rot}}$	$\text{TiO}_2    \text{SrO}$	2.39	1.86	2.93
$\Sigma 5 (210)_{\text{Ref}}$	$\text{SrO}$	2.45	2.40	2.50
$\Sigma 5 (210)_{\text{Rot}}$	$\text{SrO}    \text{TiO}_2$	2.45	1.86	3.05
$\Sigma 9 (221)_{\text{Ref}}$	$\text{SrO}$	2.56	3.15	1.96
$\Sigma 9 (221)_{\text{Rot}}$	$\text{SrO}    \text{TiO}_2$	2.56	2.05	3.07
$\Sigma 9 (221)_{\text{Ref}}$	$\text{TiO}_2$	3.55	1.16	5.97
$\Sigma 9 (221)_{\text{Rot}}$	$\text{TiO}_2    \text{SrO}$	3.55	2.05	5.09
$\Sigma 5 (310)_{\text{Ref}}$	$\text{Sr}$	2.29	3.10	1.48
$\Sigma 5 (310)_{\text{Rot}}$	$\text{Sr}    \text{TiO}$	2.29	2.01	2.58
$\Sigma 5 (310)_{\text{Ref}}$	$\text{O}$	2.30	2.00	2.60
$\Sigma 5 (310)_{\text{Rot}}$	$\text{O}    \text{O}$	2.30	2.27	2.34
$\Sigma 11 (311)_{\text{Ref}}$	$\text{SrO}_2$	2.09	2.40	1.78
$\Sigma 11 (311)_{\text{Rot}}$	$\text{SrO}_2    \text{O}$	2.09	2.03	2.16
$\Sigma 19 (331)_{\text{Ref}}$	$\text{SrO}_2$	4.03	2.88	5.17
$\Sigma 19 (331)_{\text{Rot}}$	$\text{SrO}_2    \text{O}$	4.03	2.07	5.98
$\Sigma 17 (410)_{\text{Ref}}$	$\text{TiO}_2$	2.24	1.81	2.68
$\Sigma 17 (410)_{\text{Rot}}$	$\text{TiO}_2    \text{SrO}$	2.24	2.22	2.27
$\Sigma 17 (410)_{\text{Ref}}$	$\text{SrO}$	2.21	1.98	2.45
$\Sigma 17 (410)_{\text{Rot}}$	$\text{SrO}    \text{TiO}_2$	2.21	2.22	2.21
$\Sigma 33 (441)_{\text{Ref}}$	$\text{TiO}_2$	3.37	1.64	5.10
$\Sigma 33 (441)_{\text{Rot}}$	$\text{TiO}_2    \text{SrO}$	3.37	2.00	4.73
$\Sigma 33 (441)_{\text{Ref}}$	$\text{SrO}$	3.05	2.40	3.71

**Table 5.1** - Surface stability for all surface terminations investigated with corresponding formation and cleavage energies of each interface.

A clear difference can be observed when comparing the presentation of the data in table 5.1 to table 4.1a when considering surface termination. Due to the function of the reflect/rotate procedure, when reflecting, an identical surface is present on both blocks. However, when rotating, a different surface is present. This is represented by figure 5.1b.

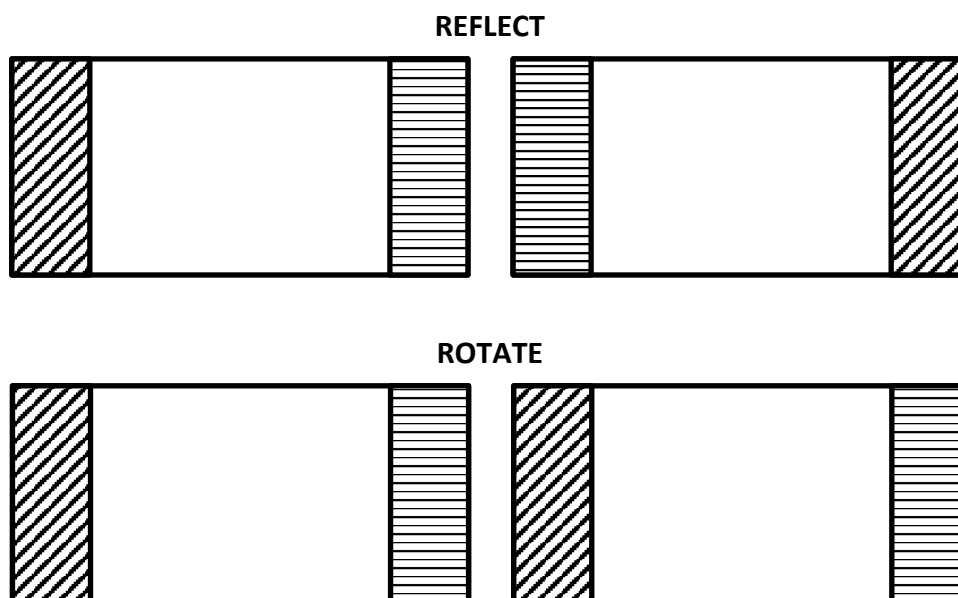


**Figure 5.1b** – Representation of reflect and rotate procedures when generating interfaces from two surfaces.

As shown in figure 5.1b, when reflecting a surface, the same termination is present on both blocks at the interface therefore a symmetric interface structure is formed. However, when rotating one of the surfaces, a different termination is present on one of the two blocks therefore two different surfaces are brought together to form the interface. When considering the striped surface regions, for ceria, this region is symmetric where the termination of this region is the same at either extreme and because of this, whether the reflection or rotation is used, the surface termination of both surfaces will be identical. Therefore, the mixed interfaces were constructed where different surface terminations could be combined to explore alternative interface structures. In the case of STO, as the striped surface regions have different terminations at either extreme, the rotation procedure is identical to combining two different surface terminations via a reflection, therefore rotated interfaces for STO are like the mixed termination interfaces of ceria. Although mixed termination interfaces of STO were explored, both their energetic data and structure were identical to the reflected and rotated interfaces of identical surfaces.

The energetic data shown in table 5.1a firstly shows that in the case of STO, in contrast to ceria, when bringing different surface terminations together to form the interface, generally a higher



energetic favourability is observed. The  $\Sigma 3$  (111) is the best example of this type of interface. The rotated structure of this interface was found to be the most stable interface with respect to the lowest formation energy. When comparing this to the  $\Sigma 3$  (111)<sub>Ref</sub> interface, the formation energy is significantly lower and the cleavage energy is significantly higher, therefore suggesting that the rotated structure and therefore mixed interface is the more stable structure. A similar relationship is observed for the  $\Sigma 3$  (112),  $\Sigma 5$  (310) and the  $\Sigma 11$  (311) interfaces where the mixed termination structure again produced the most stable interface with respect to both formation and cleavage energy. The  $\Sigma 9$  (221) interface shows a significant difference in energetics between the two terminations for the two reflected surfaces of different terminations. The reflected SrO surface was found to be the least stable of the four interfaces whereas the TiO<sub>2</sub> reflected surface was found to be the most energetically stable form of this interface where the two rotated structures exist as an intermediate between these two structures. The  $\Sigma 17$  (410) and the  $\Sigma 33$  (441) show an identical relationship where the reflected TiO<sub>2</sub> terminated surface used when forming the interface was found to be the most energetically stable with respect to both formation and cleavage energies. Like ceria no observable trend was seen between the value of  $\Sigma$  and the stability of the interface. As is the case with ceria, from the energetic results obtained it can be concluded that the value of  $\Sigma$  cannot be used to measure relative stability.

As the energetic data of each of the interface structures had been investigated, the structural models were obtained from the respective potential energy surfaces. In each case the structure will be compared to other computational or preferentially experimental examples where possible for structural characterisation.

### 5.1.3 Interface Structures

#### 5.1.3.1 $\Sigma 3$ (111) Interface

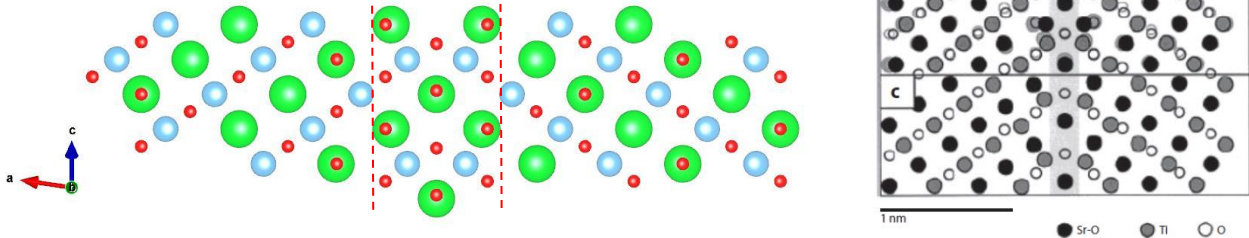


**Figure 5.1c** –  $\Sigma 3$  (111) interface structure of STO with experimental comparison derived from a HRTEM image<sup>(25)</sup>.

The interface structure shown in figure 5.1c agrees with both the computationally derived structure and the experimental structure determined using high-resolution transition electron microscopy (HRTEM) by Kienzle *et al.*<sup>(25)</sup> where the boundary plane is  $\text{SrO}_3$  terminated. Structural agreement was also observed with alternative computational methods such as the *Ab initio* random structure searching (AIRSS) method developed by Pickard *et al.*<sup>(31)</sup>. However, the AIRSS method produced other possible interface orientations such as the Ti-terminated interface which was not observed in this work. This could be a result of the ionic repulsion interactions when using an interatomic potential model. The structure obtained shows minimal distortion in the sublattice of both cations and anions as mirror symmetry is observed at the boundary plane. A zero dipole was also present at this interface.

### 5.1.3.2 $\Sigma 3$ (112) Interface

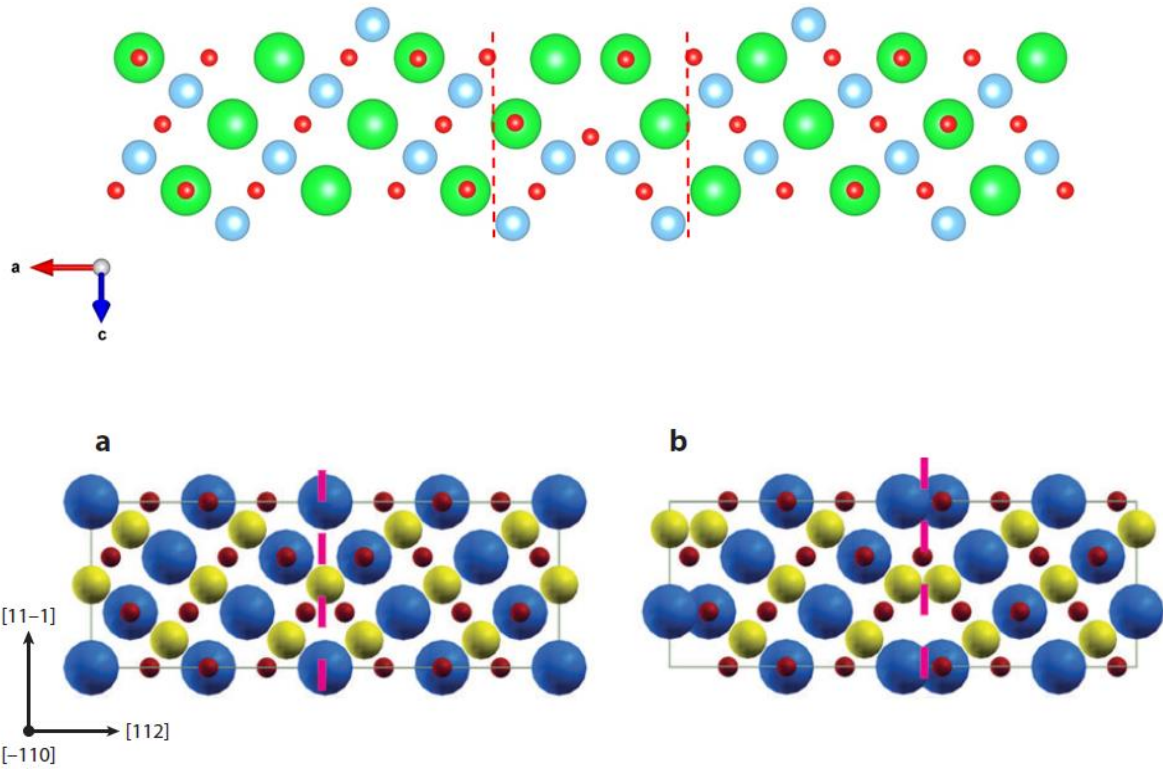


**Figure 5.1d** –  $\Sigma 3$  (112) interface structure of STO, with computationally obtained comparison of (a)  $\text{SrTiO}_3$  terminated mirror symmetrical tilt boundary and (b) O-terminated mirror glide symmetric terminated interface, structure optimisation carried out using DFT with LDA approximation by Benedek *et al.*<sup>(28)</sup>.

As shown in figure 5.1d, the structure obtained when using the METADISE code is an oxygen terminated interface which is in structural agreement with structure (b) characterised by Benedek *et al.*<sup>(28)</sup>. In order to obtain structure (a) a variety of different approaches were taken such as; growth of the surface in order to obtain more possible surface terminations, and expansion of the region 1 at the interface to ensure complete convergence had occurred and manual translation of atoms. Through the manual translation of both Sr and O atoms, the following interface structure was obtained as shown in figure 5.1e.

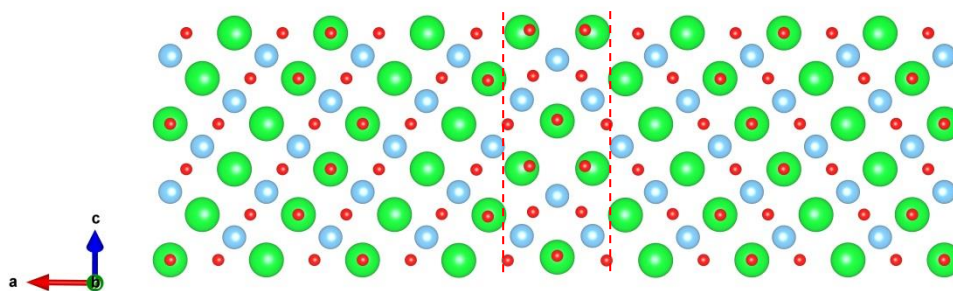


**Figure 5.1e** –  $\Sigma 3$  (112) interface structure of STO, where manual translation of atoms was required to obtain structural agreement with structure (a) shown in figure 5.1d.

In the case of the interface model shown in figure 5.1e, this is within structural agreement with the DFT optimised structure. However, the manual translation of atoms was not required with any other interface and furthermore this procedure significantly affected the interface stability resulting in this model being much less energetically stable compared to the structure obtained in the scan, where an increase and decrease in cleavage and formation energy of approximately 1.5 and 2 J m<sup>-2</sup> were observed respectively. Therefore, it should be taken into account that the structure proposed in figure 5.1d is the much more energetically stable of the two interface models proposed. This particular scan shows a potential drawback of the scanning technique with the stated step length. In order to ensure better agreement with the experimental structure, a smaller step length could be used.

### 5.1.3.3 $\Sigma 5$ (210) Interface

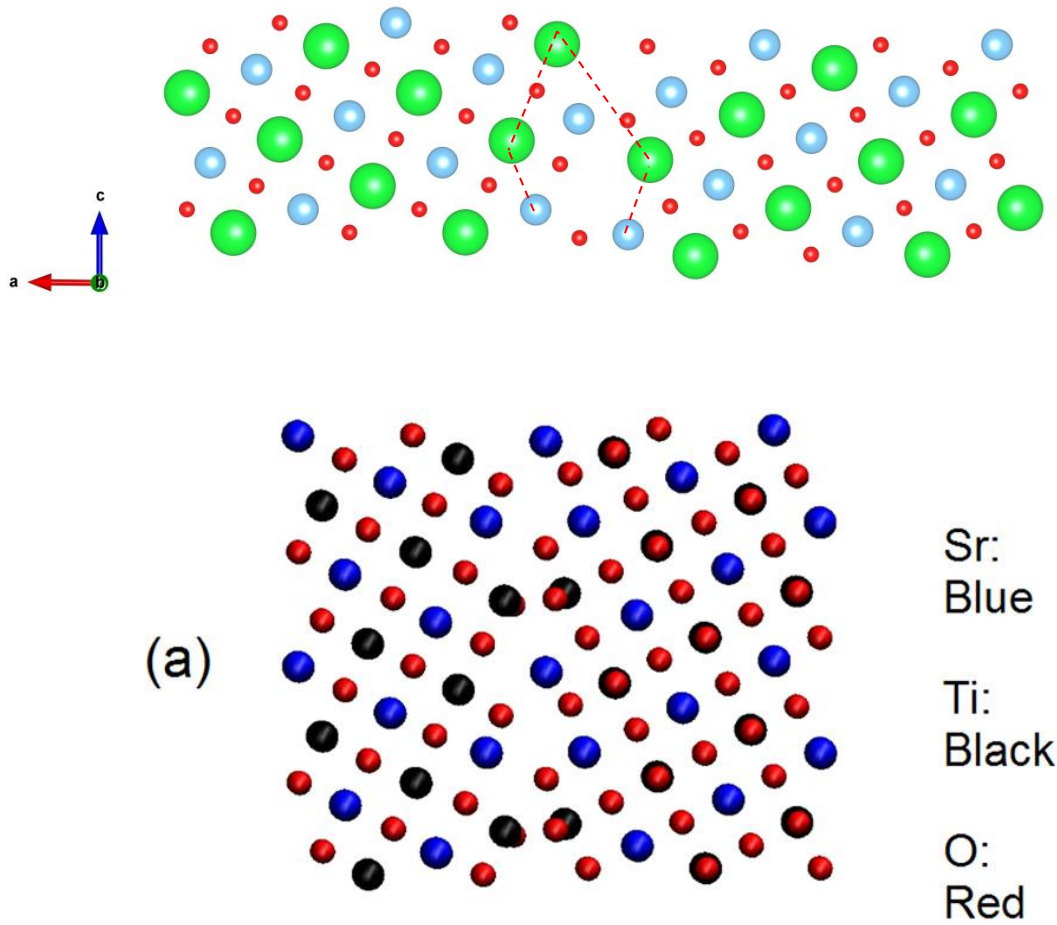


**Figure 5.1f** –  $\Sigma 5$  (210) interface structure of STO, with computational comparison which was structurally optimised using MD by Zheng *et al.*<sup>(33)</sup>.

The structure obtained for the  $\Sigma 5$  (210) interface is in structural agreement with the model proposed by Zheng *et al.*<sup>(33)</sup>. Unlike the previous two interface structures, this model is asymmetric in nature despite being the result of identical surfaces being combined, namely the  $\text{TiO}_2$  terminated (210) surface, which when constructed was the most energetically stable of the four interface structures investigated when combining (210) surfaces. The structure obtained is also in agreement with the experimental (HAADF-STEM) and calculated structure (DFT-GGA) obtained by Lee *et al.*<sup>(36)</sup>.

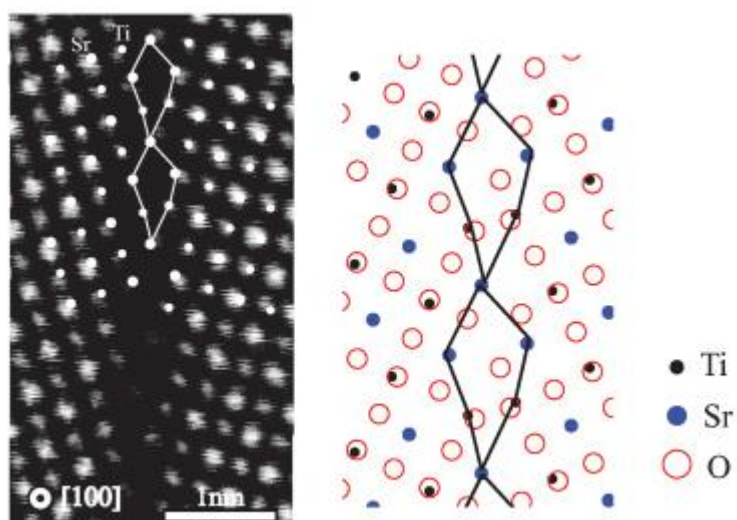


**Figure 5.1g** –  $\Sigma 5$  (210) interface of STO obtained experimentally and calculated by Lee et al.<sup>(36)</sup>.

#### 5.1.3.4 $\Sigma 9$ (221) Interface

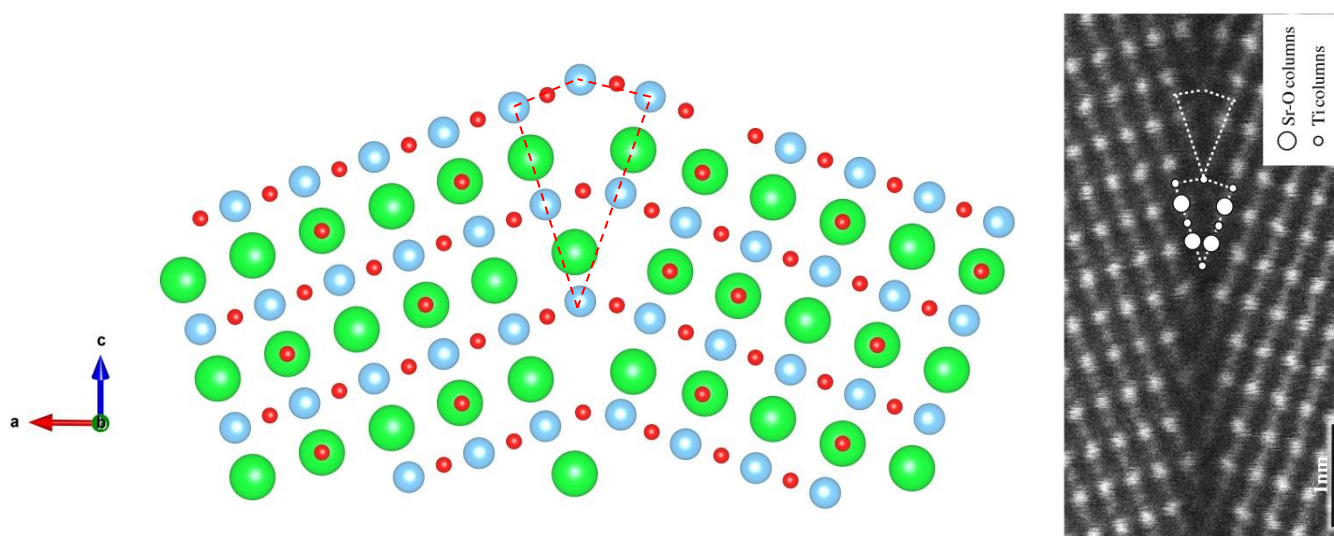


**Figure 5.1h** –  $\Sigma 5$  (221) interface structure of STO with experimental comparison of HAADF-STEM structural image by Mitsuma et al.<sup>(39)</sup>.

The structure presented in figure 5.1h is structurally like the HAADF-STEM experimental structure shown<sup>(39)</sup>. Both structures are symmetrical in nature however in the case of the experimental image there are two Sr atoms located above the bottom point Ti atom in the c (z) direction. However, elsewhere on the image a double Sr site is not visible. It does look from the simulation that there is



insufficient space for two Sr atoms. Although there is a small discrepancy between the calculated and experimental structures, in general there is a good agreement.

### 5.1.3.5 $\Sigma 5$ (310) Interface

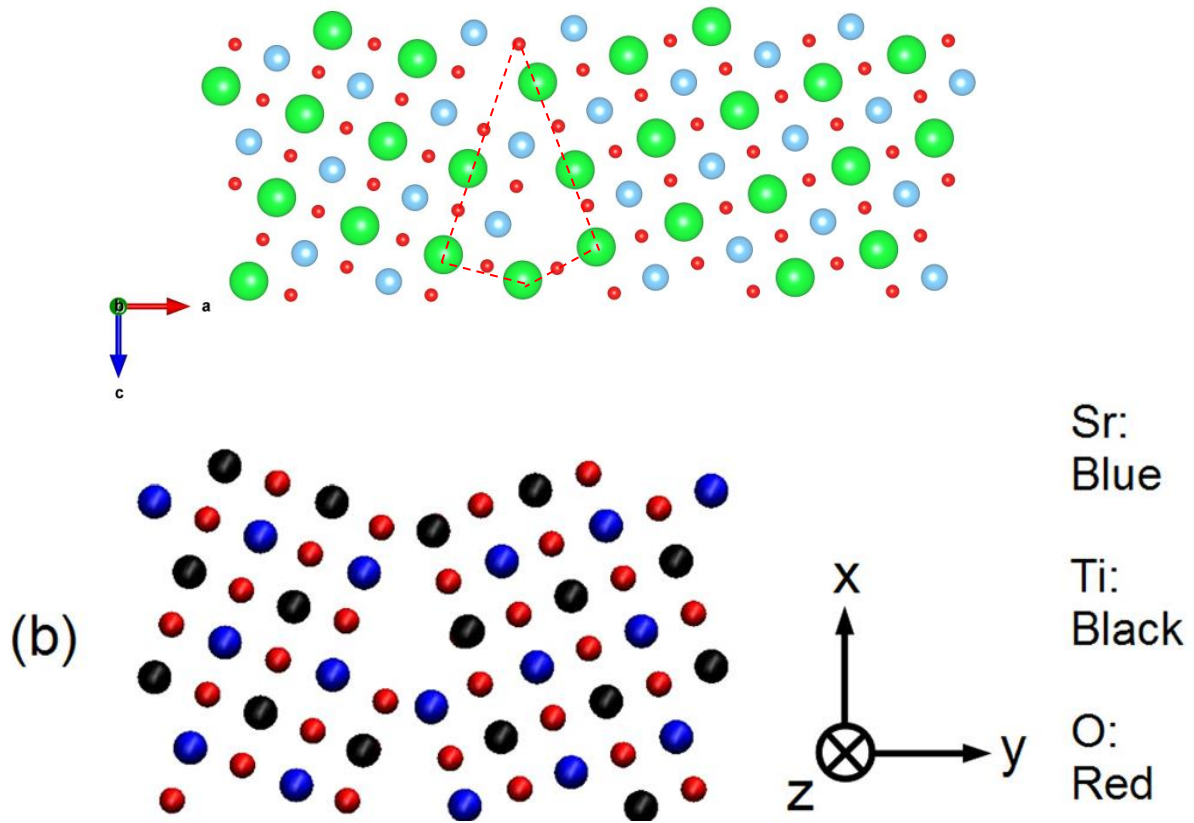


**Figure 5.1i** –  $\Sigma 5$  (310) interface structure of STO, with computational comparison which was structurally optimised using MD by Zheng *et al.*<sup>(33)</sup>.

The structure obtained for the  $\Sigma 5$  (310) interface is in structural agreement with the model proposed by Zheng *et al.*<sup>(33)</sup>. The pattern observed at the interface is similar to the  $\Sigma 9$  (221) interface. The structure observed for this interface is also in agreement with the experimentally obtained structure for both STO and BTO ( $\text{BaTiO}_3$ ) by Imaeda *et al.*<sup>(211)</sup> by HAADF-STEM.

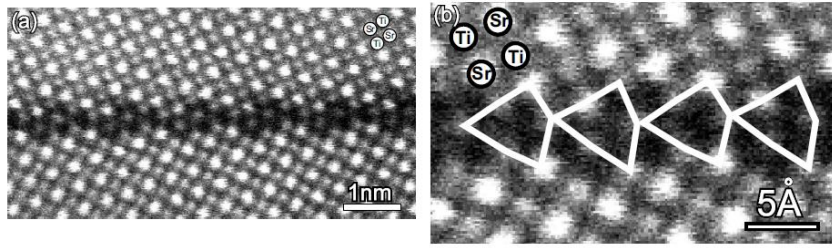


**Figure 5.1i** –  $\Sigma 5$  (310) interface structure of STO obtained experimentally using HAADF-STEM by Imaeda *et al.*<sup>(211)</sup>.

### 5.1.3.5 $\Sigma 17$ (410) Interface

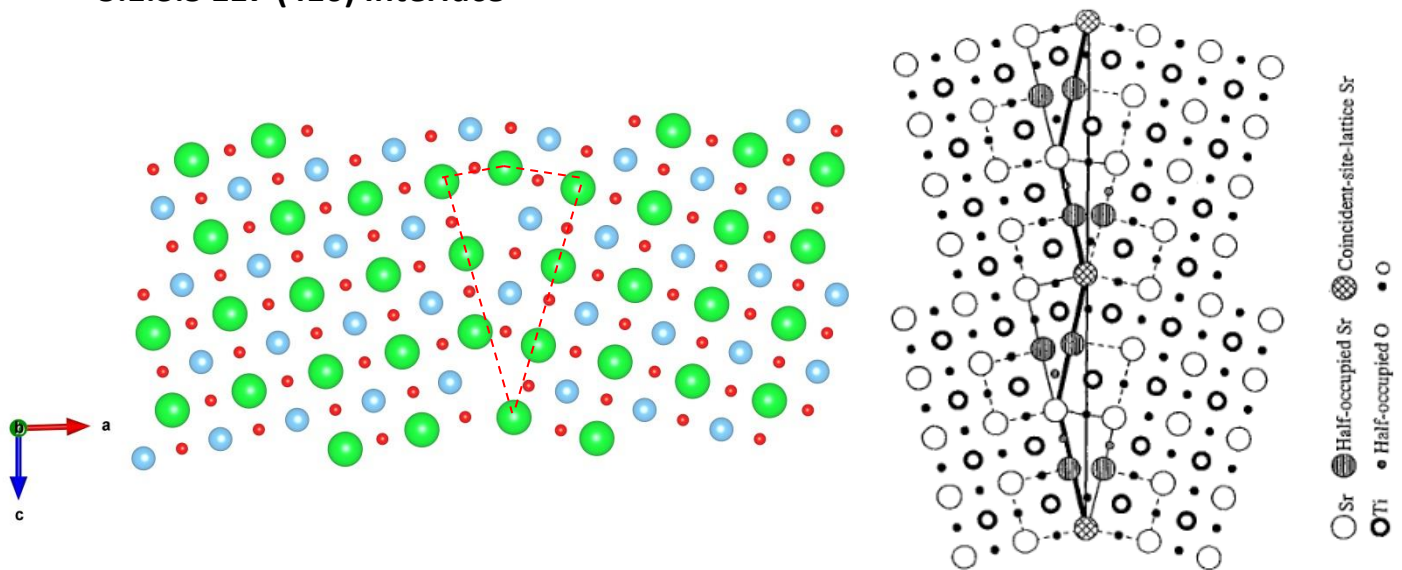


**Figure 5.1j** –  $\Sigma 17$  (410) interface structure of STO with experimental comparison obtained using Z-contrast imaging with transition electron microscopy (TEM) by Browning *et al.*<sup>(212)</sup>.

As shown in figure 5.1j, there is good structural agreement between the calculated structure and the experimental structure proposed by Browning *et al.*<sup>(212)</sup>. The interface structure is a diamond shaped pattern similar to the pattern observed for the  $\Sigma 5$  (310) and  $\Sigma 9$  (221) interfaces.

The interface structures presented so far generally have structural agreement with the experimental and other computational comparisons, despite some small discrepancies seen where the use of a smaller step length may be required. This gives confidence in the results reported so far. The following set of interfaces have all be characterised by the same method however no experimental or computational examples were available for comparison.



### 5.1.3.6 $\Sigma 11$ (311), $\Sigma 17$ (331) and $\Sigma 33$ (441) Interface

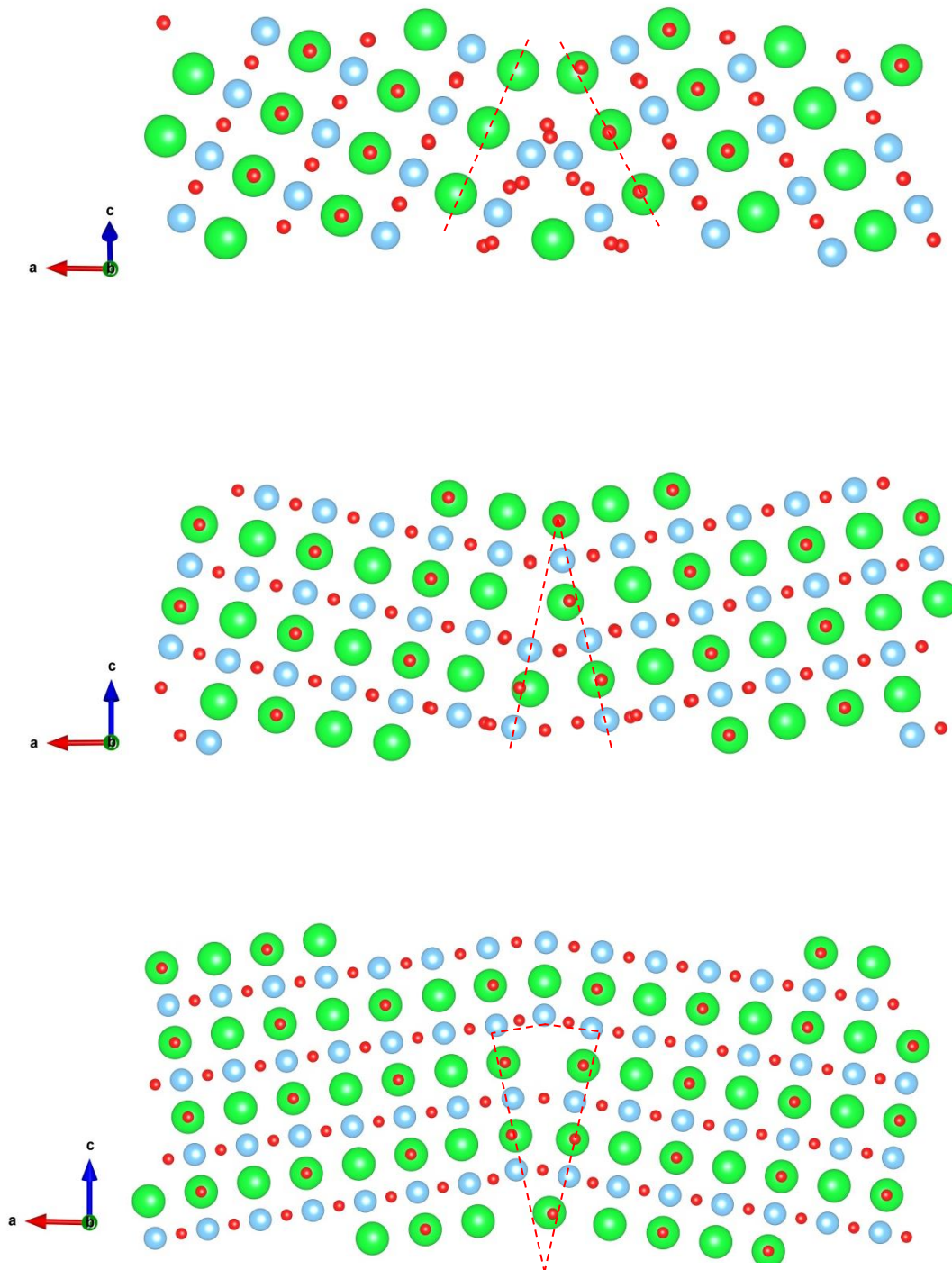


**Figure 5.1k** –  $\Sigma 11$  (311),  $\Sigma 17$  (331) and  $\Sigma 33$  (441) interface structures, respectively.

The three structures obtained are shown in descending order, namely the  $\Sigma 11$  (311),  $\Sigma 17$  (331) and  $\Sigma 33$  (441) interface structures. Firstly, the  $\Sigma 11$  (311) interface structure shows a slight similarity to

the  $\Sigma 5$  (310) interface where a descending diamond shaped pattern was observed at the interface. This interface structure however shows clear distortion of both the oxygen and titanium sublattice which is represented by the asymmetric character of the interface. The  $\Sigma 17$  (331) and  $\Sigma 33$  (441) interface structures are also similar to each other as well as the diamond shaped pattern observed in the  $\Sigma 9$  (221) interface. Although no structural comparisons were available in the literature for these three interfaces, the agreement between other calculated structures with experimental structures gives confidence in the models obtained and due to their similar energetics with those which have been structurally characterised there is future potential for the possible experimental characterisation of such boundaries.

## 5.2 Stability of STO Boundaries

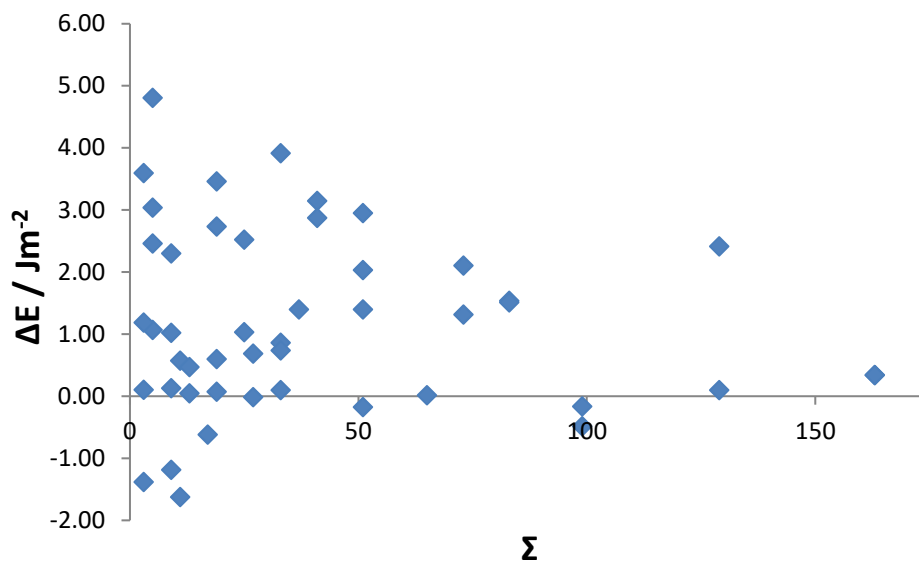


**Figure 5.2** –  $\Delta E$  vs  $\Sigma$  of the grain boundaries of STO ranging from  $\Sigma=3$ -163, where  $\Delta E$  can be used to predict the stability of each grain boundary.

As discussed in section 5.1, a reliable method had been developed for determining the structure and energetics of several grain boundaries of STO. Some of the latter examples were those of which have not been characterised experimentally, as the method used has a strong agreement with those observed experimentally. This gives confidence in the analysis of those which have not been experimentally characterised.

Like the case of ceria, approximately 90% of the analysed boundaries of STO were found to be relatively energetically stable with regards to the respective two free surfaces. STO shows a different relationship compared to ceria where many of the low Miller index boundaries were found to be relatively energetically unstable with increasing  $\Sigma$  value predicting a higher chance of relative stability. Unlike ceria, there are a higher proportion of energetically unstable boundaries. As many of the boundaries show, the energetic favourability predicts that there is a potential for these boundaries to be structurally characterised and could be of importance in application.

In these sections, a reliable method has been used for developing accurate structural models of interfaces of STO. As structural models had been obtained, the next section will focus on defect segregation in the bulk and interface regions through segregation of defective phases of STO to further quantify the likelihood of defect formation and how this may influence oxygen diffusion.

### 5.3 Intrinsic and Extrinsic Defect Segregation

In this section defect segregation profiles will be presented for the doping of STO with oxygen vacancies ( $V_o$ ), lithium ( $Li^+$ ) and lanthanum ( $La^{3+}$ ) dopants at the Sr sites. Therefore, resulting in structural similarities to the solid electrolyte, LLTO, which will be covered in detail in chapter 7. The defect energies were obtained along the x-plane up to approximately 60 Å in either direction. The profiles presented will only extend to 20 Å as the interface energies have converged into the bulk region at this point where within the bulk regions the energy values are almost all equivalent and therefore have been set to zero to observe the difference in energetic behaviour and magnitude between the bulk and interface regions. Figure 5.3 presents the segregation profile for the  $\Sigma 3$  (111) interface of STO.

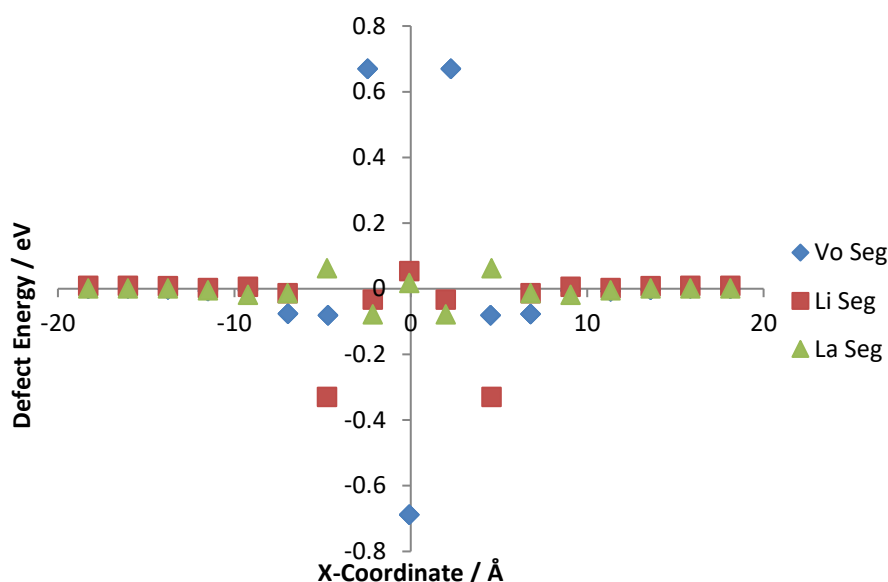


**Figure 5.3** – Segregation profile for intrinsic and extrinsic defects at the  $\Sigma 3$  (111) interface of STO.

As shown in figure 5.3, from each of the incorporated defects, the interfacial energies converge towards the bulk energies at approximately 8 Å in both x-directions, therefore suggesting that the  $\Sigma 3$  (111) interface is around 16 Å in width. As shown, defects can be both energetically favourable and unfavourable compared to the bulk defect energies in this region. As many defects located in this region are energetically favoured compared to the bulk, this promotes the likelihood of formation which could result in increased oxygen transport at the interface.

In order to quantify whether the presence of grain boundaries enhance or suppress oxygen transport in STO, this will be investigated in section 5.4.

## 5.4 Molecular Dynamics of STO Interfaces

Five of the structurally characterised stoichiometric boundaries discussed in section 5.1, all found to be relatively energetically stable with respect to the values in table 5.1, were simulated using the DL\_POLY\_Classic<sup>(141)</sup> code. By using the techniques discussed in chapter 2, initial simulations were carried out using the NST ensemble for 1.1 ns. Further simulations of 1.0 ns using the NVT ensemble were carried out over which oxygen diffusion was measured and thereby activation energies were calculated. In section 5.3 incorporation of defects into both the boundary and bulk regions were explored but were limited due to the simulations being carried out at 0 K, which is solved using MD. With regards to all six of the simulated boundaries, no long range diffusion was observed at temperatures below 2000 K and amorphization of the boundary occurred when exceeding 3000 K therefore all simulations were carried out within this range of temperatures.

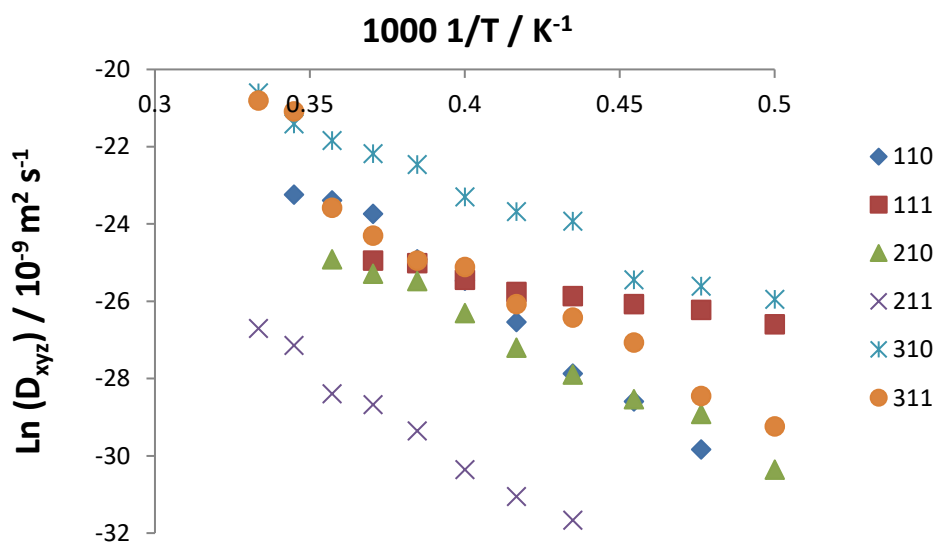


**Figure 5.4** – Arrhenius plot of natural log of total diffusion of oxygen vs reciprocal temperature for six simulation cells containing grain boundaries of STO. Simulations were carried out using the Teter potential model.

Boundary	$E_a$ / eV	$D_0$ / $\text{m}^2 \text{s}^{-1}$
(110)	$0.39 \pm 0.02$	$5.10 \times 10^{-8} \pm 3.53 \times 10^{-9}$
(111)	$2.17 \pm 0.30$	$2.65 \times 10^{-5} \pm 2.86 \times 10^{-5}$
(210)	$1.22 \pm 0.13$	$1.19 \times 10^{-6} \pm 5.39 \times 10^{-7}$
(211)	$17.12 \pm 4.42$	$8.48 \times 10^{16} \pm 1.28 \times 10^{18}$
(310)	$1.78 \pm 0.20$	$6.85 \times 10^{-6} \pm 4.74 \times 10^{-6}$
(311)	$2.53 \pm 0.17$	$8.97 \times 10^{-5} \pm 4.94 \times 10^{-5}$

**Table 5.4** – Activation Energies ( $E_A$ ) and  $D_0$  values of oxygen diffusion in the six simulated grain boundaries of STO.

Figure 5.4 and table 5.4 show the simulated diffusion data in each grain boundary of STO. As shown the simulations were carried out between 2000 K-3000 K where long range diffusion occurred above 2000 K and amorphization occurred at approximately 3000 K. As shown by the data in table 5.4, the activation energy,  $D_0$  values and their associated errors reported for the (211) boundary are significantly higher than the values reported for all other boundaries and the intrinsically defective bulk. Therefore, this boundary will not be considered as part of the comparison as the discrepancy in values suggests an error with the simulation cell which could be attributed to amorphization of the boundary structure. As no long range diffusion was observed in the stoichiometric bulk, comparisons for each boundary will be made to the intrinsically defective bulk as discussed in chapter 3 where an activation energy of  $0.95 \text{ eV} \pm 0.02 \text{ eV}$  and a  $D_0$  value of  $2.61 \times 10^{-9} \pm 0.26 \times 10^{-9} \text{ m}^2 \text{s}^{-1}$  were reported. The (110) boundary was the only boundary where a lower activation energy and a higher  $D_0$  value when compared to the bulk values was observed, suggesting that this boundary could enhance oxygen diffusion. The remaining four boundaries were all observed to have a higher activation energy when compared to the value obtained for the intrinsically defective bulk. Thus, suggesting that each of these grain boundaries would suppress oxygen transport which is consistent with experimental research<sup>(210)</sup>. As was the case with each of the ceria grain boundaries simulated using MD, the reported  $D_0$  values are significantly higher when compared to those observed in the bulk. This substantial increase in diffusion could again be the result of structural changes at the boundary that occur with increasing temperature, which are not observed in the bulk, such as a clustering of oxygen ions in the boundary region. This could correlate with a change in mechanism of diffusion with increasing temperature. Further simulations could be carried using a NEB method to determine whether this is the case. Furthermore, the obtained activation energies and  $D_0$  values account for

the combined x, y and z components of diffusion. Future work would include isolating each of these individual components to investigate the differences in oxygen transport parallel to the boundary and perpendicular to the boundary. Thus, gaining a deeper insight as to whether the presences of grain boundaries suppress or enhance oxygen diffusion in STO.

## 5.5 Chapter Summary

A high-throughput computational method has been used to investigate the structure and energetics of grain boundaries of STO. The importance of step length was further highlighted to achieve a reliable structure without the requirement of significant strain on computational resources. The computationally obtained energetics and structures of grain boundaries of STO were generally consistent with those seen experimentally, however some small structural discrepancies were observed where a smaller step length may be required to achieve a structural match for STO boundaries. Surface termination was again found to have a profound impact on the boundary stability where energetically favoured surfaces resulted in a stable grain boundary and surfaces of mixed termination, in contrast to ceria, were found to generally result in energetically favoured boundaries. Interfaces were simulated using a wide range of  $\Sigma$  values showing that most grain boundaries of STO were energetically favoured and therefore there is a potential for experimental characterisation. High-throughput techniques were further used to investigate single point defects in STO where like ceria, defects were generally found to be energetically favoured at the boundary region relative to the bulk, therefore implying that defective sites may facilitate oxygen diffusion. Oxygen migration in boundaries was further quantified using MD techniques for several experimentally characterised boundaries, where no obvious relationship between the defect energies and diffusion was observed. The presence of grain boundaries was found to generally suppress oxygen diffusion in STO compared to the bulk which is consistent with experimental research. Similar to ceria, further simulations would be required to quantify the extent of which defects could improve oxygen diffusion in STO grain boundaries. These include using intrinsic and extrinsic doping schemes with longer time scale simulations. As previously discussed, future work would also include isolating the individual x, y and z diffusion trajectories. By isolating the individual components, quantitative analysis could be used to compare diffusion parallel to the boundary and perpendicular to the boundary to further understand how the presence of grain boundaries influences oxygen transport.



## 6 Heterointerfaces in Fuel Cell Materials

This chapter will provide an insight into the  $\text{CeO}_2$  || STO interface. One particular feature of this heterogeneous interface system is the role of each phase as an electrode. As discussed in chapter 4, experimental evidence has shown ceria and GDC to be an effective candidate solid electrolyte due to the high conductivity seen at lower temperatures (500 °C-700 °C) compared to other solid electrolytes such as YSZ<sup>(196)</sup>. STO exhibits mixed conductivity, where experimentally lanthanum doped STO was found to be chemically stable during fuel cell cycling when used as an anode<sup>(198)</sup>. Furthermore, strontium titanate ferrite has been found to be a stable and effective cathode material<sup>(213)</sup>.

Fluorite-perovskite nanocomposite systems such as  $\text{BaTiO}_3$  ||  $\text{CeO}_2$  systems have been found to be successful in a number of practical applications such as; automotive uses in three way catalysis<sup>(214, 215)</sup>, microwave devices<sup>(60)</sup>, resistance to radiation damage<sup>(216-219)</sup> and high temperature superconductors<sup>(58)</sup>. The variance in properties of ceria and STO are essential in the diverse applications of these systems, as STO is ferroelectric and ceria is a low-permittivity dielectric<sup>(220)</sup>. The ferroelectric properties of STO have further been studied where ceria acted as a buffer layer during epitaxial deposition<sup>(59)</sup>. With regards to fuel cell systems, fluorite-perovskite systems have found to be effective due to their mixed ionic-electronic conductivity where the interface region has been found to influence fast-ion conduction<sup>(55, 56, 221, 222)</sup>.

Previous research on the  $\text{CeO}_2$  || STO interface is limited, however implications of both radiation damage evolution and fast ion conduction have been considered<sup>(57)</sup>. In this computational study, the steps of the surface at the interface were investigated where such regions were found to both attract and repel certain defects with respect to radiation damage. Furthermore, the presence of oxygen vacancies at the interface was attributed to a change in the thermodynamic behaviour of oxygen transport, suggesting that defective sites at the interface could be implicative for fast ion transport across the interface, effectively through amorphization.

### 6.1 Interface Models

The generation of heterointerfaces involves a more complex version of the scanning methodology by scanning one surface atop another of two differing phases with the aim of achieving a low energy, low strain lattice match. This procedure is discussed in depth in chapter 2.4.2.4. The modelling of homogeneous interfaces investigated in chapters 4 and 5 highlighted the importance of grain boundaries of identical phases, as such systems are likely to exist in polycrystalline materials. In fuel

cell systems, understanding the structure and energetics of the interface is crucial in predicting an oxygen diffusion mechanism across the interface as well as in the bulk.

For the purposes of this research, stoichiometric STO will be considered. Within this chapter, two heterogeneous interfacial systems will be investigated with respect to their structure, stability and dynamics, namely; (100) CeO<sub>2</sub> || (100) STO and (111) CeO<sub>2</sub> || (111) STO interfaces. The former of these two systems will further consider gadolinium doping (3.3%) of ceria and what significance this has on oxygen diffusion when compared to the stoichiometric phases. The simulations carried out aim to investigate how the nature of heterogeneous interfaces influences oxygen transport. These two systems were chosen due to the fact that both surfaces of both phases have been experimentally characterised, and their relatively small surface area compared to those of a larger Miller index aids in achieving a lower strain surface match without the need for very large systems (30,000+ atoms) which would be unsuitable for the used simulation codes.

### 6.1.1 (100) SrTiO<sub>3</sub> || (100) CeO<sub>2</sub> Interface Stability and Structure

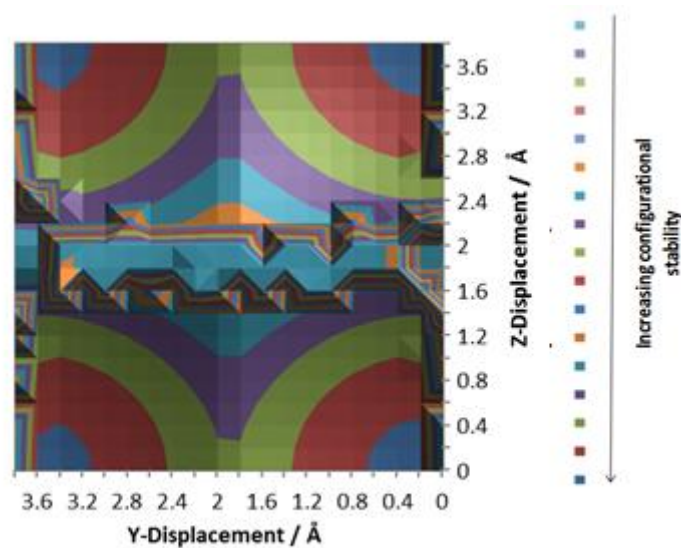


**Figure 6.1a** – Potential energy surface for the TiO<sub>2</sub> terminated (100) STO || (100) CeO<sub>2</sub> (STO Substrate)

Figure 6.1a represents one of four potential energy surfaces for the stoichiometric (100) STO || (100) CeO<sub>2</sub> interface, where a 3.6% surface mismatch was observed. Two considerations were in place when generating this boundary. Firstly, the CeO<sub>2</sub> (100) surface was found to have only one plausible surface termination when simulated using METADISE<sup>(136)</sup>, specifically an oxygen terminated surface. However, the STO (100) surface was found to have two possible terminations, SrO and TiO<sub>2</sub>. Secondly, when generating heterogeneous boundary systems, one phase is the substrate, the

second phase is then scaled to this. Thereby, as shown in table 6.1a, both terminations of the (100) surface were considered along with both phases as a proposed substrate material. Figure 6.1a represents the interface considered to be the most energetically favoured of these four schemes.

Substrate	Termination of SrTiO <sub>3</sub> (100) surface	E <sub>f</sub> / Jm <sup>-2</sup>	E <sub>c</sub> / Jm <sup>-2</sup>	Area / Å <sup>2</sup>
CeO <sub>2</sub>	SrO	3.41	1.28	14.56
CeO <sub>2</sub>	TiO <sub>2</sub>	2.15	2.36	14.56
SrTiO <sub>3</sub>	SrO	3.14	1.38	15.09
SrTiO <sub>3</sub>	TiO <sub>2</sub>	1.83	2.52	15.09

**Table 6.1a** – Formation energy, cleavage energy and surface area of (100) SrTiO<sub>3</sub> || (100) CeO<sub>2</sub> interface.

As shown in table 6.1a, the surface termination of the (100) STO surface is the dominant factor in the stability of the interface. As shown when using both substrates, the interface formation energy is approximately 1.3 J m<sup>-2</sup> more energetically favoured when constructed with the TiO<sub>2</sub> terminated surface compared to the SrO terminated surface. Secondly the cleavage energy is found to be approximately 1.1 J m<sup>-2</sup> greater for both substrates, therefore showing the improved stability of the TiO<sub>2</sub> terminated surface. When comparing the energetics of the two different substrate lattices, the results suggest that there is improved stability when an STO substrate is used. When using ceria as a substrate, the smaller surface area results in compression of the STO lattice in order to achieve the best lattice match, therefore increased strain is applied to the STO crystal, decreasing the stability of the interface. Whereas when STO is used as the substrate model, the ceria lattice is expanded which is energetically favoured over contraction, therefore when the interface is generated, less strain is present and increased energetic stability is observed. The observed behaviour is consistent with the elastic constants where there is a greater energy cost to strain STO compared to CeO<sub>2</sub>.

Upon visual inspection of the structural models obtained for each interface, the atomistic structure appears identical regardless of which substrate was used. The two interface structures shown in figure 6.1b represent the relaxed structure of the two interfaces where the termination of the (100) STO surface differs.

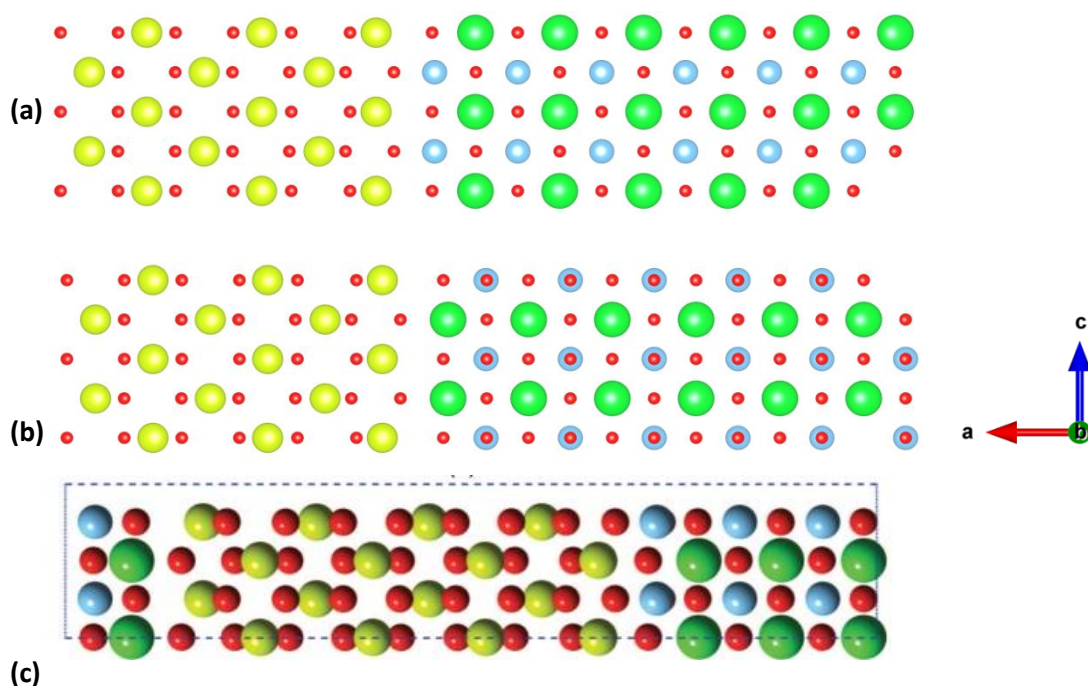


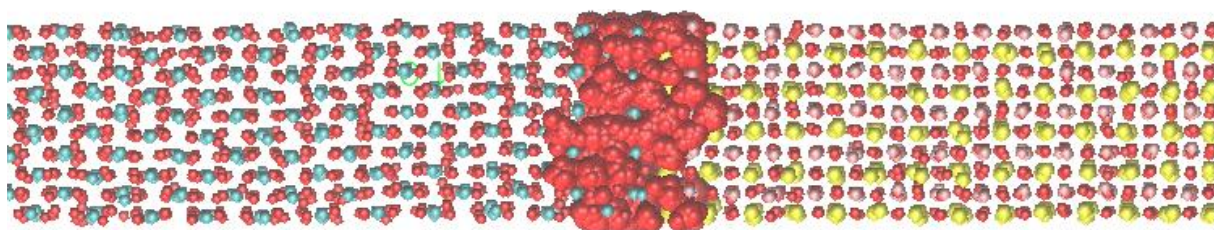
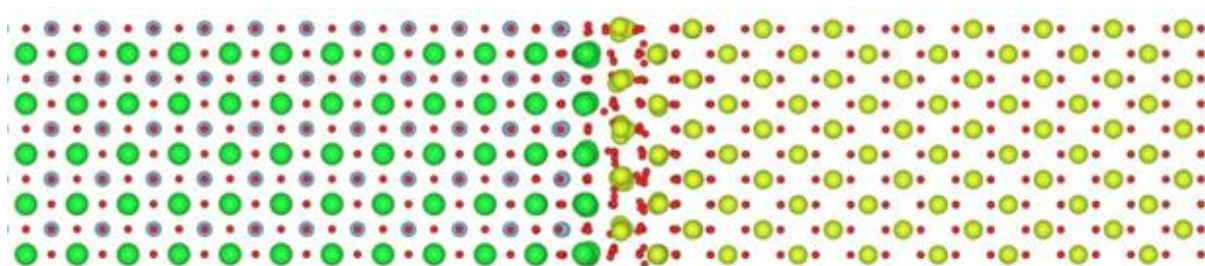
**Figure 6.1b** – (a)  $\text{TiO}_2$  terminated (100)  $\text{SrTiO}_3$  || (100)  $\text{CeO}_2$  relaxed structure (b)  $\text{SrO}$  terminated (100)  $\text{SrTiO}_3$  || (100)  $\text{CeO}_2$  relaxed structure (c) Mixed termination of interface, structural optimisation carried out using DFT+U by Dholabhai et al.<sup>(57)</sup>. O-O distance at the interface  $\approx 3.25\text{\AA}$ .

As shown in figure 6.1b, the relaxed structural models obtained are in agreement with the structure derived using DFT, thereby giving confidence in the methods used in the construction of heterointerfaces. In both relaxed structures, no observable distortion is seen any of the cationic or anionic sublattices when simulated using EM techniques. As a reliable structural model of this interfacial system had been obtained, the dynamics will be investigated further.

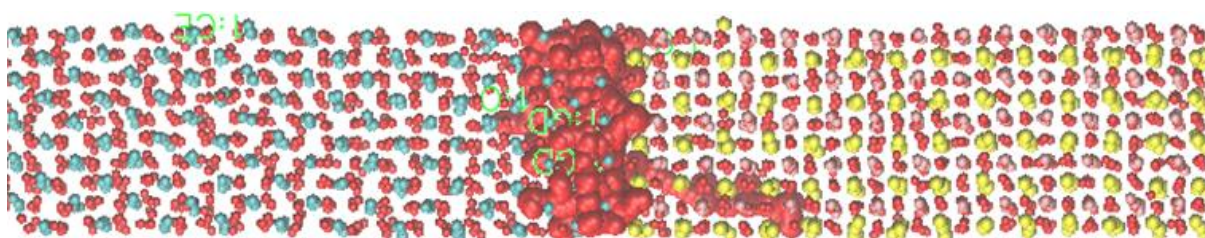
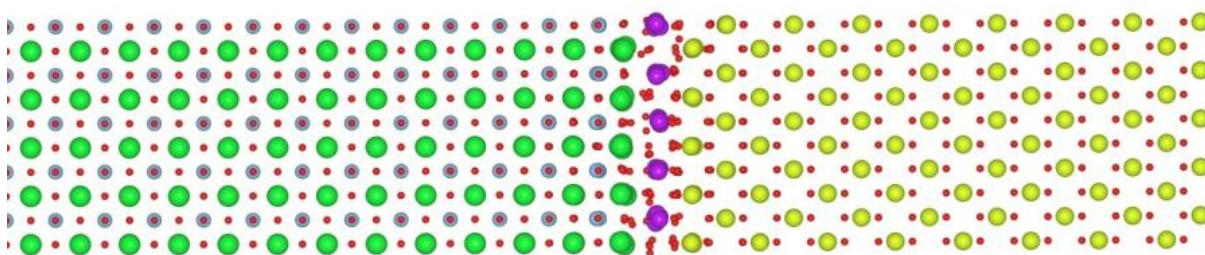
### 6.1.2 (100) $\text{SrTiO}_3$ || (100) $\text{CeO}_2$ Interface Dynamics

A detailed description of the generation of heterogeneous grain boundaries can be found in chapter 2 through use of the METADISE code<sup>(136)</sup>. Annealing of the boundaries was carried out in steps of a 300 K up to 3600 K, for 1.0 ns, to ensure no amorphization where all MD simulations were carried out using the DL\_POLY code<sup>(141)</sup>. Dynamic simulations to measure oxygen diffusion were carried out between 2000 K-3500 K where an initial simulation of the NST ensemble was used for 1.1 ns to allow the system to equilibrate at the specified temperature, and the volume was fixed using the NVT ensemble for a further 1.0 ns over which oxygen diffusion was measured.

(a)



(b)





(c)

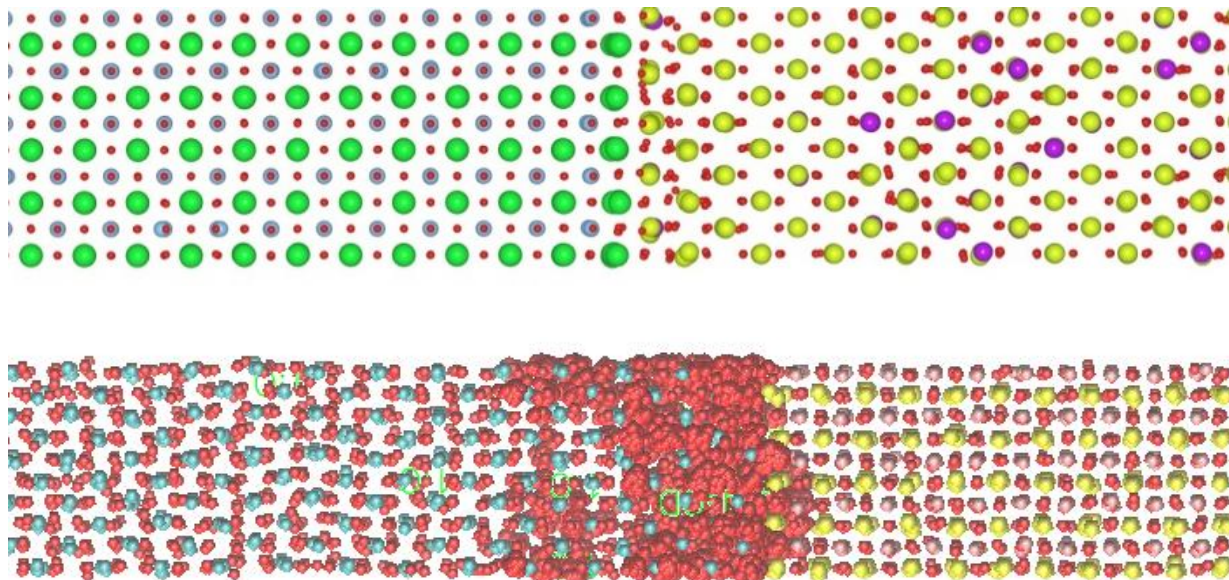


**Figure 6.1c** – Annealed structures of the (a) “stoichiometric” (b) “planar” and (c) “random” (100) STO || (100) CeO<sub>2</sub> boundaries with corresponding diffusion trajectory (2800 K) of a single oxygen ion located close to the interface. Structural information of each boundary is represented in table 6.1b.

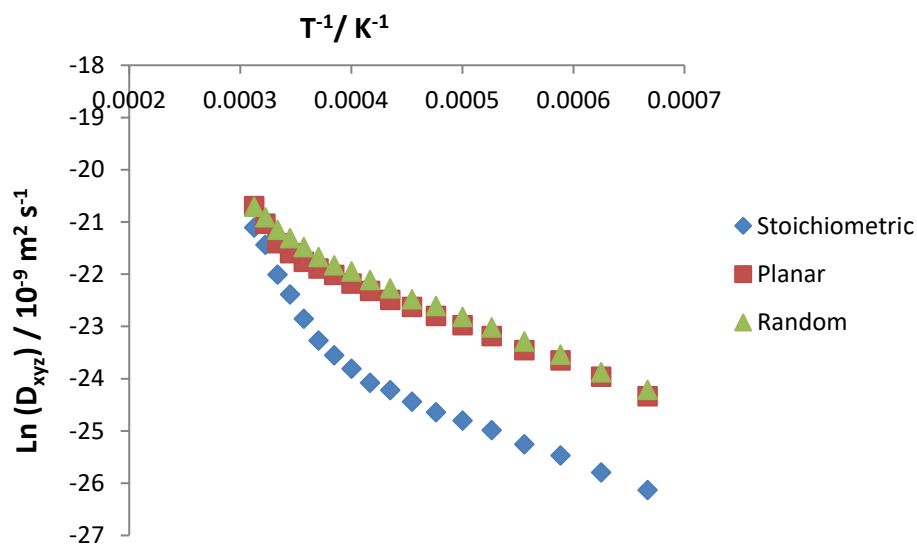


**Figure 6.1d** – Natural log of total diffusion vs reciprocal temperature of the TiO<sub>2</sub> terminated (100) SrTiO<sub>3</sub> || (100) CeO<sub>2</sub> interface, including 3.3% Gd<sup>3+</sup> doping in “planar” and “random” phases.

Phase	Formula	$E_A$ / eV	$D_0$ / $10^{-9} \text{ m}^2 \text{ s}^{-1}$
“Stoichiometric”	(100) $\text{SrTiO}_3$    (100) $\text{CeO}_2$	$1.11 \pm 0.10$	$13.28 \pm 7.03$
“Planar”	(100) $\text{SrTiO}_3$    (100) $\text{Ce}_{0.9667}\text{Gd}_{0.0333}\text{O}_{1.6}$	$0.79 \pm 0.03$	$10.56 \pm 2.00$
“Random”	(100) $\text{SrTiO}_3$    (100) $\text{Ce}_{0.9667}\text{Gd}_{0.0333}\text{O}_{1.6}$	$0.81 \pm 0.02$	$13.99 \pm 1.82$

**Table 6.1b** – Structural formulae, activation energies and  $D_0$  values of the (100) STO || (100)  $\text{CeO}_2$  boundaries. “Stoichiometric” represents both stoichiometric phases, “Planar” has defective region in close proximity to the grain boundary and “Random” has defects randomly dispersed throughout the ceria phase.

Figure 6.1c shows the annealed structure of the three STO ||  $\text{CeO}_2$  boundaries where their compositions are represented in table 6.1b. This annealing procedure was carried out up to 3000 K in which both phases of the boundary remained thermally stable. As shown, upon cooling there is clear distortion in the oxygen sublattice close to the boundary region differing from the bulk. In (b) and (c) the blue species highlighted are the  $\text{Gd}^{3+}$  dopants which occupy the  $\text{Ce}^{4+}$  sites and were charge compensated through oxygen vacancy formation. The structure represented in (b) is the “planar” phase. In this example, all  $\text{Gd}^{3+}$  substitutions and oxygen vacancies are located in close proximity to the boundary region. Whereas in (c) the defects were distributed randomly throughout the ceria phase. The purpose of this was to investigate whether the defect distribution influenced the oxygen transport and thermal stability of the boundary. Thermally, each boundary was found to be stable up to approximately 3200 K where exceeding this resulted in amorphization of the STO phase. Figure 6.1c further shows the diffusion trajectory of a typical single oxygen ion located close to the boundary region. When comparing the activation energies and  $D_0$  values to those seen in the stoichiometric bulk phases, a lower activation energy and higher diffusion is observed. Thus, suggesting that the presence of the grain boundary facilitates oxygen transport relative to the bulk. Visually the diffusion pathway appears to have a larger MSD in examples (b) and (c) which is supported by the energetics shown in figure 6.1d and table 6.1b. As shown, there is a clear reduction in activation energy between the stoichiometric and defective phases where a change of -0.32 eV and -0.30 eV in activation energies are seen, without any decrease in thermal stability. This change in activation energy suggests that the composition of the electrolyte species can be used to tune the system where much lower activation energies can be achieved. There appears to be a single diffusion mechanism based on the linear nature of the gradients in (b) and (c) whereas line (a) could be separated into two linear sections, suggesting the possibility of a transition in diffusion mechanism with increasing temperature. To quantify this, further simulations would be required which treat the boundary region explicitly. It was further shown that the distribution of defects appears to have no effect on the thermal stability, as stability was observed up to identical

temperatures and only a minor difference is seen with respect to activation energy, implying that focal distribution of defects close to the boundary has a net energetic favourability of 0.02 eV. The observed  $D_0$  value reported for the “random” boundary was slightly higher, yet the associated error for this boundary when compared with the “planar” boundary suggests that from the  $D_0$  values, oxygen transport occurs at similar rates in both phases. The observed activation energies were generally lower than those reported for the stoichiometric grain boundaries discussed in chapters 4 and 5. However, the observed  $D_0$  values were significantly lower than the homogenous grain boundaries. When considering the activation energies alone, this would suggest that oxygen diffusion is enhanced by the (100)  $\text{SrTiO}_3$  || (100)  $\text{CeO}_2$  boundary and the respective defective phases, when compared to the homogenous grain boundaries. However, when considering the  $D_0$  values, these were found to be much larger for the homogenous grain boundary systems. Therefore, further simulations would be required, in particular those which separate diffusion parallel to the boundary and perpendicular to the boundary. This could further quantify whether heterogenous boundaries enhance or suppress oxygen transport, where the latter was found to be the case for homogenous grain boundaries in both ceria and STO.

The data obtained for the (100) STO || (100)  $\text{CeO}_2$  boundary has provided an insight into the structure, stability and energetics of a heterogenous boundary system. Possible considerations into improving application in a fuel cell system where the importance of the substrate phase, location and concentration of dopants were further highlighted. Through the use of the METADISE<sup>(136)</sup> and DL\_POLY<sup>(141)</sup> codes, a plausible structure was able to be analysed due to the strong lattice match between the two surfaces coupled with the relative simplistic structure of the boundary. In section 6.2, a more complex system will be investigated which aims to expand on the results discussed in section 6.1.



## 6.2 (111) SrTiO<sub>3</sub> || (111) CeO<sub>2</sub> Interface Structure

The stoichiometric (111) STO || (111) CeO<sub>2</sub> boundary provided a challenging outlook on the construction of heterogeneous grain boundaries through the methods discussed due to the size of the system. A larger surface mismatch was observed between the two surfaces: 26.123 Å<sup>2</sup> and 12.613 Å<sup>2</sup>, respectively, correlating to a percentage mismatch of 58.8%. In comparison to the (100) STO || (100) CeO<sub>2</sub> boundary, an increase in surface area was observed (679.5 Å<sup>2</sup>) when scaling the lattice vectors of each surface to obtain the lowest possible strain energy. A more extensive search was required resulting in the formation of a much larger overall boundary structure, in excess of 17,000 atoms as a result of the scaling of lattice vectors. Scaling was between a factor of 3 and 9, hence the larger surface area. As a result of this, the METADISE<sup>(136)</sup> code was unable to calculate formation and cleavage energies of this boundary due to the code's limitations. As a result of this, only one surface termination for both STO and ceria were considered during this simulation.

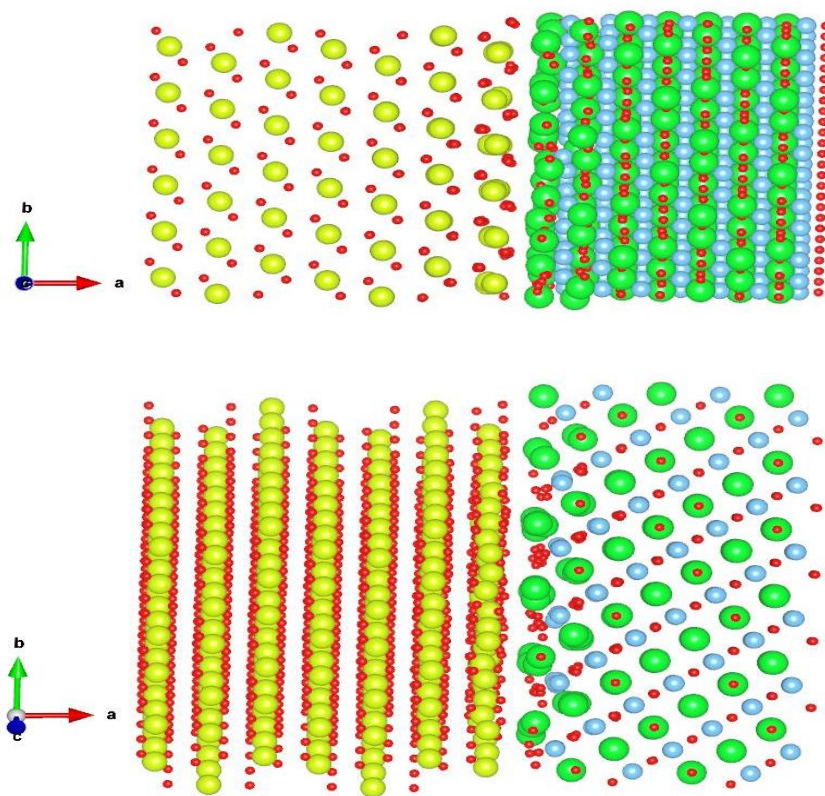


**Figure 6.2a** – *Relaxed structure of the (111) SrTiO<sub>3</sub> || (111) CeO<sub>2</sub> interface from the perspective on both surfaces*

Figure 6.2a shows two orientations of the (111) SrTiO<sub>3</sub> || (111) CeO<sub>2</sub> interface. As shown in both perspectives, distortion of all cationic sublattices is visually observed as well as clustering of oxygen atoms at the STO (100) surface. As this interface has not been structurally characterised either

experimentally or computationally, no structural comparisons to other models can be considered. Despite the limitations of the discussed EM methods, through use of the DL\_POLY<sup>(136)</sup> code up to 30,000 atoms can be simulated. Although the stability of the boundary cannot be directly calculated due to the size of the system, an estimate thermal stability can be made along with the boundary activation energy. Due to the computational resources required for the investigation of this heterogeneous interface, no defective phases will be taken into consideration.

### 6.2.1 (111) SrTiO<sub>3</sub> || (111) CeO<sub>2</sub> Interface Dynamics

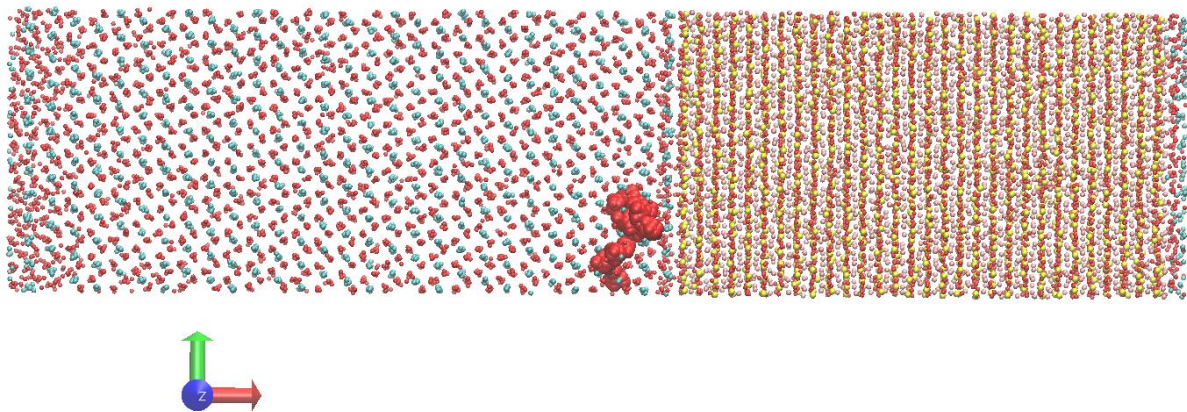


**Figure 6.2a** – Annealed structure of the (111) SrTiO<sub>3</sub> || (111) CeO<sub>2</sub> interface with corresponding diffusion trajectory of a typical single oxygen ion (2800 K).

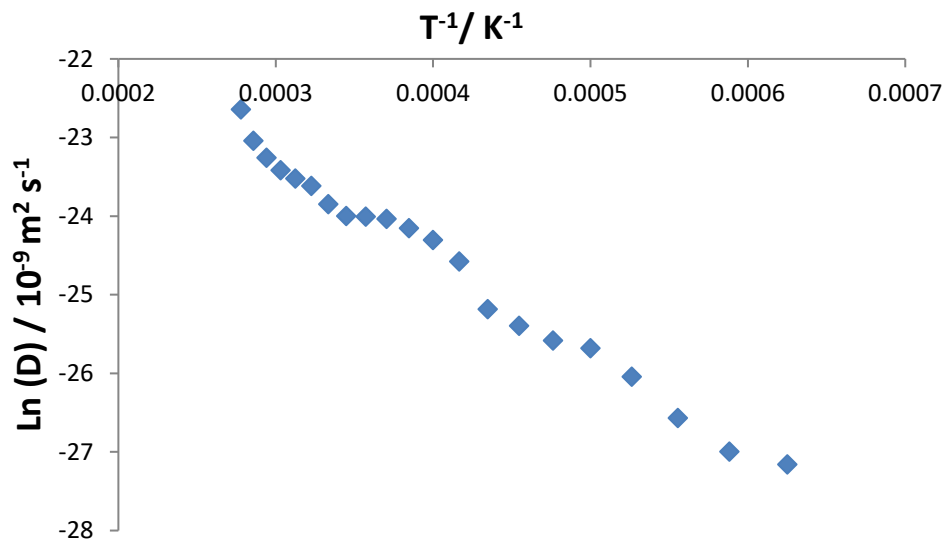


**Figure 6.2b** – Natural log of total diffusion vs reciprocal temperature of the (111) SrTiO<sub>3</sub> || (111) CeO<sub>2</sub> interface.

Boundary	$E_a$ / eV	$D_0$ / $10^{-9} \text{ m}^2 \text{ s}^{-1}$
(111) SrTiO <sub>3</sub>    (111) CeO <sub>2</sub>	$1.13 \pm 0.03$	$4.24 \pm 0.71$

**Table 6.2** –Activation energy and  $D_0$  value obtained for the (111) STO || (111) CeO<sub>2</sub> boundary.

Figure 6.2a represents the structure of the annealed stoichiometric (111) SrTiO<sub>3</sub> || (111) CeO<sub>2</sub> boundary with the corresponding typical oxygen diffusion trajectory. A similar thermal stability was observed when compared to the (100) SrTiO<sub>3</sub> || (100) CeO<sub>2</sub> boundary. The activation energy is marginally higher than the value reported for the stoichiometric (100) SrTiO<sub>3</sub> || (100) CeO<sub>2</sub> boundary. However, the  $D_0$  value is much lower. This suggests that whilst the stoichiometric (111) SrTiO<sub>3</sub> || (111) CeO<sub>2</sub> boundary would enhance oxygen diffusion relative to the bulk, the enhancement would not be as significant as that observed for the stoichiometric (100) SrTiO<sub>3</sub> || (100) CeO<sub>2</sub> boundary and further the two defective phases discussed in section 6.1. The activation energy for the (111) SrTiO<sub>3</sub> || (111) CeO<sub>2</sub> boundary was also lower than the values obtained for the equivalent homogenous grain boundaries, namely the  $\Sigma 3$  (111) boundary for both ceria and STO. However, again, the respective  $D_0$  values were significantly higher. Therefore, when considering the activation energies alone, the (111) SrTiO<sub>3</sub> || (111) CeO<sub>2</sub> boundary enhances oxygen diffusion when compared to the bulk and the respective homogenous grain boundaries. However, due to the discrepancy with the  $D_0$  values, as previously discussed, further simulations would be required, in particular those which separate diffusion parallel to the boundary and perpendicular to the boundary. This would give a better insight into how the (111) SrTiO<sub>3</sub> || (111) CeO<sub>2</sub> boundary influences oxygen transport. Future work would also include the incorporation of defects into either the STO or ceria phase, such as lanthanum or gadolinium respectively, where such defects could enhance and improve fuel cell performance. In order to investigate this, more robust codes could be considered such as those that are able to cope with larger number of atoms such as DL\_POLY\_4<sup>(223)</sup>.

## 6.3 Chapter Summary

With respect to the workflow used for the homogenous grain boundaries, a modified procedure was used within this chapter. Lattice vectors of specific surfaces were chosen in order to achieve a minimum energy strain match which thereby generated a precursor heterogenous boundary used in MD simulations to investigate transport at the grain boundary.

Two heterogeneous grain boundary systems of ceria and STO have been investigated using EM and MD techniques to deduce the structure, stability, diffusion and interfacial influence in the transport of oxygen. Initially, the importance of selecting the lowest energy candidate surface combined with the larger surface area phase as the substrate was found to be of importance when obtaining a boundary with low strain energy. The structure of the (100) STO || (100) CeO<sub>2</sub> boundary was found to be in good agreement with other computational research, specifically DFT methods<sup>(57)</sup>. Gd<sup>3+</sup> substitutions were found to improve the activation energy of oxygen by around 0.3 eV where a slight favourability tended towards to the planar incorporation of defects as opposed to random insertion. The (111) SrTiO<sub>3</sub> || (111) CeO<sub>2</sub> interface proved to be a more complex example yet provided further insight into the approach, generation and analysis of heterogeneous boundaries. The diffusion data presented for both heterogenous grain boundaries showed reduced activation energies when compared to the bulk and homogenous grain boundaries in the previous chapters. This alone would suggest that the presence of heterogenous grain boundaries result in some enhancement with regards to oxygen transport. However, due to the significantly higher  $D_0$  values reported for the homogenous grain boundaries, further simulations would be required to confirm the extent of the enhancement. By using more rigorous and robust codes, there is potential to further investigate the role of the boundary in oxygen transport and whether there is any further correlation between boundary strain, diffusion and the diffusion of defective regions which would require longer simulations (>10 ns) to further investigate. Furthermore, by isolating the x, y and z components of diffusion, this could be used to assess diffusion parallel to the boundary and perpendicular to the boundary. This would provide further quantitative evidence to show whether the presence of heterogenous grain boundaries enhance or suppress oxygen transport.

## 7 Lithium Lanthanum Titanate Oxide (LLTO)

With the recent advances in lithium battery materials as a result of an increasing energy demand, there is recognition that solid-state electrolytes have the potential of being more useful than previously used liquid electrolytes due to their relative stability and safety<sup>(224-226)</sup>. Liquid electrolytes such as  $\text{LiPF}_6$  dissolved in organic carbonates such as ethylene carbonate have previously been favoured due to their high energy densities and high ionic conductivities<sup>(64)</sup>. However, liquid electrolytes often exhibit poor chemical stability and safety due to the formation of a solid electrolyte interface (SEI) interface layer at the lithium metal anode, which has been observed to lead to significant and irreversible capacity loss when discharging<sup>(72)</sup>.

One promising candidate solid electrolyte material is lithium lanthanum titanate (LLTO) which adopts a perovskite ( $\text{ABO}_3$ ) structure,  $\text{Li}_{3x}\text{La}_{(2/3-x)}\square_{(1/3-2x)}\text{TiO}_3$ <sup>(227-229)</sup>. Early work found LLTO to have high bulk lithium ion conductivity compared to liquid electrolytes,  $1.0 \times 10^{-3} \text{ S cm}^{-1}$  at room temperature, with an activation energy of 0.4 eV where  $x \approx 0.1$ <sup>(64, 230)</sup>. The results of recent simulation studies suggest that an optimum vacancy concentration exists where  $x = 0.067$  where an activation energy of 0.22 eV was observed from dynamical data and 0.19 eV from static nudged elastic band calculations<sup>(71)</sup>.

Chen *et al.*<sup>(71)</sup> further explored the diffusion mechanism present in bulk LLTO, where it was observed that lithium ions diffuse through bottleneck structures of oxygen ions where an 8-10% expansion of the local structure was observed when a lithium ion passes through. The diffusion mechanism in bulk LLTO has also been shown to be influenced by temperature<sup>(94)</sup>, through impedance measurements between 298 K-448 K. The results identified two activation energies where temperatures below 378 K result in an activation energy of 0.37 eV. Whereas at temperatures greater than 398 K a higher activation energy of 0.47 eV was observed. The two distinct activation energies were attributed to two diffusion mechanisms where the low temperature example is considered to be simple lithium diffusion as a result of the thermal energy barrier for diffusion being exceeded. In the case of the higher temperatures, ionic redistribution was suggested to have occurred, resulting in the tilting of the  $\text{TiO}_6$  octahedra, where this tilting was proposed to facilitate the lithium diffusion mechanism at higher temperature and therefore arises an increased activation energy<sup>(93)</sup>.

Gao *et al.*<sup>(67)</sup> characterised the local structure of bulk LLTO by probing with scanning transmission electron microscopy (STEM) combined with energy electron loss spectroscopy (EELS). This structural probing detected clusters of A site vacancies present in areas where La concentration was low where

these clusters were considered to be associated with the formation of oxygen vacancies, clustering of Li ions and the tilting and distortion of the  $\text{TiO}_6$  octahedra<sup>(231, 232)</sup>. This tilting phenomenon was further found to be significant in affecting the dimension of diffusion in bulk LLTO where a high concentration of Li ions is present. In this circumstance, the space group of the structure was found to be better described as  $P4/nbm$  opposed to  $P4/mmm$  in other cubic perovskites where octahedral tilting is not observed. Two phases of LLTO were investigated, a low concentration sample ( $\text{La}_{0.62}\text{Li}_{0.16}\text{TiO}_3$ ) and a high concentration sample ( $\text{La}_{0.56}\text{Li}_{0.33}\text{TiO}_3$ ) where two mechanisms of diffusion were observed. In the case of the low concentration sample, diffusion was found to be two dimensional and thereby only occurring in layers where A site vacancies were present. In contrast, in the high concentration sample three-dimensional diffusion was observed. This was attributed to the absence of La ions which allowed Li ions to diffuse through layers which were fully occupied by La ions in the low concentration sample. First-principles calculations were used by Qian *et al.*<sup>(63)</sup> to investigate the lithium diffusion pathway and activation barrier for two phases of LLTO; a low concentration phase ( $\text{Li}_{0.125}\text{La}_{0.625}\text{TiO}_3$ ) and a high concentration phase ( $\text{Li}_{0.35}\text{La}_{0.55}\text{TiO}_3$ ). In the case of both phases, initially, the A-sites were occupied by Li and La ions and the B-sites were occupied by Ti ions. The results from the low concentration phase showed that upon relaxation, whilst the La and Ti ions still occupied the A and B sites respectively, the Li ions are found to be primarily located at “equilibrium sites”. As Li ions are coordinated by 12 oxygen ions, they can be described as square planar in each direction with respect to the central Li. These sites are located close to the centre of the vertical oxygen square planar window and diffusion was observed to occur via a curved pathway which avoided the A-sites. The results were found to be consistent with those of Catti<sup>(70, 233, 234)</sup>, however lower energies were obtained for the movement across equilibrium sites. The results were similar for the high concentration phase with regards to the positioning of Li ions upon relaxation and the curved pathways of diffusion. However, the Li diffuse to avoid both the empty A-sites as well as three other Li ions in neighbouring sites, thereby the minimum energy site path was generally higher from site to site for the high concentration phase.



## 7.1 Overview & Simulations of Bulk Phases of LLTO

Two different compositions of LLTO will be initially investigated in this research. Firstly, experimental research to date has investigated the “layered” structure of LLTO<sup>(94, 235, 236)</sup> where fully occupied layers of lanthanum and one third occupied layers of lanthanum are present where in the one third occupied layers, lithium ions are present and able to diffuse in two dimensions where due to the layering it was observed that for low temperature simulations (700 K <), minimal lithium ions would be able to diffuse through the lanthanum layers. The second composition of LLTO investigated was the “random” structure where in this circumstance, the ordering of lithium, lanthanum and vacancies were randomised throughout the structure, thereby allowing lithium ions to diffuse in three dimensions. A visual representation of both compositions is shown in figure 7.1a.

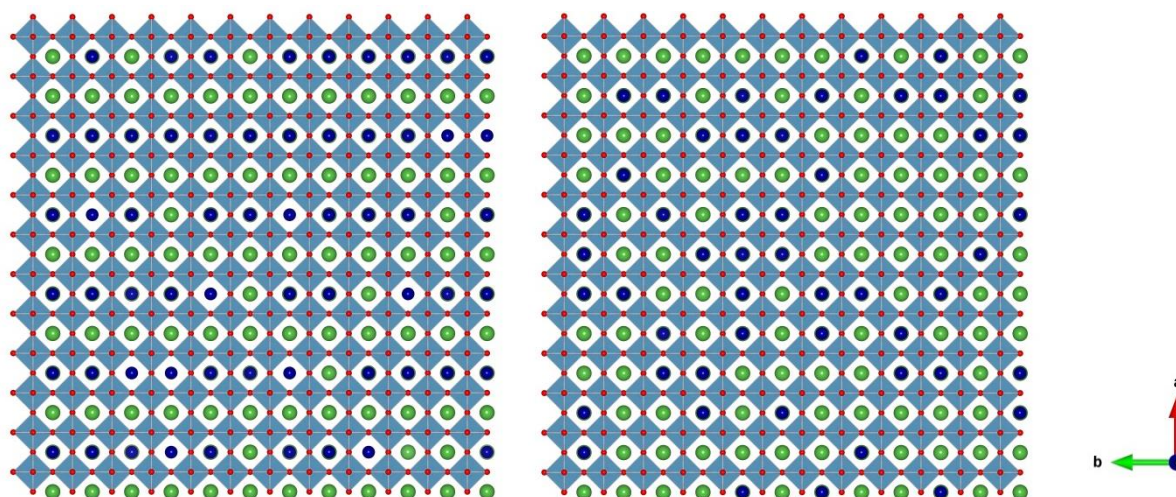


**Figure 7.1a** – (a) “layered” and (b) “random” structures of LLTO, lithium ions are shown in purple, La ions are shown in green, with the  $\text{TiO}_6$  octahedra included showing the clear distinction between layers.

This chapter initially focuses on four compositions of bulk LLTO with varying concentrations of lithium and lanthanum and how the structural variations affect the lithium ion dynamics. The initial structures shown in figure 7.1a were generated using Monte Carlo techniques<sup>(237)</sup>. Throughout this chapter, the “layered” structure will be the initial starting structure for all simulations as this structure is observed experimentally at low temperatures<sup>(235)</sup>. As there is current uncertainty of the role of grain boundaries in LLTO, calculations have been undertaken to identify the most suitable surfaces for grain boundary generation and will provide an insight as to whether grain boundaries found in practical applications would either suppress or enhance the conductivity of lithium. The chosen surfaces are consistent with those used in other computational studies<sup>(238)</sup>. Due to the

success of LLTO as a solid electrolyte, this research will investigate whether similarly high levels of diffusion and low activation energies can be observed in sodium lanthanum titanate (NLTO).

The ordering of Li and La ions in LLTO requires the calculation of the energy of numerous configurations. However, standard MD simulations are unable to overcome kinetic energy barriers. Thus, the configurations used within the MD simulations were generated using MC methods that exchange cation positions in order to sample multiple configurations. The exchange of positions is accepted or rejected by comparing the energy of the final and starting configurations and using the standard Metropolis algorithm<sup>(239)</sup>.

$$P_{o \rightarrow n} = \exp\{-\beta[U_n - U_o]\} \quad (6.1)$$

$U_n$  and  $U_o$  are the energies of the new state ( $n$ ) and original state ( $o$ ) and  $\beta$  is  $1/kT$ . The sampling of configurations remains very poor for systems such as LLTO due to the different size and charge of the Li and La cations and it is necessary to undertake some form of relaxation around the species to facilitate the exchange of positions. In the current simulations positions were exchanged between  $\text{Li}/\text{Na}^{1+}$  and  $\text{La}^{3+}$ ,  $\text{Li}/\text{Na}^{1+}$  and vacancies and  $\text{La}^{3+}$  and vacancies (ghost particles were employed to represent vacancies). After each “exchange” the structure was relaxed using the Fast Inertial Relaxation Engine technique (FIRE) so that both the residual forces on the ions were less than  $0.001 \text{ eV}/\text{\AA}$  and the energy had converged to less  $1.0 \times 10^{-5} \text{ eV}$ <sup>(240)</sup>. The internal energy and structural data were monitored over a period of 80,000 cycles, prior to which an equilibration period of 50,000 cycles was undertaken. The final configurations from these MC simulations were converted to a format suitable for DL\_POLY and subsequent MD calculations were performed to determine the Li ion diffusion coefficients as shown section 2.5.3.

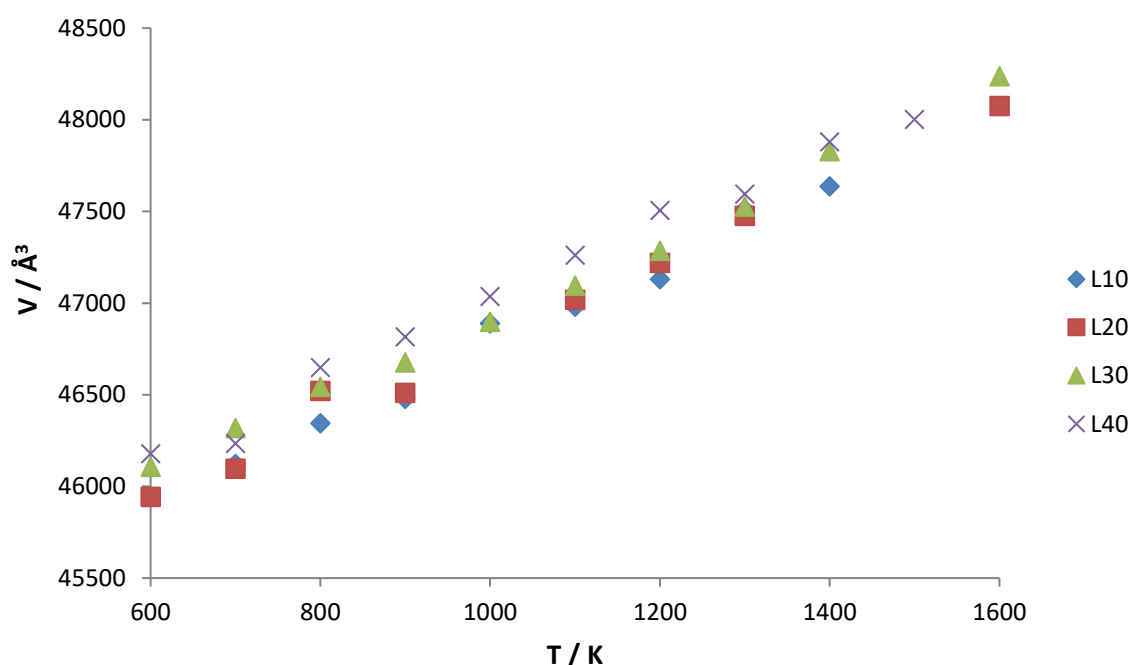
Phase	Total Atoms	x	Composition
L10	3820	0.154	$\text{Li}_{0.46}\text{La}_{0.51}\text{TiO}_3$
L20	3800	0.140	$\text{Li}_{0.42}\text{La}_{0.53}\text{TiO}_3$
L30	3780	0.128	$\text{Li}_{0.38}\text{La}_{0.54}\text{TiO}_3$
L40	3760	0.115	$\text{Li}_{0.35}\text{La}_{0.55}\text{TiO}_3$

**Table 7.1a** – Simulated phases of LLTO with varying lithium/lanthanum composition where LX is defined by the formula  $\text{Li}_{3x}\text{La}_{2/3-x}\text{TiO}_3$ .



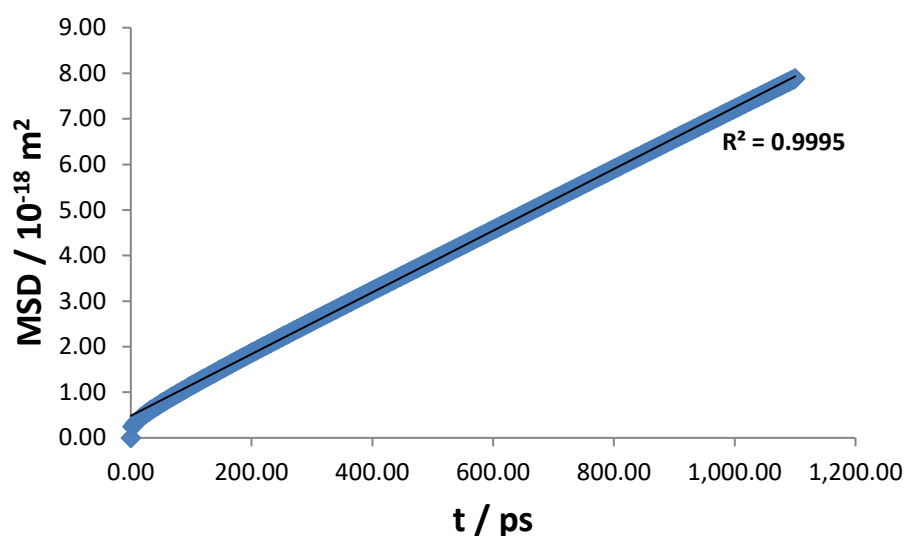
	L10	L20	L30	L40
$a_{\text{initial}} / \text{\AA}$	30.918	30.882	30.897	30.922
$a_{\text{final}} / \text{\AA}$	31.529	31.719	31.711	31.487
$b_{\text{initial}} / \text{\AA}$	30.950	30.925	30.847	30.948
$b_{\text{final}} / \text{\AA}$	31.518	31.703	31.792	31.459
$c_{\text{initial}} / \text{\AA}$	48.199	48.106	48.378	48.255
$c_{\text{final}} / \text{\AA}$	47.936	47.808	47.847	48.459
$V_{\text{initial}} / \text{\AA}^3$	46123.364	45943.036	46107.259	46178.631
$V_{\text{final}} / \text{\AA}^3$	47635.851	48074.337	48238.049	48000.906

**Table 7.1b** – Structural evolution of lattice parameters and volume for phases of LLTO where a 4x4x2 supercell was constructed from the calculated parameters presented in chapter 3.



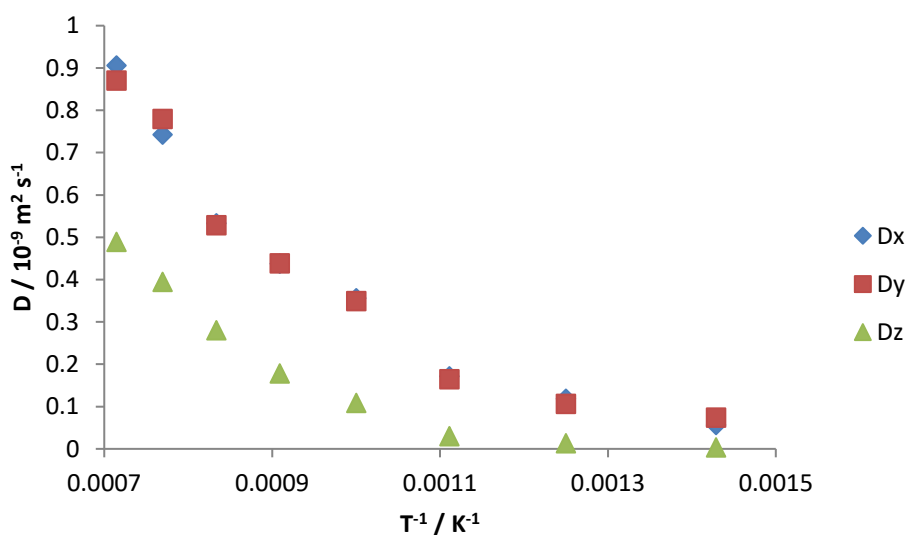
**Figure 7.1b** – Evolution of volume of LLTO phases with increasing temperature.

Table 7.1b and figure 7.1b show the evolution of the structure of each phase of LLTO with increasing temperature. For L10, L20 and L30 phases an increase is seen for the  $a$  parameter,  $b$  parameter and volume with increasing temperature; however, a decrease in  $c$  parameter is observed. A notable difference is observed for the L40 phase, where in this case all three lattice parameters increase with increasing temperature. A further contributing factor to the increase in volume is the substitution of lithium (0.7 Å) by lanthanum ions (1.302 Å) due to the increase in ionic size. As the structural components of each of the four phases have been investigated, the dynamics of lithium diffusion will further be discussed.



**Figure 7.1c** – Evolution of MSD of layered bulk LLTO over 1.1 ns at 1500 K where the gradient represents the three-dimensional diffusion coefficient ( $D_{xyz}$ ).

The trajectories obtained from the MD simulations were used to calculate the MSDs (section 2.5.3) with a typical example displayed in figure 7.1c. The MSDs were subsequently used to calculate the diffusion coefficients. From the Arrhenius behaviour of the jump-frequency one can extract a vacancy migration energy or average activation energy for Li migration as shown in table 7.1c.



**Figure 7.1d** – Diffusion coefficients as a function of reciprocal temperature for the L10 phase of LLTO.

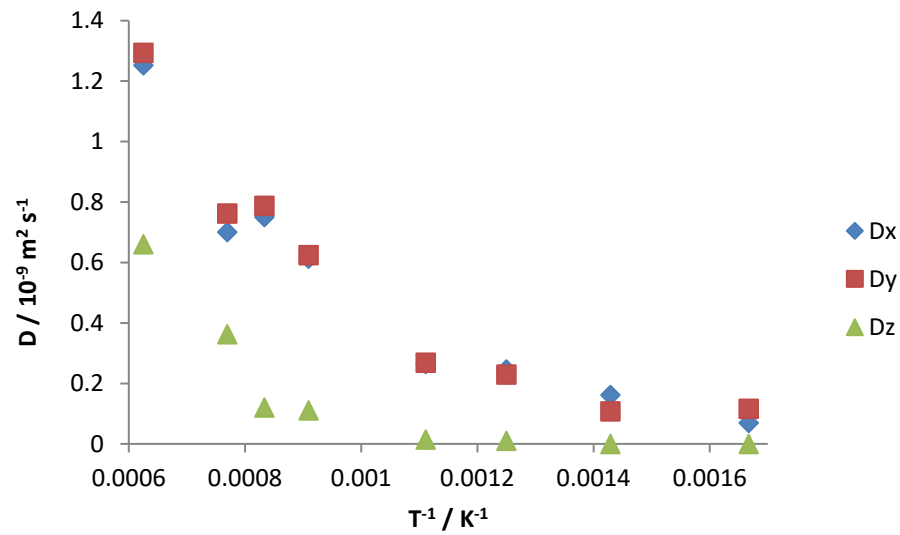


**Figure 7.1e** – Diffusion coefficients as a function of reciprocal temperature for the L20 phase of LLTO.

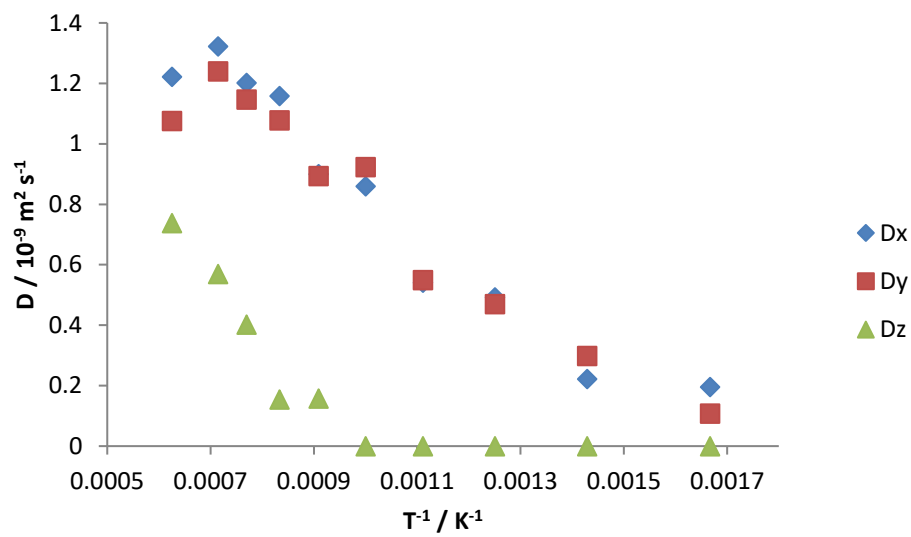


**Figure 7.1f** – Diffusion coefficients as a function of reciprocal temperature for the L30 phase of LLTO.

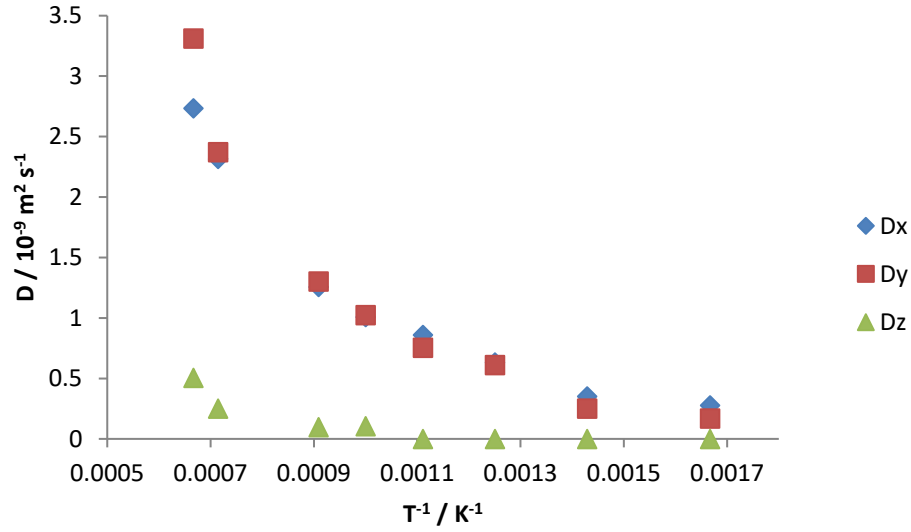


**Figure 7.1g** – Diffusion coefficients as a function of reciprocal temperature for the L40 phase of LLTO.

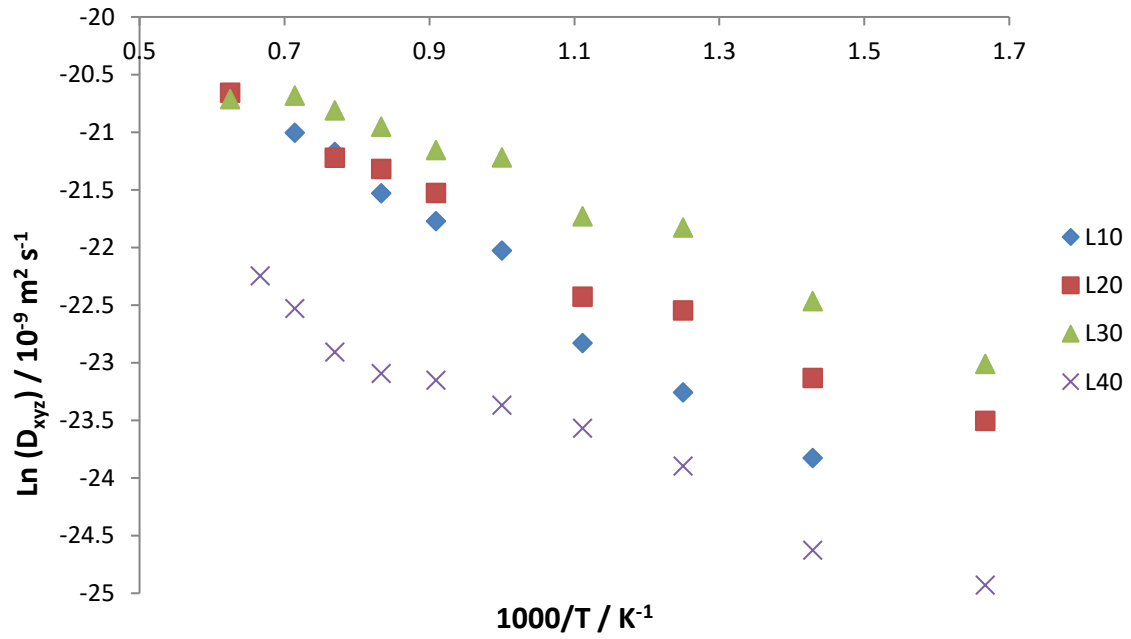


**Figure 7.1h** – Natural log of diffusion coefficient ( $D_{xyz}$ ) vs reciprocal temperature for phases of LLTO.

Phase	$E_A / \text{eV}$	$D_0 / 10^{-9} \text{ m}^2 \text{ s}^{-1}$
L10	$0.352 \pm 0.02$	$14.20 \pm 2.60$
L20	$0.240 \pm 0.01$	$5.41 \pm 1.02$
L30	$0.201 \pm 0.01$	$5.37 \pm 0.69$
L40	$0.261 \pm 0.01$	$0.95 \pm 0.16$

**Table 7.1c** – Calculated activation energies ( $E_A$ ) and  $D_0$  value with their respective uncertainties for LLTO phases.

With respect to the activation energies and  $D_0$  shown in table 7.1c, each consider a single mechanism of lithium diffusion, thereby correlating with a single activation energy and  $D_0$  value. The data shown in figures 7.1d-g show a change in the mechanism of diffusion when exceeding temperatures of 1000 K where diffusion in the z trajectory is not observed at temperatures below 1000 K.

As shown in figure 7.1h and table 7.1c, an increase in the overall diffusion and thereby a decrease in activation energy was observed for the L10-L30 phases. In each phase two-dimensional diffusion occurs up to 1000 K where exceeding this results in a three-dimensional diffusion mechanism as supported by the data shown in figures 7.1e-g. In each of these phases, as shown in table 7.1b, this correlates with the increase in  $a$  and  $b$  and decrease in  $c$  lattice parameters. From the initial phases the L10 phase has the largest initial volume. Despite this, the final volume of the L10 phase is smaller than both the L20 and L30 phases, thereby experiencing the smallest expansion which also correlates with the highest activation energy. As lithium content decreases in these three phases this compositional change accounts for the activation energy decrease, suggesting an optimal  $x$  value of 0.128 which is comparable to the  $x$  value obtained by Chen *et al.*<sup>(71)</sup>. Regarding the L40 phase as previously shown in table 7.1b, an increase in all three lattice parameters was observed, however the overall expansion is significantly smaller than the L30 phase and comparable to the L20 phase. The  $D_0$  values show a different relationship to the activation energy where decreasing lithium content results in decreased lithium diffusion. However, there are larger errors associated with the  $D_0$  when compared to the much smaller errors observed for the activation energies. This suggests that the activation energy data is more reliable.

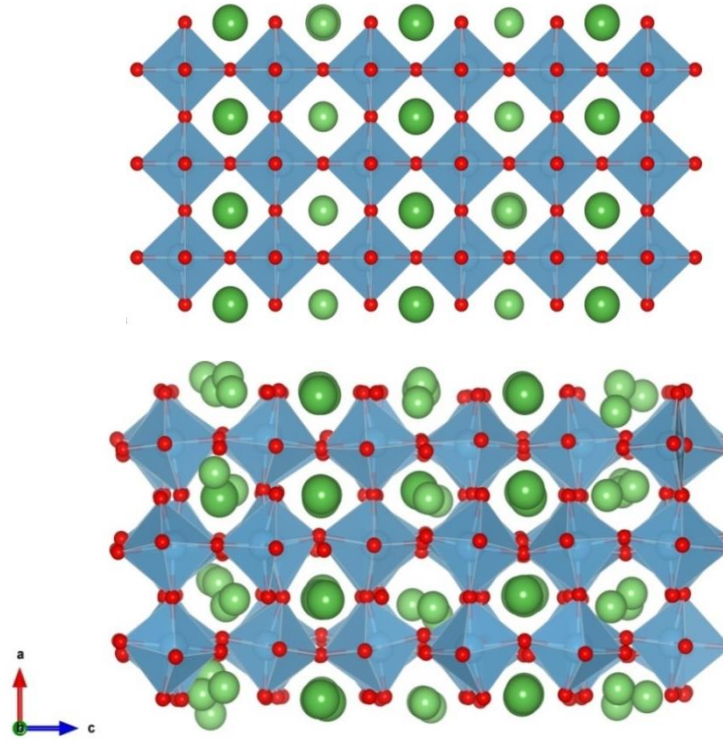


**Figure 7.1i** – (a) L10 initial structure, showing alignment for  $\text{TiO}_6$  octahedra. (b) L10 simulated structure (1400 K) showing tilting of  $\text{TiO}_6$  octahedra with increasing temperature.

One structural phenomenon that has been observed experimentally for LLTO is the tilting of the  $\text{TiO}_6$  octahedra<sup>(72, 93, 236, 241-244)</sup> which is shown in figure 7.1i. (a) is calculated from static lattice simulations where the temperature is 0 K, therefore the octahedra are aligned. When applying temperature through MD, the tilting of the  $\text{TiO}_6$  is shown in (b), where this structural distortion is present. It has been proposed that the octahedral tilting is responsible for lattice expansion of LLTO, which facilitates the bottleneck lithium diffusion mechanism, which was proposed by Chen *et al.*<sup>(71)</sup>. The mechanism for this process was discussed in chapter 1 where figure 1.11 highlights how this mechanism functions.

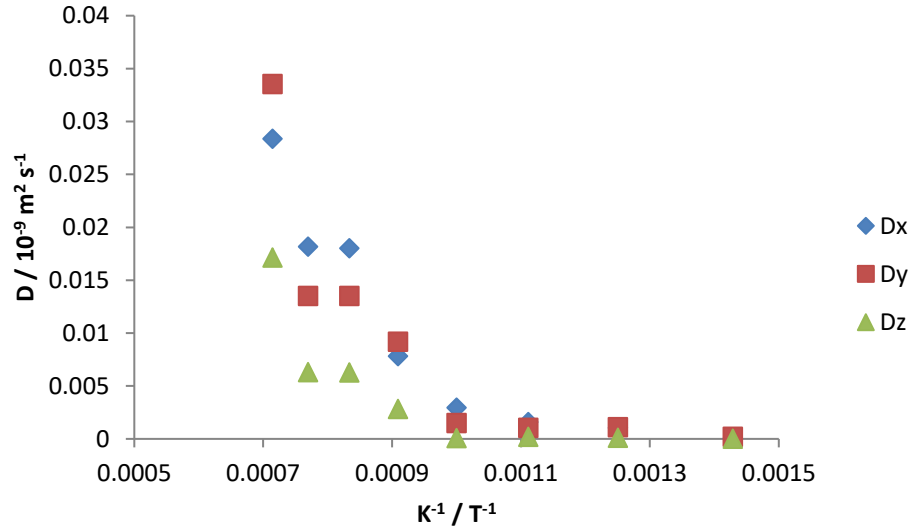


**Figure 7.1j** – Diffusion coefficients as a function of reciprocal temperature for the L10 phase of LLTO with fixed ion lattice for Ti, La and O ions.

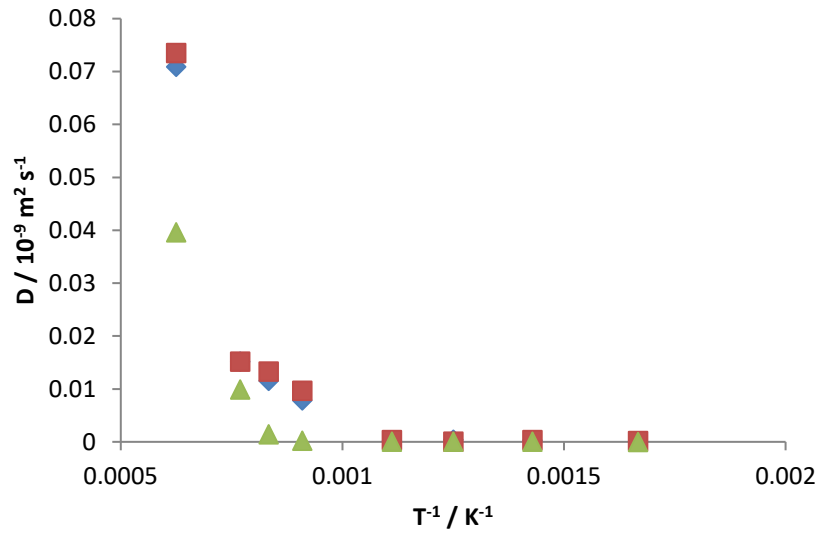


**Figure 7.1k** – Diffusion coefficients as a function of reciprocal temperature for the L20 phase of LLTO with fixed ion lattice for Ti, La and O ions.

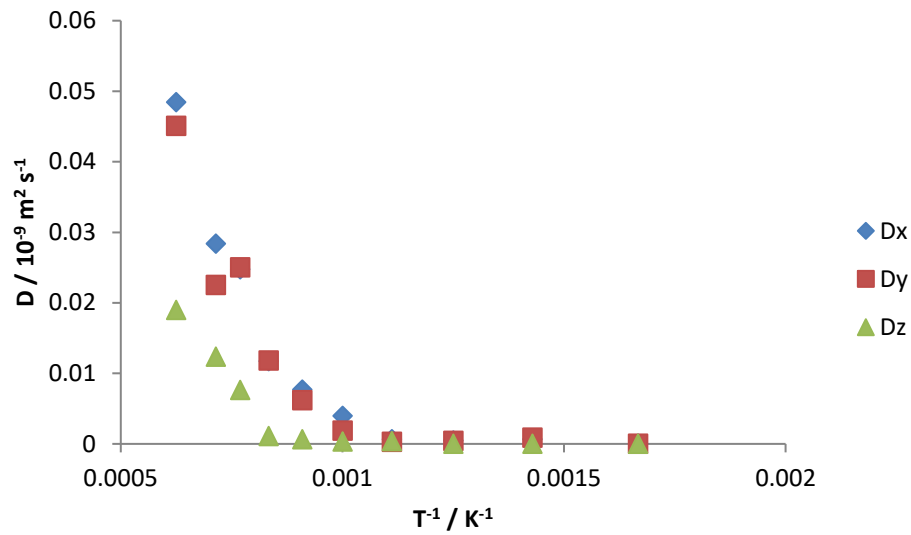


**Figure 7.1l** – Diffusion coefficients as a function of reciprocal temperature for the L30 phase of LLTO with fixed ion lattice for Ti, La and O ions.

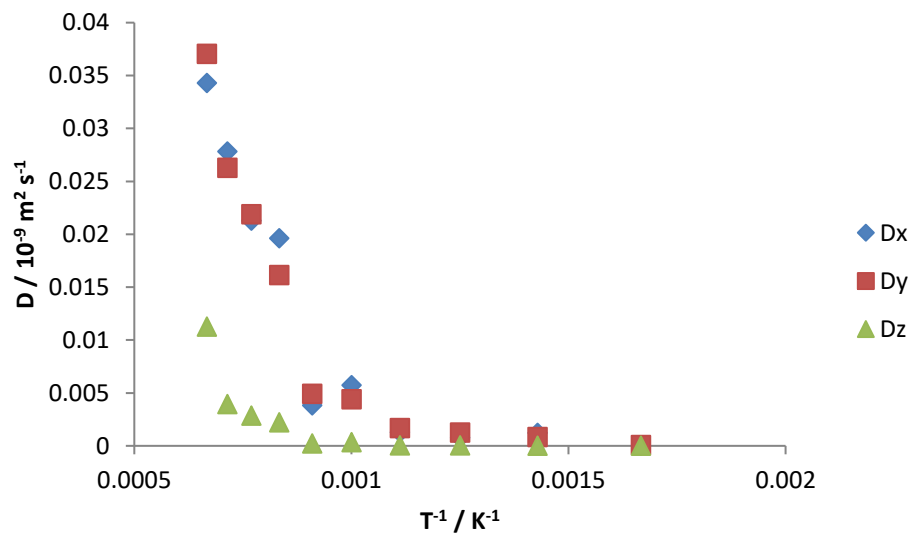


**Figure 7.1m** – Diffusion coefficients as a function of reciprocal temperature for the L40 phase of LLTO with fixed ion lattice for Ti, La and O ions.



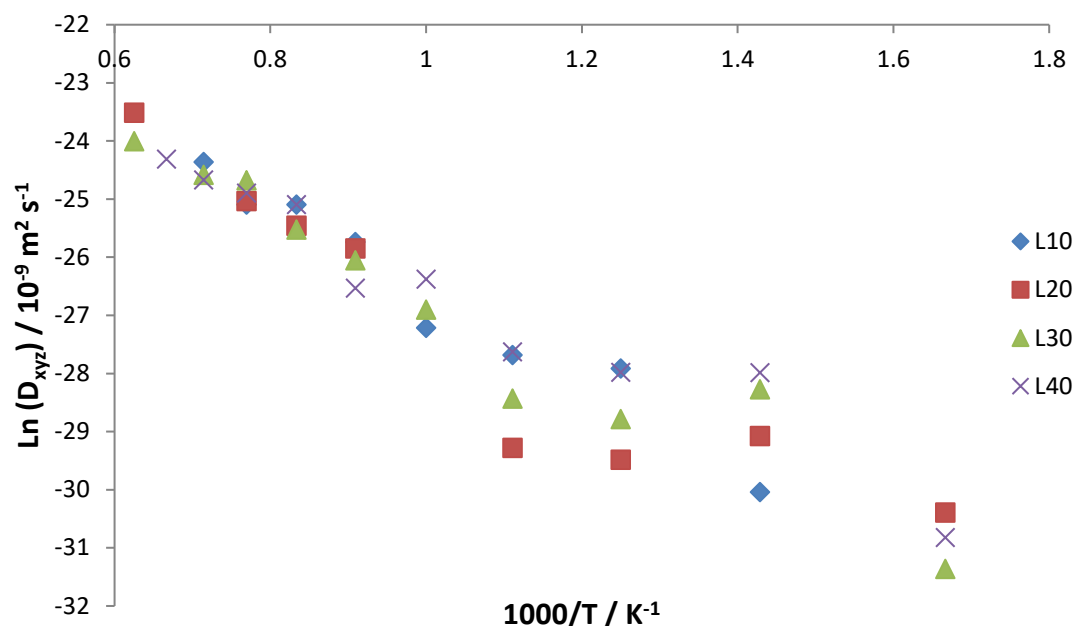


**Figure 7.1n** - Natural log of diffusion coefficient ( $D_{xyz}$ ) vs reciprocal temperature for phases of LLTO with fixed ion lattice for Ti, La and O ions.

Phase	$E_A$ / eV	$D_0$ / $10^{-9} \text{ m}^2 \text{ s}^{-1}$
L10	$0.65 \pm 0.05$	$5.14 \pm 3.28$
L20	$0.58 \pm 0.09$	$2.02 \pm 2.39$
L30	$0.58 \pm 0.05$	$2.27 \pm 1.54$
L40	$0.51 \pm 0.04$	$1.33 \pm 0.74$

**Table 7.1d** – Calculated activation energies ( $E_A$ ) and  $D_0$  values with their respective uncertainties for fixed ion lattice phases of LLTO.

As the  $\text{TiO}_6$  tilting phenomenon has been attributed to facilitating Li diffusion, in order to investigate the extent quantitatively; figures 7.1j-n and table 7.1d show the diffusion coefficients,  $D_0$  values and activation energies for each phase. In each case the La, Ti and O sublattices were held in their fixed position from the initial Monte Carlo simulations, compared to figure 7.1h where each of these sublattices were able to fully relax. A significant decrease in overall diffusion occurs in each phase where differences were observed of up to two orders of magnitude in diffusion. The fixed ion phases show a similar trend with regards to the activation energies when compared to their free ion counterparts. As Li concentration is decreased, activation energy decreased. However, unlike the free ion phases, the L40 phase had the lowest activation energy. The data shown in figures 7.1j-m shows that similar to the fixed ion phases, diffusion is primarily two dimensional below 1000 K and becomes three dimensional when exceeding 1000 K. The  $D_0$  values further suggest decreased

diffusion in the fixed ion phases, as in the L10, L20 and L30 phases, a significantly lower value of  $D_0$  was observed. The L40 phase  $D_0$  value is of a similar magnitude to the free ion phase. However, due to the larger errors associated with each of the  $D_0$  values, it is unclear whether the actual value is higher or lower than the free ion phase. The fixed ion phases resulted in activation energies approximately double the magnitude of their free ion counterparts. This suggests the importance of local structure and how the tilting of the  $\text{TiO}_6$  octahedra could be influential in enhancing Li diffusion.

As the dynamic data of LLTO has shown, in both the free and fixed ion phases, diffusion occurs predominantly within the lithium layers at low temperature. With increasing temperature this results in diffusion between layers, as previously discussed. Figure 7.10 contains visual representations of lithium diffusion at three increasing temperatures with their respective number density plots which were generated using PolyPy<sup>(245)</sup>.

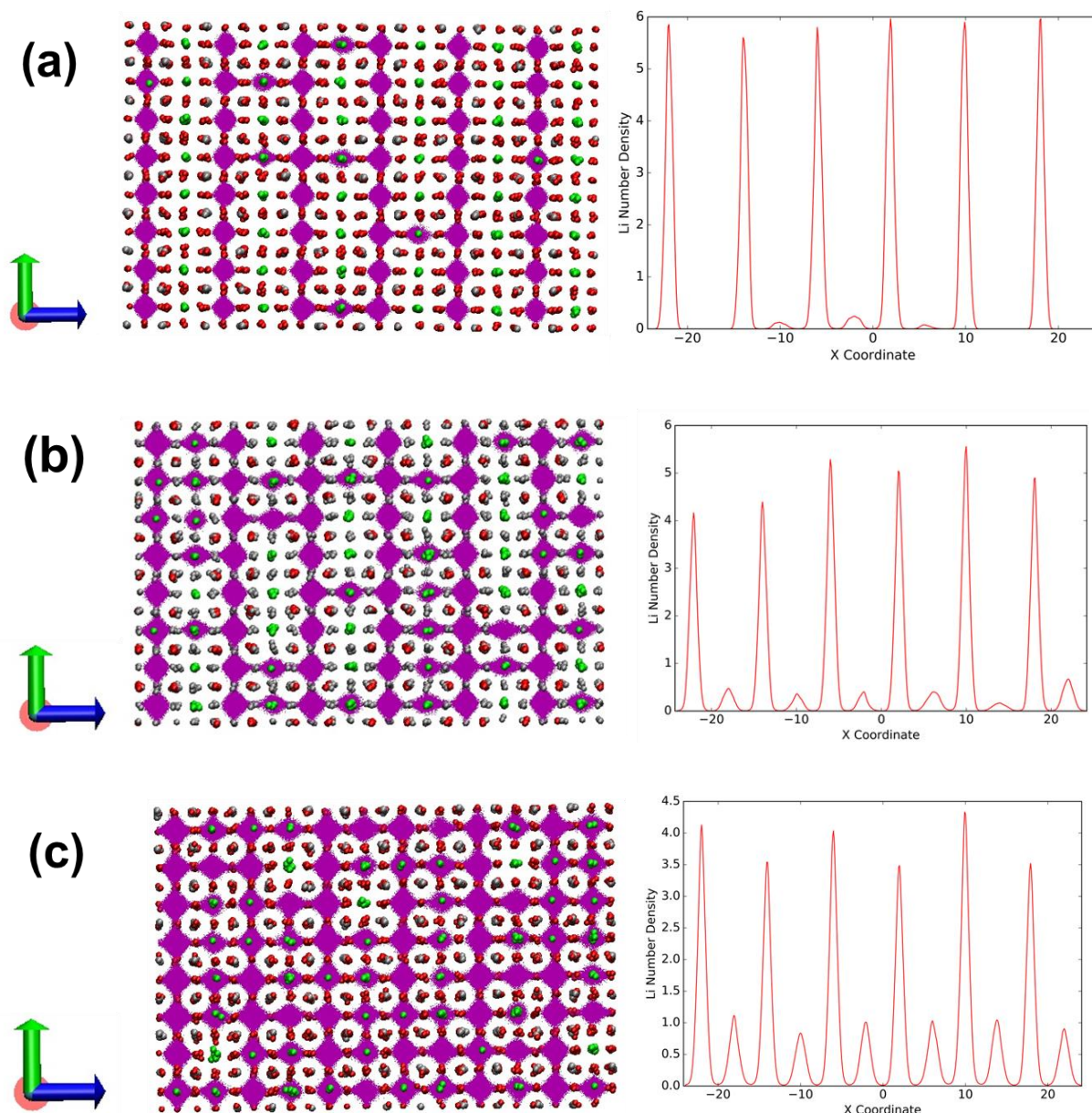


**Figure 7.1o** – VMD<sup>(246)</sup> plot showing the diffusion trajectory of lithium ions (purple) at (a) low temperature, 700 K. (b) Intermediate temperature, 1000 K. (c) High temperature, and 1400 K. Further corresponding density plots are also shown showing the lithium number density in each layer.

For the low temperature example, lithium ions predominantly diffuse in two dimensions within a layer where a small amount of diffusion through the layers is seen. This was found to be more prevalent in the L30 compared to the L10 phase due to the larger number of lithium vacancies, as shown in figure 7.1f. As a result of this the remaining lithium ions have a lower energy diffusion pathway and therefore a higher diffusion coefficient and lower activation energy is observed. As the temperature is increased, as shown in figure 7.1o, a greater proportion of available lithium ions are able to diffuse between layers as a result of the disruption of the titanium and fully occupied

lanthanum layers. This is further supported by the data presented in figures 7.1d-g. From the simulations carried out, this mechanism of diffusion between layers occurs at approximately 1000 K for each of the four phases where there appears to be little discrepancy in the transition from two dimensional to three dimensional with respect to composition. Again, this is supported by the data shown in figures 7.1d-g. When the temperature surpasses 1000 K in each phase, as previously discussed, disruption of the lanthanum and titanium layers occur. As a result of this, lithium ions are not only able to diffuse through layers, as shown in (b), but diffusion is also shown within the layers in figure 7.1o (c). This is further supported by the magnitude of diffusion coefficients where at temperatures lower than 1000 K the z direction coefficient (direction between the layers) is ~10% of the x and y directions (directions of the layers) in the case of all four phases. However, when exceeding 1000 K an average magnitude of the z direction coefficient is ~50% of the x and y values and as high as ~70% in the L20 phase. The Li number density plots show the layered nature of the LLTO structure including the concentration of lithium ions. There is significantly reduced lithium content in the alternating lanthanum layers. As previously discussed, a mechanism of diffusion through these fully occupied layers becomes energetically feasible at higher temperatures.

In each trajectory plot shown in figure 7.1o, the purple regions represent the lithium ion location, the trajectories show that during the simulation ions will predominantly occupy the A-sites where the larger purple spheres are observed. Upon the opening on the bottleneck, lithium ions are able to diffuse through to the adjacent unoccupied A-site through the interstitial sites within the octahedra.

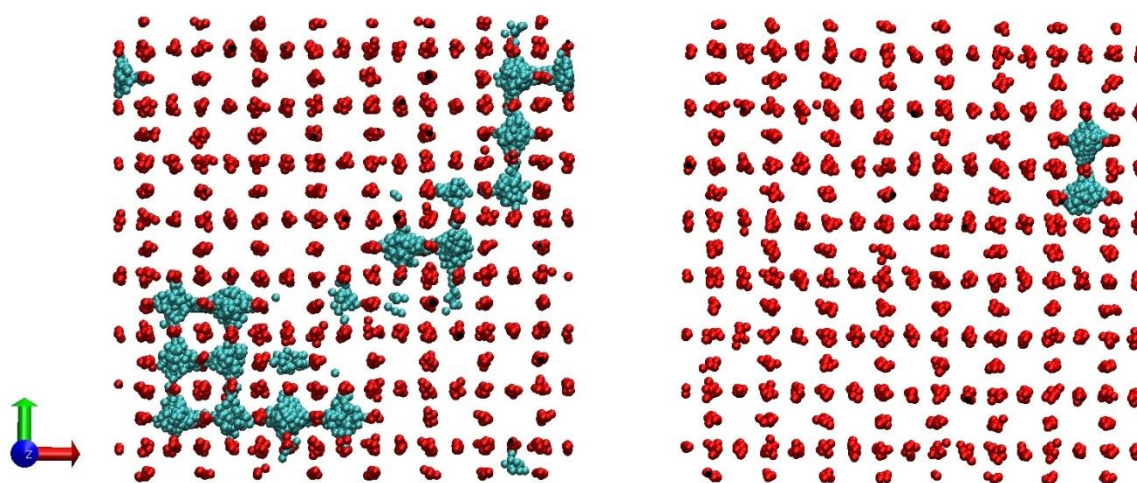


**Figure 7.1p** – (a) Trajectory of single lithium ion (turquoise) in L40 phase at 1600 K, where anionic ( $O^{2-}$ ) and cationic ( $Ti^{4+}$  and  $La^{3+}$ ) sublattices are allowed to relax (b) (a) Trajectory of single lithium ion

*in L40 phase at 1600 K, where anionic ( $O^{2-}$ ) and cationic ( $Ti^{4+}$  and  $La^{3+}$ ) sublattices are held fixed. Both simulations occurred over a 1.0 ns timeframe.*

Figure 7.1p highlights the importance of the previously discussed bottleneck structure proposed by Chen *et al.*<sup>(71)</sup> as within the same timeframe, a much longer diffusion trajectory is observed for the free ion phase. In the case of (b), the sublattice of all non-lithium species were held fixed, and the mobility of lithium is significantly limited over a smaller distance due to the inability of the oxygen sublattice to form the bottleneck structure. The constraints were not applied to the structure shown in (a); therefore, the mobility of lithium was vastly increased, as supported by the activation energy which was roughly half the magnitude of (b). The relative ease of the diffusion of lithium in this structure occurs through the bottleneck of oxygen ions. With comparison to the fixed ion sublattice, the oxygen-oxygen distance was found to be  $\sim 2.55 \text{ \AA}$  when fixed, with an area of  $7.5 \text{ \AA}^2$  when measured using VMD<sup>(246)</sup>. When the bottleneck forms, the oxygen-oxygen distance was found to expand to  $\sim 3.19 \text{ \AA}$  therefore increasing the area to  $\sim 10.18 \text{ \AA}^2$  resulting in an overall local lattice expansion of  $\sim 56\%$ . This further highlights how the local structure, in particular, the opening of the bottleneck has an important role in facilitating lithium diffusion.

## 7.2 Sodium Lanthanum Titanate (NLTO)

In order to expand on the results obtained for LLTO, the same methods were used to investigate the diffusion dynamics of sodium diffusion in NLTO. The models of NLTO used identical layered ionic compositions by substituting all lithium with sodium ions and carrying out the simulations as previously described.

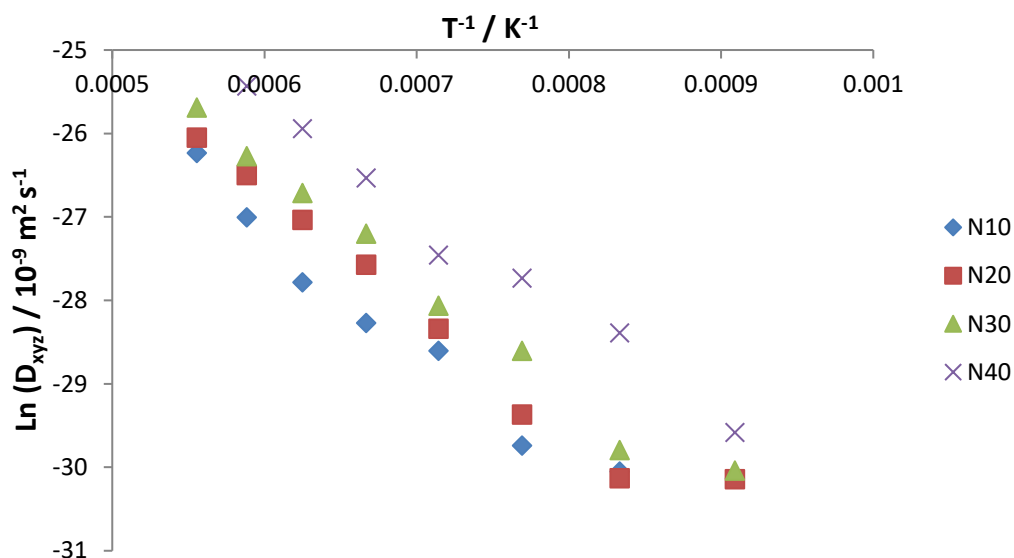


**Figure 7.2** – Natural log of diffusion coefficient ( $D_{xyz}$ ) vs reciprocal temperature for phases of NLTO.

Phase	$E_A$ / eV	$D_0$ / $10^{-9} m^2 s^{-1}$
N10	$0.97 \pm 0.11$	$1.22 \pm 1.17$
N20	$1.10 \pm 0.09$	$5.16 \pm 3.93$
N30	$1.11 \pm 0.06$	$7.88 \pm 4.06$
N40	$1.09 \pm 0.08$	$8.11 \pm 5.49$

**Table 7.2** – Calculated activation energies ( $E_A$ ) and  $D_0$  values for phases of NLTO.

As shown in figure 7.2 and table 7.2, the diffusion of sodium appears much lower than that of the lithium counterparts with respect to the calculated activation energies. The diffusion coefficients and  $D_0$  values were calculated over 1100 K for NLTO as no long range diffusion was observed at temperatures below this. The significantly higher energy barrier of sodium diffusion compared to lithium diffusion could be attributed to the larger ionic size of sodium ions. As a result of this, NLTO appears to be a poorer ionically conductive material when compared to LLTO based on the results of this study and is consistent with other computational research<sup>(256)</sup>.

### 7.3 Grain Boundaries of LLTO

In section 7.1, the structure and dynamics of bulk LLTO were investigated. The study was extended to investigate some of the low Miller indices surfaces and grain boundaries of LLTO, using the L30 phase in generation of surfaces and interfaces. The candidate surfaces were generated using the previously discussed METADISE<sup>(136)</sup> method. The Miller indices of the six grain boundaries were chosen due to the structural similarity to STO. Many of these boundary structures have been structurally characterised for perovskite phases and therefore are likely to be observed experimentally<sup>(238)</sup>. The boundary widths were estimated when the lithium number density reverted to the value observed for the bulk region. The aim of this section was to investigate whether the presence of grain boundaries enhance or suppress the diffusion of lithium and to what extent this occurs.

Boundary	Termination	$\gamma / \text{Jm}^{-2}$	Area / $\text{\AA}^2$	$E_f / \text{Jm}^{-2}$	$E_c / \text{Jm}^{-2}$	$E_A / \text{eV}$	$D_0 / 10^{-9} \text{m}^2 \text{s}^{-1}$
(110)	O	1.91	170.28	1.94	5.68	$0.23 \pm 0.01$	$19.54 \pm 0.88$
(111)	Ti-O	2.07	180.45	0.83	3.30	$0.22 \pm 0.01$	$15.00 \pm 1.40$
(210)	Li-La-O	1.91	269.23	3.44	0.39	$0.21 \pm 0.01$	$12.99 \pm 1.34$
(211)	Li-La-O	1.65	275.78	2.20	1.10	$0.22 \pm 0.01$	$11.94 \pm 1.39$
(310)	O	2.14	380.76	1.80	1.97	$0.21 \pm 0.01$	$11.12 \pm 0.59$
(311)	O	2.16	385.41	2.11	1.56	DNC	DNC

**Table 7.3** – Surface indices, termination, surface energy ( $\gamma$ ), area, formation energy ( $E_f$ ), cleavage energy ( $E_c$ ) activation energy ( $E_A$ ) and  $D_0$  values for six LLTO interfaces. (DNC = Did not converge when simulated using MD).

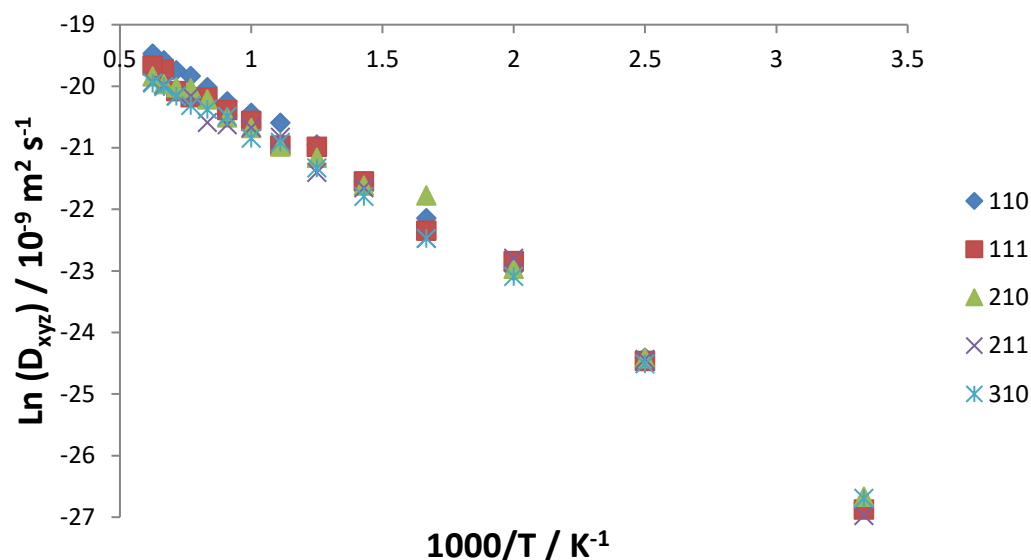


**Figure 7.3a** – Natural log of diffusion coefficient ( $D_{xyz}$ ) vs reciprocal temperature for five LLTO grain boundaries

The results in table 7.3 are a structural and energetic representation of each surface and corresponding boundary. The orientation of the chosen boundaries was of particular importance to achieve alignment in which lithium diffusion would not be completely blocked by boundary orientation. In section 7.1, the data presented showed that at low temperatures, diffusion within the bulk occurred primarily within the lithium layers. As a result of this, the presence of grain boundaries where the lithium layers were unaligned would certainly suppress diffusion, especially at low temperatures. Therefore, boundaries were chosen in which lithium layers were closely aligned. With respect to surface energy, the (211) surface resulted in the lowest free energy where all six surfaces were within a range of  $\sim 0.5 \text{ J m}^{-2}$ . In terms of free surface energies there is no distinctive observable trend between the Miller indices and surface energy. However, the two highest energies obtained were for both of the 3 directive indices, therefore there is a possibility of increasing surface energy with increasing indices value and increasing surface area. The stability of each of the six boundaries is further shown where the (110) and (111) grain boundaries are examples of stable boundaries as in both cases the formation energy is significantly lower than the cleavage energy. This however is not the case for the remaining boundaries as in each case the cleavage energy is greater than the formation energy, particularly in the case of the (210) boundary. The energetics analysis of LLTO surfaces would therefore suggest that the lower Miller index surfaces provide a suitable precursor for generating a stable grain boundary irrespective of the free surface energy. Regarding the MD simulations, despite the differences in stability and structure, the activation energies obtained for each boundary were found to be similar in value. The activation energies obtained for each boundary



were comparable to those seen for the bulk. This implies that the presence of grain boundaries in a polycrystalline phase of LLTO would have little effect on diffusion through the interface. However, the obtained  $D_0$  values are consistently higher in each of the boundary systems when compared to those seen in the bulk. This suggests that higher rates of diffusion were observed because of the presence of the grain boundary and therefore could result in enhanced lithium diffusion. In the case of the (311) boundary, when annealing the structure obtained from the scanning process, energetic convergence could not be achieved due to instability. Due to the energetic instability of this boundary, the dynamics could not be investigated. The potential energy surface for each boundary along with the corresponding structure from the local minima are shown in figure 7.3b.

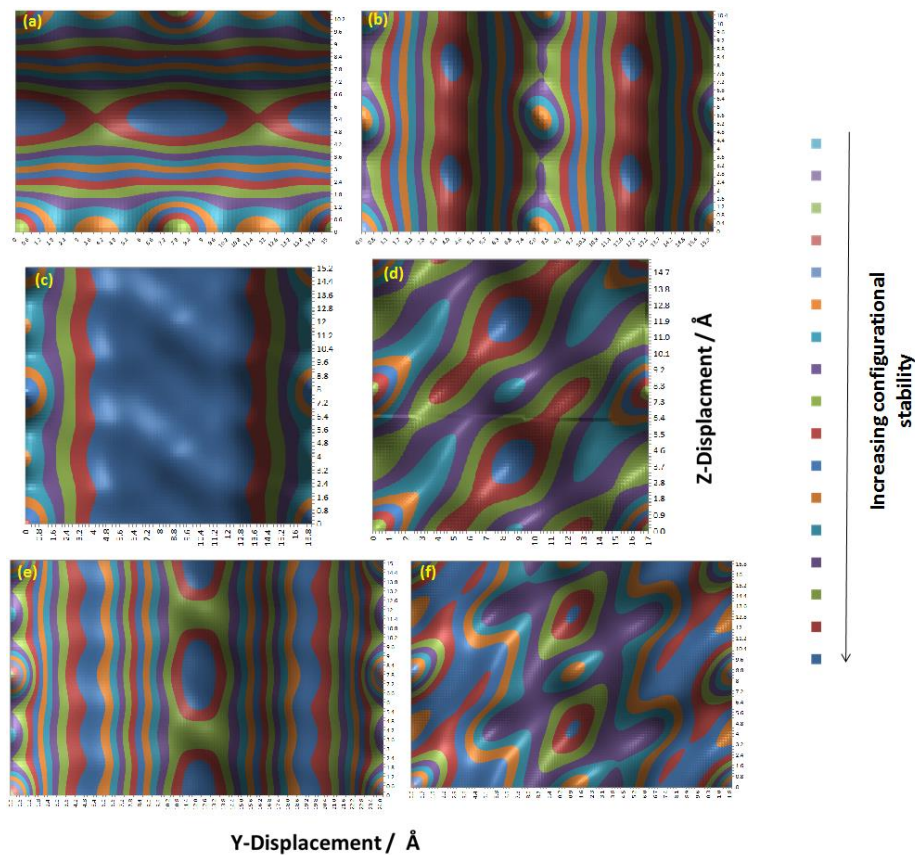


**Figure 7.3b** – Potential energy surfaces (a) 110 (b) 111 (c) 210 (d) 211 (e) 310 (f) 311 of LLTO grain boundaries where the blue regions define the local minima where multiple are seen as shown in the centre of (a) which contains the displacement of the minimum energy structure.

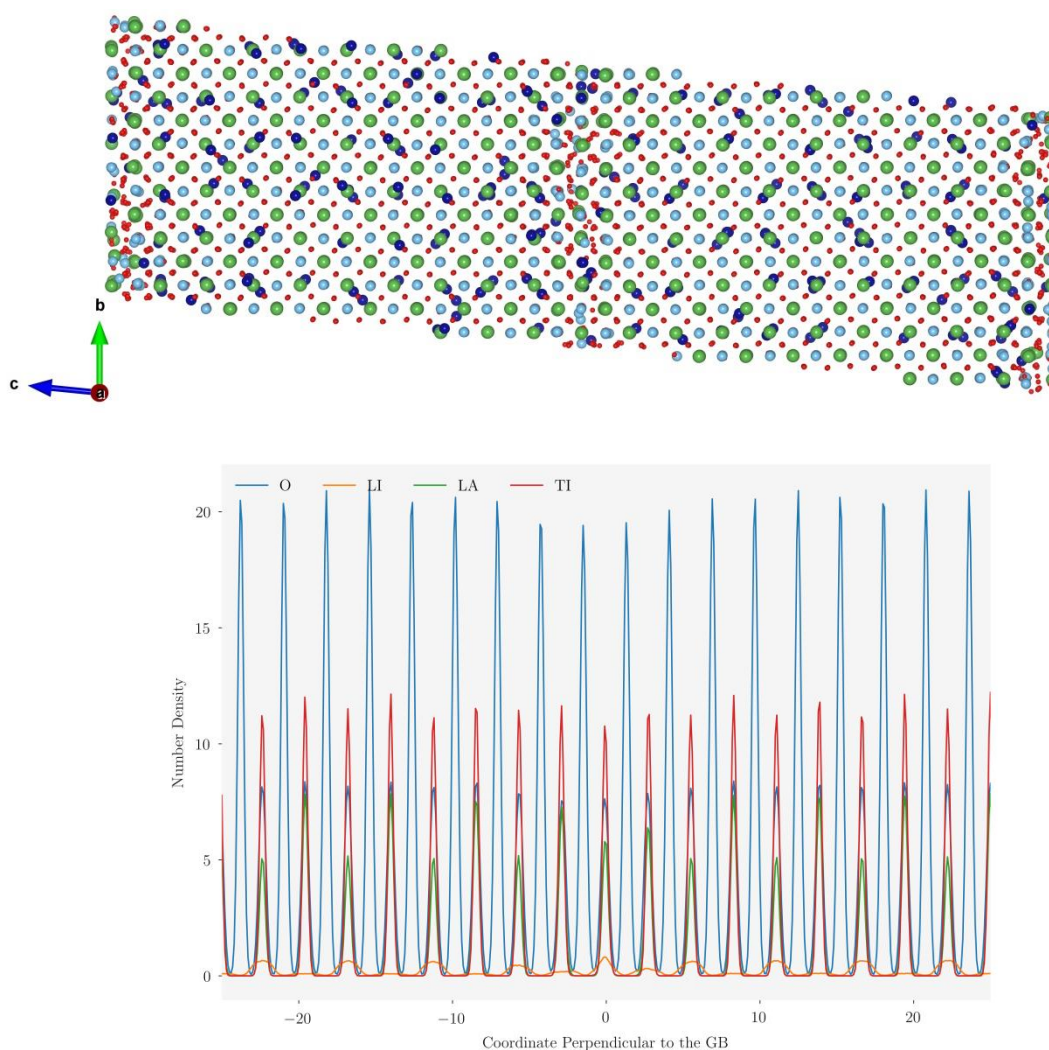


**Figure 7.3c** – Annealed structure and corresponding atom number density profile (1500 K) of the (110) LLTO boundary.

As shown in figure 7.3c, when the (110) LLTO boundary is simulated using MD, the boundary region densities are consistent with those seen in the bulk. The activation energy however is slightly higher (0.03 eV) when compared to the bulk value which could be the result of the slightly lower concentration of lithium at the boundary relative to the bulk concentration. The (110) boundary exhibited the highest  $D_0$  value suggesting that the presence of this boundary could result in enhanced lithium diffusion in a polycrystalline system. Unfortunately, due to the size of the boundary with respect to the number of atoms, the individual x, y and z diffusion coefficients could not be isolated, due to limitations of the code used. In terms of stability, with reference to the values in table 7.3, the (110) boundary was found to be the most energetically favoured.

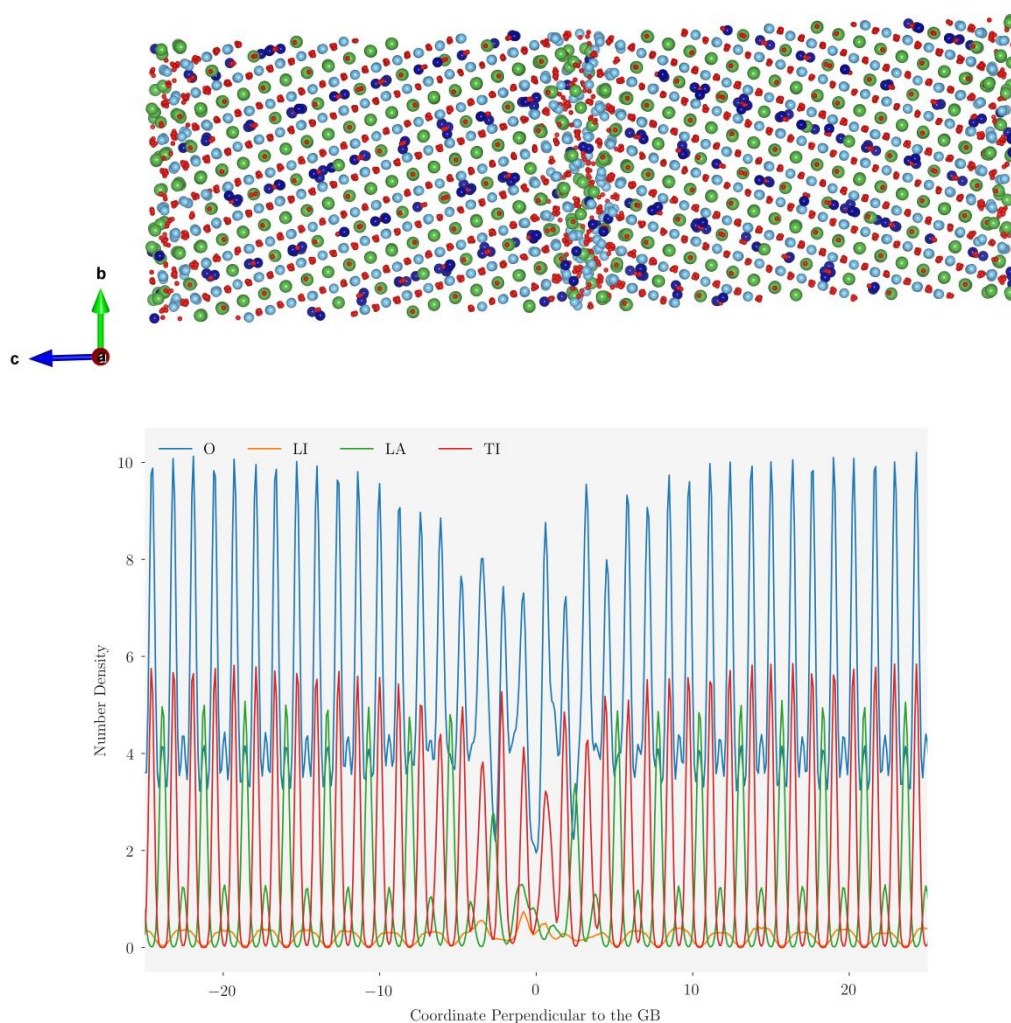


**Figure 7.3d** – Annealed structure and corresponding atom number density profile (1500 K) of the (111) LLTO boundary.

The (111) and three remaining boundaries differ from the (110) boundary in that the structure that is formed deviates from the bulk like structure of the (110) boundary. Similar to the (110) boundary, the (111) boundary was found to be energetically stable with a very low formation energy. As shown in figure 7.3d, a decrease in the number density of lanthanum, oxygen and titanium is seen in the boundary region. The boundary region size of the (111) boundary was approximately 10 Å in diameter and asymmetric in nature with respect to all ions. Again, this boundary has a slightly higher activation energy than the bulk, suggesting that there may be some suppression of lithium diffusion at the boundary. However, the large  $D_0$  value when compared to the bulk would suggest that there is some enhancement of lithium diffusion because of the boundary.



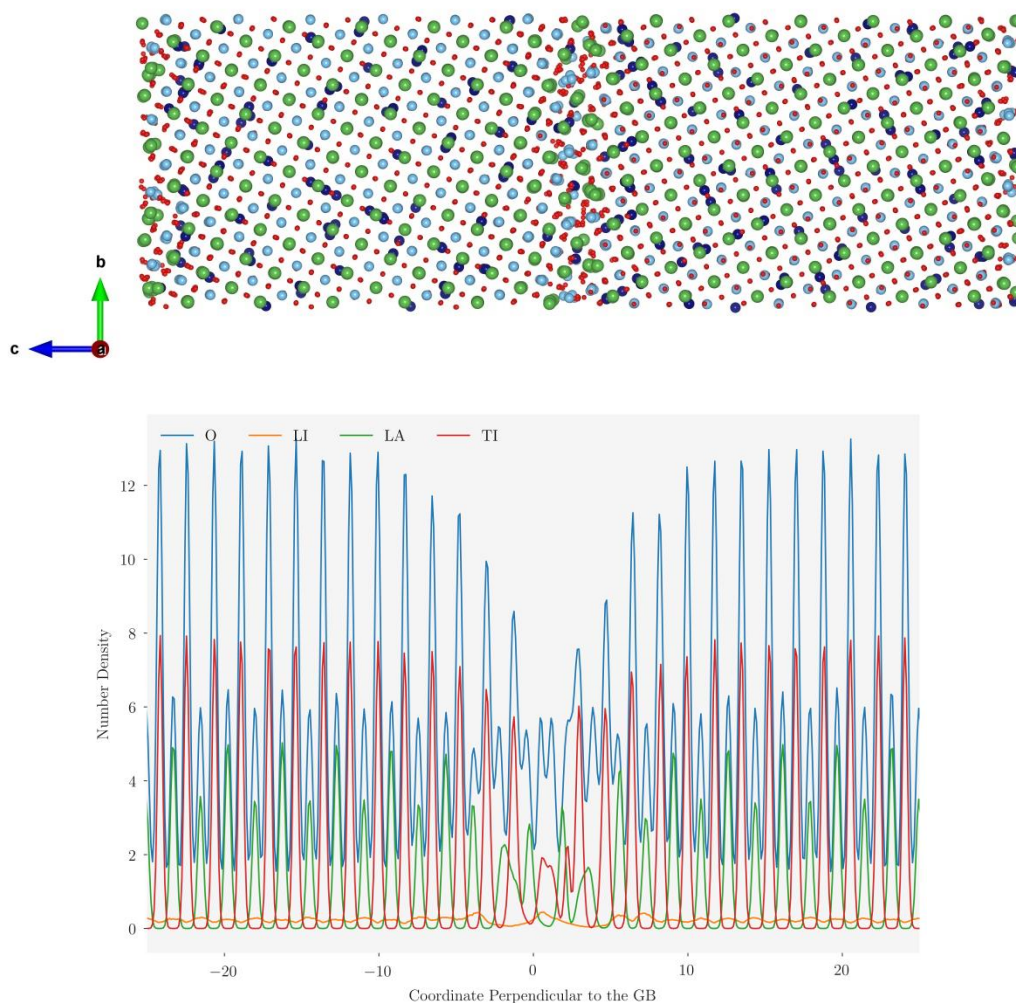


**Figure 7.3e** – Annealed structure and corresponding atom number density profile (1500 K) of the (210) LLTO boundary.

The (210) boundary of LLTO has an approximate boundary width of 10 Å. This boundary was found to be the least energetically stable with reference to the large formation energy compared to the low cleavage energy shown in table 7.3. As shown in figure 7.3e, the oxygen density remains consistent with the alternating layers in the bulk region. A small decrease in the lanthanum and titanium density at the boundary region is further observed. The activation energy for the (210) boundary is comparable to that seen in the bulk region. However, enhanced lithium diffusion is possibly observed again as the  $D_0$  value is considerably higher than the bulk value. The significant instability of this boundary may result in unsuitability in applications without prior stabilisation.

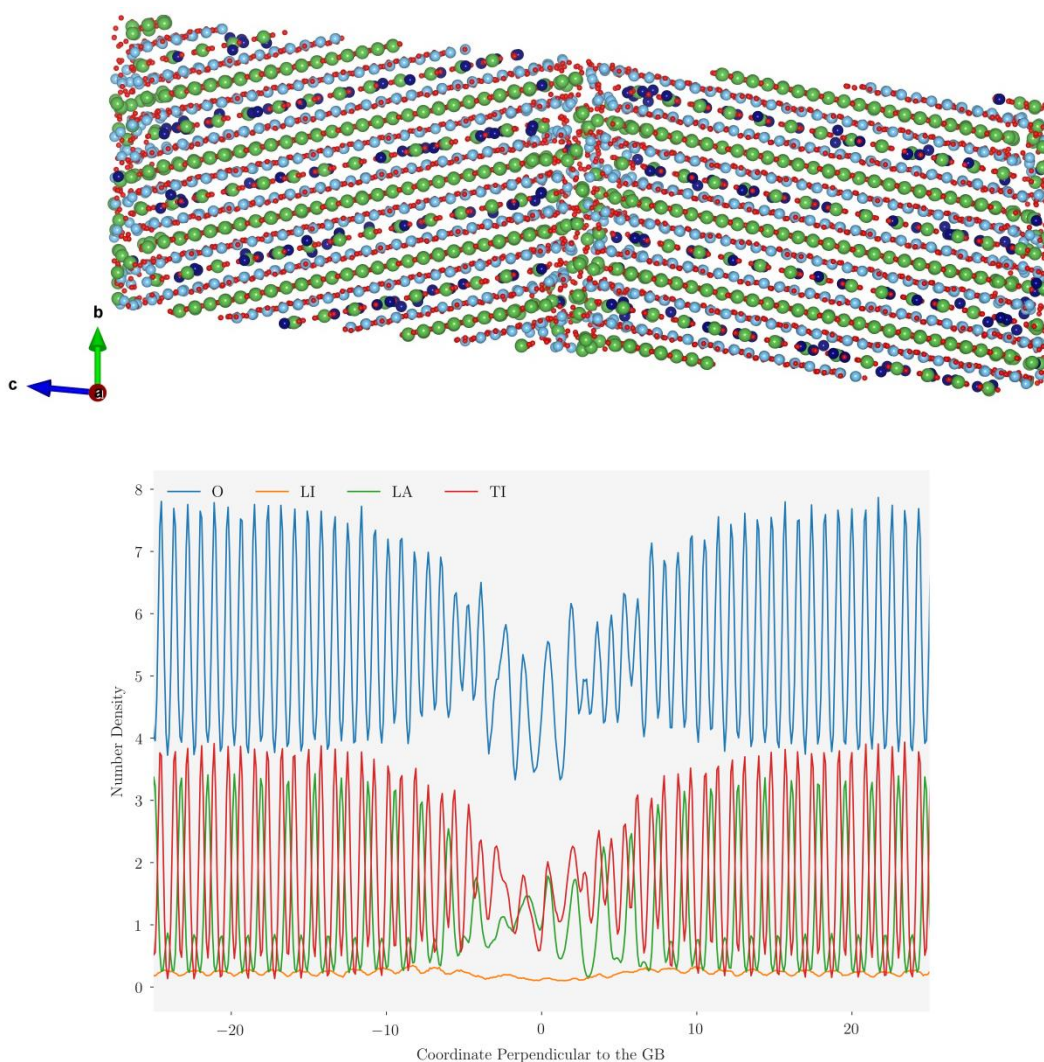


**Figure 7.3f** – Annealed structure and corresponding atom number density profile (1500 K) of the (211) LLTO boundary.

The (211) boundary appears to have a larger boundary region width than those previously analysed, approximately 16 Å. As shown in figure 7.3f, there appears to be very few lithium ions segregating into the boundary region, which is supported by the density profile. There is a further depletion in all other ions relative to the bulk. As a result of this, the calculated activation energy and  $D_0$  value may be more relevant to the bulk, as the lithium ion concentration at the boundary is depleted. Furthermore, as the (211) exhibits poor stability as shown in table 7.3 combined with the poor diffusion seen at the boundary, this results in the (211) boundary potentially being an ineffective choice in application.

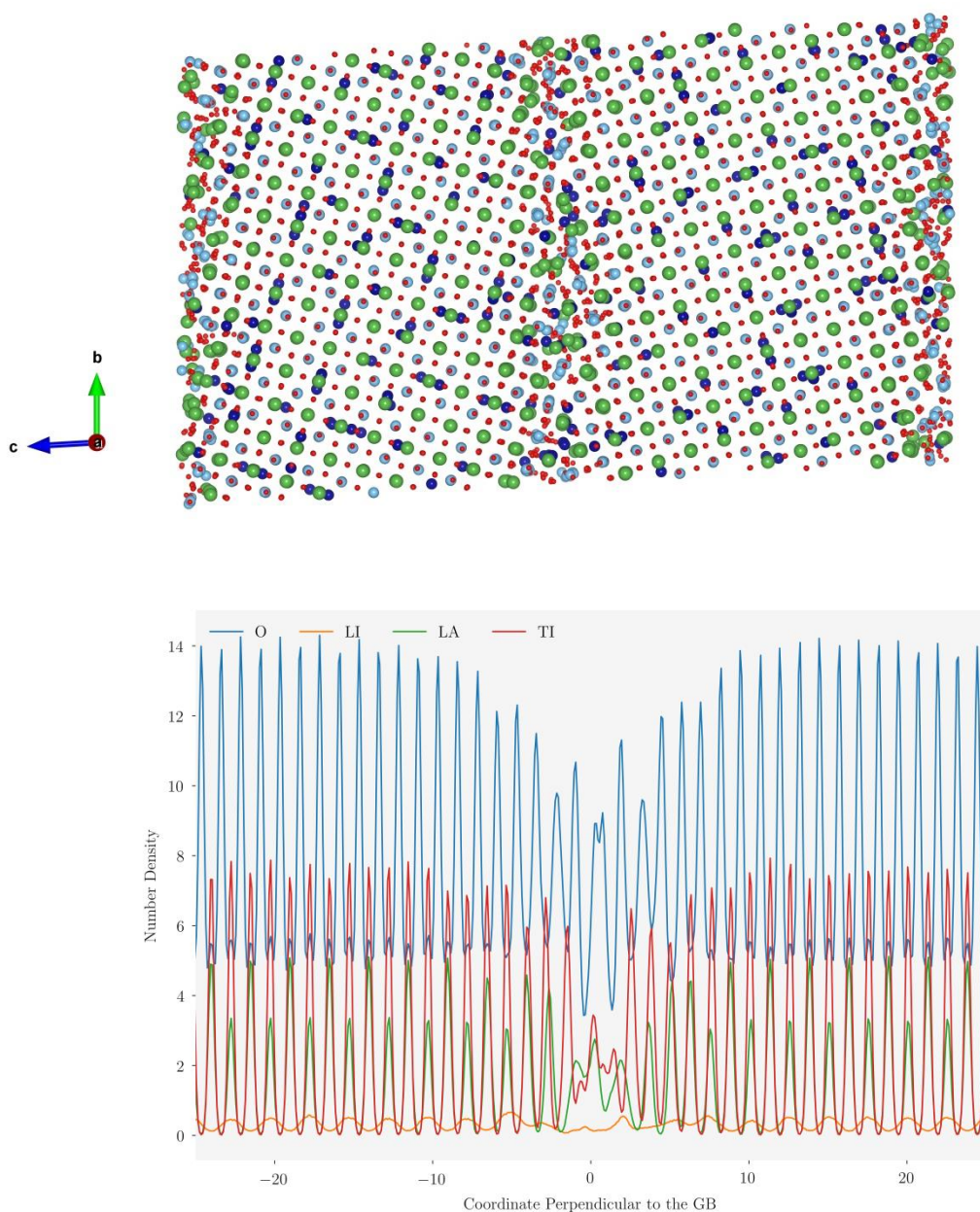


**Figure 7.3g** – Annealed structure and corresponding atom number density profile (1500 K) of the (310) LLTO boundary.

The final simulated boundary of LLTO was the (310) which has an approximate boundary width of 14 Å. The overall nature of the structure of this boundary appears to be symmetric with reference to oxygen, lanthanum, and titanium ions. Again, the concentration of lithium appears low within the boundary region and the activation energy may therefore correlate with that seen in the bulk region. Of the simulated boundaries the (310) had the lowest activation energy of lithium, suggesting that despite the small window of stability, it may be a successful candidate boundary when considering lithium diffusion by increasing the defect concentration.

Of the six boundaries investigated, with respect to MD simulations (as low as 3 K), the (311) boundary was found to be incompatible when simulations were carried out to anneal the boundary, amorphization of the unrelaxed boundary structure occurred. To obtain diffusion data for the (311) boundary, further investigation would be required to either select a stable surface termination, or by the introduction of defects with the aim of achieving stabilisation. As previously discussed, several thousands of atoms were required to model a grain boundary that is energetically stable. Due to the size of each structure and limitations of the code used, the individual x, y and z components for the grain boundary could not be isolated. In order to better understand how the presence of grain boundaries influences lithium diffusion in LLTO, these individual components would need to be separated so that diffusion parallel and perpendicular to the interface could be treated explicitly.



## 7.4 Chapter Summary

In this chapter the energetics and dynamics of layered LLTO phases have been investigated. The bulk results were consistent with regards to both structure and dynamics when compared to experiments. The importance of the local structure is demonstrated by the tilting of the  $\text{TiO}_6$  octahedra. The tilting was found to be a factor in the formation of a bottleneck through which lithium ions could diffuse. The results show the L30 bulk phase had the lowest activation energy, which was comparable to those seen experimentally. Therefore, this phase composition was chosen in the construction of low Miller index grain boundaries of LLTO. The interfacial structure appeared to be stable up to  $\sim 1600$  K where amorphization occurs, compared to  $>2000$  K for amorphization of bulk. Calculations were carried out for phases of sodium lanthanum titanate (NLTO), however bulk activation energies were found to be significantly higher than LLTO ( $E_A \approx 0.97$  eV- 1.11 eV) and it was therefore concluded that this structure was unsuitable when constructing grain boundaries. The obtained activation energies were consistent with the value obtained for the bulk. However, the  $D_0$  values were considerably higher suggesting that the presence of grain boundaries may result in enhanced lithium diffusion in polycrystalline phases. Limitations of the code used have been discussed when considering the size of each grain boundary with respect to the number of atoms required to construct each boundary. In order to obtain a more substantial conclusion on how the presence of grain boundaries affect lithium diffusion in LLTO; the x, y and z components of diffusion would need to be isolated where diffusion both parallel and perpendicular to the boundary could be quantified. Further investigation of LLTO boundaries would require addressing the stabilisation issues occurring in the case of the (311) boundary. Understanding such issues could be used to expand beyond these five boundaries by using surfaces with higher Miller indices including the incorporation of lithium defects to improve and facilitate lithium diffusion at the interface. Finally, the presence of intrinsic defects was found to improve lithium diffusion, therefore possible extrinsic dopants could be considered to further enhance lithium diffusion.



## 8 Lithium Lanthanum Zirconate

Lithium lanthanum zirconate (LLZO) has been found to be a promising candidate solid electrolyte material due to the high ionic conductivity and stability at ambient temperature and pressure<sup>(88)</sup>. LLZO adopts a garnet structure with  $\text{Li}^+$  ions occupying the A-sites<sup>(247)</sup>. The high temperature metastable cubic phase of LLZO has been found to be highly conductive through experiments<sup>(101, 104)</sup>. The typical stoichiometry of garnet materials is  $\text{A}_7\text{B}_2\text{C}_3\text{O}_{12}$  where the cations which occupy the A, B and C sites have an oxygen coordination of four-fold, six-fold and eight-fold, respectively<sup>(248)</sup>. In the crystal structure of LLZO, the cubic A-sites are occupied by lanthanum, the tetrahedral C-sites are occupied by zirconium and lithium ions occupy the tetrahedral B-sites<sup>(247, 248)</sup>. Experimentally a proposed description of the lithium ion diffusion mechanism was carried out by Awaka *et al.*<sup>(249)</sup> through single crystal X-ray diffraction. A 3D network of lithium ion diffusion was suggested through loop junctions between the tetrahedral lithium sites, which when connected formed a pathway for ionic conduction.

One of the key challenges when addressing the functionality of LIBs is the formation of dendrites with the charging-discharging cycle, thereby resulting in both functionality and safety concerns. Experimentally it has been shown that LLZO can greatly reduce dendritic formation when compared to liquid electrolytes, resulting in both improved safety and lifespan of the system<sup>(85, 113)</sup>. However, further experimental studies have shown LLZO to exhibit high rigidity, which could potentially limit the desired compatibility within an anode-electrode-cathode system<sup>(250)</sup> when attempting to achieve a stable match at the interface. The presence of dendrites has been observed to disrupt the interfacial structure of LLZO boundaries resulting in dysfunctionality of the battery system<sup>(61, 83, 125, 251, 252)</sup> where it has been proposed that the microstructural effects of LLZO should be further considered when designing battery systems<sup>(250, 253)</sup>.

To date, experimental research has focused predominantly on bulk LLZO where cationic<sup>(115)</sup> and anionic<sup>(101)</sup> doping schemes have been proposed to enhance lithium diffusion and further stabilise the highly conductive cubic phase. Monte Carlo simulations have been used to further investigate the dynamics of LLZO grain boundaries particularly focussing on polycrystalline phases<sup>(127)</sup>. Simulations showed that lithium transportation was slower in the boundary region relative to the bulk suggesting that the presence of said boundaries contributes to moderate resistance where the proposed presence of dopants could be effective in decreasing resistance<sup>(127)</sup>. Further studies of boundary resistance have been reported in LLZO<sup>(120-124, 126)</sup> where said resistance has been decreased by the tuning of synthesis conditions<sup>(126)</sup> to improve grain boundary contact.

This chapter will investigate the energetics of the bulk phase addressing both intrinsic and extrinsic defects of LLZO. Stoichiometric LLZO will further be used in the construction of six homogenous, low Miller index grain boundaries. The transport properties of the grain boundaries will be investigated to observe their effect on lithium transport.

## 8.1 Bulk Dynamics of LLZO

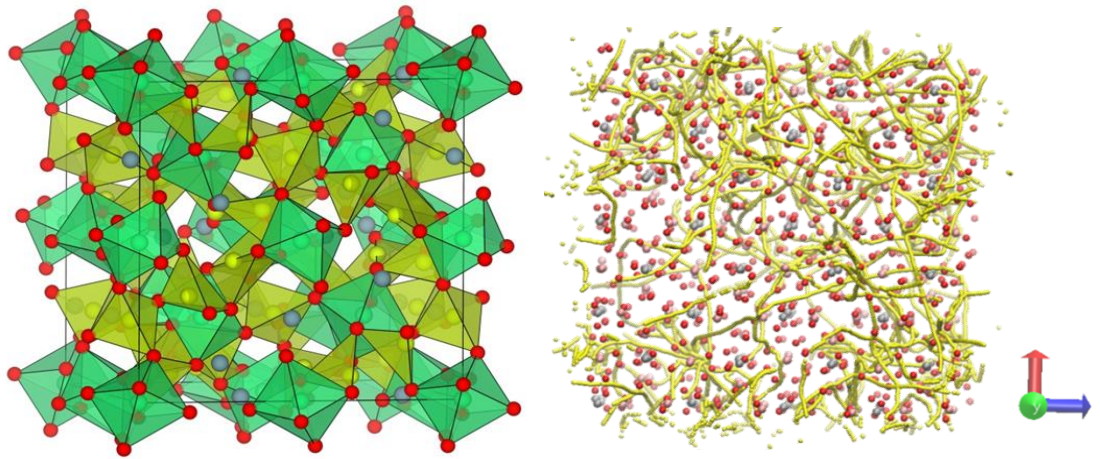


**Figure 8.1a** – Structural representation of the garnet structure of LLZO (left) showing octahedral tilting with diffusion pathway (yellow) of lithium (right).

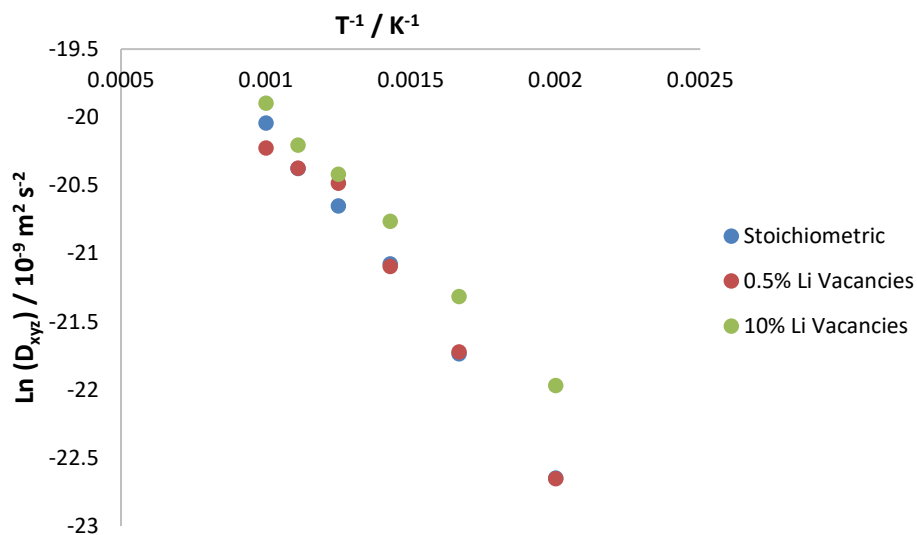


**Figure 8.1b** – Natural log of total diffusion coefficient as a function of reciprocal temperature for bulk compositions of LLZO (Pedone potential model).

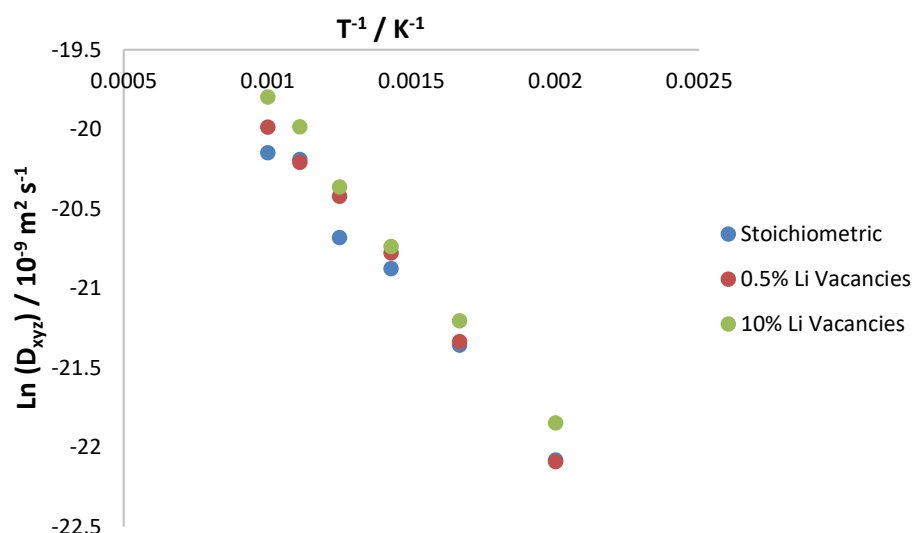


**Figure 8.1c** – Natural log of total diffusion coefficient as a function of reciprocal temperature for bulk compositions of LLZO (Teter potential model).

Stoichiometry	$E_a$ (Pedone) / eV	$D_0$ (Pedone) / $10^{-9} \text{ m}^2 \text{ s}^{-1}$	$E_a$ (Teter) / eV	$D_0$ (Teter) / $10^{-9} \text{ m}^2 \text{ s}^{-1}$
$\text{Li}_7\text{La}_3\text{Zr}_2\text{O}_{12}$	$0.22 \pm 0.01$	$26.26 \pm 2.22$	$0.17 \pm 0.01$	$13.48 \pm 2.13$
$\text{Li}_{6.965}\text{La}_3\text{Zr}_2\text{O}_{11.997}$	$0.22 \pm 0.01$	$23.69 \pm 5.77$	$0.18 \pm 0.01$	$18.06 \pm 1.69$
$\text{Li}_{6.3}\text{La}_3\text{Zr}_2\text{O}_{11.4}$	$0.18 \pm 0.01$	$17.32 \pm 1.16$	$0.18 \pm 0.01$	$19.82 \pm 1.47$

**Table 8.1a** – Activation energies and  $D_0$  value of stoichiometric and intrinsically defective phases of LLZO with their respective uncertainties.

The justification of the potential model used was discussed in chapter 3<sup>(132)</sup>. When investigating LLZO, both the Teter and Pedone potential models have initially been used. Whilst the Pedone potential model was successful when modelling the structure of LLZO, the availability of the potential interactions when considering extrinsic defects was limited. Therefore, in the case of investigating the extrinsic defects, the Teter potential was used due to the increased availability of potential interactions. The calculated structures were found to have a small orthorhombic distortion as opposed to the low temperature tetragonal phase observed experimentally<sup>(168)</sup>. This is considered to be caused by the choice of ionic positions and a small simulation cell.

The bulk cells were generated through the use of the METADISE code<sup>(136)</sup> where each lattice parameter was increased by a factor of two in order to generate a 2x2x2 supercell in order to have a sufficient number of atoms in which to effectively tune the concentration when carrying out MD

simulations. Initial simulations were carried out using MD on a stoichiometric phase of LLZO and two intrinsically defective phases where lithium vacancies were incorporated randomly in concentrations of 0.5% and 10%. Charge compensation was achieved in each system by incorporation of oxygen vacancies. Each composition was initially simulated for 1.1 ns using the NST ensemble to allow the system to effectively equilibrate. Secondly, this equilibrated orthorhombic phase was further simulated for 10.0 ns using the NVT ensemble, thereby keeping the volume fixed over which diffusion of lithium was measured.

The results from these NVT simulations are shown in figures 8.1b and 8.1c and table 8.1a. Two contrasting results are observed when comparing the two potential models. The Pedone potential model shows that with decreasing lithium concentration, vacant sites provide a pathway for lithium diffusion resulting in a decreased activation energy when compared to the stoichiometric phase, which is consistent with experimental evidence<sup>(115)</sup>. Although the  $D_0$  values suggest decreased lithium diffusion, the larger associated errors compared to those observed for the activation energies suggest that these values may not be as reliable. On the contrary, the results for the Teter potential disagree with both the Pedone potential model results and experimental studies. Despite the poor performance of the Teter potential model when investigating the intrinsic defect properties of LLZO, it has a wider variation of fitted potential interactions compared to the Pedone potential model and will therefore be used when investigating extrinsic defect incorporation. A number of different cationic dopants have been experimentally reported to arise a decrease in LLZO activation energy<sup>(115, 254, 255)</sup>. Three extrinsically defective LLZO phases were further investigated which had been experimentally suggested to facilitate diffusion. Using identical MD methods, defective phases were compared to the stoichiometric phase; these results are represented in figure 8.1d with the corresponding activation energies shown in table 8.1b.

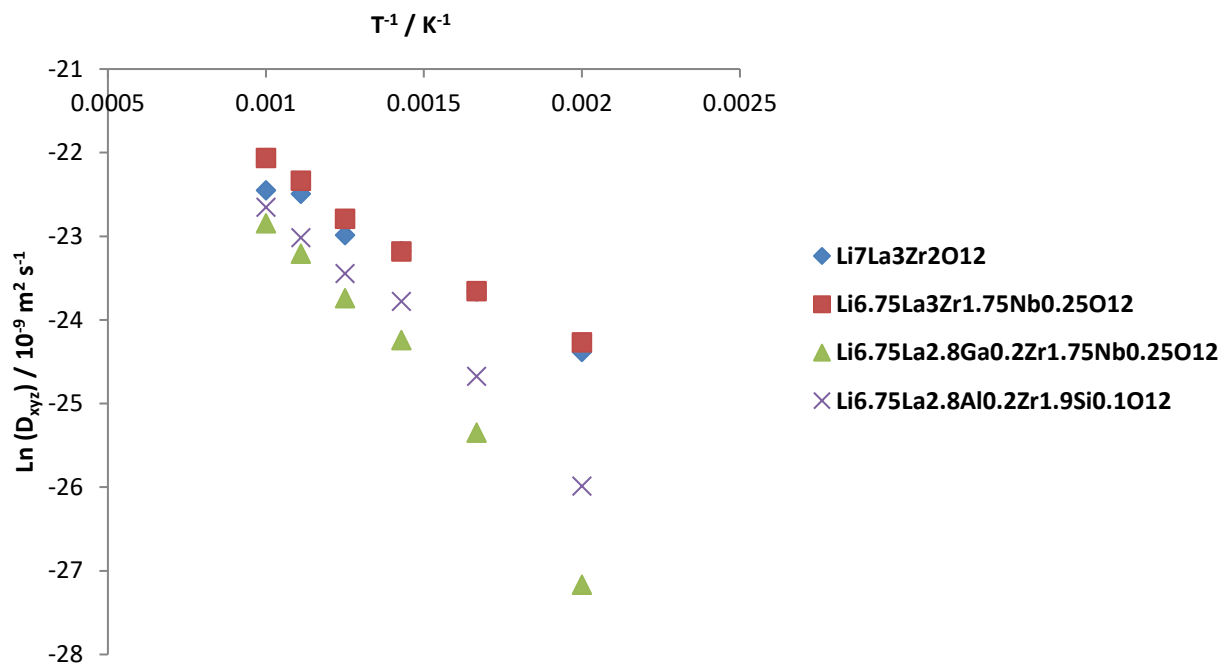


**Figure 8.1d** – Natural log of total diffusion coefficient as a function of reciprocal temperature for stoichiometric and defective phases of LLZO.

Composition	$E_a$ / eV	$D_0$ / $10^{-9} \text{ m}^2 \text{ s}^{-1}$
$\text{Li}_7\text{La}_3\text{Zr}_2\text{O}_{12}$	$0.17 \pm 0.01$	$1.34 \pm 0.20$
$\text{Li}_{6.75}\text{La}_3\text{Zr}_{1.75}\text{Nb}_{0.25}\text{O}_{12}$	$0.19 \pm 0.01$	$2.18 \pm 0.40$
$\text{Li}_{6.75}\text{La}_{2.8}\text{Al}_{0.2}\text{Zr}_{1.9}\text{Si}_{0.1}\text{O}_{12}$	$0.28 \pm 0.01$	$10.00 \pm 3.68$
$\text{Li}_{6.75}\text{La}_{2.8}\text{Ga}_{0.2}\text{Zr}_{1.75}\text{Nb}_{0.25}\text{O}_{12}$	$0.37 \pm 0.02$	$4.04 \pm 0.99$

**Table 8.1b** – Activation energies and  $D_0$  values of bulk stoichiometric and defective phases of LLZO with their respective uncertainties.

The three phases investigated in figure 8.1d show a similar trend to the intrinsically defective LLZO phases in terms of the niobium doped phase. In this particular phase, the overall diffusion was seen to be comparable to the stoichiometric phase yet slightly higher overall activation energy was seen. In the case of the Al/Si and Ga/Nb dopant schemes, in both cases there is significantly reduced diffusion and increased activation energy in both phases. The results obtained suggest that the stoichiometric phase of LLZO has the lowest lithium activation energy when compared with each of the defective phases, which disagrees with experimental research. The influence of co-doping of LLZO was found to increase the activation energy of lithium diffusion in all three phases. These results could be for two possible reasons; firstly, the size of the defective ions could result in a suppression of the lithium diffusion pathway. Thus, resulting in a greater energy barrier of diffusion. Secondly, there is the potential for lithium ion clustering because of the defective sites thereby

resulting in a further suppression to diffusion. To quantify these possible hypotheses, further simulations would be required. In the case of the results calculated in this study, the Teter potential model appears unsuitable when modelling LLZO.

To conclude the bulk study of LLZO, several different compositions were simulated using MD incorporating both intrinsic and extrinsic defects. The results obtained show that the Pedone potential model produced results consistent with experimental data. On the contrary, the results obtained for both intrinsic and extrinsic defects when using the Teter potential model contradicted previous experimental evidence and therefore it was deemed that this potential model is unsuitable for modelling LLZO. The Pedone potential model has been chosen to model the grain boundaries of LLZO due to the better performance when modelling the intrinsic defects of LLZO.

## 8.2 Grain Boundaries of LLZO

As LLZO adopts a garnet structure, this allows diffusion in three dimensions. This can be visualised as shown in figure 8.1a and is also observable quantitatively in each of the simulated phases as the calculated directional diffusion was found to be roughly isotropic. This feature is important in the construction of grain boundaries, as unlike with perovskite type solid electrolytes such as LLTO, the orientation of the surface is unimportant with regards to the diffusion; therefore, it becomes easier to select candidate surfaces as lithium diffusion would be viable no matter how the LLZO surface is orientated. As shown with the interfaces of ceria and STO, experimentally the grain boundaries which have been structurally observed are those of a low Miller index ( $\leq 3$ ), hence why such boundaries were chosen for LLZO simulations. Furthermore the surface energies represented in table 8.2a are those of the lowest energy termination of those found when generating the surfaces using the METADISE code<sup>(136)</sup>. In the study of grain boundaries of LLZO, five low Miller index boundaries were simulated using similar techniques to the bulk diffusion however with a reduced timeframe (1.0 ns NVT ensemble) due to the large increase in size compared to the bulk and therefore increase in computational time and expense. Figure 8.3a shows a preliminary calculation carried out on the (100) mirror twin boundary of LLZO where both the boundary structure and the diffusion pathway of a single lithium ion is shown. This boundary was chosen due to the smaller size compared to the other simulated boundaries where due to computational limitations other simulation profiles are not presented.

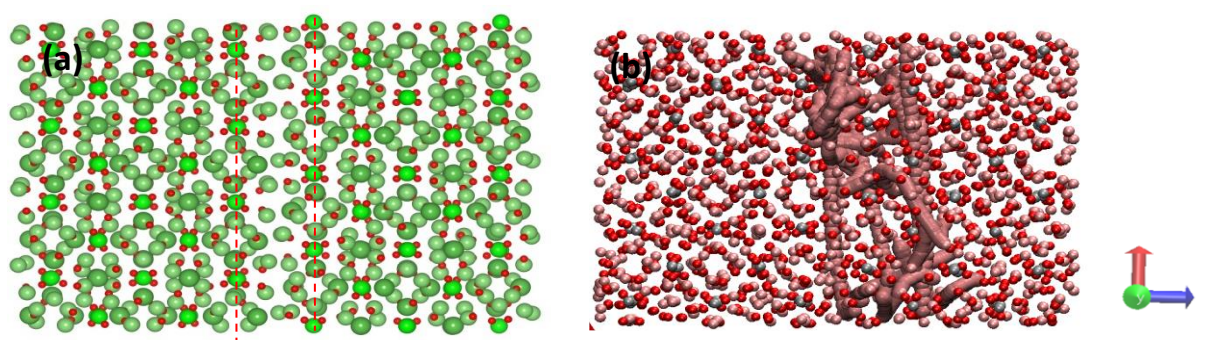


**Figure 8.2a** – (a) Relaxed grain boundary structure of the (001) LLZO boundary (b) Diffusion pathway of a single lithium ion.

Boundary	Termination	$\gamma$ / Jm <sup>-2</sup>	Area / Å <sup>2</sup>	$E_f$ / Jm <sup>-2</sup>	$E_c$ / Jm <sup>-2</sup>	$E_A$ / eV	$D_0$ / 10 <sup>-9</sup> m <sup>2</sup> s <sup>-1</sup>
(110)	Zr-Li	2.04	235.44	0.13	3.95	0.23 ± 0.01	20.21 ± 1.01
(111)	Li-O	1.49	291.52	2.03	0.94	0.19 ± 0.01	20.61 ± 1.55
(210)	O	1.39	373.39	1.12	1.65	0.22 ± 0.01	23.01 ± 1.76
(211)	Zr-O-La	1.96	411.06	1.59	2.32	0.21 ± 0.01	19.70 ± 1.79
(310)	La	1.53	528.57	1.50	1.56	0.23 ± 0.01	22.51 ± 1.35
(311)	Li-O	1.51	555.82	1.54	1.47	DNC	DNC

**Table 8.2a** - Surface indices, termination, surface energy ( $\gamma$ ), area, formation energy ( $E_f$ ), cleavage energy ( $E_c$ ), activation energy ( $E_A$ ) and  $D_0$  values of LLZO interfaces. (DNC = Did not converge when simulated using MD).

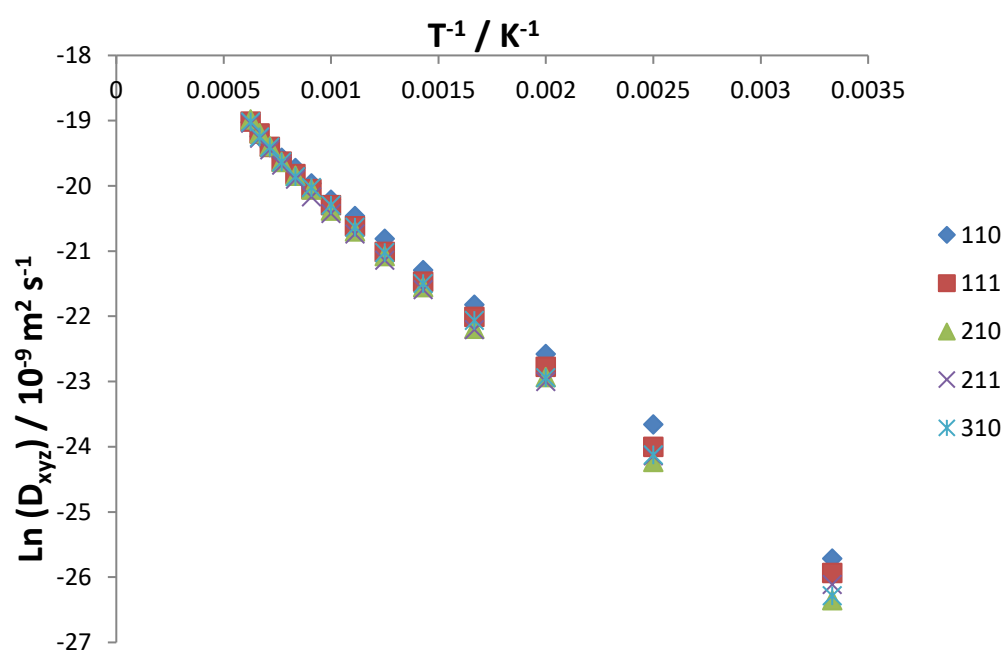


**Figure 8.2b** – Natural log of total diffusion coefficient as a function of reciprocal temperature for grain boundaries of LLZO.



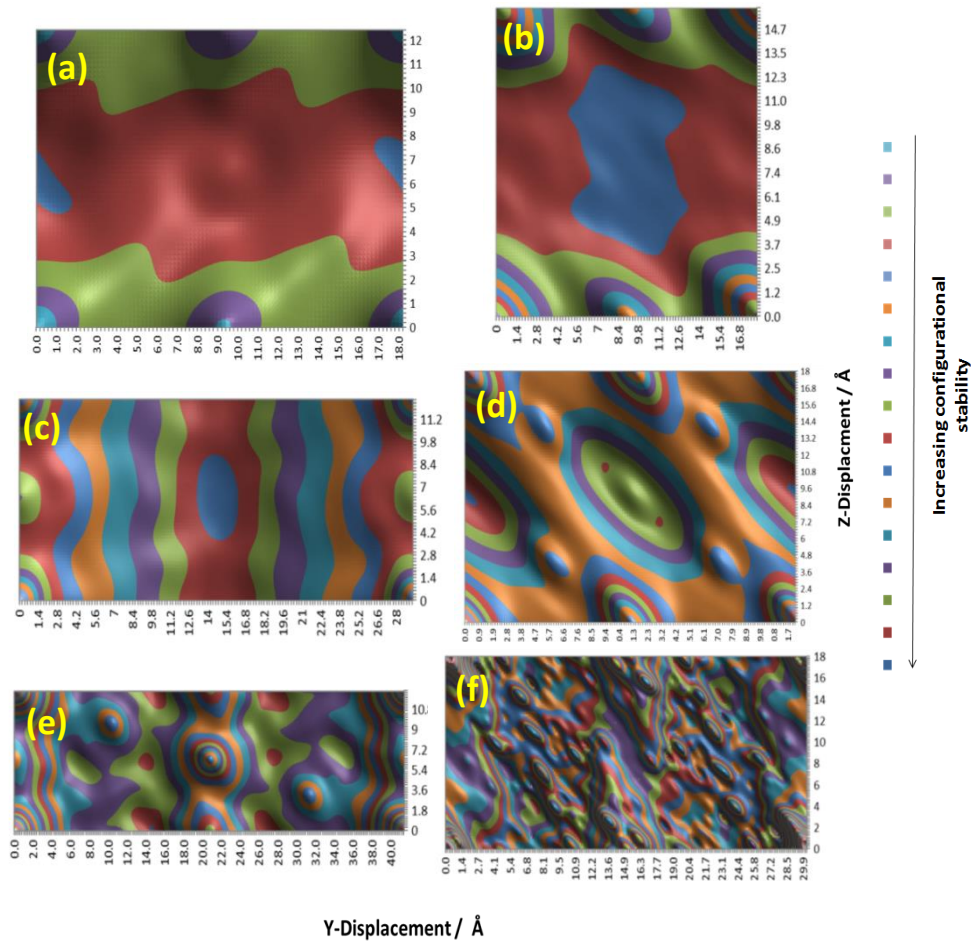


**Figure 8.2c** – Potential energy surfaces (a) 110 (b) 111 (c) 210 (d) 211 (e) 310 (f) 311 of LLZO grain boundaries where the blue regions define the local minima where multiple are seen as shown in the centre of (b) which contains the displacement of the minimum energy structure.

Table 8.2a and figure 8.2a show the energetic and structural information of the simulated grain boundaries and the free surfaces from which they were constructed. From table 8.2a, with increasing Miller indices, an increase in surface area occurred. However, no such trend with surface energies was observed, in fact the highest energy free surface, namely the (110) surface, resulted in both the lowest formation energy and highest cleavage energy, therefore implying that this is the most energetically stable boundary. The (111) boundary was found to be the least energetically favoured boundary due to the relatively large formation energy compared to the cleavage energy. In the case of the (210), (211) and (310) boundaries, these boundaries were also found to be energetically stable when considering the formation and cleavage energies. The (311) is energetically unfavourable and as a result was energetically unstable when carrying out MD simulations. The potential energy surfaces for each boundary are shown in figure 8.2c where a visual increase in complexity is observed with increasing surface area. Therefore, the smaller the surface area, the

easier it becomes to identify the global minimum. The structure of the potential energy surfaces is of further importance when considering the boundary dynamics. The increasing of temperature could result in the sliding of one surface resulting in a shift in the boundary structure. The significance of this can be seen when comparing two examples; as (b) shows a deep central trough, the shift is unlikely to cause any significant structural change whereas (f) has much smaller, deeper local minima, where increasing temperature could result in a significant shift in overall boundary structure.

Using the structural data obtained for the grain boundaries of LLZO, the annealed boundaries were simulated using MD, where five out of the six were found to be stable. The (311) boundary was observed to be unstable when carrying out MD simulations, even as low as 3 K. This instability could possibly be attributed to the formation and cleavage energies calculated in table 8.2a. In the case of the five boundaries, the structure and atom density profiles are considered at 1500 K in order to obtain a clearer picture of both the general boundary structure and their influence on lithium diffusion. The boundary width was approximated in each case using the number density profiles where the region in which lithium depletion occurs from the 0 Å boundary centre until it tended back towards the bulk density. The total region width in each example was approximately 30 Å (~15000 atoms) between boundaries so that a clear distinction could be made between the boundary and bulk regions. In each case the lithium ions have been highlighted in blue with the reduction in size of lanthanum ions in order to clearly visualise lithium positions.

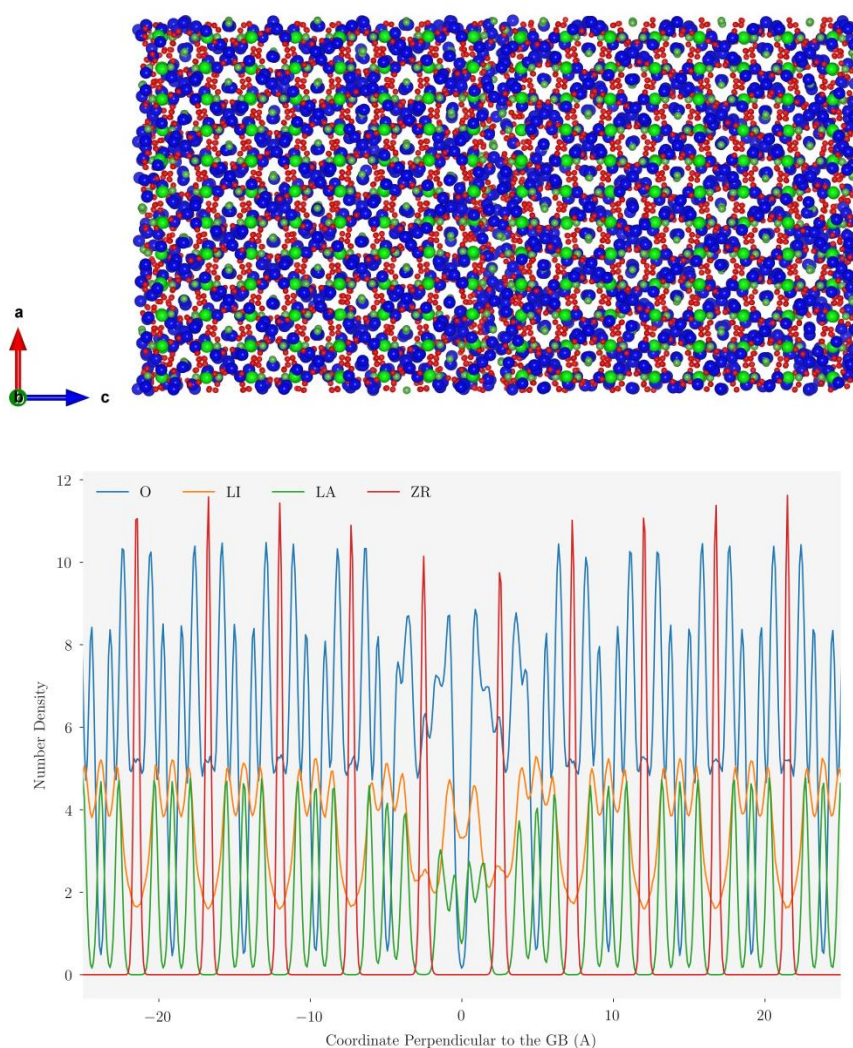


**Figure 8.2d** – Annealed structure and corresponding atom number density profile (1500 K) of the 110 LLZO boundary.

As shown in Figure 8.2d, the boundary region is approximately 10 Å in width as previously described. With regards to this boundary region the density of zirconium and lanthanum is significantly depleted in the central boundary region whereas the lithium and oxygen concentrations deplete slightly from those observed in the bulk region. This structural consequence at the boundary is visually observable as shown in figure 8.2d where an abundance of blue lithium ions is seen. Furthermore, when observing the diffusion profile this suggests symmetric nature of the (110) boundary. The (110) boundary has an activation energy marginally higher than the value observed for the bulk and a  $D_0$  value lower than that observed for bulk. Together this suggests that the presence of the (110) boundary would suppress lithium diffusion.

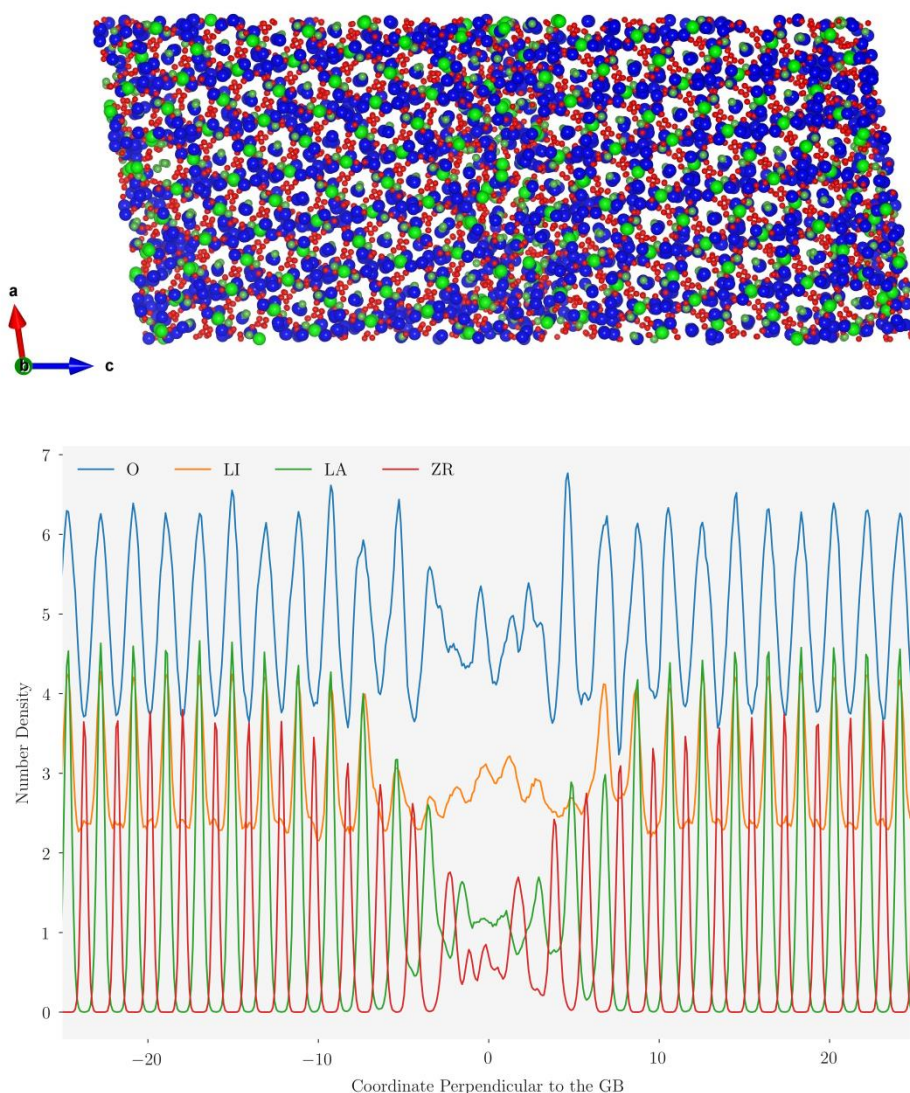


**Figure 8.2e** – Annealed structure and corresponding atom number density profile (1500 K) of the 111 LLZO boundary.

The width of the (111) boundary was found to be approximately 8 Å. In the case of this boundary, whilst there is a small depletion in the number densities of oxygen and lithium relative to the bulk, the number density of both remains high in the boundary region, unlike with the (110) where sharp depletion regions are present. The relationship between the bulk and boundary zirconium and lanthanum is similar to that of oxygen and lithium yet with much lower number densities. The energetics of the (111) boundary shown in table 8.2a suggests that although being relatively energetically unstable, this boundary had the lowest overall activation energy with a  $D_0$  value like those seen for other boundaries. Therefore, in a theoretical polycrystalline system, if the (111) boundary were energetically stable, it could enhance lithium diffusion.



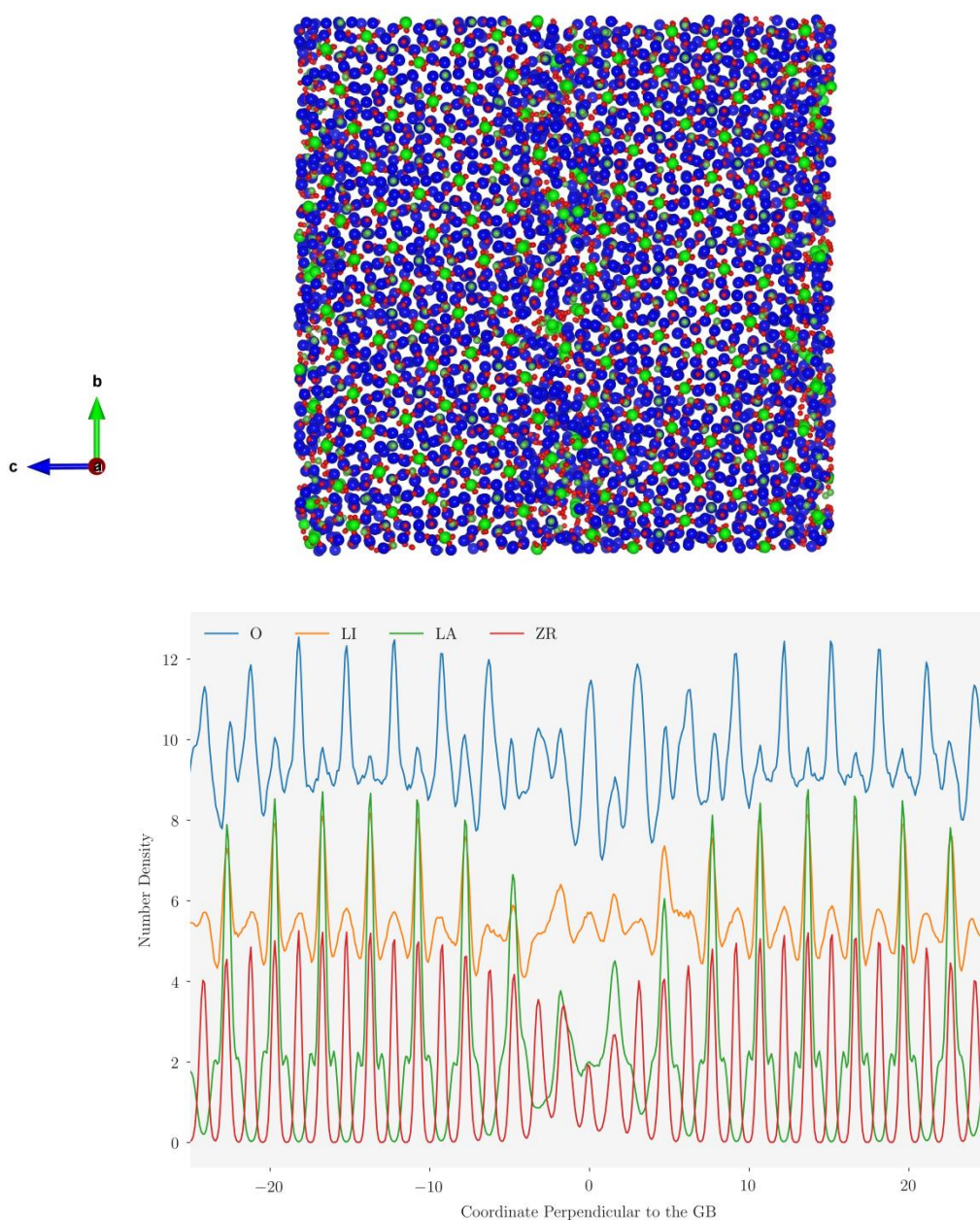


**Figure 8.2f** – Annealed structure and corresponding atom number density profile (1500K) of the 210 LLZO boundary.

The (210) boundary shows consistencies with the size and number density profiles of the (111) boundary with approximately an 8 Å boundary region with a similar atomic layout. These two boundaries unlike the (110) boundary appear less symmetric in nature at the boundary core. However, in the (210) boundary, the zirconium and lanthanum appear to have a focal distribution as opposed to the even distribution seen in both diffusion profiles. The energetics were similar to the (110) boundary with respect to activation energy. However, a higher  $D_0$  value was observed, closer to the reported bulk value. This suggests that the (210) boundary may be slightly less suppressive for lithium diffusion than the (110) boundary.

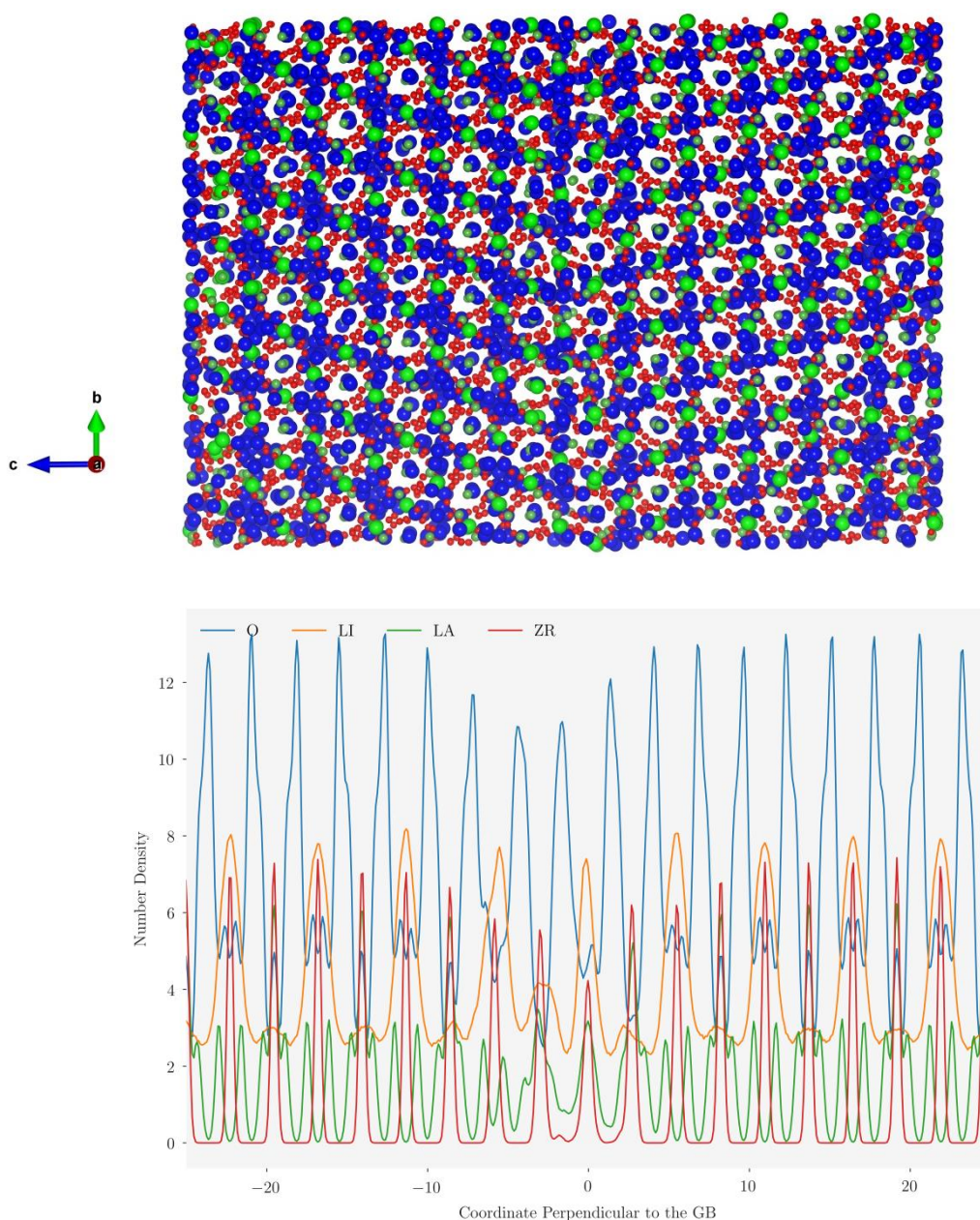


**Figure 8.2g** – Annealed structure and corresponding atom number density profile (1500 K) of the 211 LLZO boundary.

The (211) boundary again shows similar structural similarities with the previously discussed boundaries. Despite less energetic stability, the density profile is very similar with respect to the symmetric nature of the profile and the relative atomic distribution. The reported activation energy for the (211) boundary was similar to those reported for all other boundaries. However, the reported  $D_0$  value was the lowest for all of the investigated boundary suggesting that the (211) boundary could suppress lithium diffusion.



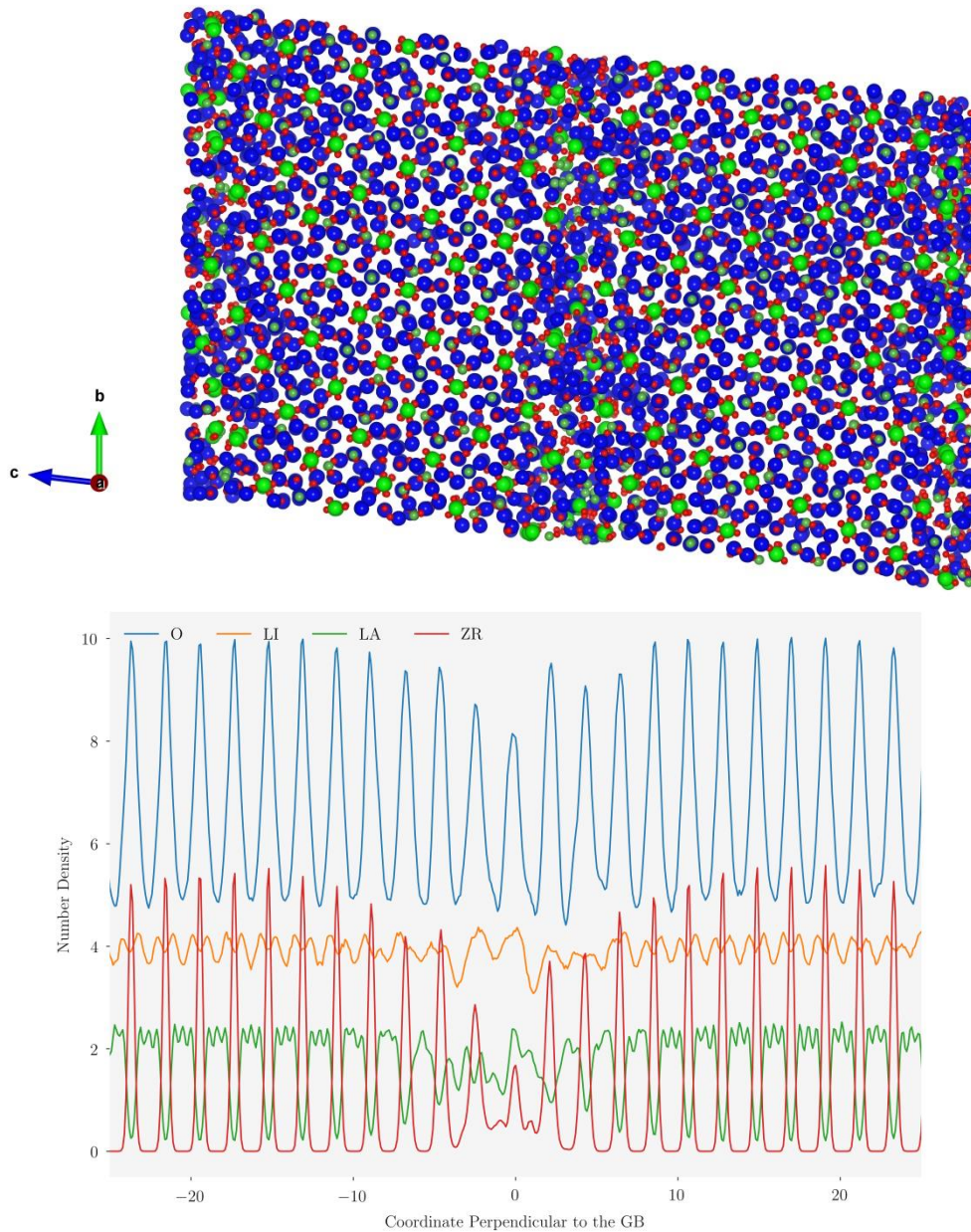


**Figure 8.2h** – Annealed structure and corresponding atom number density profile (1500K) of the 310 LLZO boundary.

The (310) boundary has approximately the smallest of the boundary regions with a size of around 6 Å. Whilst the relationship of oxygen, lanthanum and zirconium is consistent with the (110) and (211) boundaries, an increased number density of lithium is seen within the boundary region, suggesting an accumulation in this region. The reported activation energy is identical to the (110) boundary with a slightly higher  $D_0$  value. This suggests that whilst the (310) could suppress lithium diffusion, it may not be as suppressive as the (110) boundary.

The (311) boundary was the final of those investigated in case of this research. In this circumstance, this boundary was deemed to be unstable with regards to MD. In the initial annealing procedure when attempting to simulate this boundary at temperatures as low as 3 K, the structure of the boundary would amorphise. In order to further investigate this boundary, either a different termination of the (311) surface or the incorporation of types of defects used in the bulk phases could be used to address the instability.

In general, the results show that the presence of grain boundaries in LLZO appear to slightly suppress lithium diffusion which is consistent with experimental studies<sup>(127)</sup>. The reported activation energies and  $D_0$  values for each boundary were similar to those observed for the bulk. As discussed with LLTO, to further understand quantitatively that effect that the presence grain boundaries have on LLZO; further simulations would be required. In particular, observing to what extent lithium diffusion occurs parallel to the boundary as opposed to perpendicular to the boundary.



### 8.3 Chapter Summary

In conclusion, the simulations carried out on LLZO used a combination of energy minimisation and MD techniques. Simulations of bulk LLZO were carried out using two different potential models. The Teter potential model results disagree with other computational and experimental studies, suggesting that this potential model is unsuitable for modelling LLZO. The results obtained for the Pedone potential model were consistent with other studies, despite the lack of potential interactions available when considering extrinsic defects. The initial simulation cell was orthorhombic. As discussed, through experiments, a structural change is observed when exceeding 600 K from tetragonal to cubic. As the structural analysis of LLZO with increasing temperature was not addressed as part of this research, future work would include structural data to observe whether the orthorhombic structure transitions to a cubic structure at high temperatures. The results have shown that boundaries of LLZO were stable up to around 1600 K and influence lithium diffusion dependent on the boundary structure. This was consistent with other computational studies<sup>(127)</sup>. In the case of all investigated stable boundaries, the activation energies calculated were found to be slightly higher than the bulk and the  $D_0$  values were generally consistent with those seen in the bulk. Thus, implying that the presence of grain boundaries suppresses lithium diffusion to small yet differing extents, showing further consistency with experimental evidence<sup>(127)</sup>. Furthermore, the activation energies and  $D_0$  values obtained were comparable to those observed in the bulk region. Therefore, it should be considered that due to the bulk region being much larger than the boundary region, the obtained energy may correspond to that of the bulk region. Therefore, the boundary region could be isolated and treated explicitly to ensure that the activation energies and  $D_0$  values only consider the diffusion within the quantified boundary region. Furthermore, investigating diffusion parallel to the boundary and opposed to perpendicular to the boundary would provide a greater insight as to whether lithium diffusion is suppressed or enhanced. Whilst this research focuses solely on homogenous grain boundaries of LLZO, heterogeneous grain boundaries could also be modelled with the inclusion of further cationic and anionic defects within the boundary region to observe how lithium transport is affected.

## 9 Conclusions and Future Work

This final chapter reviews the main findings of the work carried out and summarises areas for future research.

### 9.1 Potential Models

Chapter 3 described the application and assessment of potential model parameters which were a partial charge, rigid ion model. Potential model based atomistic simulations depend for their reliability on the quality and transferability of their parameters. The charges are simply scaled valence charges which means that charged defects can be considered without further scaling of charges, and due to the rigid ion nature they can be evaluated rapidly and are therefore highly suitable for large scale or multiple simulations.

The initial criteria set for the justification of potential models were within 3% of the structural parameters reported through computational and experimental research. This range accounted for the differences observed by different computational and experimental methods seen within the literature. With respect to this range, the potential models used in this study all reproduced accurate structures with respect to those observed in the literature. Further properties were considered to justify the validity of the potential models. These included elastic constants and bulk moduli where a general agreement of within  $\pm 10\%$  of the experimental values was observed. A larger margin of error was considered when calculating such properties due to the simulations being carried out at 0 K and no three body interactions were included. Further simulations investigated bulk single point defects, doping schemes and bulk activation energies. The calculated defect energies were generally slightly higher than those seen in literature possibly due to model design, when compared with more sophisticated classical and quantum methods such as the incorporation of a shell model or by using DFT. Bulk diffusion of oxygen using MD techniques showed a mechanistic consistency with Arima *et al.*<sup>(171)</sup> where the importance of oxygen vacancy formation was highlighted. However, overall the simulations showed acceptable agreement with experimental studies.

The purpose of using a rigid ion, partial charge potential model was due to the ability to simulate high-throughput calculations within a reasonable timeframe and have shown to be very efficient. Extensions could be made by using a shell model. By fitting this type of potential, this could be used to address some of the structural discrepancies observed for the calculated grain boundary structures compared to experimental structures, in particular the  $\Sigma 5$  (112) boundary of STO, as this would generate lower defect energies by allowing more modes of relaxation.

## 9.2 Grain Boundaries of Ceria and Strontium Titanate

In chapters 4 and 5, the potentials were used with a high-throughput method to generate the structural and energetic data for grain boundaries of ceria and strontium titanate ranging between  $\Sigma 3$ -163. A range of scripts to automate the search and analysis were used. This methodology resulted in a high degree of structural accuracy for the ceria grain boundaries, however some structural discrepancies were observed for STO. As previously suggested, the use of a shell model may be more successful, or adjusting the search algorithm, for example a smaller step length may have greater success in accurately describing the structures consistent with those observed experimentally. Furthermore, the use of Monte Carlo simulations or DFT could be further implemented to generate boundary structures. A structural comparison of uncharacterised grain boundaries was produced for approximately fifty grain boundaries of each material which suggested that the vast majority of boundary structures were energetically favoured and thereby could be potentially experimentally characterised. The high-throughput scripts were also employed to calculate single point defect energies in both the bulk and boundary regions for a number of boundaries which have been structurally identified. Both cationic and anionic defects were found to be generally energetically favoured in the boundary region compared to the bulk region. The MD simulations for the grain boundaries suggested that in general, the presence of grain boundaries resulted in the suppression of oxygen transport. It was speculated that the point defect energies may have correlated with boundary diffusion and hence would have been a useful screening tool. However, there were none and hence further MD simulations would be required to understand the relationship between the two.

Due to the vast amount of structural and energetic data obtained for the grain boundaries of ceria and STO, considerations of how to further display the data for future publication are currently being undertaken. As discussed, the single point defect calculations suggested the energetic favourability of defect formation in the boundary region, implying that grain boundaries will favour ion migration due to the increased number of defects, but further MD simulations would be required to check.

### 9.3 Heterogeneous Grain Boundaries of STO || CeO<sub>2</sub>

Two structural models of grain boundaries between STO || CeO<sub>2</sub> were investigated with regards to structure, energetics and dynamics. An adapted version of the methodology used in chapters 4 and 5 was used in order to achieve a low strain, highly stable surface match. The simulations carried out highlighted the further importance of substrate phase and surface termination when considering stability. The dynamics of heterogeneous boundaries were further explored where the presence of Gd<sup>3+</sup> and thereby oxygen vacancies was found to significantly increase oxygen diffusion and as a result a reduction in activation energy of 0.3 eV was achieved. The activation energies obtained suggested that the heterogeneous boundary systems enhanced oxygen transport when compared to the bulk and homogeneous grain boundary examples.

Due to the size of heterogeneous boundaries, the simulations carried out were over 1.0 ns, significantly shorter than the 10.0 ns simulations for bulk. In order to achieve a more reliable and extensive representation of transport at the boundary, more robust and rigorous simulation codes could be considered such as DL\_POLY\_4<sup>(223)</sup> which is suitable for simulation systems upwards of 30,000 atoms. Furthermore, more extensive defect schemes could be considered including intrinsic and extrinsic dopants of STO such as La<sup>3+</sup> or Fe<sup>3+</sup> to further investigate the dynamics of oxygen transport. Finally, by isolating the x, y and z components of diffusion, this could be used to assess diffusion parallel to the boundary and perpendicular to the boundary. This would provide further quantitative evidence to show whether the presence of heterogeneous grain boundaries enhance or suppress oxygen transport.

## 9.4 Bulk and Grain Boundaries of LLTO and LLZO

The final two sections focussed on the candidate solid electrolyte materials, LLTO and LLZO, respectively. Each section initially focussed on the dynamics of bulk diffusion in order to investigate whether the potential model used could accurately replicate activation energies consistent with those observed experimentally.

In the case of LLTO, four compositions of intrinsically defective phases were simulated where the lowest activation energy, 0.2 eV, was consistent with experimental data. The importance of the local structure was also investigated for LLTO where the tilting of the  $\text{TiO}_6$  octahedra was highlighted as a factor in facilitating lithium ion diffusion. Simulations were also carried out on the sodium equivalent, NLTO. However, significantly higher activation energies were observed, suggesting that this material would be unsuitable in application. Six grain boundaries of LLTO were structurally and energetically characterised and MD was used to investigate lithium ion transport. The activation energies obtained implied that the presence of grain boundaries in LLTO had little effect on lithium diffusion. However, the  $D_0$  values observed for the grain boundary simulations suggested increased lithium diffusion when compared to the bulk. Due to the activation energies obtained being very close to the bulk value, it was considered that due to the size difference between the boundary and the bulk region, the measured diffusion could possibly account for that in the bulk, therefore more precise techniques would be required to ensure that the diffusion measured is only that within the boundary region. In particular, isolating the x, y and z components of diffusion for each of the grain boundary systems could be used to assess diffusion parallel and perpendicular to the boundary.

Initial simulations of bulk LLZO were carried out to compare the diffusion in the stoichiometric and defective phases. The stoichiometric phase used in simulations was orthorhombic. Experimentally a change in structure from tetragonal to cubic is observed at high temperatures. Future work would include evaluating structural changes of LLZO with increasing temperature to assess whether this structural change occurs when heated using simulations. The Teter potential model was deemed unsuitable for the modelling of LLZO as the extrinsic defect schemes suppressed lithium diffusion, which is not the case experimentally. Similar to LLTO, again six grain boundaries of LLZO were structurally and energetically characterised and further simulated to investigate lithium ion transport. The activation energies and  $D_0$  values obtained implied that the presence of grain boundaries in LLZO had little effect on lithium diffusion. Again, similar approaches would be required to accurately quantify the lithium transport at the boundary. As previously discussed, by isolating the x, y and z components of diffusion, this could be used to assess diffusion parallel and perpendicular to the boundary.

As previously discussed in section 9.2, heterogeneous interfaces of solid electrode materials are an area in which the literature is lacking. Again, using codes such as `DL_POLY_4`<sup>(223)</sup> could be used to model heterogeneous interfaces in LIB examples, such as between one of the two solid electrolyte materials presented with lithium cobalt oxide (LCO) in order to generate a cathode||electrolyte simulation cell which could be used to further assess the role of the interface in lithium ion transport.

## References

1. Sayle TXT, Parker SC, Sayle DC. Ionic conductivity in nano-scale CeO<sub>2</sub>/YSZ heterolayers. *Journal of Materials Chemistry*. 2006;16(11):1067-81.
2. Balachandran U, Eror NG. ELECTRICAL-CONDUCTIVITY IN STRONTIUM-TITANATE. *Journal of Solid State Chemistry*. 1981;39(3):351-9.
3. Catlow CRA. Computer simulation studies of strontium titanate. *J Am Ceram Soc*. 1995;78(12):421-28.
4. Kanchana V, Vaitheeswaran G, Svane A, Delin A. First-principles study of elastic properties of CeO<sub>2</sub>, ThO<sub>2</sub> and PoO<sub>2</sub>. *Journal of Physics-Condensed Matter*. 2006;18(42):9615-24.
5. Chen X, Wu NJ, Smith L, Ignatiev A. Thin-film heterostructure solid oxide fuel cells. *Applied Physics Letters*. 2004;84(14):2700-2.
6. Leng YJ, Chan SH, Jiang SP, Khor KA. Low-temperature SOFC with thin film GDC electrolyte prepared in situ by solid-state reaction. *Solid State Ionics*. 2004;170(1-2):9-15.
7. Atkinson A, Barnett S, Gorte RJ, Irvine JTS, McEvoy AJ, Mogensen M, et al. Advanced anodes for high-temperature fuel cells. *Nature Materials*. 2004;3(1):17-27.
8. Merkle R, Maier J. Defect association in acceptor-doped SrTiO<sub>3</sub>: case study for Fe<sup>3+</sup> V-Ti(O)center dot center dot and Mn<sup>2+</sup> V-Ti(O)center dot center dot. *Physical Chemistry Chemical Physics*. 2003;5(11):2297-303.
9. Chan NH, Smyth DM. NONSTOICHIOMETRY IN SRTIO<sub>3</sub>. *Journal of the Electrochemical Society*. 1978;125(3):C129-C.
10. Eror NG, Balachandran U. HIGH-TEMPERATURE DEFECT STRUCTURE OF ACCEPTOR-DOPED STRONTIUM-TITANATE. *Journal of the American Ceramic Society*. 1982;65(9):426-31.
11. Ohta H. Thermoelectrics based on strontium titanate. *Materials Today*. 2007;10(10):44-9.
12. Hicks LD, Dresselhaus MS. THERMOELECTRIC FIGURE OF MERIT OF A ONE-DIMENSIONAL CONDUCTOR. *Physical Review B*. 1993;47(24):16631-4.
13. Ohta S, Nomura T, Ohta H, Hirano M, Hosono H, Koumoto K. Large thermoelectric performance of heavily Nb-doped SrTiO<sub>3</sub> epitaxial film at high temperature. *Applied Physics Letters*. 2005;87(9).
14. Yamamoto M, Ohta H, Koumoto K. Thermoelectric phase diagram in a CaTiO<sub>3</sub>-SrTiO<sub>3</sub>-BaTiO<sub>3</sub> system. *Applied Physics Letters*. 2007;90(7).
15. Ohta S, Nomura T, Ohta H, Koumoto K. High-temperature carrier transport and thermoelectric properties of heavily La-or Nb-doped SrTiO<sub>3</sub> single crystals. *Journal of Applied Physics*. 2005;97(3):034106.
16. Ravichandran J, Siemons W, Oh DW, Kardel JT, Chari A, Heijmerikx H, et al. High-temperature thermoelectric response of double-doped SrTiO<sub>3</sub> epitaxial films. *Physical Review B*. 2010;82(16).
17. Wang YF, Lee KH, Ohta H, Koumoto K. Thermoelectric properties and their relation to crystal structure of rare earth (RE = La, Nd, Sm and Gd)-doped SrO(SrTiO<sub>3</sub>)<sub>2</sub> Ruddelseden–Popper phase. *IEEE*. 2006:156-60.
18. Koumoto K, Wang YF, Zhang RZ, Kosuga A, Funahashi R. Oxide 'Thermoelectric Materials: A Nanostructuring Approach. In: Clarke DR, Ruhle M, Zok F, editors. *Annual Review of Materials Research*, Vol 40. Palo Alto: Annual Reviews; 2010. p. 363-94.
19. Wang HC, Wang CL, Su WB, Liu J, Zhao Y, Peng H, et al. Enhancement of thermoelectric figure of merit by doping Dy in La<sub>0.1</sub>Sr<sub>0.9</sub>TiO<sub>3</sub> ceramic. *Materials Research Bulletin*. 2010;45(7):809-12.
20. Wang N, Han L, He H, Ba Y, Koumoto K. Effects of mesoporous silica addition on thermoelectric properties of Nb-doped SrTiO<sub>3</sub>. *Journal of Alloys and Compounds*. 2010;497(1):308-11.
21. Kinaci A, Sevik C, Cagin T. Electronic transport properties of SrTiO<sub>3</sub> and its alloys: Sr<sub>1-x</sub>La<sub>x</sub>TiO<sub>3</sub> and SrTi<sub>1-x</sub>M<sub>x</sub>O<sub>3</sub> (M = Nb, Ta). *Physical Review B*. 2010;82(15).

22. Ohta H, Sugiura K, Koumoto K. Recent progress in oxide thermoelectric materials: p-type  $\text{Ca}_3\text{Co}_4\text{O}_9$  and n-type  $\text{SrTiO}_3$ . *Inorganic Chemistry*. 2008;47(19):8429-36.
23. Lewis GV, Catlow CRA. DEFECT STUDIES OF DOPED AND UNDOPED BARIUM-TITANATE USING COMPUTER-SIMULATION TECHNIQUES. *Journal of Physics and Chemistry of Solids*. 1986;47(1):89-97.
24. Yeandel SR, Molinari M, Parker SC. The impact of tilt grain boundaries on the thermal transport in perovskite  $\text{SrTiO}_3$  layered nanostructures. A computational study. *Nanoscale*. 2018;10(31):15010-22.
25. Kienzle O, Exner M, Ernst F. Atomistic structure of  $\Sigma = 3, (111)$  grain boundaries in strontium titanate. *physica status solidi (a)*. 1998;166(1):57-71.
26. Gale JD. GULP: A computer program for the symmetry-adapted simulation of solids. *Journal of the Chemical Society-Faraday Transactions*. 1997;93(4):629-37.
27. De Souza RA, Fleig J, Maier J, Kienzle O, Zhang ZL, Sigle W, et al. Electrical and structural characterization of a low-angle tilt grain boundary in iron-doped strontium titanate. *Journal of the American Ceramic Society*. 2003;86(6):922-8.
28. Benedek NA, Chua AL-S, Elsässer C, Sutton AP, Finnis MW. Interatomic potentials for strontium titanate: An assessment of their transferability and comparison with density functional theory. *Physical Review B*. 2008;78(6):064110.
29. Imai Y, Mukaida M, Tsunoda T. Calculation of electronic energy and density of state of iron-disilicides using a total-energy pseudopotential method, CASTEP. *Thin Solid Films*. 2001;381(2):176-82.
30. Dudeck KJ, Cockayne DJH. Quantitative high resolution electron microscopy image matching applied to the strontium titanate  $\Sigma 3(112)$  grain boundary. In: Baker RT, editor. *Electron Microscopy and Analysis Group Conference 2009*. Bristol: Iop Publishing Ltd; 2010.
31. Schusteritsch G, Pickard CJ. Predicting interface structures: From  $\text{SrTiO}_3$  to graphene. *Physical Review B*. 2014;90(3).
32. Chua ALS, Benedek NA, Chen L, Finnis MW, Sutton AP. A genetic algorithm for predicting the structures of interfaces in multicomponent systems. *Nature Materials*. 2010;9(5):418-22.
33. Zheng ZX, Chen X, Deng BW, Chernatynskiy A, Yang SF, Xiong LM, et al. Phonon thermal transport through tilt grain boundaries in strontium titanate. *Journal of Applied Physics*. 2014;116(7).
34. Schelling PK, Phillpot SR, Keblinski P. Phonon wave-packet dynamics at semiconductor interfaces by molecular-dynamics simulation. *Applied Physics Letters*. 2002;80(14):2484-6.
35. Schelling PK, Phillpot SR, Keblinski P. Kapitza conductance and phonon scattering at grain boundaries by simulation. *Journal of Applied Physics*. 2004;95(11):6082-91.
36. Lee HS, Mizoguchi T, Mistui J, Yamamoto T, Kang SJL, Ikuhara Y. Defect energetics in  $\text{SrTiO}_3$  symmetric tilt grain boundaries. *Physical Review B*. 2011;83(10).
37. Ravikumar V, Dravid V, Wolf D. Atomic structure and properties of the  $(310)$  symmetrical tilt grain boundary (STGB) in  $\text{SrTiO}_3$ . Part I: Atomistic simulations. *Interface Science*. 2000;8(2-3):157-75.
38. Dravid VP, Ravikumar V. Atomic structure and properties of the  $(310)$  symmetrical tilt grain boundary (STGB) in  $\text{SrTiO}_3$  - Part II: Comparison with experimental studies. *Interface Science*. 2000;8(2-3):177-87.
39. Mitsuma T, Tohei T, Shibata N, Mizoguchi T, Yamamoto T, Ikuhara Y. Structures of a  $\Sigma = 9, [110]/[221]$  symmetrical tilt grain boundary in  $\text{SrTiO}_3$ . *Journal of Materials Science*. 2011;46(12):4162-8.
40. Waldow SP, De Souza RA. Computational Study of Oxygen Diffusion along a 100 Dislocations in the Perovskite Oxide  $\text{SrTiO}_3$ . *ACS applied materials & interfaces*. 2016;8(19):12246-56.
41. Waser R. Redox-Based Resistive Switching Memories. *J Nanosci Nanotechnol*. 2012;12(10):7628-40.



42. Wang J, Ye XX, Yaer XB, Zhang BY, Ma W, Miao L. High thermoelectric performance of niobium-doped strontium titanate bulk material affected by all-scale grain boundary and inclusions. *Scripta Materialia*. 2015;99:25-8.
43. Chueh WC, Falter C, Abbott M, Scipio D, Furler P, Haile SM, et al. High-Flux Solar-Driven Thermochemical Dissociation of CO<sub>2</sub> and H<sub>2</sub>O Using Nonstoichiometric Ceria. *Science*. 2010;330(6012):1797-801.
44. Liu Z, Ding D, Liu M, Ding X, Chen D, Li X, et al. High-performance, ceria-based solid oxide fuel cells fabricated at low temperatures. *Journal of Power Sources*. 2013;241:454-9.
45. Wachsman ED, Lee KT. Lowering the Temperature of Solid Oxide Fuel Cells. *Science*. 2011;334(6058):935-9.
46. Feng B, Sugiyama I, Hojo H, Ohta H, Shibata N, Ikuhara Y. Atomic structures and oxygen dynamics of CeO<sub>2</sub> grain boundaries. *Scientific Reports*. 2016;6.
47. An J, Shim JH, Kim Y-B, Park JS, Lee W, Gür TM, et al. MEMS-based thin-film solid-oxide fuel cells. *Mrs Bulletin*. 2014;39(9):798-804.
48. Yuan FL, Liu B, Zhang YW, Weber WJ. Segregation and Migration of the Oxygen Vacancies in the Sigma 3 (111) Tilt Grain Boundaries of Ceria. *Journal of Physical Chemistry C*. 2016;120(12):6625-32.
49. Yuan F, Zhang Y, Weber WJ. Vacancy–Vacancy Interaction Induced Oxygen Diffusion Enhancement in Undoped Nonstoichiometric Ceria. *The Journal of Physical Chemistry C*. 2015;119(23):13153-9.
50. Walsh A, Woodley SM, Catlow CRA, Sokol AA. Potential energy landscapes for anion Frenkel-pair formation in ceria and india. *Solid State Ionics*. 2011;184(1):52-6.
51. Woodley SM, Walker AM. New software for finding transition states by probing accessible, or ergodic, regions. *Molecular Simulation*. 2007;33(15):1229-31.
52. Yasunaga K, Yasuda K, Matsumura S, Sonoda T. Electron energy-dependent formation of dislocation loops in CeO<sub>2</sub>. *Nuclear Instruments and Methods in Physics Research Section B: Beam Interactions with Materials and Atoms*. 2008;266(12–13):2877-81.
53. Souza ECC, Goodenough JB. The origin of grain boundary capacitance in highly doped ceria. *Physical Chemistry Chemical Physics*. 2016;18(8):5901-4.
54. Göbel MC, Gregori G, Maier J. Electronically blocking grain boundaries in donor doped cerium dioxide. *Solid State Ionics*. 2012;215:45-51.
55. Fabbri E, Pergolesi D, Traversa E. Ionic conductivity in oxide heterostructures: the role of interfaces. *Sci Technol Adv Mater*. 2010;11(5).
56. Garcia-Barriocanal J, Rivera-Calzada A, Varela M, Sefrioui Z, Iborra E, Leon C, et al. Colossal ionic conductivity at interfaces of epitaxial ZrO<sub>2</sub> : Y<sub>2</sub>O<sub>3</sub>/SrTiO<sub>3</sub> heterostructures. *Science*. 2008;321(5889):676-80.
57. Dholabhai PP, Aguiar JA, Misra A, Uberuaga BP. Defect interactions with stepped CeO<sub>2</sub>/SrTiO<sub>3</sub> interfaces: Implications for radiation damage evolution and fast ion conduction. *Journal of Chemical Physics*. 2014;140(19).
58. Wakana H, Michikami O. Preparation of CeO<sub>2</sub> / SrTiO<sub>3</sub> bilayers as a barrier material for SIS Josephson junctions. *Physica C: Superconductivity*. 2001;357–360, Part 2:1440-3.
59. Hollmann E, Schubert J, Kutzner R, Wördenweber R. Stress generated modifications of epitaxial ferroelectric SrTiO<sub>3</sub> films on sapphire. *Journal of Applied Physics*. 2009;105(11):114104.
60. Petrov PK, Carlsson EF, Larsson P, Friesel M, Ivanov ZG. Improved SrTiO<sub>3</sub> multilayers for microwave application: Growth and properties. *Journal of Applied Physics*. 1998;84(6):3134-40.
61. Ren YY, Shen Y, Lin YH, Nan CW. Direct observation of lithium dendrites inside garnet-type lithium-ion solid electrolyte. *Electrochem Commun*. 2015;57:27-30.
62. Chen CH, Amine K. Ionic conductivity, lithium insertion and extraction of lanthanum lithium titanate. *Solid State Ionics*. 2001;144(1-2):51-7.

63. Qian DN, Xu B, Cho HM, Hatsukade T, Carroll KJ, Meng YS. Lithium Lanthanum Titanium Oxides: A Fast Ionic Conductive Coating for Lithium-Ion Battery Cathodes. *Chemistry of Materials*. 2012;24(14):2744-51.
64. Inaguma Y, Chen LQ, Itoh M, Nakamura T, Uchida T, Ikuta H, et al. HIGH IONIC-CONDUCTIVITY IN LITHIUM LANTHANUM TITANATE. *Solid State Communications*. 1993;86(10):689-93.
65. Hua CX, Fang XP, Wang ZX, Chen LQ. Lithium storage in perovskite lithium lanthanum titanate. *Electrochem Commun*. 2013;32:5-8.
66. Abhilash KP, Selvin PC, Nalini B, Somasundaram K, Sivaraj P, Bose AC. Study of the temperature dependent transport properties in nanocrystalline lithium lanthanum titanate for lithium ion batteries. *Journal of Physics and Chemistry of Solids*. 2016;91:114-21.
67. Gao X, Fisher CAJ, Kimura T, Ikuhara YH, Moriwake H, Kuwabara A, et al. Lithium Atom and A-Site Vacancy Distributions in Lanthanum Lithium Titanate. *Chemistry of Materials*. 2013;25(9):1607-14.
68. Jay EE, Rushton MJD, Chroneos A, Grimes RW, Kilner JA. Genetics of superionic conductivity in lithium lanthanum titanates. *Physical Chemistry Chemical Physics*. 2015;17(1):178-83.
69. Šalkus T, Kazakevičius E, Kežionis A, Orliukas AF, Badot JC, Bohnke O. Determination of the non-Arrhenius behaviour of the bulk conductivity of fast ionic conductors LLTO at high temperature. *Solid State Ionics*. 2011;188(1):69-72.
70. Catti M. Short-range order and Li<sup>+</sup> ion diffusion mechanisms in Li<sub>5</sub>La<sub>9</sub>□<sub>2</sub>(TiO<sub>3</sub>)<sub>16</sub> (LLTO). *Solid State Ionics*. 2011;183(1):1-6.
71. Chen CH, Du JC. Lithium Ion Diffusion Mechanism in Lithium Lanthanum Titanate Solid-State Electrolytes from Atomistic Simulations. *Journal of the American Ceramic Society*. 2015;98(2):534-42.
72. Stramare S, Thangadurai V, Weppner W. Lithium lanthanum titanates: A review. *Chemistry of Materials*. 2003;15(21):3974-90.
73. SWAMY DT, BABU KE, VEERAAH V. Evidence for high ionic conductivity in lithium–lanthanum titanate, Li<sub>0.29</sub>La<sub>0.57</sub>TiO<sub>3</sub>. *Bulletin of Materials Science*. 2013;36(6):1115-9.
74. Furusawa S-i, Tabuchi H, Sugiyama T, Tao S, Irvine JTS. Ionic conductivity of amorphous lithium lanthanum titanate thin film. *Solid State Ionics*. 2005;176(5–6):553-8.
75. Uhlmann C, Braun P, Illig J, Weber A, Ivers-Tiffée E. Interface and grain boundary resistance of a lithium lanthanum titanate (Li<sub>3</sub>xLa<sub>2/3</sub>-xTiO<sub>3</sub>, LLTO) solid electrolyte. *Journal of Power Sources*. 2016;307:578-86.
76. Imanishi N, Takeda Y, Yamamoto O. Aqueous Lithium-Air Rechargeable Batteries. *Electrochemistry*. 2012;80(10):706-15.
77. Fanah SJ, Yu M, Huq A, Ramezanipour F. Insight into lithium-ion mobility in Li<sub>2</sub>La(TaTi)O-7. *Journal of Materials Chemistry A*. 2018;6(44):22152-60.
78. Hu ZX, Sheng JL, Chen JH, Sheng GQ, Li YM, Fu XZ, et al. Enhanced Li ion conductivity in Ge-doped Li<sub>0.33</sub>La<sub>0.56</sub>TiO<sub>3</sub> perovskite solid electrolytes for all-solid-state Li-ion batteries. *New J Chem*. 2018;42(11):9074-9.
79. Lee SJ, Bae JJ, Son JT. Structural and Electrical Effects of Y-doped Li<sub>0.33</sub>La<sub>0.56</sub>-xYxTiO<sub>3</sub> Solid Electrolytes on All-Solid-State Lithium Ion Batteries. *J Korean Phys Soc*. 2019;74(1):73-7.
80. Yu K, Tian Y, Gu R, Jin L, Ma RP, Sun HC, et al. Ionic conduction, colossal permittivity and dielectric relaxation behavior of solid electrolyte Li<sub>3</sub>xLa<sub>2/3</sub>-xTiO<sub>3</sub> ceramics. *Journal of the European Ceramic Society*. 2018;38(13):4483-7.
81. Ma C, Chen K, Liang CD, Nan CW, Ishikawa R, More K, et al. Atomic-scale origin of the large grain-boundary resistance in perovskite Li-ion-conducting solid electrolytes. *Energy & Environmental Science*. 2014;7(5):1638-42.
82. Geng HX, Lan JL, Mel A, Lin YH, Nan CW. Effect of sintering temperature on microstructure and transport properties of Li<sub>3</sub>xLa<sub>2/3</sub>-xTiO<sub>3</sub> with different lithium contents. *Electrochimica Acta*. 2011;56(9):3406-14.

83. Yan JH, Yu JY, Ding B. Mixed Ionic and Electronic Conductor for Li-Metal Anode Protection. *Advanced Materials*. 2018;30(7).
84. Xu W, Wang JL, Ding F, Chen XL, Nasybutin E, Zhang YH, et al. Lithium metal anodes for rechargeable batteries. *Energy & Environmental Science*. 2014;7(2):513-37.
85. Liu K, Pei A, Lee HR, Kong B, Liu N, Lin DC, et al. Lithium Metal Anodes with an Adaptive "Solid-Liquid" Interfacial Protective Layer. *Journal of the American Chemical Society*. 2017;139(13):4815-20.
86. Zhu YR, Yi TF, Li XY, Xie Y, Luo SH. Improved rate performance of  $\text{LiNi}_{0.5}\text{Mn}_{1.5}\text{O}_4$  as cathode of lithium-ion battery by  $\text{Li}_{0.33}\text{La}_{0.56}\text{TiO}_3$  coating. *Materials Letters*. 2019;239:56-8.
87. Yi TF, Li YM, Li XY, Pan JJ, Zhang Q, Zhu YR. Enhanced electrochemical property of  $\text{FePO}_4$ -coated  $\text{LiNi}_{0.5}\text{Mn}_{1.5}\text{O}_4$  as cathode materials for Li-ion battery. *Sci Bull*. 2017;62(14):1004-10.
88. Wolfenstine J, Allen JL, Sakamoto J, Siegel DJ, Choe H. Mechanical behavior of Li-ion-conducting crystalline oxide-based solid electrolytes: a brief review. *Ionics*. 2018;24(5):1271-6.
89. Cho YH, Wolfenstine J, Rangasamy E, Kim H, Choe H, Sakamoto J. Mechanical properties of the solid Li-ion conducting electrolyte:  $\text{Li}_{0.33}\text{La}_{0.57}\text{TiO}_3$ . *Journal of Materials Science*. 2012;47(16):5970-7.
90. Hu XT, Yan G, Cheng X, Malzbender J, Qiang WJ, Huang BX. Electrochemical and mechanical stability of  $\text{Li}_x\text{La}_{0.557}\text{TiO}_3$ -perovskite electrolyte at various voltages. *Journal of the American Ceramic Society*. 2019;102(4):1953-60.
91. Trong LD, Thao TT, Dinh NN. Characterization of the Li-ionic conductivity of  $\text{La}_{(2/3-x)}\text{Li}_3\text{TiO}_3$  ceramics used for all-solid-state batteries. *Solid State Ionics*. 2015;278:228-32.
92. Wolfenstine J, Allen JL, Read J, Sakamoto J, Gonzalez-Doncel G. Hot-pressed  $\text{Li}_{0.33}\text{La}_{0.57}\text{TiO}_3$ . *Journal of Power Sources*. 2010;195(13):4124-8.
93. Kawai H, Kuwano J. LITHIUM ION CONDUCTIVITY OF A-SITE DEFICIENT PEROVSKITE SOLID-SOLUTION  $\text{La}_{0.67}\text{XLi}_{3-x}\text{TiO}_3$ . *Journal of the Electrochemical Society*. 1994;141(7):L78-L9.
94. Kwon WJ, Kim H, Jung KN, Cho W, Kim SH, Lee JW, et al. Enhanced  $\text{Li}^+$  conduction in perovskite  $\text{Li}_3\text{La}_{2/3-x}\text{square } 1/3-2\text{TiO}_3$  solid-electrolytes via microstructural engineering. *Journal of Materials Chemistry A*. 2017;5(13):6257-62.
95. Guo X, Maram PS, Navrotsky A. A correlation between formation enthalpy and ionic conductivity in perovskite-structured  $\text{Li}_3\text{La}_{0.67-x}\text{TiO}_3$  solid lithium ion conductors. *Journal of Materials Chemistry A*. 2017;5(25):12951-7.
96. Wu JF, Guo X. Origin of the low grain boundary conductivity in lithium ion conducting perovskites:  $\text{Li}_3\text{La}_{0.67-x}\text{TiO}_3$ . *Physical Chemistry Chemical Physics*. 2017;19(8):5880-7.
97. Bruce PG, Freunberger SA, Hardwick LJ, Tarascon JM. Li-O<sub>2</sub> and Li-S batteries with high energy storage. *Nature Materials*. 2012;11(1):19-29.
98. Thangadurai V, Pinzaru D, Narayanan S, Baral AK. Fast Solid-State Li Ion Conducting Garnet-Type Structure Metal Oxides for Energy Storage. *J Phys Chem Lett*. 2015;6(2):292-9.
99. Wagner R, Redhammer GJ, Rettenwander D, Tippelt G, Welzl A, Taibl S, et al. Fast Li-Ion-Conducting Garnet-Related  $\text{Li}_{7-3x}\text{Fe}_x\text{La}_3\text{Zr}_2\text{O}_{12}$  with Uncommon  $\text{I}(4)_{\text{over-bar}}3\text{d}$  Structure. *Chemistry of Materials*. 2016;28(16):5943-51.
100. Thompson T, Yu SH, Williams L, Schmidt RD, Garcia-Mendez R, Wolfenstine J, et al. Electrochemical Window of the Li-Ion Solid Electrolyte  $\text{Li}_7\text{La}_3\text{Zr}_2\text{O}_{12}$ . *ACS Energy Lett*. 2017;2(2):462-8.
101. Yeandel SR, Chapman BJ, Slater PR, Goddard P. Structure and Lithium-Ion Dynamics in Fluoride-Doped Cubic  $\text{Li}_7\text{La}_3\text{Zr}_2\text{O}_{12}$  (LLZO) Garnet for Li Solid-State Battery Applications. *Journal of Physical Chemistry C*. 2018;122(49):27811-9.
102. Liu C, Wen ZY, Rui K. High Ion Conductivity in Garnet-type F-doped  $\text{Li}_7\text{La}_3\text{Zr}_2\text{O}_{12}$ . *J Inorg Mater*. 2015;30(9):995-1000.
103. Chen Y, Rangasamy E, dela Cruz CR, Liang CD, An K. A study of suppressed formation of low-conductivity phases in doped  $\text{Li}_7\text{La}_3\text{Zr}_2\text{O}_{12}$  garnets by in situ neutron diffraction. *Journal of Materials Chemistry A*. 2015;3(45):22868-76.

104. Wolfenstine J, Rangasamy E, Allen JL, Sakamoto J. High conductivity of dense tetragonal  $\text{Li}_7\text{La}_3\text{Zr}_2\text{O}_{12}$ . *Journal of Power Sources*. 2012;208:193-6.
105. Murugan R, Thangadurai V, Weppner W. Fast lithium ion conduction in garnet-type  $\text{Li}_7\text{La}_3\text{Zr}_2\text{O}_{12}$ . *Angewandte Chemie-International Edition*. 2007;46(41):7778-81.
106. Howard MA, Clemens O, Kendrick E, Knight KS, Apperley DC, Anderson PA, et al. Effect of Ga incorporation on the structure and Li ion conductivity of  $\text{La}_3\text{Zr}_2\text{Li}_7\text{O}_{12}$ . *Dalton Transactions*. 2012;41(39):12048-53.
107. Allen JL, Wolfenstine J, Rangasamy E, Sakamoto J. Effect of substitution (Ta, Al, Ga) on the conductivity of  $\text{Li}_7\text{La}_3\text{Zr}_2\text{O}_{12}$ . *Journal of Power Sources*. 2012;206:315-9.
108. Ohta S, Kobayashi T, Asaoka T. High lithium ionic conductivity in the garnet-type oxide  $\text{Li}_{7-x}\text{La}_3(\text{Zr}_2\text{-X, Nb-X})\text{O}_{12}$  ( $x=0-2$ ). *Journal of Power Sources*. 2011;196(6):3342-5.
109. Thompson T, Wolfenstine J, Allen J, Johannes M, Huq A, Sakamoto J. Tetragonal vs. cubic phase stability in Al - free Ta doped  $\text{Li}_7\text{La}_3\text{Zr}_2\text{O}_{12}$  garnet Li ion solid electrolyte. *Abstracts of Papers of the American Chemical Society*. 2014;248.
110. Geiger CA, Alekseev E, Lazic B, Fisch M, Armbruster T, Langner R, et al. Crystal Chemistry and Stability of " $\text{Li}_7\text{La}_3\text{Zr}_2\text{O}_{12}$ " Garnet: A Fast Lithium-Ion Conductor. *Inorganic Chemistry*. 2011;50(3):1089-97.
111. Rettenwander D, Blaha P, Laskowski R, Schwarz K, Bottke P, Wilkening M, et al. DFT Study of the Role of  $\text{Al}^{3+}$  in the Fast Ion-Conductor  $\text{Li}_{7-3x}\text{Al}_x\text{La}_3\text{Zr}_2\text{O}_{12}$  Garnet. *Chemistry of Materials*. 2014;26(8):2617-23.
112. Burbano M, Carlier D, Boucher F, Morgan BJ, Salanne M. Sparse Cyclic Excitations Explain the Low Ionic Conductivity of Stoichiometric  $\text{Li}_7\text{La}_3\text{Zr}_2\text{O}_{12}$ . *Physical Review Letters*. 2016;116(13).
113. Canepa P, Dawson JA, Gautam GS, Satham JM, Parker SC, Islam MS. Particle Morphology and Lithium Segregation to Surfaces of the  $\text{Li}_7\text{La}_3\text{Zr}_2\text{O}_{12}$  Solid Electrolyte. *Chemistry of Materials*. 2018;30(9):3019-27.
114. Brugge RH, Kilner JA, Aguadero A. Germanium Germanium as a donor dopant in garnet electrolytes. *Solid State Ionics*. 2019;337:154-60.
115. Xiang X, Chen F, Shen Q, Zhang LM, Chen CL. Effect of the lithium ion concentration on the lithium ion conductivity of Ga-doped LLZO. *Mater Res Express*. 2019;6(8).
116. Wang XS, Liu J, Yin R, Xu YC, Cui YH, Zhao L, et al. High lithium ionic conductivity of garnet-type oxide  $\text{Li}_{7+x}\text{La}_3\text{Zr}_2\text{-xSm}_x\text{O}_{12}$  ( $x=0-0.1$ ) ceramics. *Materials Letters*. 2018;231:43-6.
117. Kerman K, Luntz A, Viswanathan V, Chiang YM, Chen ZB. Review-Practical Challenges Suppressing the Development of Solid State Li Ion Batteries. *Journal of the Electrochemical Society*. 2017;164(7):A1731-A44.
118. Porz L, Swamy T, Sheldon BW, Rettenwander D, Fromling T, Thaman HL, et al. Mechanism of Lithium Metal Penetration through Inorganic Solid Electrolytes. *Adv Energy Mater*. 2017;7(20).
119. Kim Y, Yoo A, Schmidt R, Sharafi A, Lee H, Wolfenstine J, et al. Electrochemical Stability of  $\text{Li}_{6.5}\text{La}_3\text{Zr}_{1.5}\text{M}_{0.5}\text{O}_{12}$  ( $M = \text{Nb}$  or  $\text{Ta}$ ) against Metallic Lithium. *Front Energy Res*. 2016;4.
120. Ohta S, Seki J, Yagi Y, Kihira Y, Tani T, Asaoka T. Co-sinterable lithium garnet-type oxide electrolyte with cathode for all-solid-state lithium ion battery. *Journal of Power Sources*. 2014;265:40-4.
121. Tenhaeff WE, Rangasamy E, Wang YY, Sokolov AP, Wolfenstine J, Sakamoto J, et al. Resolving the Grain Boundary and Lattice Impedance of Hot-Pressed  $\text{Li}_7\text{La}_3\text{Zr}_2\text{O}_{12}$  Garnet Electrolytes. *ChemElectroChem*. 2014;1(2):375-8.
122. Li YQ, Wang Z, Li CL, Cao Y, Guo XX. Densification and ionic-conduction improvement of lithium garnet solid electrolytes by flowing oxygen sintering. *Journal of Power Sources*. 2014;248:642-6.
123. El Shinawi H, Janek J. Stabilization-of cubic lithium-stuffed garnets of the type " $\text{Li}_7\text{La}_3\text{Zr}_2\text{O}_{12}$ " by addition of gallium. *Journal of Power Sources*. 2013;225:13-9.

124. David IN, Thompson T, Wolfenstine J, Allen JL, Sakamoto J. Microstructure and Li-Ion Conductivity of Hot- Pressed Cubic  $\text{Li}_7\text{La}_3\text{Zr}_2\text{O}_{12}$ . *Journal of the American Ceramic Society*. 2015;98(4):1209-14.
125. Tsai CL, Roddatis V, Chandran CV, Ma QL, Uhlenbruck S, Bram M, et al.  $\text{Li}_7\text{La}_3\text{Zr}_2\text{O}_{12}$  Interface Modification for Li Dendrite Prevention. *ACS applied materials & interfaces*. 2016;8(16):10617-26.
126. Thompson T, Sharafi A, Johannes MD, Huq A, Allen JL, Wolfenstine J, et al. A Tale of Two Sites: On Defining the Carrier Concentration in Garnet-Based Ionic Conductors for Advanced Li Batteries. *Adv Energy Mater*. 2015;5(11).
127. Yu S, Siegel DJ. Grain Boundary Contributions to Li-Ion Transport in the Solid Electrolyte  $\text{Li}_7\text{La}_3\text{Zr}_2\text{O}_{12}$  (LLZO). *Chemistry of Materials*. 2017;29(22):9639-47.
128. Born M, Huang K. *Dynamical Theory of Crystal Lattices*. Press OU, editor. Oxford 1954.
129. Ewald PP. Die Berechnung optischer und elektrostatischer Gitterpotentiale. *Annalen der Physik*. 1921;369(3):253-87.
130. Parry DE. ELECTROSTATIC POTENTIAL IN SURFACE REGION OF AN IONIC-CRYSTAL. *Surface Science*. 1975;49(2):433-40.
131. Buckingham RA. The Classical Equation of State of Gaseous Helium, Neon and Argon 1938 1938-10-25 00:00:00. 264-83 p.
132. Canepa P. *New Insights on Iron and Lead-based Materials Beyond Density Functional Theory*: University of Kent; 2012.
133. Pedone A, Malavasi G, Menziani MC, Cormack AN, Segre U. A new self-consistent empirical interatomic potential model for oxides, silicates, and silica-based glasses. *Journal of Physical Chemistry B*. 2006;110(24):11780-95.
134. Sayle TXT, Molinari M, Das S, Bhatta UM, Mobus G, Parker SC, et al. Environment-mediated structure, surface redox activity and reactivity of ceria nanoparticles. *Nanoscale*. 2013;5(13):6063-73.
135. John Purton, Private Communication
136. Watson GW, Kelsey ET, deLeeuw NH, Harris DJ, Parker SC. Atomistic simulation of dislocations, surfaces and interfaces in MgO. *Journal of the Chemical Society-Faraday Transactions*. 1996;92(3):433-8.
137. Tasker PW, Duffy DM. The structure and properties of the stepped surfaces of MgO and NiO. *Surface Science*. 1984;137(1):91-102.
138. Fletcher R, Reeves CM. Function minimization by conjugate gradients. *The Computer Journal*. 1964;7(2):149-54.
139. Norgett MJ, Fletcher R. Fast matrix methods for calculating the relaxation about defects in crystals. *Journal of Physics Part C Solid State Physics*. 1970;3(11):L190-&.
140. Broyden CG. The Convergence of a Class of Double-rank Minimization Algorithms 1. General Considerations. *IMA Journal of Applied Mathematics*. 1970;6(1):76-90.
141. Smith W, Forester TR. DL\_POLY\_2.0: A general-purpose parallel molecular dynamics simulation package. *Journal of Molecular Graphics*. 1996;14(3):136-41.
142. Hoover WG. Canonical dynamics: equilibrium phase-space distributions. *Physical Review A*. 1985;31(3):1695-7.
143. Catlow R. *Solids: Computer Modeling*. Encyclopedia of Inorganic and Bioinorganic Chemistry: John Wiley & Sons, Ltd; 2011.
144. Mott N, Littleton M. Conduction in polar crystals. I. Electrolytic conduction in solid salts. *Transactions of the Faraday Society*. 1938.
145. Hellenbrandt M. The Inorganic Crystal Structure Database (ICSD)—Present and Future. *Crystallography Reviews*. 2004;10(1):17-22.
146. TASKER, PW, DUFFY, DM. ON THE STRUCTURE OF TWIST GRAIN-BOUNDARIES IN IONIC OXIDES. 1983;47.

147. Tasker PW. Stability of Ionic-Crystal Surfaces. *Journal of Physics C-Solid State Physics*. 1979;12(22):4977-84.
148. Tasker PW. SURFACE ENERGIES, SURFACE TENSIONS AND SURFACE-STRUCTURE OF THE ALKALI-HALIDE CRYSTALS. *Philosophical Magazine a-Physics of Condensed Matter Structure Defects and Mechanical Properties*. 1979;39(2):119-36.
149. Lejcek P, Hofmann S. THERMODYNAMICS AND STRUCTURAL ASPECTS OF GRAIN-BOUNDARY SEGREGATION. *Crit Rev Solid State Mat Sci*. 1995;20(1):1-85.
150. Lejcek P. Grain Boundary Segregation in Metals. *Grain Boundary Segregation in Metals* 2010. p. 1-239.
151. Wolf D, Lutsko JF. ON THE GEOMETRICAL RELATIONSHIP BETWEEN TILT AND TWIST GRAIN-BOUNDARIES. *Zeitschrift Fur Kristallographie*. 1989;189(3-4):239-62.
152. Sutton AP, Balluffi RW. *Interfaces in Crystalline Materials*. 1995:819.
153. Brandon DG. The structure of high-angle grain boundaries. *Acta Metallurgica*. 1966;14:1479-84.
154. Winning M, Gottstein G, Shvindlerman LS. On the mechanisms of grain boundary migration. *Acta Materialia*. 2002;50(2):353-63.
155. Ashby MF, Spaepen F, Williams S. The structure of grain boundaries described as a packing of polyhedra. *Acta Metallurgica*. 1978;26(11):1647-63.
156. Gleiter H, Chalmers B. HIGH-ANGLE GRAIN-BOUNDARIES. *Progress in Materials Science*. 1972;16:1-+.
157. Kronberg ML, Wilson FH. SECONDARY RECRYSTALLIZATION IN COPPER. *Transactions of the American Institute of Mining and Metallurgical Engineers*. 1949;185(8):501-14.
158. Watanabe T. AN APPROACH TO GRAIN-BOUNDARY DESIGN FOR STRONG AND DUCTILE POLYCRYSTALS. *Res Mechanica*. 1984;11(1):47-84.
159. Bispo GFD, Jackson RA, Valerio MEG. Modelling of Intrinsic Defects in CaYAl<sub>3</sub>O<sub>7</sub>. *Acta Phys Pol A*. 2018;133(4):781-4.
160. Araujo RM, Valerio MEG, Jackson RA. Computer Modelling of Hafnium Doping in Lithium Niobate. *Crystals*. 2018;8(3).
161. Araujo RM, Valerio MEG, Jackson RA. Computer modelling of trivalent metal dopants in lithium niobate. *Journal of Physics-Condensed Matter*. 2008;20(3).
162. Momma K, Izumi F. VESTA: a three-dimensional visualization system for electronic and structural analysis. *Journal of Applied Crystallography*. 2008;41:653-8.
163. Almeida BG, Pietka A, Caldelas P, Mendes JA, Ribeiro JL. Determination of infrared optical parameters of SrTiO<sub>3</sub> thin films from the reflectivity spectrum. *Thin Solid Films*. 2006;513(1-2):275-82.
164. Azough F, Jackson SS, Ekren D, Freer R, Molinari M, Yeandel SR, et al. Concurrent La and A-Site Vacancy Doping Modulates the Thermoelectric Response of SrTiO<sub>3</sub>: Experimental and Computational Evidence. *ACS applied materials & interfaces*. 2017;9(48):41988-2000.
165. Ekuma CE, Jarrell M, Moreno J, Bagayoko D. First principle electronic, structural, elastic, and optical properties of strontium titanate. *AIP Adv*. 2012;2(1).
166. Srivastava M, Das AK, Khanra P, Uddin ME, Kim NH, Lee JH. Characterizations of in situ grown ceria nanoparticles on reduced graphene oxide as a catalyst for the electrooxidation of hydrazine. *Journal of Materials Chemistry A*. 2013;1(34):9792-801.
167. John Purton, Private Communications, Daresbury Laboratory
168. Larraz G, Orera A, Sanjuan ML. Cubic phases of garnet-type Li<sub>7</sub>La<sub>3</sub>Zr<sub>2</sub>O<sub>12</sub>: the role of hydration. *Journal of Materials Chemistry A*. 2013;1(37):11419-28.
169. Thomas BS, Marks NA, Begg BD. Defects and threshold displacement energies in SrTiO<sub>3</sub> perovskite using atomistic computer simulations. *Nuclear Instruments & Methods in Physics Research Section B-Beam Interactions with Materials and Atoms*. 2007;254(2):211-8.
170. Wang XF, Lu XM, Zhang C, Wu XB, Cai W, Peng S, et al. Oxygen-vacancy-related high-temperature dielectric relaxation in SrTiO<sub>3</sub> ceramics. *Journal of Applied Physics*. 2010;107(11).

171. Arima T, Yamasaki S, Inagaki Y, Idemitsu K. Evaluation of thermal properties of UO<sub>2</sub> and PuO<sub>2</sub> by equilibrium molecular dynamics simulations from 300 to 2000 K. *Journal of Alloys and Compounds*. 2005;400(1-2):43-50.
172. Arima T, Yamasaki S, Inagaki Y, Idemitsu K. Evaluation of thermal conductivity of hypostoichiometric (U, Pu)O<sub>2-x</sub> solid solution by molecular dynamics simulation at temperatures up to 2000 K. *Journal of Alloys and Compounds*. 2006;415(1-2):43-50.
173. Arima T, Yoshida K, Idemitsu K, Inagaki Y, Sato I. Molecular dynamics analysis of diffusion of uranium and oxygen ions in uranium dioxide. In: Rao L, Tobin JG, Shuh DK, editors. *Actinides 2009*. Bristol: Iop Publishing Ltd; 2010.
174. Ackermann S, Scheffe JR, Steinfeldt A. Diffusion of Oxygen in Ceria at Elevated Temperatures and Its Application to H<sub>2</sub>O/CO<sub>2</sub> Splitting Thermochemical Redox Cycles. *Journal of Physical Chemistry C*. 2014;118(10):5216-25.
175. Steele BCH. Fuel-cell technology - Running on natural gas. *Nature*. 1999;400(6745):619-+.
176. Steele BCH, Heinzel A. Materials for fuel-cell technologies. *Nature*. 2001;414(6861):345-52.
177. Shao ZP, Haile SM. A high-performance cathode for the next generation of solid-oxide fuel cells. *Nature*. 2004;431(7005):170-3.
178. Chueh WC, Hao Y, Jung W, Haile SM. High electrochemical activity of the oxide phase in model ceria-Pt and ceria-Ni composite anodes. *Nature Materials*. 2012;11(2):155-61.
179. Papaefthimiou V, Shishkin M, Niakolas DK, Athanasiou M, Law YT, Arrigo R, et al. On the Active Surface State of Nickel-Ceria Solid Oxide Fuel Cell Anodes During Methane Electrooxidation. *Adv Energy Mater*. 2013;3(6):762-9.
180. Chen D, Bishop SR, Tuller HL. Praseodymium-cerium oxide thin film cathodes: Study of oxygen reduction reaction kinetics. *Journal of Electroceramics*. 2012;28(1):62-9.
181. Guo X, Waser R. Electrical properties of the grain boundaries of oxygen ion conductors: Acceptor-doped zirconia and ceria. *Progress in Materials Science*. 2006;51(2):151-210.
182. Sato Y, Buban JP, Mizoguchi T, Shibata N, Yodogawa M, Yamamoto T, et al. Role of Pr segregation in acceptor-state formation at ZnO grain boundaries. *Physical Review Letters*. 2006;97(10).
183. Symington, A., Molinari M., Statham, J. Wu, J., Parker, S.C. The role of dopant segregation on the oxygen vacancy distribution and oxygen diffusion in CeO<sub>2</sub> grain boundaries. *J. Phys. Energy*. 1-13. 2019.
184. Sun LX, Marrocchelli D, Yildiz B. Edge dislocation slows down oxide ion diffusion in doped CeO<sub>2</sub> by segregation of charged defects. *Nat Commun*. 2015;6.
185. Inaba H, Tagawa H. Ceria-based solid electrolytes - Review. *Solid State Ionics*. 1996;83(1-2):1-16.
186. Jaiswal N, Tanwar K, Suman R, Kumar D, Upadhyay S, Parkash O. A brief review on ceria based solid electrolytes for solid oxide fuel cells. *Journal of Alloys and Compounds*. 2019;781:984-1005.
187. Eguchi K, Setoguchi T, Inoue T, Arai H. ELECTRICAL-PROPERTIES OF CERIA-BASED OXIDES AND THEIR APPLICATION TO SOLID OXIDE FUEL-CELLS. *Solid State Ionics*. 1992;52(1-3):165-72.
188. Mori T, Drennan J, Lee JH, Li JG, Ikegami T. Oxide ionic conductivity and microstructures of Sm- or La-doped CeO<sub>2</sub>-based systems. *Solid State Ionics*. 2002;154:461-6.
189. Kharton VV, Marques FMB, Atkinson A. Transport properties of solid oxide electrolyte ceramics: a brief review. *Solid State Ionics*. 2004;174(1-4):135-49.
190. Williams NR, Molinari M, Parker SC, Storr MT. Atomistic investigation of the structure and transport properties of tilt grain boundaries of UO<sub>2</sub>. *Journal of Nuclear Materials*. 2015;458(0):45-55.
191. Shibata N, Oba F, Yamamoto T, Sakuma T, Ikuhara Y. Grain-boundary faceting at a Sigma=3, 110 /{112} grain boundary in a cubic zirconia bicrystal. *Philosophical Magazine*. 2003;83(19):2221-46.
192. Fisher CAJ, Matsubara H. The influence of grain boundary misorientation on ionic conductivity in YSZ. *Journal of the European Ceramic Society*. 1999;19:703-7.

193. Shibata N, Oba F, Yamamoto T, Ikuhara Y. Structure, energy and solute segregation behaviour of 110 symmetric tilt grain boundaries in yttria-stabilized cubic zirconia. *Philosophical Magazine*. 2004;84(23):2381-415.
194. Irshad M, Siraj K, Raza R, Javed F, Ahsan M, Shakir I, et al. High performance of SDC and GDC core shell type composite electrolytes using methane as a fuel for low temperature SOFC. *AIP Adv*. 2016;6(2).
195. Gunn DSD, Allan NL, Purton JA. Adaptive kinetic Monte Carlo simulation of solid oxide fuel cell components. *Journal of Materials Chemistry A*. 2014;2(33):13407-14.
196. Reddy KR, Karan K. Sinterability, mechanical, microstructural, and electrical properties of gadolinium-doped ceria electrolyte for low-temperature solid. *Journal of Electroceramics*. 2005;15(1):45-56.
197. Liu J, Tu TP, Peng KP. Preparation and properties of LSB-doped GDC electrolytes for intermediate temperature solid oxide fuel cells. *Ionics*. 2018;24(11):3543-54.
198. Marina OA, Canfield NL, Stevenson JW. Thermal, electrical, and electrocatalytic properties of lanthanum-doped strontium titanate. *Solid State Ionics*. 2002;149(1-2):21-8.
199. Tuller HL, Jung W, Haga K. Investigation of Cathode Behavior of Model Thin Film SrTi(1-x)Fe(x)O(3-delta) Mixed Ionic-Electronic Conducting Electrodes. In: Traversa E, Armstrong TR, Eguchi K, Palacin MR, editors. *Solid-State Ionics-2008*. Warrendale: Materials Research Society; 2009. p. 3-13.
200. Zhang SL, Wang HQ, Lu MY, Zhang AP, Moggi LV, Liu QY, et al. Cobalt-substituted SrTi<sub>0.3</sub>Fe<sub>0.7</sub>O<sub>3-δ</sub>: a stable high-performance oxygen electrode material for intermediate-temperature solid oxide electrochemical cells. *Energy & Environmental Science*. 2018;11(7):1870-9.
201. Yoo KB, Park BH, Choi GM. Stability and performance of SOFC with SrTiO<sub>3</sub>-based anode in CH<sub>4</sub> fuel. *Solid State Ionics*. 2012;225:104-7.
202. Ahn K, Jung S, Vohs JM, Gorte RJ. A support layer for solid oxide fuel cells. *Ceramics International*. 2007;33(6):1065-70.
203. Slater PR, Fagg DP, Irvine JTS. Synthesis and electrical characterisation of doped perovskite titanates as potential anode materials for solid oxide fuel cells. *Journal of Materials Chemistry*. 1997;7(12):2495-8.
204. Li X, Zhao HL, Gao F, Zhu ZM, Chen N, Shen W. Synthesis and electrical properties of Co-doped Y<sub>0.08</sub>Sr<sub>0.92</sub>TiO<sub>3-δ</sub> as a potential SOFC anode. *Solid State Ionics*. 2008;179(27-32):1588-92.
205. Szot K, Speier W, Bihlmayer G, Waser R. Switching the electrical resistance of individual dislocations in single-crystalline SrTiO<sub>3</sub>. *Nature Materials*. 2006;5(4):312-20.
206. Kienzle O, Ernst F. Effect of shear stress on the atomistic structure of a grain boundary in strontium titanate. *Journal of the American Ceramic Society*. 1997;80(7):1639-44.
207. Zhang ZL, Sigle W, Phillipp F, Ruhle M. Direct atom-resolved imaging of oxides and their grain boundaries. *Science*. 2003;302(5646):846-9.
208. Astala R, Bristowe PD. First-principles calculations of an oxygen deficient Sigma=3 (111) 10(1)over-bar grain boundary in strontium titanate. *Journal of Physics-Condensed Matter*. 2002;14(25):6455-67.
209. Gemming S, Schreiber M. Impurity and vacancy clustering at the Sigma 3(111) 1-10 grain boundary in strontium titanate. *Chemical Physics*. 2005;309(1):3-13.
210. Metlenko V, Ramadan AHH, Gunkel F, Du HC, Schraknepper H, Hoffmann-Eifert S, et al. Do dislocations act as atomic autobahns for oxygen in the perovskite oxide SrTiO<sub>3</sub>? *Nanoscale*. 2014;6(21):12864-76.
211. Imaeda M, Mizoguchi T, Sato Y, Lee H-S, Findlay S, Shibata N, et al. Atomic structure, electronic structure, and defect energetics in [001](310) Σ 5 grain boundaries of SrTiO<sub>3</sub> and BaTiO<sub>3</sub>. *Physical Review B*. 2008;78(24):245320.
212. Browning ND, Pennycook SJ, Chisholm MF, McGibbon MM, McGibbon AJ. Observation of structural units at symmetric [001] tilt boundaries in SrTiO<sub>3</sub>. *Interface Science*. 1995;2(4):397-423.



213. Jung W, Tuller HL. Impedance study of  $\text{SrTi}_{1-x}\text{Fe}_x\text{O}_{3-\delta}$  ( $x=0.05$  to  $0.80$ ) mixed ionic-electronic conducting model cathode. *Solid State Ionics*. 2009;180(11-13):843-7.
214. Overbury SH, Huntley DR, Mullins DR, Ailey KS, Radulovic PV. Surface studies of model supported catalysts: NO adsorption on Rh/CeO<sub>2</sub>(001). *J Vac Sci Technol A*. 1997;15(3):1647-52.
215. Kim YJ, Gao Y, Herman GS, Thevuthasan S, Jiang W, McCready DE, et al. Growth and structure of epitaxial CeO<sub>2</sub> by oxygen-plasma-assisted molecular beam epitaxy. *J Vac Sci Technol A*. 1999;17(3):926-35.
216. Sickafus KE, Grimes RW, Valdez JA, Cleave A, Tang M, Ishimaru M, et al. Radiation-induced amorphization resistance and radiation tolerance in structurally related oxides. *Nature Materials*. 2007;6(3):217-23.
217. Uberuaga BP, Smith R, Cleave AR, Montalenti F, Henkelman G, Grimes RW, et al. Structure and mobility of defects formed from collision cascades in MgO. *Physical Review Letters*. 2004;92(11).
218. Sickafus KE, Matzke H, Hartmann T, Yasuda K, Valdez JA, Chodak P, et al. Radiation damage effects in zirconia. *Journal of Nuclear Materials*. 1999;274(1-2):66-77.
219. Weber WJ, Ewing RC, Catlow CRA, de la Rubia TD, Hobbs LW, Kinoshita C, et al. Radiation effects in crystalline ceramics for the immobilization of high-level nuclear waste and plutonium. *Journal of Materials Research*. 1998;13(6):1434-84.
220. Yamada T, Sandu CS, Gureev M, Sherman VO, Noeth A, Muralt P, et al. Self-Assembled Perovskite-Fluorite Oblique Nanostructures for Adaptive (Tunable) Electronics. *Advanced Materials*. 2009;21(13):1363-7.
221. Sadykov VA, Borchert YV, Alikina GM, Lukashevich AI, Mezentseva NV, Muzykantov VS, et al. Synthesis and properties of nanocomposites with mixed ionic-electronic conductivity on the basis of oxide phases with perovskite and fluorite structures. *Glass Phys Chem*. 2007;33(4):320-34.
222. Sadykov V, Usoltsev V, Yermeev N, Mezentseva N, Pelipenko V, Krieger T, et al. Functional nanoceramics for intermediate temperature solid oxide fuel cells and oxygen separation membranes. *Journal of the European Ceramic Society*. 2013;33(12):2241-8.
223. Martin P, Spagnoli D, Marmier A, Parker SC, Sayle DC, Watson G. Application of molecular dynamics DL\_POLY codes to interfaces of inorganic materials. *Molecular Simulation*. 2006;32(12-13):1079-93.
224. Lee JM, Kim SH, Tak Y, Yoon YS. Study on the LLT solid electrolyte thin film with LiPON interlayer intervening between LLT and electrodes. *Journal of Power Sources*. 2006;163(1):173-9.
225. Abe T, Sagane F, Ohtsuka M, Iriyama Y, Ogumi Z. Lithium-ion transfer at the interface between lithium-ion conductive ceramic electrolyte and liquid electrolyte - A key to enhancing the rate capability of lithium-ion batteries. *Journal of the Electrochemical Society*. 2005;152(11):A2151-A4.
226. Hara M, Nakano H, Dokko K, Okuda S, Kaeriyama A, Kanamura K. Fabrication of all solid-state lithium-ion batteries with three-dimensionally ordered composite electrode consisting of  $\text{Li}_{0.35}\text{La}_{0.55}\text{TiO}_3$  and  $\text{LiMn}_2\text{O}_4$ . *Journal of Power Sources*. 2009;189(1):485-9.
227. Inaguma Y, Katsumata T, Itoh M. Lithium ion conductivity in A-site deficient perovskites  $\text{Sr}_{0.5}\text{La}_{0.05}\text{Li}_{0.35}$  square  $0.1\text{Ti}_{0.5}\text{Ta}_{0.5}\text{O}_3$  and  $\text{Sr}_{0.35}\text{La}_{0.15}\text{Li}_{0.35}$  square  $0.15\text{Ti}_{0.5}\text{Ta}_{0.5}\text{O}_3$ . *Electrochemistry*. 2000;68(6):534-6.
228. Mizumoto K, Hayashi S. Lithium ion mobility and activation energy for lithium ion conduction in A-site deficient perovskites  $\text{La}_{1/3-x}\text{Li}_x\text{TaO}_3$ . *J Ceram Soc Jpn*. 1998;106(4):369-71.
229. Inaguma Y, Katsumata T, Itoh M, Morii Y. Crystal structure of a lithium ion-conducting perovskite  $\text{La}_{2/3-x}\text{Li}_x\text{TiO}_3$  ( $x=0.05$ ). *Journal of Solid State Chemistry*. 2002;166(1):67-72.
230. Harada Y, Hirakoso Y, Kawai H, Kuwano J. Order-disorder of the A-site ions and lithium ion conductivity in the perovskite solid solution  $\text{La}_{0.67-x}\text{Li}_x\text{TiO}_3$  ( $x=0.11$ ). *Solid State Ionics*. 1999;121(1-4):245-51.
231. Fourquet JL, Duroy H, CrosnierLopez MP. Structural and microstructural studies of the series  $\text{La}_{2/3-x}\text{Li}_x$  square  $1/3-2\text{TiO}_3$ . *Journal of Solid State Chemistry*. 1996;127(2):283-94.

232. Ruiz AI, Lopez ML, Veiga ML, Pico C. Structural refinement by neutron diffraction of  $\text{La}_{1.12}\text{Li}_{0.62}\text{Ti}_2\text{O}_6$ . *Journal of Solid State Chemistry*. 1999;148(2):329-32.
233. Catti M. Ion mobility pathways of the  $\text{Li}^+$  conductor  $\text{Li}_{0.125}\text{La}_{0.625}\text{TiO}_3$  by ab initio simulations. *Journal of Physical Chemistry C*. 2008;112(29):11068-74.
234. Catti M. First-principles modeling of lithium ordering in the LLTO ( $\text{Li}_x\text{La}_{2/3-x}\text{TiO}_3$ ) superionic conductor. *Chemistry of Materials*. 2007;19(16):3963-72.
235. Garcia-Martin S, Alario-Franco MA, Ehrenberg H, Rodriguez-Carvajal J, Amador U. Crystal structure and microstructure of some  $\text{La}_{2/3-x}\text{Li}_x\text{TiO}_3$  oxides: An example of the complementary use of electron diffraction and microscopy and synchrotron X-ray diffraction to study complex materials. *Journal of the American Chemical Society*. 2004;126(11):3587-96.
236. Wu J, Chen LL, Song T, Zou ZY, Gao J, Zhang WQ, et al. A review on structural characteristics, lithium ion diffusion behavior and temperature dependence of conductivity in perovskite-type solid electrolyte  $\text{Li}_3\text{La}_{2/3-x}\text{TiO}_3$ . *Funct Mater Lett*. 2017;10(3).
237. John Purton, Private Communications, Daresbury Laboratory
238. Symington AR, Molinari M, Dawson JA, Statham JM, Purton J, Canepa P, et al. Elucidating the nature of grain boundary resistance in lithium lanthanum titanate. *Journal of Materials Chemistry A*. 2021;9(10):6487-98.
239. Metropolis N, Rosenbluth AW, Rosenbluth MN, Teller AH, Teller E. EQUATION OF STATE CALCULATIONS BY FAST COMPUTING MACHINES. *Journal of Chemical Physics*. 1953;21(6):1087-92.
240. Purton JA. Diffusion in gadolinium doped ceria thin films: a combined Monte Carlo and molecular dynamics study. *Physical Chemistry Chemical Physics*. 2019;21(19):9802-9.
241. Hu XB, Fisher CAJ, Kobayashi S, Ikuhara YH, Fujiwara Y, Hoshikawa K, et al. Atomic scale imaging of structural changes in solid electrolyte lanthanum lithium niobate upon annealing. *Acta Materialia*. 2017;127:211-9.
242. Zheng JQ, Li YF, Yang R, Li G, Ding XK. Lithium ion conductivity in the solid electrolytes  $(\text{Li}_{0.25}\text{La}_{0.25})(1-x)\text{MO}_{0.5}\text{NbO}_3$  ( $\text{M}=\text{Sr}, \text{Ba}, \text{Ca}, x=0.125$ ) with perovskite-type structure. *Ceramics International*. 2017;43(2):1716-21.
243. Brown HG, Ishikawa R, Sanchez-Santolino G, Lugg NR, Ikuhara Y, Allen LJ, et al. A new method to detect and correct sample tilt in scanning transmission electron microscopy bright-field imaging. *Ultramicroscopy*. 2017;173:76-83.
244. Hu XB, Kobayashi S, Ikuhara YH, Fisher CAJ, Fujiwara Y, Hoshikawa K, et al. Atomic scale imaging of structural variations in  $\text{La}_{(1-x)/3}\text{Li}_x\text{NbO}_3$  ( $0 \leq x \leq 0.13$ ) solid electrolytes. *Acta Materialia*. 2017;123:167-76.
245. Symington A. polypy - Analysis Tools for Solid State Molecular Dynamics and Monte Carlo Trajectories. *The Journal of Open Source Software*. 2021;6:2824.
246. Humphrey W, Dalke A, Schulten K. VMD: Visual molecular dynamics. *Journal of Molecular Graphics*. 1996;14(1):33-8.
247. Meier K, Laino T, Curioni A. Solid-State Electrolytes: Revealing the Mechanisms of Li-Ion Conduction in Tetragonal and Cubic LLZO by First-Principles Calculations. *Journal of Physical Chemistry C*. 2014;118(13):6668-79.
248. Cussen EJ. Structure and ionic conductivity in lithium garnets. *Journal of Materials Chemistry*. 2010;20(25):5167-73.
249. Awaka J, Takashima A, Kataoka K, Kijima N, Idemoto Y, Akimoto J. Crystal Structure of Fast Lithium-ion-conducting Cubic  $\text{Li}_7\text{La}_3\text{Zr}_2\text{O}_{12}$ . *Chem Lett*. 2011;40(1):60-2.
250. Yu S, Schmidt RD, Garcia-Mendez R, Herbert E, Dudney NJ, Wolfenstine JB, et al. Elastic Properties of the Solid Electrolyte  $\text{Li}_7\text{La}_3\text{Zr}_2\text{O}_{12}$  (LLZO). *Chemistry of Materials*. 2016;28(1):197-206.
251. Cheng EJ, Sharafi A, Sakamoto J. Intergranular Li metal propagation through polycrystalline  $\text{Li}_{6.25}\text{Al}_{0.25}\text{La}_3\text{Zr}_2\text{O}_{12}$  ceramic electrolyte. *Electrochimica Acta*. 2017;223:85-91.
252. Suzuki Y, Kami K, Watanabe K, Watanabe A, Saito N, Ohnishi T, et al. Transparent cubic garnet-type solid electrolyte of  $\text{Al}_2\text{O}_3$ -doped  $\text{Li}_7\text{La}_3\text{Zr}_2\text{O}_{12}$ . *Solid State Ionics*. 2015;278:172-6.

253. Monroe C, Newman J. The impact of elastic deformation on deposition kinetics at lithium/polymer interfaces. *Journal of the Electrochemical Society*. 2005;152(2):A396-A404.
254. Zhu YS, Connell JG, Tepavcevic S, Zapol P, Garcia-Mendez R, Taylor NJ, et al. Dopant-Dependent Stability of Garnet Solid Electrolyte Interfaces with Lithium Metal. *Adv Energy Mater*. 2019;9(12).
255. Smetaczek S, Wachter-Welzl A, Wagner R, Rettenwander D, Amthauer G, Andrejs L, et al. Local Li-ion conductivity changes within Al stabilized  $\text{Li}_7\text{La}_3\text{Zr}_2\text{O}_{12}$  and their relationship to three-dimensional variations of the bulk composition. *Journal of Materials Chemistry A*. 2019;7(12):6818-31.
256. Symington, A, Molinari, M, Dawson J A, Statham J M, Purton J, Canepa P, Parker S C, et al. Elucidating the nature of grain boundary resistance in lithium lanthanum titanate. *Journal of Materials Chemistry A*. 2021;9(10):6487-6498.
257. Adcock, A, McCammon, J, A. *Molecular Dynamics: Survey of Methods for Simulating the Activity of Proteins*. Chem. Rev. 2006, 106, 5, 1589-1675.

***“My philosophy is worrying means you suffer twice.”***

- Newt Scamander